

UNIVERSITY OF BIRMINGHAM

THE SIGNIFICANCE OF METHODOLOGY IN THE SYNTHESIS OF FRAMEWORK MATERIALS

by

JENNIFER HELEN ROBERTSON

A thesis submitted to the University of Birmingham for the degree of DOCTOR OF PHILOSOPHY

School of Chemistry
College of Engineering and Physical Science
University of Birmingham
June 2023

UNIVERSITY OF
BIRMINGHAM

University of Birmingham Research Archive

e-theses repository

This unpublished thesis/dissertation is copyright of the author and/or third parties. The intellectual property rights of the author or third parties in respect of this work are as defined by The Copyright Designs and Patents Act 1988 or as modified by any successor legislation.

Any use made of information contained in this thesis/dissertation must be in accordance with that legislation and must be properly acknowledged. Further distribution or reproduction in any format is prohibited without the permission of the copyright holder.

Abstract

In order to harness the diverse potential applications of framework materials it is necessary to understand how to efficiently and precisely control their structures and properties, and to develop robust, reproducible methods for their preparation. This thesis examines the synthesis and analysis of metal-organic frameworks and hydrogen-bonded materials, investigating how small variations in synthetic conditions and the use of different synthetic techniques influence the resulting structures. This work complements studies into the challenges of reproducibility in framework material synthesis, emphasising the importance of methodological consistency and highlighting the capability to leverage system sensitivity to control product outcomes.

Given the group's interest in studying reactivity within framework materials, Chapters 2 and 3 employ imidazolium-containing linkers, which offer exciting possibilities to study a wide range of chemistry within the framework environment if control over the identity of the resulting structures can be achieved.

Chapter 2 reports five new single crystal copper metal-organic framework (MOF) structures synthesised using 1,3-bis(4-carboxyphenyl)imidazolium compounds. Minor changes to the organic linker and adaptations to the crystallisation conditions were found to directly impact the structures formed. The new frameworks are described in detail and results analysed in context with existing structures in the literature.

Chapter 3 focuses on the synthesis of hydrogen-bonded organic frameworks, with five new structures produced using imidazolium-centred ligands. Strong carboxylate-amidinium hydrogen bonding interactions are leveraged in this work to produce highly crystalline frameworks. Influence over the resulting products was realised via methyl substitution at the imidazolium and controlled deprotonation of carboxylic acid groups. A potentially porous framework was synthesised through these adaptations and some preliminary explorations into the potential for metal complex incorporation were performed.

In Chapters 4 and 5 the capability of mechanochemistry to provide alternative routes for synthesis is explored in the context of hydrogen-bonded co-crystals and frameworks. Chapter 4 reports the development of a reliable methodology for the synthesis of a family of cyanuric acid and trithiocyanuric acid containing co-crystals using ball milling. Comparisons are drawn between the mechanochemical products and related co-crystals synthesised from solution.

Finally, Chapter 5 reports the use of mechanochemistry to synthesise a bulk-phase perylene diimide and melamine hydrogen-bonded organic framework. This result is particularly notable as this framework had until now been accessible only by surface deposition, as a thin layer. X-ray diffraction analysis in conjunction with computational modelling of predicted structures allowed the identification of the mechanochemical product as a layered honeycomb HOF. This work highlights the relevance of unconventional techniques for material discovery.

Acknowledgements

This thesis would not have been possible without support and guidance from a number of people. I would firstly like to thank Professor Neil Champness for his insight and encouragement throughout the past four years, and for supporting me in pursuing avenues of investigation that got me excited. Thank you also to the EPSRC and the University of Birmingham for providing funding for this work.

It has been an honour to collaborate through this time with some brilliant scientists. Thank you particularly to Dr Matthew Addicoat who performed the computational modelling of structures for Chapter 5. To Professor Paul Raithby, thank you for introducing me to the wonderful world of crystallography, and thanks to the crystallographers who then patiently helped me to develop my skills, namely Dr Louise Male and Dr Josh Deakin in Birmingham, and Dr Sarah Barnett, Dr Mark Warren and Dr David Allan at Diamond beamline i19.

To the wonderful postdocs who have taught me how to be a better scientist, I will be eternally grateful. Thank you for your unending patience in answering my (also unending) questions. Dr Georgia Orton and Dr Sarah Griffin, I can't name all the ways you have been invaluable. Just thank you. To Dr Nic Pearce, thank you for always being willing to help assign spectra and read abstracts or applications. Dr Javier Castells-Gil – I am immensely grateful for the time you took to teach me to refine my powder data.

Thank you to the past and present members of labs B52 in Nottingham and 610 in Birmingham for your camaraderie. A special mention goes to my fumehood neighbours Asia and Alex. Georgia, Danielle and Grady, your friendship and our wine nights kept me sane and have been an irrevocable joy in my life. To Benedict Parkes, thank you for your hard work building the foundations of the research reported in Chapter 4 and for being a model Master's student.

Dr Chiara Arno, thank you for your mentorship over the last year, I really would have found reaching this stage so much harder without your reassurance. Jodie, friend, I wouldn't have wanted to have started and gone through this journey with anyone else. Thank you for being there through the highs and lows, near or far.

To my family - especially Dad, Mum, Judith and Jo - thank you for always pushing me forwards and building me up. This would not have been possible without you behind me. Finally, to Max, my wonderful husband-to-be, thank you for allowing me to chase my dreams and following me around the country to wherever they have taken me. Thank you for your quiet assurance and for never missing an opportunity to laugh either with or at me.

Abbreviations

MOF	Metal-organic framework
COF	Covalent organic framework
HOF	Hydrogen-bonded organic framework
CCDC	Cambridge Crystallographic Data Centre
CSD	Cambridge Structural Database
NHC	N-Heterocyclic carbene
SBU	Secondary building unit
PSM	Post-synthetic modification
LAG	Liquid-assisted grinding
TM	Transition metal
OLED	Organic light-emitting diode
ICT	Inter-ligand charge transfer
SCXRD	Single-crystal X-ray diffraction
PXRD	Powder X-ray diffraction
NMR	Nuclear magnetic resonance
FTIR	Fourier transform infrared
TGA	Thermogravimetric analysis
SEM	Scanning electron microscopy
DMF	N,N-Dimethylformamide
DEF	N,N-Diethylformamide
DMA	N,N-Dimethylacetamide
NMP	N-Methylpyrrolidone
DCM	Dichloromethane
MeOH	Methanol
THF	Tetrahydrofuran
MeCN	Acetonitrile
DMEDA	1,2-Dimethylethylenediamine
CA	Cyanuric acid
TCA	Trithiocyanuric acid
M	Melamine
DPE	Trans-1,2-bis(4-pyridyl)ethene
BPY	4,4’-Bipyridine
TAZ	1,3,5-Triazine
PAZ	Pyrazine
PTCDI	3,4,9,10-Perylene tetracarboxylic diimide
NTCDI	1,4,5,8-Naphthalene tetracarboxylic diimide
RT	Room temperature
w.r.t.	With respect to

Table of Contents

The Significance of Methodology in the Synthesis of Framework Materials i

Abstract ii

Acknowledgements iv

Abbreviations v

Table of Contents vi

1 CHAPTER ONE: Introduction 1

1.1 Framework Materials 1

1.2 Metal-Organic Frameworks 2

1.3 Hydrogen-Bonded Organic Frameworks 16

1.4 Co-Crystals 21

1.5 Mechanochemical Synthesis 25

1.6 N-Heterocyclic Carbenes 29

1.7 Aims 33

1.8 References 35

2 CHAPTER TWO: Copper 1,3-bis(4-carboxyphenyl)imidazolium MOFs 46

2.1 Introduction 46

2.2 Aims 49

2.3 Results and Discussion 50

2.4 Conclusions 76

2.5 Experimental 78

2.6 References 95

3 CHAPTER THREE: Imidazolium-functionalised amidinium-carboxylate HOFs.....97

3.1 Introduction.....97

3.2 Aims.....100

3.3 Results and Discussion.....101

3.4 Conclusions.....123

3.5 Experimental.....124

3.6 References.....143

4 CHAPTER FOUR: Mechanochemical synthesis of co-crystals.....145

4.1 Introduction.....145

4.2 Aims.....147

4.3 Results And Discussion.....147

4.4 Conclusions.....179

4.5 Experimental.....181

4.6 References.....186

5 CHAPTER FIVE: Mechanochemical synthesis of a PTCDI/Melamine HOF.....188

5.1 Introduction.....188

5.2 Aims.....190

5.3 Results and Discussion.....190

5.4 Conclusions.....204

5.5 Experimental.....205

5.6 References.....207

6 CONCLUSIONS.....209

7 APPENDIX.....212

1 CHAPTER ONE

Introduction

1.1 Framework Materials

Supramolecular chemistry is a broad research area, often described as "chemistry beyond the molecule". It spans many scientific disciplines including biological, physical, inorganic and materials chemistry, and involves the study of molecular assembly via non-covalent interactions and the properties of the resultant materials.[1] Host-guest chemistry is a defining element of supramolecular chemistry, involving the binding of one molecular entity in the cavity of another by some attractive forces to form, or to template formation of, the overall assembly.[2]

Framework material synthesis and study of their behaviour comes under the umbrella of supramolecular chemistry. Framework materials can describe a range of structures, including metal-organic frameworks (MOFs), covalent organic frameworks (COFs) and hydrogen-bonded organic frameworks (HOFs). These structures, as implied by their names, differ in the bonding used for their construction. All may be described as the "host" component of a host-guest structure and have tuneable properties which influence the guest molecules that may be present.

1.2 Metal-Organic Frameworks

1.2.1 History

Metal-organic frameworks (MOFs), also known as porous coordination polymers (PCPs) are arguably the most heavily studied class of framework materials. The name stems from the components used to build these structures – networks of metal ions or clusters are interconnected by coordinating organic ligands, which are frequently referred to as linkers.[3,4] MOFs vary hugely in terms of structures and uses.[5,6] They can be highly stable materials, able to withstand high temperature conditions and a variety of chemical environments.[7] Early examples of MOFs can be traced back to the 1960s, and in the late 1980s they were reintroduced by Hoskins and Robson, who proposed a new class of materials that could be made by linking octahedral or tetrahedral centres together using "rod-like" structures.[8,9] They reported an early example of a MOF in the same paper (Figure 1.1A). The term "metal-organic framework" was not used until 1995 however, and was coined by Yaghi, who is widely considered a pioneer of MOF chemistry.[10] The publication of two MOF structures in particular sparked wider interest in these materials and set off the increase in popularity of the field over the past 25 years.[11] Both were published in 1999: HKUST-1, a copper MOF reported by Williams (Figure 1.1B); and MOF-5, a zinc framework published by Yaghi (Figure 1.1C).[12,13] These structures were particularly notable due to their structural robustness as well as high

surface area and porosity, which for the first time were comparable with, or greater than, that of zeolites, the previous "gold-standard" porous material.[14]

Tens of thousands of MOF structures have now been reported, and the number of publications pertaining to MOF chemistry continues to increase year on year.[15]

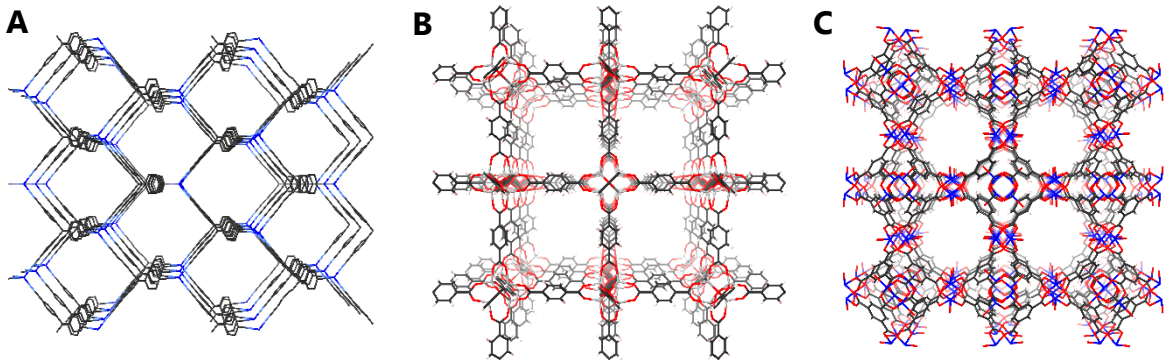


Figure 1.1: Structures of (A) Hoskins and Robson's MOF (B) HKUST-1 (C) MOF-5. Figures reproduced from CCDC depositions 1182897, 112954 and 256965 respectively. [8,12,13]

1.2.2 Ligand design

The organic linkers used for synthesising MOFs are varied, and the linker chosen to make a particular framework depends on the intended purpose of the material and the properties required. They do however often share similar features. A major consideration is the type and number of terminal groups which are intended as coordination sites for the metal ions. Many early MOFs were synthesised using linkers with nitrogen-based connecting groups, particularly pyridyl groups, for example 4,4'-bipyridine (Figure 1.2A).[16] These are still commonly used, however carboxylate groups have generally become the group of choice.[17] A major reason for this is the fact that

they can form stronger bonds with metal ions, which often leads to more structurally robust MOFs.[18] Well-known examples of carboxylate linkers include benzene-1,4-dicarboxylate (Figure 1.2B) and benzene-1,3,5-tricarboxylate (Figure 1.2C).[19–21] Denticity, in the context of MOF ligands, can be described as the "*number of donor interactions they make with an individual metal centre or cluster"* and topicity as the *"number of different sites at which they coordinate"*.[22] Ligand topicity and denticity, in conjunction with the choice of metal node, influence the dimensionality of the framework formed.

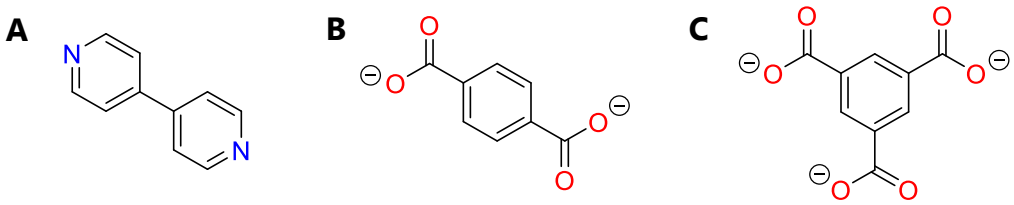


Figure 1.2: Common MOF ligands (A) 4,4'-bipyridine (B) benzene 1,4-dicarboxylic acid (C) benzene 1,3,5-tricarboxylic acid.

The main body of linkers varies considerably more than the terminal groups. It is common for linkers to contain phenyl rings, which provide a degree of structural rigidity, as well as predictability in terms of the geometry of the coordinating groups and other functional groups.[17] These phenyl rings can also relatively easily be functionalised, the benefits of which will be discussed later in more detail. Additionally, the length of a linker can influence the structure of a MOF, particularly the surface area and porosity, with longer linkers having the potential to give rise to larger pore size (within moderation – more on this in section 1.2.4).[23,24]

1.2.3 Metals

MOFs have been synthesised using a wide range of metals from all parts of the periodic table, but transition metals are by far the most commonly used.[25] As stated previously, the coordination number and geometry of the metal chosen heavily influences the structure of the resulting MOF.[26] Different metals can also impart different properties on the framework. For example, zirconium and other group 4 metals are known for forming particularly stable MOFs, due to their high charge density leading to strong metal-oxygen bonds.[27]

1.2.4 Dimensionality, Interpenetration and Catenation

Due to the vast range of metal and organic components that can be used to synthesise MOFs, there is an almost infinite number of potential frameworks. MOFs may exist as 1-dimensional chains, 2-dimensional sheets or fully interconnected 3-dimensional frameworks, depending on the connectivity of the metal node(s) and organic linker(s). A fundamental tool used for predicting the topology of a MOF is secondary building units (SBUs). SBUs are strongly bonded metal-oxo clusters which are formed by the coordination of linker carboxylate groups to a metal cation in-situ during synthesis.[28,29] These SBUs are connected to each other by the organic sections of the linkers. This offers an alternative, and potentially simpler, way to consider the structure of MOFs. SBUs have fixed geometry and thus MOFs with the same SBU are likely to share the same topology provided the geometry of the linking molecule is the same.[30]

Isoreticular series are groups of MOFs which share the same network topology.[31] Variations in the length and/or functionality of the organic sections can lead to differences in porosity and functionality between frameworks in an isoreticular series, whilst retaining the same overall structure and connectivity.[14] The first reported and most widely known example of an isoreticular series of MOFs is the IRMOF series which is based on the structure of MOF-5 and utilises an octahedral $Zn_4O(CO_2)_6$ SBU (Figure 1.3).[29,31]

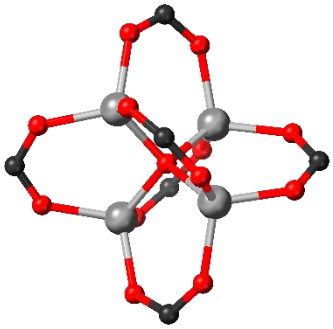


Figure 1.3: $Zn_4O(CO_2)_6$ SBU used in the IRMOF isoreticular series. Reproduced from CCDC deposition 256965. Atom colours: carbon = black, oxygen = red, zinc = silver.

The overall structure of a MOF doesn't solely depend on the metal-linker coordination bonds. 1D and 2D MOFs can assemble into extended 3D structures by taking advantage of intermolecular interactions such as hydrogen-bonding and π-π stacking.[32] Frameworks may assemble via layering, interpenetration or polycatenation. Interpenetration is a widely known phenomenon in MOF chemistry, which involves the growth of one or more frameworks inside the pores of another. It is common when using longer-length linkers in attempts to synthesise MOFs with larger pore sizes, as it reduces the amount of thermodynamically unfavourable free void space in a structure.[32,33]

Polycatenation is arguably less well known, and the distinction between the two is not always made.[34] The major distinguishing factor between interpenetration and polycatenation is that the former results in an extended structure of the same dimensionality as that of its components, whereas the latter results in an increase in dimensionality compared with the components (Figure 1.4).[35] Additionally, interpenetration involves entanglement of a finite number of components, whereas in polycatenation the number of components is infinite. For example, IRMOF-9, reported Yaghi et al. in 2002 is a 3D interpenetrated MOF which is constructed from two interlinked cubic 3D nets.[31] The framework $[Zn(azpy)_2(H_2O)_2]SiF_6$, reported by Proserpio et al. in 1998 is a 3D structure composed of catenated 2D nets.[36]

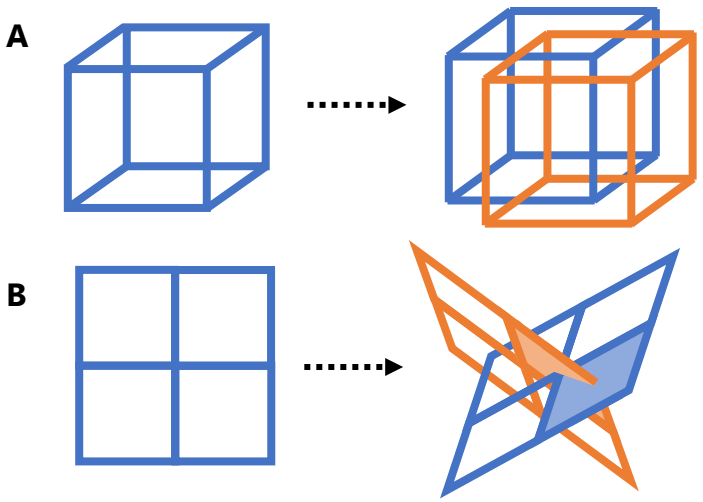


Figure 1.4: Schematics illustrating (A) interpenetration and (B) polycatenation. (A) was adapted from Ref. 37 with permission from the author. (B) was adapted from Ref. 38 with permission from the Royal Society of Chemistry.

Structures with these interwoven characteristics can be considered undesirable to some researchers due to the reduction in porosity, however for certain applications this can be favourable. Interpenetration and polycatenation can increase selectivity to guest

molecules, which is beneficial in applications such as separation and sensing.[39,40] They can also introduce interesting properties such as magnetism, as is seen for example in a cobalt(II) MOF reported by Cao et al. in 2016.[41] The ability to control the degree of interpenetration or polycatenation is of interest for the reasons stated above, with tactics often involving modification of the length and bulkiness of the linkers employed in framework synthesis.[42,43]

1.2.5 Synthesis

A variety of methods have been used to synthesise MOFs. The most common is solvothermal synthesis, which involves heating a reaction mixture of solvent, linker and metal salt for a period of time, which can range from hours to days, until crystallisation occurs.[44]

N,N′-Dimethylformamide (DMF) and other amide bases such as N,N′-dimethylacetamide (DMA) and N-methyl-2-pyrrolidone (NMP) are commonly used as a solvents in MOF synthesis. There are a number of reasons for this, including their high polarity which aid dissolution of the starting materials, and high boiling points which facilitate synthesis at raised temperatures.[45] Another benefit of using these types of solvents is that they undergo a degree of thermal decomposition at these raised temperatures, producing weakly basic amines which are slowly released into the reaction mixture.[46] This aids deprotonation of the carboxylate binding groups on the organic linker and thus encourages coordination to metal ions. Mixed-solvent systems

can also be used, particularly when solubility is an issue. At times these systems can be biphasic, in which the metal salt is dissolved in a polar solvent and the organic linker is soluble in a non-polar solvent, and in these cases, crystallisation can occur at the phase boundary.[47,48]

Once a suitable synthetic procedure has been developed for synthesising a particular material, it is important to be consistent in the method used. Even very small changes to the reaction conditions can have a significant impact on the material formed and can result in the formation of frameworks with different topologies, a reduction in crystallinity or even a complete lack of crystalline material.[45]

The synthesis of MOFs as single crystals is beneficial as it allows in-depth structure determination and analysis by single-crystal X-ray diffraction. It can however be difficult to find conditions suitable for single crystal growth to occur. Use of monotopic coordinating species, known as modulators, can be used in some syntheses to aid formation of single crystals, by competing with the linkers for coordination to the metal ion and thus slowing the rate of crystallisation.[49,50] Mono-carboxylic acids such as benzoic and acetic acid are commonly used, and these have the additional benefit of aiding the formation of the SBU.[51,52] Amino acids such as L-proline have also been found to be effective modulators for zirconium and hafnium MOFs.[53]

Other methods for MOF synthesis include microwave and mechanochemical techniques, the latter of which will be discussed in more detail later in this chapter.[54,55]

1.2.6 Properties

As implied by their alternative name, porous coordination polymers, porosity is an important property of MOFs, and these materials frequently have surface areas of 1000-7000 m^2g^{-1}.[56] As-synthesised, MOFs retain solvent guest molecules in the void space of the structure, and the process of removing these guest molecules is known as activation.[57] Supercritical CO_2 is commonly used for activation, as well as heating under vacuum.[58] Permanently porous frameworks are those which retain crystallinity and porosity upon activation. Many early MOFs contained large pores upon synthesis, however the frameworks collapsed upon activation which reduced their potential for use in practical applications (Figure 1.5).[59] Since the use of carboxylate connecting groups on linkers has increased however, MOFs with permanent porosity have become more common due to the strength of the metal-ligand bonds.[18] Thermogravimetric analysis (TGA) is often used in conjunction with powder X-ray diffraction (PXRD) in order to establish the thermal stability of a framework - TGA determines the temperatures at which solvent removal and framework decomposition occur, and variable temperature PXRD allows assessment of the crystallinity of the framework throughout the heating process.[60]

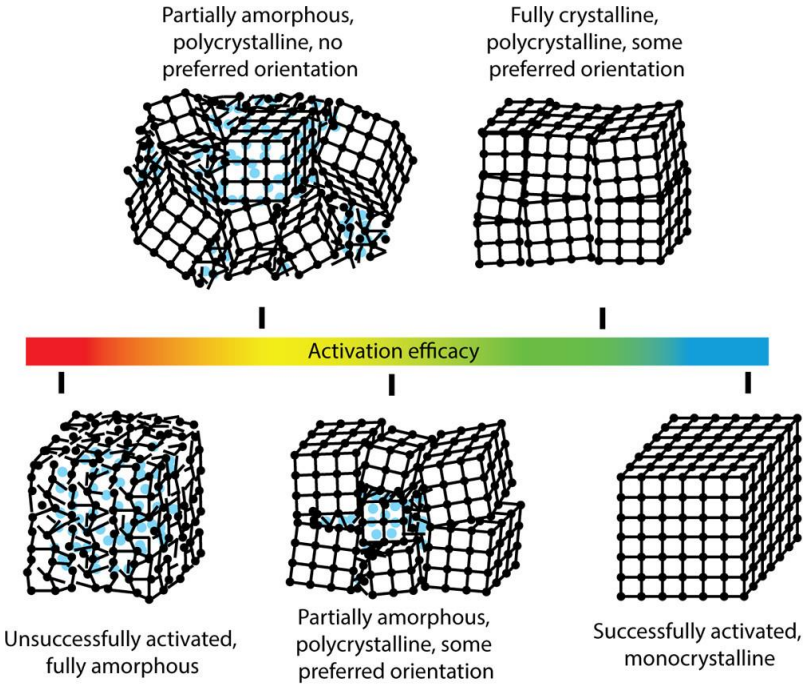


Figure 1.5: Schematic illustrating framework the potential outcomes of MOF activation. Reprinted with permission from Ref. 61. Copyright 2018 American Chemical Society.

MOFs additionally tend to be chemically robust, and able to retain their structure under harsh conditions. This chemical stability again depends to a significant degree upon the stability of the SBU, as decomposition often occurs via breaking of the metal-linker bonds.[62] In some cases, digestion in concentrated acid is required to break down frameworks into their component parts. Zirconium oxalate frameworks are good examples of chemically stable MOFs.[63]

1.2.7 Post-Synthetic Modification (PSM)

The physical and chemical properties of MOFs can be relatively easily tuned, which is a major advantage of these materials. One way to achieve this is by designing functionalised organic linkers and using these to synthesise frameworks with the

desired properties for their intended application.[64,65] There are cases however where the direct synthesis of a desired framework is not possible, for example in situations where the linker would not withstand the conditions of the MOF synthesis, or where a functional group would interfere with the formation of the MOF.[66] In these cases, the ability of MOFs to undergo post-synthetic modification (PSM) is important.

Post-synthetic modification can come in many forms, including ion and solvent exchange in the pores, and even the exchange of metals in the SBU or of the original linker after the framework has been formed.[67–70] Another type is the modification of groups on the organic linker. A vast range of chemistry can be applied to this, such as condensations, reductions and click reactions.[71] An early example of this type of PSM was the reaction of the amine group on the NH_2-BDC linker of IRMOF-3 with acetic anhydride, for conversion to an amide (Figure 1.6).[72]

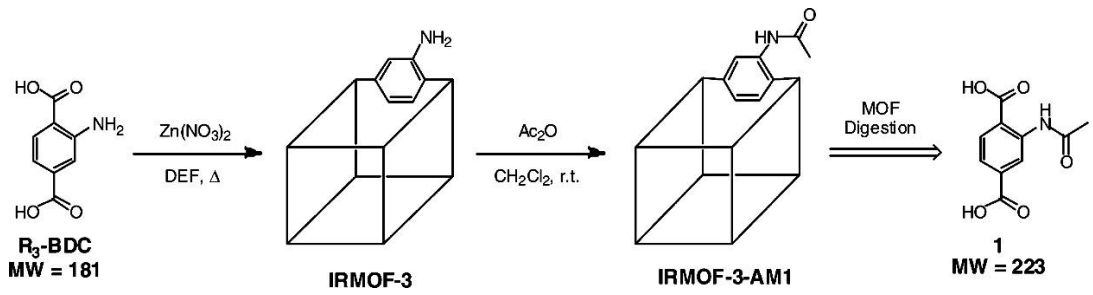


Figure 1.6: Post-synthetic modification of IRMOF-3 with acetic anhydride. Reproduced with permission from Ref. 72. Copyright 2007 American Chemical Society.

1.2.8 Applications

The high porosity and stability of MOFs combined with their ease of customisation with respect to chemical functionality and physical properties makes them attractive candidates for research into practical applications.

The largest areas of research for applications of MOFs are catalysis and gas storage. Catalytic reactions inside MOF pores can make use of active sites on the organic linkers or the metal nodes.[73] MOFs have been shown to act as catalysts for a variety of reactions, including additions, oxidations and coupling reactions.[74–76] For example, HKUST-1 ($[Cu_3(btc)_2]_n$, (btc = benzene-1,3,5-tricarboxylate)) has been shown to act as a Lewis acid catalyst, making use of free coordination sites on the Cu(II) ions which are made available upon solvent removal.[77] For uses of MOFs in gas storage and separation, much of the research has focussed on environmentally beneficial applications such as removal of CO_2 from the atmosphere and H_2 storage for renewable energy.[14,78] One example of a MOF that has a high hydrogen uptake capacity is NU-100 ($[Cu_3(L)(H_2O)_3]_n$, L = 1,3,5-tris[(1,3-carboxylate-5-(4-(ethynyl)phenyl))ethynyl]-benzene)), which can store up to 10% of the MOF's weight in H_2.[79,80]

The ability to finely tune the selectivity of MOFs for particular guest molecules is of benefit in both of these major applications. There are several factors which contribute to the selectivity of MOFs. The size and shape of guest molecules that can move in and out of a host framework is limited physically by the dimensions of the pores, and in

some cases this can be enhanced by framework interpenetration.[81] Host-guest interactions in terms of intermolecular forces or bonding interactions can also be a very large contributor to selectivity and activity of MOFs.[82] Frameworks can be specifically designed therefore to interact favourably with the desired guest molecules, for example for selective gas separation.[83]

Potential uses for MOFs beyond catalysis and gas storage are wide-ranging, with increasing amounts of research being conducted into novel applications for these materials. A relatively new area of research involves using MOFs as scaffolds to investigate the mechanisms of chemical processes. In the field of molecular crystals, the practice of using single crystal X-ray diffraction (SCXRD) to study single crystal to single crystal transformations of metal complexes is well established.[84–86] A significant advantage of using SCXRD is that any changes in the crystal structure can be analysed in great detail. Metal complexes can be anchored in the pores of MOFs, and this presents an opportunity to extend this field of research to gain insight into species and processes that would not usually be possible to analyse by SCXRD.

There are several methods by which metal species of interest may be incorporated into MOFs. Firstly, reactive sites at metal nodes can be exposed by post-synthetic modification, for example by exchanging the node cation itself (Figure 1.7A) or by coordinating a reactive species to the node.[87] The organic linker can also be used as the binding site for the complex, either by pre-metalation of the linker and direct synthesis of the desired framework (Figure 1.7B) or by post-synthetic metalation of the

linker (Figure 1.7C).[88,89] Finally, metal species or aggregates can be grown or encapsulated within the pores, stabilised by the pore chemical or physical environment (Figure 1.7D).[90]

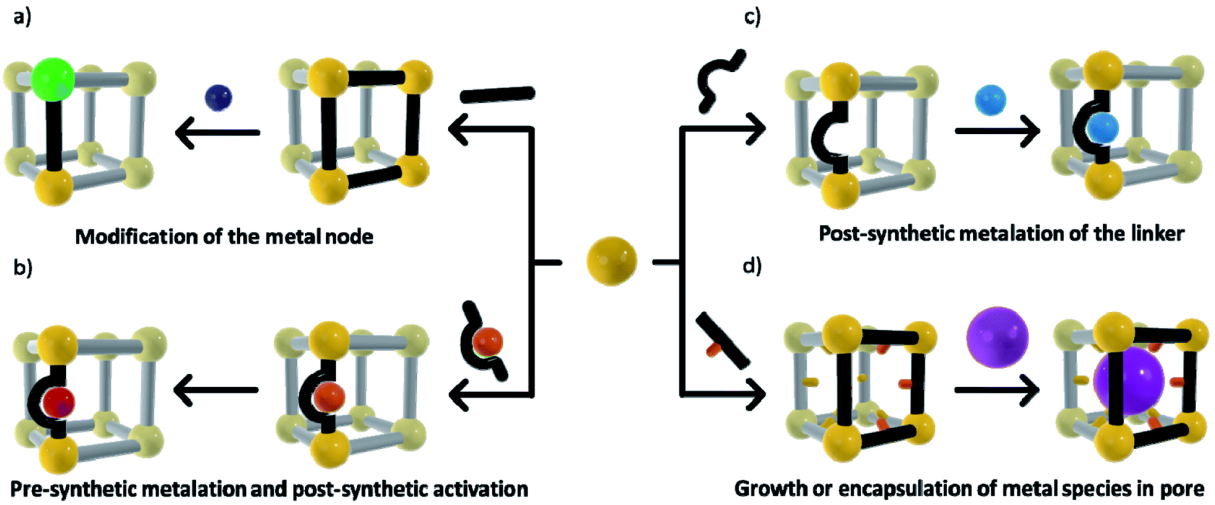


Figure 1.7: Schematic showing methods for isolating metal species in MOFs: (a) Modification of/at the metal node (b) Pre-synthetic metalation of the linker (c) Post-synthetic metalation of the linker (d) Growth or encapsulation of metal species in the pore. Reproduced from Ref. 91 with permission from the Royal Society of Chemistry.

Although it is possible to synthesise MOFs containing a range of metal complexes, there are often challenges in analysing the metalated frameworks. This is particularly an issue where the reactive species is located at the metal node, as these sites are often on special positions within the unit cell meaning that quantitative post-synthetic modification is required to avoid averaging out of the coordination environment in the resulting SCXRD structure.[91] Metalating at linker sites generally overcomes this problem, however there are often still challenges simply due to difficulties in obtaining

single crystals of the metalated MOF and maintaining that crystallinity in the reacting/reacted species.

Despite these obstacles there are examples of systems for which it has been possible to follow reactions by SCXRD. A manganese-based MOF containing a bis(4-(4-carboxyphenyl)-1*H*-3,5-dimethylpyrazolyl)methane linker (Figure 1.8) has been used as a matrix within which reactions of several complexes have been studied, from structural rearrangements of Co(II) complexes to organometallic catalysis with Rh(I) species.[92–95] Success in retaining crystallinity of the MOF structure throughout metalation and subsequent processes has been attributed to the flexibility of the linker, and by extension, of the MOF. This flexibility allows the framework to adapt the size and shape of the pores in order to reduce any strain caused by changes within the structure.[96]

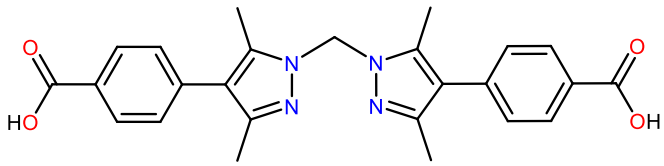


Figure 1.8: Bis(4-(4-carboxyphenyl)-1*H*-3,5-dimethylpyrazolyl)methane linker

1.3 Hydrogen-Bonded Organic Frameworks

1.3.1 History

Hydrogen-bonded organic frameworks (HOFs) are porous crystalline materials composed entirely of organic molecules, arranged into a crystalline structure held together by intermolecular hydrogen-bonding interactions.[97] The crystal structure of

trimesic acid, reported in 1969 by Marsh and Duchamp, is widely cited as the first example of a HOF.[98] In the 1990s Wuest et al. developed an approach known as molecular tectonics to aid in the design of HOF materials.[99,100] This involves the use of organic building blocks with rigid geometries to construct frameworks, a technique which is still highly relevant in the design of new porous materials.[100] It was close to another 20 years however before permanent porosity was demonstrated in these materials. In 2010 Schroder et al. reported a material they named SOF-1 (Figure 1.9A) (SOF being an acronym for supramolecular organic framework), constructed from a tetrapyridyl-terminated anthracene compound, which could withstand solvent removal via heating.[101] Soon after this, in 2011 Chen et al. showed that HOF-1, the structure originally reported by Wuest et al. as Tecton 1 (Figure 1.9B), is also stable to solvent removal and that the evacuated framework can be used for gas separation.[102,103] Incidentally, this publication was also the first example of the term HOF being used to describe this type of material.

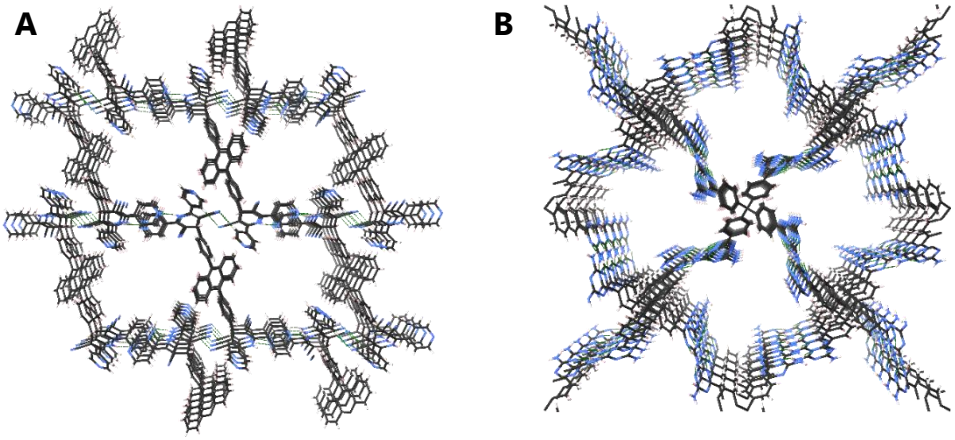


Figure 1.9: (A) SOF-1 (B) HOF-1. Figures produced from CCDC depositions 822582 and 1250560 respectively. Atom colours: carbon = black; hydrogen = pink; nitrogen = blue. Hydrogen bonds are represented as green dashed lines.

1.3.2 Design

Clearly an important consideration in the design of HOFs is the functional group(s) employed to elicit the attractive interactions which lead to framework construction. The concept of "supramolecular synthons" as used in crystal engineering is commonly leveraged in the selection of functional groups for HOF synthesis.[97,104] Supramolecular synthons are structural units with directionality, arising from complementary intermolecular interactions.[105,106] Common examples include the carboxylic acid dimer, carboxylic acid-pyridine, amide-acid and nitro-iodo synthons (Figure 1.10).

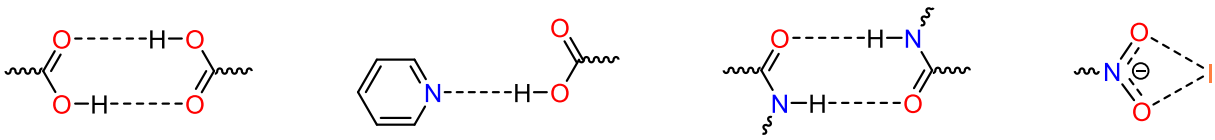


Figure 1.10: Examples of supramolecular synthons. From left to right: carboxylic acid dimer; carboxylic acid-pyridine; amide dimer; nitro-iodo.[107]

The molecular tectonics approach introduced by Wuest et al. pairs the concept of supramolecular synthons with carefully designed molecular cores that have rigid geometries.[108] The aim is to design molecules that "*cannot normally form crystals in which packing and specific directional interactions are both optimized at the same time*".[109] The desired outcome is for the strong intermolecular interactions of the synthons to be preferred over close packing, increasing the likelihood of producing a porous framework.[110] Although hydrogen bonding is the major source of structural

interactions in HOFs, additional intermolecular forces, most notably π-π stacking, often provide additional stabilisation, particularly in 2-dimensional frameworks.[111–113]

Another method employed to increase the robustness of HOFs is the use of supramolecular synthons formed from charge-assisted hydrogen bonding interactions.[114,115] Examples of effective functional group pairings include pyridinium-carboxylate, amidinium-carboxylate and guanidinium-sulfonate (Figure 1.11).[116–118] Due to the use of different functional groups, it is common for frameworks constructed using these synthons to be composed of two different building blocks, as opposed to the single component HOFs which have been discussed to this point.[119] Charge-assisted hydrogen bonding is expanded upon in Chapter 3.

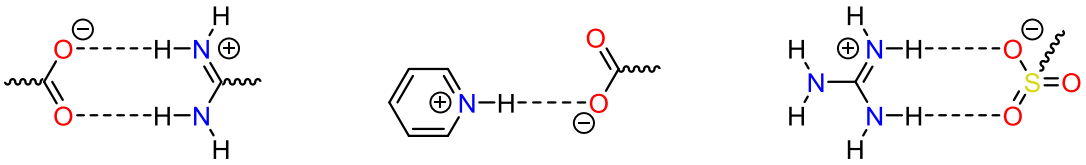


Figure 1.11: Examples of some charge-assisted supramolecular synthons utilised in HOF synthesis. From left to right: Carboxylate-amidinium; pyridinium-carboxylate; guanidinium-sulfonate.

1.3.3 Synthesis and Properties

HOFs tend to be synthesised using milder conditions than the solvothermal method used for MOFs. Synthesis via room-temperature recrystallisation or co-crystallisation of building blocks from solution is the most common method by which HOFs are obtained.[119] Liquid/vapour diffusion, solvothermal and electrophoretic deposition have also been employed more recently.[120–123]

Hydrogen bonds are the strongest form of non-covalent interaction, however they remain relatively weak in comparison with covalent and coordinate bonds. This creates both advantages and disadvantages in HOF materials. It can be challenging to synthesise permanently porous HOFs, with frameworks having a tendency to collapse upon removal of solvent molecules.[101,102] They also tend to be less able to withstand harsh conditions than MOFs and COFs.[111] On the other hand, as hydrogen-bond formation is reversible, HOFs can often be dissolved and regenerated from solution, a property precluded in structures reliant on covalent bonds.[124] The reversible nature of the interactions aids the formation of highly crystalline materials, as structures are amenable to self-healing during crystal growth.[125] Growth of single crystals is highly advantageous to many studies, as it enables detailed structural analysis by single-crystal X-ray diffraction.

Like MOFs, the properties of HOFs may be tuned for desired applications. In some cases this arises from the strategic selection of supramolecular synthons. For example, HOFs constructed from acid-base pairs (charge-assisted synthons) have been shown to be effective proton transfer agents.[114,115] More recently, the concept of isoreticular chemistry as earlier discussed with respect to MOFs has been applied to HOFs by Farha et al.. A series of HOFs based on HOF-101 (Figure 1.12A), first reported as PFC-1, were synthesised using analogous linkers with a range of functionalities on the phenyl rings attached to the pyrene core of the building block (Figure 1.12B).[112,126] The fluorinated

analogue of this structure was shown to exhibit impressive antibacterial properties when used as a coating on textiles.[126]

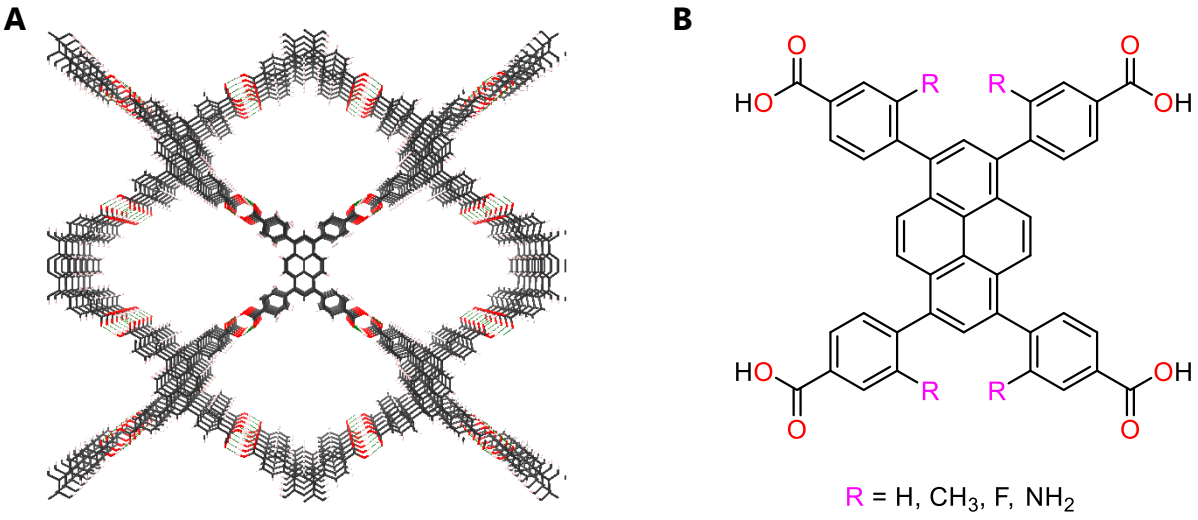


Figure 1.12: (A) Crystal structure of HOF-101. Atom colours: carbon = black; hydrogen = pink; oxygen = red. Figure reproduced from CCDC deposition 1826763. (B) Tectons used in synthesising HOF-101 and analogues.

1.4 Co-Crystals

1.4.1 History, Terminology and Applications

In 2012 a publication by 45 authors arising from an Indo–U.S. Bilateral Meeting entitled "The Evolving Role of Solid State Chemistry in Pharmaceutical Science" in the same year put forth a suggested definition of co-crystals as *"solids that are crystalline single phase materials composed of two or more different molecular and/or ionic compounds generally in a stoichiometric ratio"*.[127] This definition includes salts under the remit of co-crystals, a matter which is much debated. A 2018 book on co-crystals presented a flowchart (Figure 1.13) in which solvates, hydrates and salts were each distinguished

from co-crystals.[128] It remains common however for the term co-crystal to be used to describe each of these types of material.

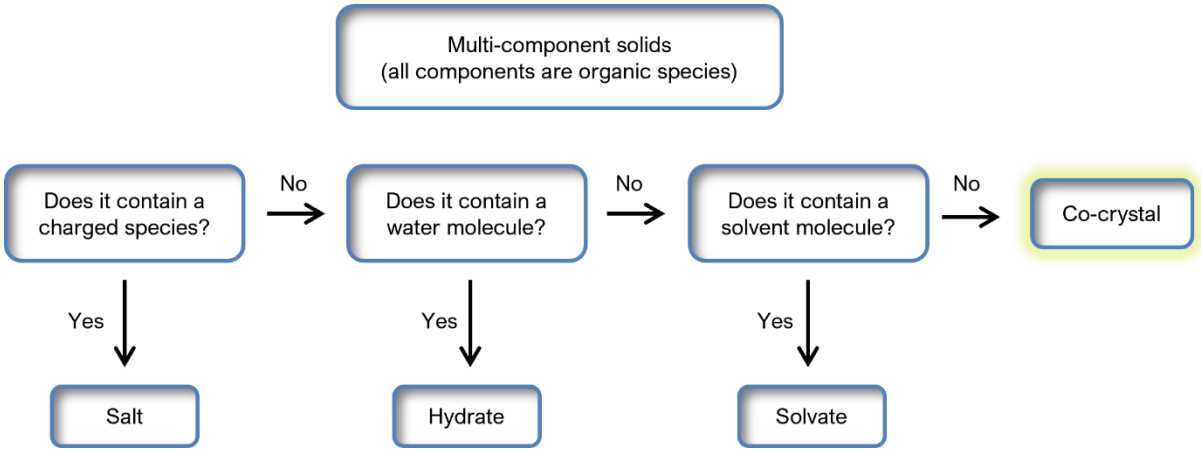


Figure 1.13: Flowchart classifying multi-component organic solids. Reproduced from Ref. 128 with permission from the Royal Society of Chemistry.

The crystallisation of quinhydrone, from solutions of quinone and hydroquinone, by Friedrich Wöhler in 1844, was the first example of a co-crystal.[129] It was more than 100 years after its discovery that the crystal structure of quinhydrone was published, by Osaki et al. (Figure 1.14).[130] Large numbers of co-crystals were published in that time frame, including many considered for pharmaceutical and other commercial applications.[131] It was found that the properties of multicomponent materials could differ from those of the individual components, particularly with respect to solubilities. For example, Kranz et al. reported that a glycine co-crystal of sodium theophyllinate was more water soluble than theophylline independently.[132] The pharmaceutical potential of co-crystals was increasingly investigated in the latter half of the 20th century. Aqueous dissolution rates were investigated for a range of co-crystals

containing known active pharmaceutical ingredients (APIs), with a recognised potential link between these measurements and bioavailability.[133,134] In addition to pharmaceutical research, co-crystals have also been created for applications in a wide range of other fields including textiles and agriculture.[135–139]

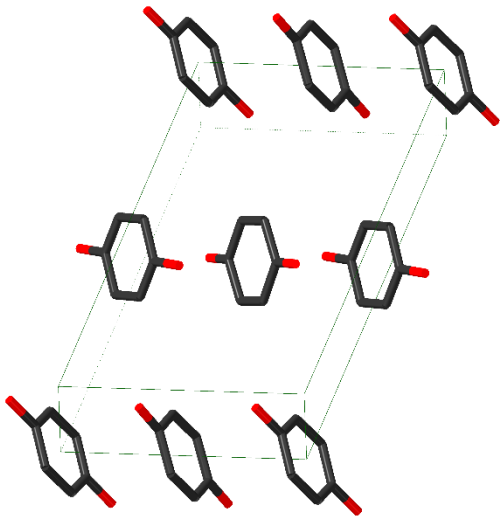


Figure 1.14: First reported crystal structure of quinhydrone.[130] Reproduced from CCDC deposition 1245606.

1.4.2 Design and Synthesis

For many years after the first report of a co-crystal, the modes of interaction of the components were not well understood, partially due to the lack of capability to determine the structure. Several suggestions as to the structure of quinhydrone were made by different researchers before the X-ray structural solution was published in 1958.[130,140–142] Nowadays understanding of intermolecular interactions is far greater,

which allows crystal engineering principles to be used in the design of these materials. These principles align with those described previously in the context of HOFs.

The Cambridge Structural Database (CSD) contains comprehensive records of published small molecule crystal structures.[143] It is a valuable tool in many respects, with associated programmes which allow systematic searching of the database, as well as visualisation and analysis of the results.[144–146] Data mining of the CSD is a common starting point for co-crystal studies in the modern day.[128] This facilitates the selection of suitable synthons in the design of co-crystals with certain desired properties, by interrogation of the functional group(s) and likely intermolecular interactions.[147]

Even with careful planning and consideration, the structure of co-crystals is not always predictable. Polymorphism is common, as well as the inclusion of additional molecules to form solvates and hydrates.[148] Polymorphism in the context of co-crystals is the formation of unique crystal structures from the same component molecules. Polymorphs of the same system can exhibit different properties and behaviour, thus it can be an important factor to consider in co-crystal studies.[148] For example, in a study concerning caffeine hydration, two polymorphs of caffeine and glutaric acid were found to exhibit significantly different stabilities to hydration when exposed to environments of controlled humidities. [149] The formation of polymorphs often arises from the use of different methods or conditions in the synthesis of the materials.[150,151]

Both solid-state and solution-based methods are commonly employed for the synthesis of co-crystals.[152] Mechanochemical grinding techniques have been used

since the late 19th century, with further developments made by Paul and Curtin, as well as Etter et al., in the 1990s.[153–157] Solution-based methods are more common, in part due to the higher likelihood of single-crystal growth which allows for in-depth structural analysis by SCXRD. Co-crystallisation from solution is often performed by evaporation, antisolvent addition or cooling, amongst others.[158–162] Variables such as solvent, component concentrations and temperature can be manipulated in order to produce desired structures.

1.5 Mechanochemical Synthesis

1.5.1 History and Principles

Solid-state synthesis techniques have been known and used for hundreds of years, but there has recently been a marked increase in research in the field.[163] Motivations for the renewed interest in these methods come in a large part from the increasing global concern for the environment - mechanochemical techniques often require less solvent and reduced energy input compared with reactions in the solution phase.[163] Historically the underlying principles surrounding solid-state reactions have not been well understood, however modern techniques and technologies have opened up the potential to gain new insights.[164] Techniques such as X-ray crystallography and Raman spectroscopy are used to monitor reactions in-situ in order to deepen understanding of the processes as they occur.[165–168]

Mechanochemical synthesis is a primarily solid-state technique, although small quantities of solvent are sometimes added to perform liquid-assisted grinding (LAG), also referred to as solvent drop grinding. The inclusion of solvent in the reaction vessel has been shown in some cases to increase reaction efficiency, as well as to control the crystalline phase produced.[169–172] For example, in a study using caffeine and glutamic acid, Jones et al. reported that LAG using added cyclohexane produced a majority of one polymorph, form I, whilst the addition of chloroform to the grinding mixture produced a different phase, form II.[173]

1.5.2 Equipment

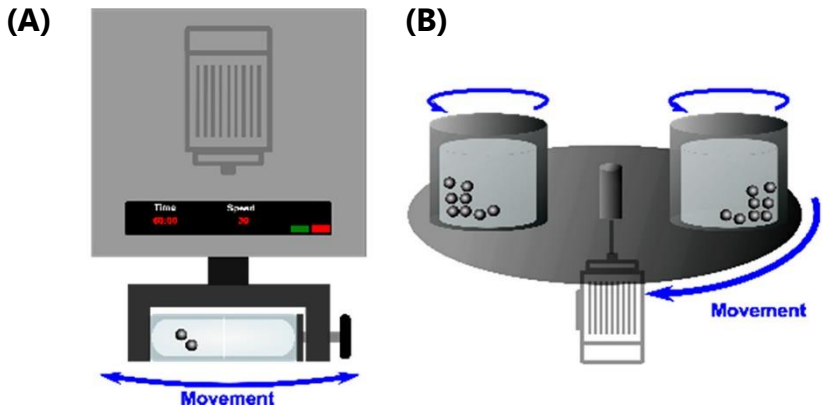


Figure 1.15: Schematic showing different types of ball mill and the movement of milling jars for each. (A) Shaker mill (B) Planetary mill. Reproduced with permission from Ref. 174. Copyright 2022 American Chemical Society.

A variety of techniques fall under the umbrella of mechanochemistry, including manual grinding, extrusion, and ball milling.[174] Ball milling involves mixing of solid starting materials and small amounts of liquid, if required, in a jar along with ball bearings which

produce impact and aid mixing of the reagents. Jars and balls can be made of a variety of materials, with common options including stainless steel and zirconium oxide. Planetary mills and shaker mills are commonly used apparatus (Figure 1.15). Mixer mills work via a simple mechanism, vibrating back and forth at a defined frequency. Planetary mills rotate around a central axis, with each jar additionally rotating on its own axis (Figure 1.16).[175] Variables such as jar size, fill ratio of material to jar volume, and the number of balls may be experimented with to tune the reaction conditions.[174]

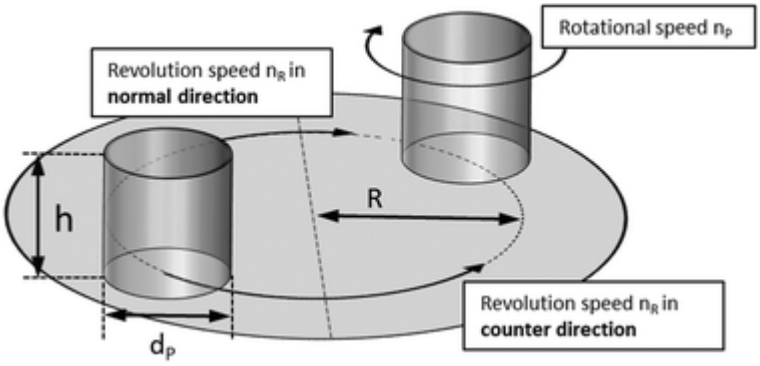


Figure 1.16: Schematic showing modes of rotation in a planetary ball mill. Reproduced from Ref. 175 with permission from the Royal Society of Chemistry.

1.5.3 Applications

Materials from simple organics, through hybrid materials to inorganics have been synthesised using mechanochemistry.[176–182] As previously alluded to, green chemistry is a significant driving force behind the development of mechanochemical methodology. A significant reduction in solvent requirements as well as a shorter reaction time is advantageous both environmentally and economically.[183] For

applications such as pharmaceuticals, in which products may be designed for consumption, the capability to perform solvent-free syntheses is of additional benefit in removal of a potentially harmful component of production.[184]

An early example of a mechanochemically prepared co-crystal was reported in 1945 by Bailey et al., who produced a 1:1 adduct of nicotinamide and ascorbic acid (vitamin C and vitamin B3).[185] A study in 2019 on the same system focused on optimising methods for scaled-up industrial processes as well as controlling the morphology of the co-crystals (Figure 1.17).[186] Another interesting recent study employed temperature control whilst milling to manage polymorphism in glutamic acid and isonicotinamide co-crystals.[187] Metal-organic frameworks such as UiO-66 have also been synthesised using ball milling techniques.[188] The ability to monitor reactions in-situ by powder X-ray crystallography, such as in experiments performed on MOF-74 by Vaqueiro et al., provides opportunities to gain new insights into the mechanism by which framework formation occurs.[189]

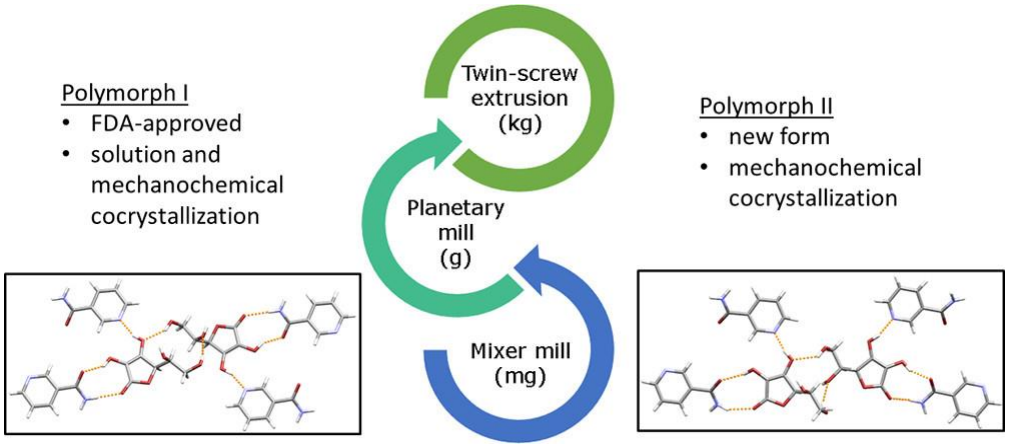


Figure 1.17: Schematic illustrating polymorphs of asorbic acid and nicotinamide co-crystals and mechanochemical techniques used at different scales. Reprinted with permission from Ref. 186. Copyright 2019 American Chemical Society.

Mechanochemistry has additionally proved to be valuable in permitting access to chemicals that are inaccessible via solution-state chemistry. An early example of this was the use of mechanochemical techniques to isolate a family of organic reactive intermediates previously believed to be unisolable, reported in 2015 by Friščić et al.[190]

1.6 N-Heterocyclic Carbenes

Compounds containing precursors to N-heterocyclic carbenes (NHCs) are used as linkers for MOF and HOF synthesis in Chapters 2 and 3 of this thesis.

Carbenes were long considered as reaction intermediates which existed only as transient species. However, in 1991 Arduengo et al. reported the first isolable and *"bottleable"* carbene, which made way for significant further research into these compounds.[191] Arduengo's carbene (Figure 1.18) is an example of an N-heterocyclic

carbene (NHC). The carbene in these species is stabilised by both inductive and mesomeric effects from the nitrogen atoms, and many NHCs also benefit from additional steric stabilisation from bulky side groups.[192]

NHCs are most commonly observed as ligands in transition metal (TM) complexes, and these were known long before Arduengo's discovery of the first stable NHC. The first examples of NHC-TM complexes were published in the late 1960s by Wanzlick and Öfele, independently, and nowadays NHC complexes of every transition metal have been synthesised.[193–195]

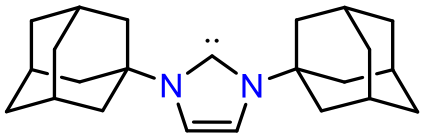


Figure 1.18: Arduengo's carbene

Some NHC-TM complexes display photoluminescence, which is a property of interest to some work presented in Chapter 3 of this thesis. In recent years research into photoluminescent NHC complexes has placed emphasis on their potential for use in OLED devices. In current OLED devices, complexes of heavy metals such as iridium and platinum are widely used as dopants to increase the efficiency of light emission.[196,197] Use of these metals is not ideal however, due to their high prices and toxicity. A class of NHC-TM complexes known as carbene-metal-amides can display highly efficient photoluminescence and have thus been identified as alternatives to heavy metal dopants. The potential of these compounds for use in OLEDs was first investigated in

2017 by Di et al., who proposed that the efficiency of light emission from these complexes is dependent on the relative rotation of the two ligands about the metal centre.[198] This study prompted the development of many more examples of carbene-metal-amide complexes, within which the use of carbazole as the amide ligand is common.[199–201]

For example, a series of NHC-Cu(I)-carbazole complexes were reported in 2019 by Shi et al. (Figure 1.19).[202] These molecules show high levels of photoluminescence, which is attributed to intramolecular, inter-ligand charge transfer (ICT) between the approximately coplanar ligands.[203] The donor ability of the carbazole and acceptor ability of the carbene was shown to impact the energy of the ICT emission, which allowed tuning of the ICT energy, and thus the colour of the light emitted alongside other luminescence-related properties of these complexes.

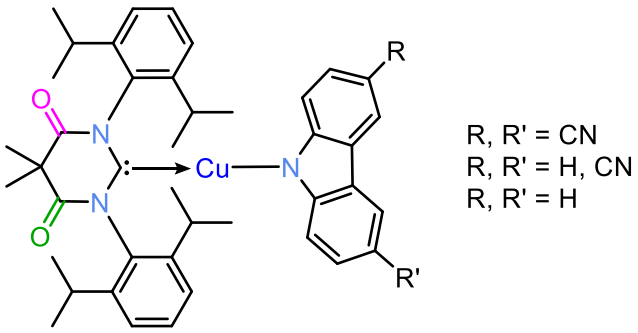


Figure 1.19: Representation of NHC-Cu(I)-carbazole complexes synthesised by Shi et al. Six complexes were studied, with varying R groups and number of carbonyl groups. Reprinted with permission from Ref. 202. Copyright 2019 American Chemical Society.

There are several examples of NHC-containing MOFs, many of which utilise imidazolium linkers.[204] A number of these MOFs were synthesised with catalytic

applications in mind, making the inclusion of metal complexes in the pores relevant.[205–208] As mentioned previously, there are several routes to complex-containing MOFs. NHC-complex containing MOFs have been made by direct synthesis of the framework using the NHC-metal complex as the linker, or by use of an NHC precursor as the linker followed by PSM to bind the metal (Figure 1.20).[209]

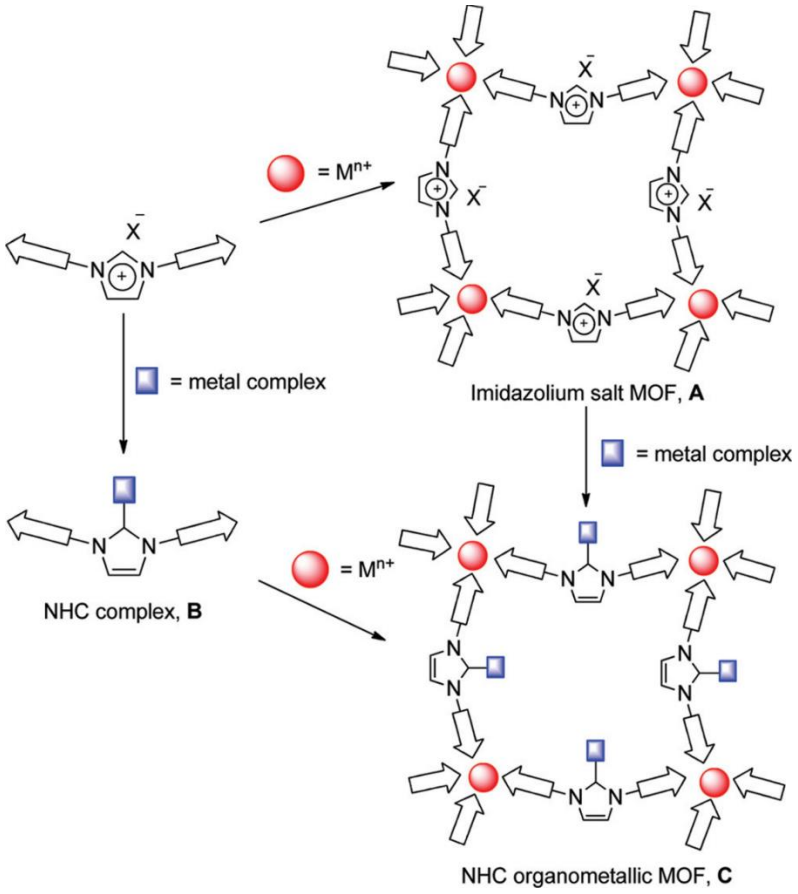


Figure 1.20: Potential synthetic pathways to NHC-complex containing MOFs. Reproduced with permission from Ref. 209. Copyright 2010 American Chemical Society.

1.7 Aims

The research presented in this thesis is dedicated to the synthesis and analysis of a range of metal-organic and hydrogen-bonded materials. The focus of this work was to probe the complex relationship between synthetic conditions and techniques and their influence on resulting structures.

In Chapters 2 and 3 imidazolium-containing carboxylate ligands are employed in solution-phase syntheses of single crystal MOFs and HOFs. The primary aim of these chapters was to explore the range of supramolecular architectures that can be formed through the systematic variation of synthetic parameters, which in turn makes way for tailored framework production.

The work performed in Chapter 2 aimed to consolidate and expand upon the results of several reported copper MOF syntheses, performing studies using equivalent linkers to probe the variety of structures accessible by adjusting variables such as solvent, counterion and reaction duration. In Chapter 3 we aimed to synthesise imidazolium-containing HOFs by exploiting strong charge-assisted hydrogen-bonding interactions between carboxylate and amidinium functional groups. A secondary interest behind the use of imidazolium linkers in these studies is the potential for expansion into future studies relating to incorporation of NHC-metal complexes tethered to the framework architecture.

Chapters 4 and 5 revolve around the use of mechanochemical techniques for the preparation of co-crystals and HOFs. In Chapter 4 we aimed to develop a reliable methodology for the synthesis of a range of 2-component co-crystal systems. This would then make way for comparisons to be drawn between the structures formed from the mechanochemical procedures and reported solution-phase crystallisations. Chapter 5 develops on the co-crystal work and utilises the insights gained therein to develop a method for the production of the first known example of a mechanochemically synthesised 2-component HOF.

Through these research projects, this thesis aims to shed light on the intricacy and sensitivity of framework synthesis; to leverage this for structural control; and to emphasise the relevance and importance of applying non-conventional synthetic techniques for the formation of new as well as known materials. The specific aims for each chapter are given in more detail in their respective introduction sections.

1.8 References

1 J. W. Steed and J. L. Atwood, in *Supramolecular Chemistry*, John Wiley & Sons, Incorporated, Hoboken, N.J., 2009, pp. 1–48.

2 P. Beer, T. Barendt and J. Lim, in *Supramolecular Chemistry: Fundamentals and Applications*, Oxford University Press, Oxford, 2022, pp. 70–89.

3 H.-C. Zhou and S. Kitagawa, *Chem Soc Rev*, 2014, **43**, 5415–5418.

4 S. R. Batten, N. R. Champness, X.-M. Chen, J. Garcia-Martinez, S. Kitagawa, L. Öhrström, M. O'Keeffe, M. P. Suh and J. Reedijk, *CrystEngComm*, 2012, **14**, 3001–3004.

5 H.-C. Zhou, J. R. Long and O. M. Yaghi, *Chem Rev*, 2012, **112**, 673–674.

6 L. Ma, C. Abney and W. Lin, *Chem Soc Rev*, 2009, **38**, 1248–1256.

7 A. J. Howarth, Y. Liu, P. Li, Z. Li, T. C. Wang, J. T. Hupp and O. K. Farha, *Nat Rev Mater*, 2016, **1**, 15018.

8 B. F. Hoskins and R. Robson, *J Am Chem Soc*, 1989, **111**, 5962–5964.

9 E. A. Tomic, *J Appl Polym Sci*, 1965, **9**, 3745–3752.

10 O. M. Yaghi and H. Li, *J Am Chem Soc*, 1995, **117**, 10401–10402.

11 O. Vaughan, *Nature*, 2014, **511**, 19.

12 H. Li, M. Eddaoudi, M. O'Keeffe and O. M. Yaghi, *Nature*, 1999, **402**, 276–279.

13 S. S.-Y. Chui, S. M.-F. Lo, J. P. H. Charmant, A. G. Orpen and I. D. Williams, *Science*, 1999, **283**, 1148–1150.

14 H. Furukawa, K. E. Cordova, M. O'Keeffe and O. M. Yaghi, *Science*, 2013, **341**, 1230444.

15 J. R. Long and O. M. Yaghi, *Chem Soc Rev*, 2009, **38**, 1213–1214.

16 M. Fujita, Y. J. Kwon, S. Washizu and K. Ogura, *J Am Chem Soc*, 1994, **116**, 1151–1152.

17 W. Lu, Z. Wei, Z.-Y. Gu, T.-F. Liu, J. Park, J. Park, J. Tian, M. Zhang, Q. Zhang, T. Gentle III, M. Bosch and H.-C. Zhou, *Chem Soc Rev*, 2014, **43**, 5561–5593.

18 J. L. C. Rowsell and O. M. Yaghi, *Microporous Mesoporous Mater*, 2004, **73**, 3–14.

19 M. O'Keeffe, M. Eddaoudi, H. Li, T. Reineke and O. M. Yaghi, *J Solid State Chem*, 2000, **152**, 3–20.

20 O. M. Yaghi, H. Li and T. L. Groy, *J Am Chem Soc*, 1996, **118**, 9096–9101.

21 H. Li, M. Eddaoudi, T. L. Groy and O. M. Yaghi, *J Am Chem Soc*, 1998, **120**, 8571–8572.

22 B. S. Pilgrim and N. R. Champness, *Chempluschem*, 2020, **85**, 1842–1856.

23 D. Sun, Y. Ke, T. M. Mattox, S. Parkin and H.-C. Zhou, *Inorg Chem*, 2006, **45**, 7566–7568.

24 S. Bureekaew, V. Balwani, S. Amirjalayer and R. Schmid, *CrystEngComm*, 2015, **17**, 344–352.

25 S. L. Griffin and N. R. Champness, *Coord Chem Rev*, 2020, **414**, 213295.

26 R. J. Hill, D.-L. Long, N. R. Champness, P. Hubberstey and M. Schröder, *Acc Chem Res*, 2005, **38**, 335–348.

27 S. Yuan, J.-S. Qin, C. T. Lollar and H.-C. Zhou, *ACS Cent Sci*, 2018, **4**, 440–450.

28 M. Eddaoudi, D. B. Moler, H. Li, B. Chen, T. M. Reineke, M. O'Keeffe and O. M. Yaghi, *Acc Chem Res*, 2001, **34**, 319–330.

29 O. M. Yaghi, M. O'Keeffe, N. W. Ockwig, H. K. Chae, M. Eddaoudi and J. Kim, *Nature*, 2003, **423**, 705–714.

30 A. Schoedel and O. M. Yaghi, in *The Chemistry of Metal-Organic Frameworks: Synthesis, Characterization and Applications*, ed. S. Kaskel, Wiley VCH, Weinheim, Germany, 2016, vol. 1, pp. 41–72.

31 M. Eddaoudi, J. Kim, N. Rosi, D. Vodak, J. Wachter, M. O'Keeffe and O. M. Yaghi, *Science*, 2002, **295**, 469–472.

32 S. Kitagawa, R. Kitaura and S. Noro, *Angew Chem Int Ed*, 2004, **43**, 2334–2375.

33 S. R. Batten and R. Robson, *Angew Chem Int Ed*, 1998, **37**, 1460–1494.

34 Y.-N. Gong, D.-C. Zhong and T.-B. Lu, *CrystEngComm*, 2016, **18**, 2596–2606.

35 L. Carlucci, G. Ciani and D. M. Proserpio, *Coord Chem Rev*, 2003, **246**, 247–289.

36 L. Carlucci, G. Ciani and D. M. Proserpio, *New J Chem*, 1998, **22**, 1319–1321.

37 S. Griffin, PhD Thesis, University of Glasgow, 2019.

38 E. v Alexandrov, V. A. Blatov and D. M. Proserpio, *CrystEngComm*, 2017, **19**, 1993–2006.

39 D. Rani, K. K. Bhasin and M. Singh, *Dalton Trans*, 2021, **50**, 13430–13437.

40 B. Li, X. Cui, D. O'Nolan, H.-M. Wen, M. Jiang, R. Krishna, H. Wu, R.-B. Lin, Y.-S. Chen, D. Yuan, H. Xing, W. Zhou, Q. Ren, G. Qian, M. J. Zaworotko and B. Chen, *Adv Mater*, 2017, **29**, 1704210.

41 B. Xu, X. Lin, Z. He, Z. Lin and R. Cao, *Chem Comm*, 2011, **47**, 3766–3768.

42 A. Ferguson, L. Liu, S. J. Tapperwijn, D. Perl, F.-X. Coudert, S. Van Cleuvenbergen, T. Verbiest, M. A. van der Veen and S. G. Telfer, *Nat Chem*, 2016, **8**, 250–257.

43 M. Gupta and J. J. Vittal, *Coord Chem Rev*, 2021, **435**, 213789.

44 C. P. Raptopoulou, *Materials*, 2021, **14**, 310.

45 N. Stock and S. Biswas, *Chem Rev*, 2012, **112**, 933–969.

46 M. M. Heravi, M. Ghavidel and L. Mohammadkhani, *RSC Adv*, 2018, **8**, 27832–27862.

47 D. Banerjee, H. Wang, B. J. Deibert and J. Li, in *The Chemistry of Metal–Organic Frameworks*, 2016, pp. 73–103.

48 P. M. Forster, P. M. Thomas and A. K. Cheetham, *Chem Mater*, 2002, **14**, 17–20.

49 T. Liu, Y. Liu, L. Yao, W. Yang, L. Tian, H. Liu, D. Liu and C. Wang, *Nanoscale*, 2018, **10**, 13194–13201.

50 J. Park, Z. U. Wang, L.-B. Sun, Y.-P. Chen and H.-C. Zhou, *J Am Chem Soc*, 2012, **134**, 20110–20116.

51 B. Bueken, H. Reinsch, N. Reimer, I. Stassen, F. Vermoortele, R. Ameloot, N. Stock, C. E. A. Kirschhock and D. de Vos, *Chem Comm*, 2014, **50**, 10055–10058.

52 A. Schaate, P. Roy, A. Godt, J. Lippke, F. Waltz, M. Wiebcke and P. Behrens, *Chem Eur J*, 2011, **17**, 6643–6651.

53 R. J. Marshall, C. L. Hobday, C. F. Murphie, S. L. Griffin, C. A. Morrison, S. A. Moggach and R. S. Forgan, *J Mater Chem A Mater*, 2016, **4**, 6955–6963.

54 S. Głowniak, B. Szczęśniak, J. Choma and M. Jaroniec, *Mater Today*, 2021, **46**, 109–124.

55 I. Thomas-Hillman, A. Laybourn, C. Dodds and S. W. Kingman, *J Mater Chem A Mater*, 2018, **6**, 11564–11581.

56 O. K. Farha, I. Eryazici, N. C. Jeong, B. G. Hauser, C. E. Wilmer, A. A. Sarjeant, R. Q. Snurr, S. T. Nguyen, A. Ö. Yazaydın and J. T. Hupp, *J Am Chem Soc*, 2012, **134**, 15016–15021.

57 J. E. Mondloch, O. Karagiaridi, O. K. Farha and J. T. Hupp, *CrystEngComm*, 2013, **15**, 9258–9264.

58 X. Zhang, Z. Chen, X. Liu, S. L. Hanna, X. Wang, R. Taheri-Ledari, A. Maleki, P. Li and O. K. Farha, *Chem Soc Rev*, 2020, **49**, 7406–7427.

59 S. Kitagawa and M. Kondo, *Bull Chem Soc Jpn*, 1998, **71**, 1739–1753.

60 D. D. Kachhadiya, A. V. Sonawane and Z. V. P. Murthy, in *Metal-Organic Frameworks (MOFs) as Catalysts*, ed. S. Gulati, Springer Nature Singapore, Singapore, 2022, pp. 165–180.

61 R. A. Dodson, A. G. Wong-Foy and A. J. Matzger, *Chem Mater*, 2018, **30**, 6559–6565.

62 I. J. Kang, N. A. Khan, E. Haque and S. H. Jhung, *Chem Eur J*, 2011, **17**, 6437–6442.

63 J. H. Cavka, S. Jakobsen, U. Olsbye, N. Guillou, C. Lamberti, S. Bordiga and K. P. Lillerud, *J Am Chem Soc*, 2008, **130**, 13850–13851.

64 R. Banerjee, H. Furukawa, D. Britt, C. Knobler, M. O'Keeffe and O. M. Yaghi, *J Am Chem Soc*, 2009, **131**, 3875–3877.

65 T. Devic, P. Horcajada, C. Serre, F. Salles, G. Maurin, B. Moulin, D. Heurtaux, G. Clet, A. Vimont, J.-M. Grenèche, B. le Ouay, F. Moreau, E. Magnier, Y. Filinchuk, J. Marrot, J.-C. Lavalley, M. Daturi and G. Férey, *J Am Chem Soc*, 2010, **132**, 1127–1136.

66 Z. Wang and S. M. Cohen, *Chem Soc Rev*, 2009, **38**, 1315–1329.

67 J. An and N. L. Rosi, *J Am Chem Soc*, 2010, **132**, 5578–5579.

68 G. Calleja, J. A. Botas, M. Sánchez-Sánchez and M. G. Orcajo, *Int J Hydrogen Energy*, 2010, **35**, 9916–9923.

69 M. Lalonde, W. Bury, O. Karagiaridi, Z. Brown, J. T. Hupp and O. K. Farha, *J Mater Chem A Mater*, 2013, **1**, 5453–5468.

70 O. Karagiaridi, W. Bury, J. E. Mondloch, J. T. Hupp and O. K. Farha, *Angew Chem Int Ed*, 2014, **53**, 4530–4540.

71 S. M. Cohen, *Chem Rev*, 2012, **112**, 970–1000.

72 Z. Wang and S. M. Cohen, *J Am Chem Soc*, 2007, **129**, 12368–12369.

73 J. Lee, O. K. Farha, J. Roberts, K. A. Scheidt, S. T. Nguyen and J. T. Hupp, *Chem Soc Rev*, 2009, **38**, 1450–1459.

74 A. Phan, A. U. Czaja, F. Gándara, C. B. Knobler and O. M. Yaghi, *Inorg Chem*, 2011, **50**, 7388–7390.

75 Y. Lu, M. Tonigold, B. Bredenkötter, D. Volkmer, J. Hitzbleck and G. Langstein, *Z Anorg Allg Chem*, 2008, **634**, 2411–2417.

76 B. Xiao, H. Hou and Y. Fan, *J Organomet Chem*, 2007, **692**, 2014–2020.

77 L. Alaerts, E. Séguin, H. Poelman, F. Thibault-Starzyk, P. A. Jacobs and D. E. de Vos, *Chem Eur J*, 2006, **12**, 7353–7363.

78 D. J. Collins, S. Ma and H.-C. Zhou, in *Metal-Organic Frameworks: Design and Application*, ed. L. R. MacGillivray, John Wiley & Sons, Incorporated, Hoboken, N.J., 2010, pp. 249–266.

79 O. K. Farha, A. Özgür Yazaydın, I. Eryazici, C. D. Malliakas, B. G. Hauser, M. G. Kanatzidis, S. T. Nguyen, R. Q. Snurr and J. T. Hupp, *Nat Chem*, 2010, **2**, 944–948.

80 A. Ahmed, S. Seth, J. Purewal, A. G. Wong-Foy, M. Veenstra, A. J. Matzger and D. J. Siegel, *Nat Commun*, 2019, **10**, 1568.

81 H. Kim, H. Chun and K. Kim, in *Metal-Organic Frameworks: Design and Application*, ed. L. R. MacGillivray, John Wiley & Sons, Inc., Hoboken, N.J., 2010, pp. 215–248.

82 D. Yang and B. C. Gates, *ACS Catal*, 2019, **9**, 1779–1798.

83 D. Farrusseng, S. Aguado and C. Pinel, *Angew Chem Int Ed*, 2009, **48**, 7502–7513.

84 M. D. Carducci, M. R. Pressprich and P. Coppens, *J Am Chem Soc*, 1997, **119**, 2669–2678.

85 M. E. van der Boom, *Angew Chem Int Ed*, 2011, **50**, 11846–11848.

86 M. Kawano, Y. Kobayashi, T. Ozeki and M. Fujita, *J Am Chem Soc*, 2006, **128**, 6558–6559.

87 C. K. Brozek and M. Dincă, *Chem Soc Rev*, 2014, **43**, 5456–5467.

88 J. D. Evans, C. J. Sumby and C. J. Doonan, *Chem Soc Rev*, 2014, **43**, 5933–5951.

89 C. A. Kent, B. P. Mehl, L. Ma, J. M. Papanikolas, T. J. Meyer and W. Lin, *J Am Chem Soc*, 2010, **132**, 12767–12769.

90 K. Ikemoto, Y. Inokuma, K. Rissanen and M. Fujita, *J Am Chem Soc*, 2014, **136**, 6892–6895.

91 R. J. Young, M. T. Huxley, E. Pardo, N. R. Champness, C. J. Sumby and C. J. Doonan, *Chem Sci*, 2020, 11, 4031–4050.

92 W. M. Bloch, A. Burgun, C. J. Coghlan, R. Lee, M. L. Coote, C. J. Doonan and C. J. Sumby, *Nat Chem*, 2014, **6**, 906–912.

93 M. Huxley, C. J. Coghlan, A. Burgun, A. Tarzia, K. Sumida, C. J. Sumby and C. J. Doonan, *Dalton Trans*, 2016, **45**, 4431–4438.

94 A. Burgun, C. J. Coghlan, D. M. Huang, W. Chen, S. Horike, S. Kitagawa, J. F. Alvino, G. F. Metha, C. J. Sumby and C. J. Doonan, *Angew Chem Int Ed*, 2017, **56**, 8412–8416.

95 M. T. Huxley, C. J. Coghlan, W. M. Bloch, A. Burgun, C. J. Doonan and C. J. Sumby, *Phil Trans R Soc A*, 2017, **375**, 20160028.

96 Michael. T. Huxley, A. Burgun, H. Ghodrati, C. J. Coghlan, A. Lemieux, N. R. Champness, D. M. Huang, C. J. Doonan and C. J. Sumby, *J Am Chem Soc*, 2018, **140**, 6416–6425.

97 P. Li, M. R. Ryder and J. F. Stoddart, *Acc Mater Res*, 2020, **1**, 77–87.

98 D. J. Duchamp and R. E. Marsh, *Acta Crystallogr B*, 1969, **25**, 5–19.

99 X. Wang, M. Simard and J. D. Wuest, *J Am Chem Soc*, 1994, **116**, 12119–12120.

100 M. Simard, D. Su and J. D. Wuest, *J Am Chem Soc*, 1991, **113**, 4696–4698.

101 W. Yang, A. Greenaway, X. Lin, R. Matsuda, A. J. Blake, C. Wilson, W. Lewis, P. Hubberstey, S. Kitagawa, N. R. Champness and M. Schröder, *J Am Chem Soc*, 2010, **132**, 14457–14469.

102 Y. He, S. Xiang and B. Chen, *J Am Chem Soc*, 2011, **133**, 14570–14573.

103 P. Brunet, M. Simard and J. D. Wuest, *J Am Chem Soc*, 1997, **119**, 2737–2738.

104 G. R. Desiraju, J. J. Vittal and A. Ramanan, *Crystal Engineering: A Textbook*, World Scientific Publishing Company, Singapore, 2011.

105 D. S. Reddy, Y. E. Ovchinnikov, O. V Shishkin, Y. T. Struchkov and G. R. Desiraju, *J Am Chem Soc*, 1996, **118**, 4085–4089.

106 G. R. Desiraju, *Angew Chem Int Ed*, 1995, **34**, 2311–2327.

107 G. R. Desiraju, *J Am Chem Soc*, 2013, **135**, 9952–9967.

108 S. A. Boer, M. Morshedi, A. Tarzia, C. J. Doonan and N. G. White, *Chem Eur J*, 2019, **25**, 10006–10012.

109 J. D. Wuest, *Chem Comm*, 2005, 5830–5837.

110 P. J. Langley and J. Hulliger, *Chem Soc Rev*, 1999, **28**, 279–291.

111 K. Ma, P. Li, J. H. Xin, Y. Chen, Z. Chen, S. Goswami, X. Liu, S. Kato, H. Chen, X. Zhang, J. Bai, M. C. Wasson, R. R. Maldonado, R. Q. Snurr and O. K. Farha, *Cell Rep Phys Sci*, 2020, **1**, 100024.

112 Q. Yin, P. Zhao, R.-J. Sa, G.-C. Chen, J. Lü, T.-F. Liu and R. Cao, *Angew Chem Int Ed*, 2018, **57**, 7691–7696.

113 T.-H. Chen, I. Popov, W. Kaveevivitchai, Y.-C. Chuang, Y.-S. Chen, O. Daugulis, A. J. Jacobson and O. Š. Miljanić, *Nat Commun*, 2014, **5**, 5131.

114 G. Xing, T. Yan, S. Das, T. Ben and S. Qiu, *Angew Chem Int Ed*, 2018, **57**, 5345–5349.

115 M.-J. Wei, Y. Gao, K. Li, B. Li, J.-Q. Fu, H.-Y. Zang, K.-Z. Shao and Z.-M. Su, *CrystEngComm*, 2019, **21**, 4996–5001.

116 W. Liang, F. Carraro, M. B. Solomon, S. G. Bell, H. Amenitsch, C. J. Sumby, N. G. White, P. Falcaro and C. J. Doonan, *J Am Chem Soc*, 2019, **141**, 14298–14305.

117 Y.-H. Luo, X.-T. He, D.-L. Hong, C. Chen, F.-H. Chen, J. Jiao, L.-H. Zhai, L.-H. Guo and B.-W. Sun, *Adv Funct Mater*, 2018, **28**, 1804822.

118 J. A. Swift, A. M. Reynolds and M. D. Ward, *Chem Mater*, 1998, **10**, 4159–4168.

119 X. Song, Y. Wang, C. Wang, D. Wang, G. Zhuang, K. O. Kirlikovali, P. Li and O. K. Farha, *J Am Chem Soc*, 2022, **144**, 10663–10687.

120 D. W. Kang, M. Kang, H. Kim, J. H. Choe, D. W. Kim, J. R. Park, W. R. Lee, D. Moon and C. S. Hong, *Angew Chem Int Ed*, 2019, **58**, 16152–16155.

121 Y. Yang, L. Li, R.-B. Lin, Y. Ye, Z. Yao, L. Yang, F. Xiang, S. Chen, Z. Zhang, S. Xiang and B. Chen, *Nat Chem*, 2021, **13**, 933–939.

122 J. Feng, T.-F. Liu and R. Cao, *Angew Chem Int Ed*, 2020, **59**, 22392–22396.

123 Y.-H. Luo, L. Zhang, W.-X. Fang, S.-H. Ma, H. Dong, S. Su, Z.-Y. Zheng, D.-N. Li and L.-H. Zhai, *Chem Comm*, 2021, **57**, 5901–5904.

124 F. Hu, C. Liu, M. Wu, J. Pang, F. Jiang, D. Yuan and M. Hong, *Angew Chem Int Ed*, 2017, **56**, 2101–2104.

125 R.-B. Lin, Y. He, P. Li, H. Wang, W. Zhou and B. Chen, *Chem Soc Rev*, 2019, **48**, 1362–1389.

126 Y. Wang, K. Ma, J. Bai, T. Xu, W. Han, C. Wang, Z. Chen, K. O. Kirlikovali, P. Li, J. Xiao and O. K. Farha, *Angew Chem Int Ed*, 2022, **61**, e202115956.

127 S. Aitipamula, R. Banerjee, A. K. Bansal, K. Biradha, M. L. Cheney, A. R. Choudhury, G. R. Desiraju, A. G. Dikundwar, R. Dubey, N. Duggirala, P. P. Ghogale, S. Ghosh, P. K. Goswami, N. R. Goud, R. R. K. R. Jetti, P. Karpinski, P. Kaushik, D. Kumar, V. Kumar, B. Moulton, A. Mukherjee, G. Mukherjee, A. S. Myerson, V. Puri, A. Ramanan, T. Rajamannar, C. M. Reddy, N. Rodriguez-Hornedo, R. D. Rogers, T. N. G. Row, P. Sanphui, N. Shan, G. Shete, A. Singh, C. C. Sun, J. A. Swift, R. Thaimattam, T. S. Thakur, R. Kumar Thaper, S. P. Thomas, S. Tothadi, V. R. Vangala, N. Variankaval, P. Vishweshwar, D. R. Weyna and M. J. Zaworotko, *Cryst Growth Des*, 2012, **12**, 2147–2152.

128 G. R. Desiraju, in *Co-crystals: Preparation, Characterization and Applications*, eds. C. B. Aakeröy and A. S. Sinha, The Royal Society of Chemistry, 2018, pp. 1–26.

129 F. Wöhler, *Justus Liebigs Ann Chem*, 1844, **51**, 145–163.

130 H. Matsuda, K. Osaki and I. Nitta, *Bull Chem Soc Jpn*, 1958, **31**, 611–620.

131 G. P. Stahly, *Cryst Growth Des*, 2009, **9**, 4212–4229.

132 J. C. Krantz, J. M. Holbert, H. K. Iwamoto and C. J. Carr, J Am Pharm Assoc, 1947, **36**, 248–250.

133 K. Sekiguchi and K. Ito, *Chem Pharm Bull*, 1965, **13**, 405–413.

134 S. Gerald E., J. W. Bettis, J. L. Lach and J. Hood, *Am J Hosp Pharm*, 1973, **30**, 240–243.

135 L. F. Hartje, D. A. Andales, L. P. Gintner, L. B. Johnson, Y. V Li and C. D. Snow, *Crystals*, 2023, **13**, 352.

136 C. Naegeli and H. Kaltman, *Helv Chim Acta*, 1933, **16**, 980–988.

137 P. P. Mazzeo, C. Carraro, A. Monica, D. Capucci, P. Pelagatti, F. Bianchi, S. Agazzi, M. Careri, A. Raio, M. Carta, F. Menicucci, M. Belli, M. Michelozzi and A. Bacchi, *ACS Sustain Chem Eng*, 2019, **7**, 17929–17940.

138 X. Niu, R. Yang, H. Zhang and J. Yang, *Advanced Agrochem*, 2022, **1**, 39–60.

139 Y. Xiao, C. Wu, L. Zhou, Q. Yin and J. Yang, *Green Chem*, 2022, **24**, 8088–8099.

140 C. L. Jackson and G. Oenslager, *Ber Dtsch Chem Ges*, 1895, **28**, 1614–1617.

141 R. Willstätter and J. Piccard, *Ber Dtsch Chem Ges*, 1908, **41**, 1458–1475.

142 T. Posner, *Justus Liebigs Ann Chem*, 1904, **336**, 85–167.

143 C. R. Groom, I. J. Bruno, M. P. Lightfoot and S. C. Ward, *Acta Crystallogr B*, 2016, **72**, 171–179.

144 I. J. Bruno, J. C. Cole, P. R. Edgington, M. Kessler, C. F. Macrae, P. McCabe, J. Pearson and R. Taylor, *Acta Crystallogr B*, 2002, **58**, 389–397.

145 C. F. Macrae, I. J. Bruno, J. A. Chisholm, P. R. Edgington, P. McCabe, E. Pidcock, L. Rodriguez-Monge, R. Taylor, J. van de Streek and P. A. Wood, *J Appl Crystallogr*, 2008, **41**, 466–470.

146 C. F. MacRae, I. Sovago, S. J. Cottrell, P. T. A. Galek, P. McCabe, E. Pidcock, M. Platings, G. P. Shields, J. S. Stevens, M. Towler and P. A. Wood, *J Appl Crystallogr*, 2020, **53**, 226–235.

147 P. A. Wood, N. Feeder, M. Furlow, P. T. A. Galek, C. R. Groom and E. Pidcock, *CrystEngComm*, 2014, **16**, 5839–5848.

148 S. Aitipamula, P. S. Chow and R. B. H. Tan, *CrystEngComm*, 2014, **16**, 3451–3465.

149 A. V Trask, W. D. S. Motherwell and W. Jones, *Cryst Growth Des*, 2005, **5**, 1013–1021.

150 T. Ueto, N. Takata, N. Muroyama, A. Nedu, A. Sasaki, S. Tanida and K. Terada, *Cryst Growth Des*, 2012, **12**, 485–494.

151 M. D. Eddleston, S. Sivachelvam and W. Jones, *CrystEngComm*, 2013, **15**, 175–181.

152 J. B. Ngilirabanga and H. Samsodien, *Nano Select*, 2021, **2**, 512–526.

153 A. O. Patil, D. Y. Curtin and I. C. Paul, *J Am Chem Soc*, 1984, **106**, 348–353.

154 M. C. Etter, Z. Urbanczyk-Lipkowska, M. Zia-Ebrahimi and T. W. Panunto, *J Am Chem Soc*, 1990, **112**, 8415–8426.

155 M. C. Etter and D. A. Adsmond, *J Chem Soc Chem Commun*, 1990, 589–591.

156 M. D. Hollingsworth, M. E. Brown, B. D. Santarsiero, J. C. Huffman and C. R. Goss, *Chem Mater*, 1994, **6**, 1227–1244.

157 A. R. Ling and J. L. Baker, *J Chem Soc, Trans*, 1893, **63**, 1314–1327.

158 M. Karimi-Jafari, L. Padrela, G. M. Walker and D. M. Croker, *Cryst Growth Des*, 2018, **18**, 6370–6387.

159 C. Neurohr, A. Erriguible, S. Laugier and P. Subra-Paternault, *J Chem Eng*, 2016, **303**, 238–251.

160 S. Basavoju, D. Boström and S. P. Velaga, *Cryst Growth Des*, 2006, **6**, 2699–2708.

161 K. Wittering, J. King, L. H. Thomas and C. C. Wilson, *Crystals*, 2014, **4**, 123–140.

162 N. Pawar, A. Saha, N. Nandan and J. V Parambil, *Crystals*, 2021, **11**, 303.

163 S. L. James, C. J. Adams, C. Bolm, D. Braga, P. Collier, T. Friščić, F. Grepioni, K. D. M. Harris, G. Hyett, W. Jones, A. Krebs, J. Mack, L. Maini, A. G. Orpen, I. P. Parkin, W. C. Shearouse, J. W. Steed and D. C. Waddell, *Chem Soc Rev*, 2012, **41**, 413–447.

164 T. Friščić and W. Jones, *Cryst Growth Des*, 2009, **9**, 1621–1637.

165 K. Užarević, I. Halasz and T. Friščić, *J Phys Chem Lett*, 2015, **6**, 4129–4140.

166 D. Gracin, V. Štrukil, T. Friščić, I. Halasz and K. Užarević, *Angew Chem Int Ed*, 2014, **53**, 6193–6197.

167 L. Batzdorf, F. Fischer, M. Wilke, K.-J. Wenzel and F. Emmerling, *Angew Chem Int Ed*, 2015, **54**, 1799–1802.

168 I. Halasz, S. A. J. Kimber, P. J. Beldon, A. M. Belenguer, F. Adams, V. Honkimäki, R. C. Nightingale, R. E. Dinnebier and T. Friščić, *Nat Protoc*, 2013, **8**, 1718–1729.

169 N. Shan, F. Toda and W. Jones, *Chem Comm*, 2002, 2372–2373.

170 D. R. Weyna, T. Shattock, P. Vishweshwar and M. J. Zaworotko, *Cryst Growth Des*, 2009, **9**, 1106–1123.

171 D. Hasa and W. Jones, *Adv Drug Deliv Rev*, 2017, **117**, 147–161.

172 N. R. Rightmire and T. P. Hanusa, *Dalton Trans*, 2016, **45**, 2352–2362.

173 A. V Trask, W. D. S. Motherwell and W. Jones, *Chem Comm*, 2004, 890–891.

174 P. A. Julien and T. Friščić, *Cryst Growth Des*, 2022, **22**, 5726–5754.

175 C. F. Burmeister and A. Kwade, *Chem Soc Rev*, 2013, **42**, 7660–7667.

176 R. Mocci, E. Colacino, L. De Luca, C. Fattuoni, A. Porcheddu and F. Delogu, *ACS Sustain Chem Eng*, 2021, **9**, 2100–2114.

177 C. Gazzurelli, A. Migliori, P. P. Mazzeo, M. Carcelli, S. Pietarinen, G. Leonardi, A. Pandolfi, D. Rogolino and P. Pelagatti, *ACS Sustain Chem Eng*, 2020, **8**, 14886–14895.

178 L. Wang, B. Xin, A. Elsukova, P. Eklund and N. Solin, *ACS Sustain Chem Eng*, 2020, **8**, 17368–17378.

179 F. Puccetti, C. Schumacher, H. Wotruba, J. G. Hernández and C. Bolm, *ACS Sustain Chem Eng*, 2020, **8**, 7262–7266.

180 M. Gombotz and H. M. R. Wilkening, *ACS Sustain Chem Eng*, 2021, **9**, 743–755.

181 M. Pilloni, F. Padella, G. Ennas, S. Lai, M. Bellusci, E. Rombi, F. Sini, M. Pentimalli, C. Delitala, A. Scano, V. Cabras and I. Ferino, *Microporous Mesoporous Mater*, 2015, **213**, 14–21.

182 M. Klimakow, P. Klobes, A. F. Thünemann, K. Rademann and F. Emmerling, *Chem Mater*, 2010, **22**, 5216–5221.

183 F. Cuccu, L. De Luca, F. Delogu, E. Colacino, N. Solin, R. Mocci and A. Porcheddu, *ChemSusChem*, 2022, **15**, e202200362.

184 K. Grodowska and A. Parczewski, *Acta Pol Pharm*, 2010, **67**, 3–12.

185 C. W. Bailey, J. R. Bright and J. J. Jasper, *J Am Chem Soc*, 1945, **67**, 1184–1186.

186 T. Stolar, S. Lukin, M. Tireli, I. Sović, B. Karadeniz, I. Kereković, G. Matijašić, M. Gretić, Z. Katančić, I. Dejanović, M. di Michiel, I. Halasz and K. Užarević, *ACS Sustain Chem Eng*, 2019, **7**, 7102–7110.

187 K. Linberg, B. Röder, D. Al-Sabbagh, F. Emmerling and A. A. L. Michalchuk, *Faraday Discuss*, 2023, **241**, 178–193.

188 K. Užarević, T. C. Wang, S.-Y. Moon, A. M. Fidelli, J. T. Hupp, O. K. Farha and T. Friščić, *Chem Comm*, 2016, **52**, 2133–2136.

189 J. Beamish-Cook, K. Shankland, C. A. Murray and P. Vaqueiro, *Cryst Growth Des*, 2021, **21**, 3047–3055.

190 V. Štrukil, D. Gracin, O. V Magdysyuk, R. E. Dinnebier and T. Friščić, *Angew Chem Int Ed*, 2015, **54**, 8440–8443.

191 A. J. Arduengo, R. L. Harlow and M. Kline, *J Am Chem Soc*, 1991, **113**, 361–363.

192 D. Bourissou, O. Guerret, F. P. Gabbaï and G. Bertrand, *Chem Rev*, 2000, **100**, 39–92.

193 H.-W. Wanzlick and H.-J. Schönherr, *Angew Chem Int Ed*, 1968, **7**, 141–142.

194 K. Öfele, *J Organomet Chem*, 1968, **12**, P42–P43.

195 F. E. Hahn and M. C. Jahnke, *Angew Chem Int Ed*, 2008, **47**, 3122–3172.

196 M. A. Baldo, D. F. O'Brien, Y. You, A. Shoustikov, S. Sibley, M. E. Thompson and S. R. Forrest, *Nature*, 1998, **395**, 151–154.

197 D. Kourkoulos, C. Karakus, D. Hertel, R. Alle, S. Schmeding, J. Hummel, N. Risch, E. Holder and K. Meerholz, *Dalton Trans*, 2013, **42**, 13612–13621.

198 D. Di, A. S. Romanov, L. Yang, J. M. Richter, J. P. H. Rivett, S. Jones, T. H. Thomas, M. Abdi Jalebi, R. H. Friend, M. Linnolahti, M. Bochmann and D. Credgington, *Science*, 2017, **356**, 159.

199 A. Ruduss, B. Turovska, S. Belyakov, K. A. Stucere, A. Vembris, G. Baryshnikov, H. Ågren, J.-C. Lu, W.-H. Lin, C.-H. Chang and K. Traskovskis, *ACS Appl Mater Interfaces*, 2022, **14**, 15478–15493.

200 N. V Tzouras, E. A. Martynova, X. Ma, T. Scattolin, B. Hupp, H. Busen, M. Saab, Z. Zhang, L. Falivene, G. Pisanò, K. Van Hecke, L. Cavallo, C. S. J. Cazin, A. Steffen and S. P. Nolan, *Chem Eur J*, 2021, **27**, 11904–11911.

201 A. S. Romanov, S. T. E. Jones, Q. Gu, P. J. Conaghan, B. H. Drummond, J. Feng, F. Chotard, L. Buizza, M. Foley, M. Linnolahti, D. Credgington and M. Bochmann, *Chem Sci*, 2020, **11**, 435–446.

202 S. Shi, M. C. Jung, C. Coburn, A. Tadle, D. M. R. Sylvinson, P. I. Djurovich, S. R. Forrest and M. E. Thompson, *J Am Chem Soc*, 2019, **141**, 3576–3588.

203 R. Hamze, J. L. Peltier, D. Sylvinson, M. Jung, J. Cardenas, R. Haiges, M. Soleilhavoup, R. Jazzar, P. I. Djurovich, G. Bertrand and M. E. Thompson, *Science*, 2019, **363**, 601.

204 C. I. Ezugwu, N. A. Kabir, M. Yusubov and F. Verpoort, *Coord Chem Rev*, 2016, 307, 188–210.

205 F. Carson, E. Martínez-Castro, R. Marcos, G. G. Miera, K. Jansson, X. Zou and B. Martín-Matute, *Chem Comm*, 2015, **51**, 10864–10867.

206 W. T. Schumacher, M. J. Mathews, S. A. Larson, C. E. Lemmon, K. A. Campbell, B. T. Crabb, B. J.-A. Chicoine, L. G. Beauvais and M. C. Perry, *Polyhedron*, 2016, **114**, 422–427.

207 M. Albert-Soriano and I. M. Pastor, *European J Org Chem*, 2016, **2016**, 5180–5188.

208 G.-Q. Kong, X. Xu, C. Zou and C.-D. Wu, *Chem Comm*, 2011, **47**, 11005–11007.

209 R. S. Crees, M. L. Cole, L. R. Hanton and C. J. Sumby, *Inorg Chem*, 2010, **49**, 1712–1719.

2 CHAPTER TWO

Copper 1,3-bis(4-carboxyphenyl)imidazolium MOFs

2.1 Introduction

As discussed in Chapter 1, the use of imidazolium-containing linkers for metal-organic framework (MOF) synthesis offers the potential to study a wide range of chemistry within the framework environment.[1] This study uses 1,3-bis(4-carboxyphenyl)imidazolium compounds, for which there are several examples in the literature of MOFs synthesised with metals including zinc, copper and cadmium as well as some lanthanides.[2–6] This group of linkers is of particular interest since the bent geometry of the carboxylate groups with respect to one another (an angle of approximately 137° using the imidazolium moiety as the centre[5]) is relatively unusual in ditopic MOF linkers, and gives rise to a range of interesting structures. There have been several reports over the last 10 years of copper MOFs synthesised with this linker, either as-is or substituted at the 2- and/or 6- positions on the phenyl rings (Figure 2.1). Amongst the reported examples there is a tendency for these MOFs to form a 2-dimensional square net construction (sql net) as the base unit, which assemble into extended structures via layering or catenation.

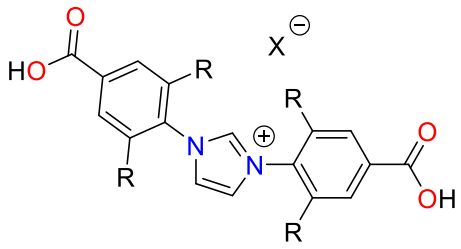


Figure 2.1: 1,3-bis(4-carboxyphenyl)imidazolium with anion, X = Cl^-, NO_3^-, ClO_4^-. R = H, Me.

In 2013 a copper MOF was reported by Nickerl et al., using 1,3-bis(4-carboxy-2,6-dimethylphenyl)imidazolium chloride as the linker and copper nitrate as the metal source.[7] The framework reported from this reaction comprised of a 3-dimensional structure formed of polycatenated 2D MOF nets. The nets are formed of copper paddlewheel secondary building units, joined by linker molecules equatorially and capped by solvent molecules at the axial positions (Figure 2.2A). These nets are interlinked in three directions, forming a Kagome-type lattice structure with large hexagonal and smaller triangular channels running parallel to the c-crystallographic axis (Figure 2.2B).

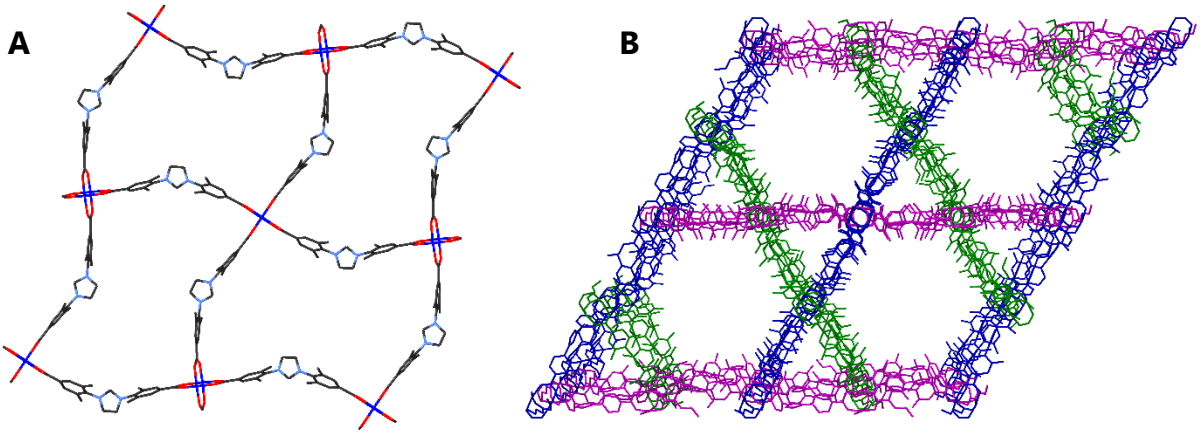


Figure 2.2: (A) Net structure (B) Channels of polycatenated MOF synthesised by Nickerl et al. with nets coloured by symmetry. Figure reproduced using data from CCDC Deposition 860563.[7]

In 2017 a series of three copper MOFs were reported by Lee et al., in which the unsubstituted 1,3-bis(4-carboxyphenyl)imidazolium chloride was used as the linker.[8] In this case, either copper(II) perchlorate or copper(I) chloride were used to provide the metal ions. Figure 2.3 summarises the conditions and results from these syntheses. Frameworks Im-MOF-1 and Im-MOF-3 had the same underlying 2D net topology as seen by Nickerl et al., however the nets assembled via stacking rather than catenation in order to form the extended structures. Im-MOF-3 is metalated with -Cu(I)Cl at the N-**C**-N carbon of the imidazolium moiety. Im-MOF-2 has different connectivity of the linkers and metal clusters, resulting in a 3-dimensional MOF with diamond shaped channels.

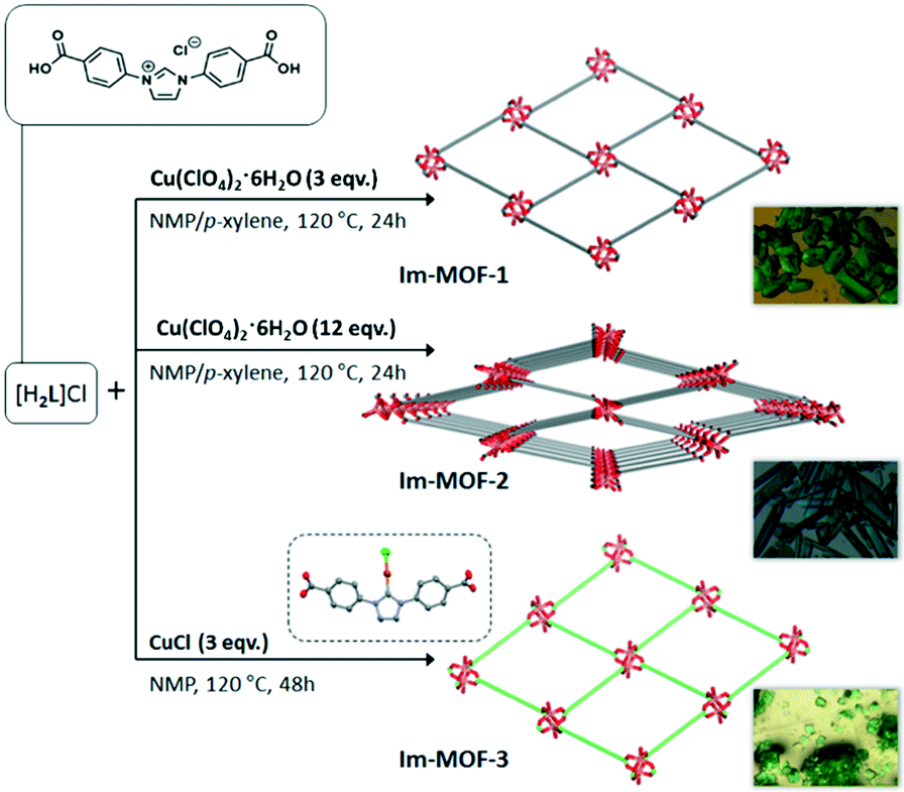


Figure 2.3: MOFs synthesised by Lee et al.. Figure reproduced from Ref. 8 with permission from the Royal Society of Chemistry.

Soon after this, in 2019 Yao et al. reported the synthesis of two isoreticular MOFs with 1,3-bis(4-carboxy-2-methylphenyl)imidazolium linkers.[9] In this case, both the nitrate and chloride salts of the linker were used, with the chloride variant containing a metalated imidazolium unit (-Cu(I)Cl, as seen in Lee's Im-MOF-3). A crystal structure was reported only for the synthesis using the chloride salt. The topology of the net was again consistent with that previously discussed. This MOF was catenated in two directions, resulting in diamond-shaped channels (Figure 2.4). The non-metalated MOF synthesised with the nitrate salt of the linker was reported to have the same structure according to powder X-ray diffraction analysis.

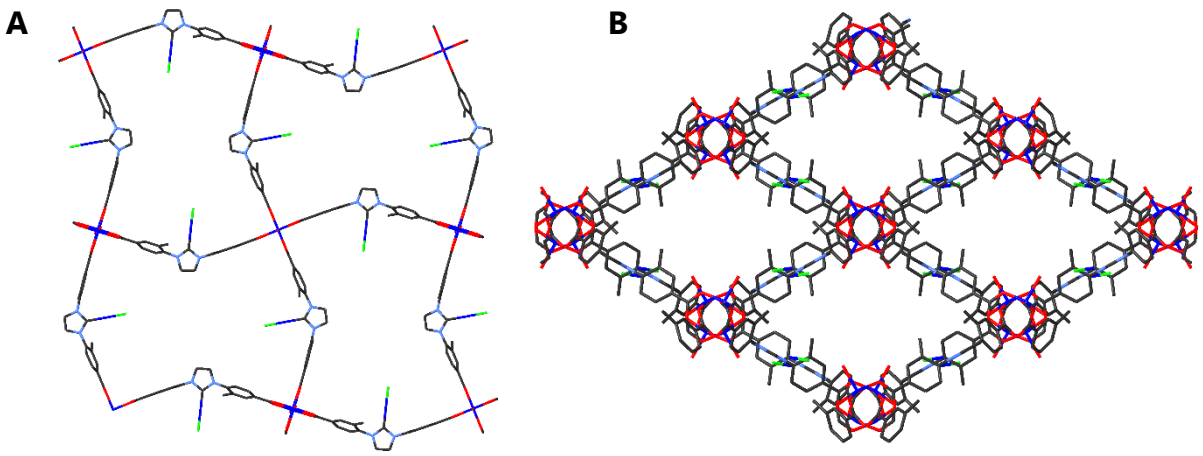


Figure 2.4: (A) Net structure and (B) Channels in the metalated MOF reported by Yao et al.. Figure reproduced using data from CCDC Deposition 1572628.[9]

2.2 Aims

In this study we were interested in bringing together the results from the aforementioned studies and obtaining a more complete picture of the range of copper MOF structures obtainable using methyl-substituted 1,3-bis(4-

carboxyphenyl)imidazolium linkers, and how control over product identity could be achieved. We investigated how small changes to synthetic conditions and methyl group substitution of the ligand influence the structures formed.

2.3 Results and Discussion

2.3.1 Organic Synthesis

Three linkers were used for the synthesis of MOFs in this work (Figure 2.5). All are based on the same core - an imidazolium centre with phenyl rings attached to both nitrogen atoms, each of which in turn are functionalised with a carboxylic acid at the 4-position. The linkers vary in the presence and number of methyl groups at the 2- and 5-positions on the phenyl rings, labelled R in the figure below. In all three cases the molecule is symmetrical in terms of substitution - i.e. if one phenyl ring is substituted, the other also is in the same manner. This is crystallographically more convenient in terms of structural analysis of the MOFs, due to less inherent disorder being present compared with an asymmetrically substituted molecule. It also simplifies the method for synthesis and purification of the linkers themselves. The first molecule, **1.**2H, has no methyl groups and thus has hydrogens at the R positions, as used by Lee et al..[8] A second ligand, **2.**2H, has a single methyl group on each phenyl ring, as used by Yao et al..[9] The final ligand explored, **3.**2H, has two methyl groups on each phenyl ring, as used by Nickerl et al..[7]

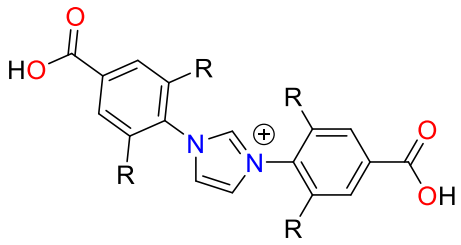
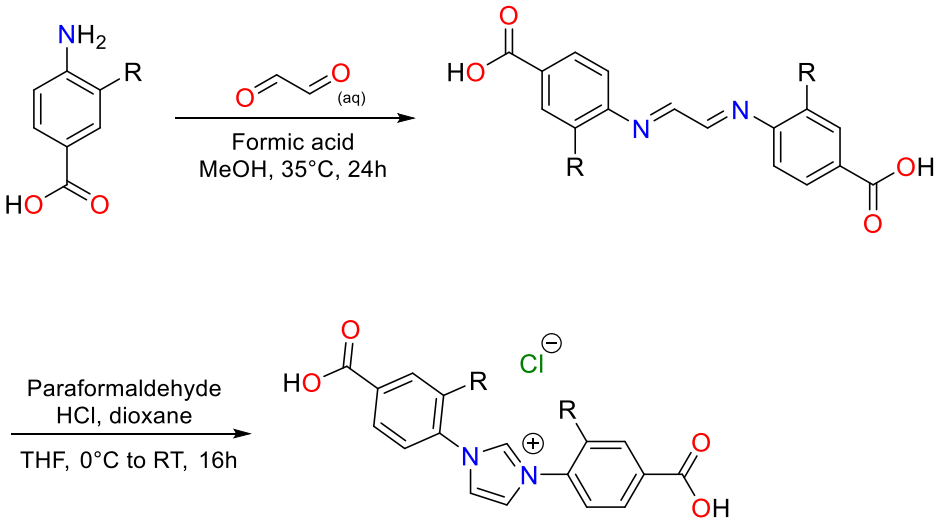
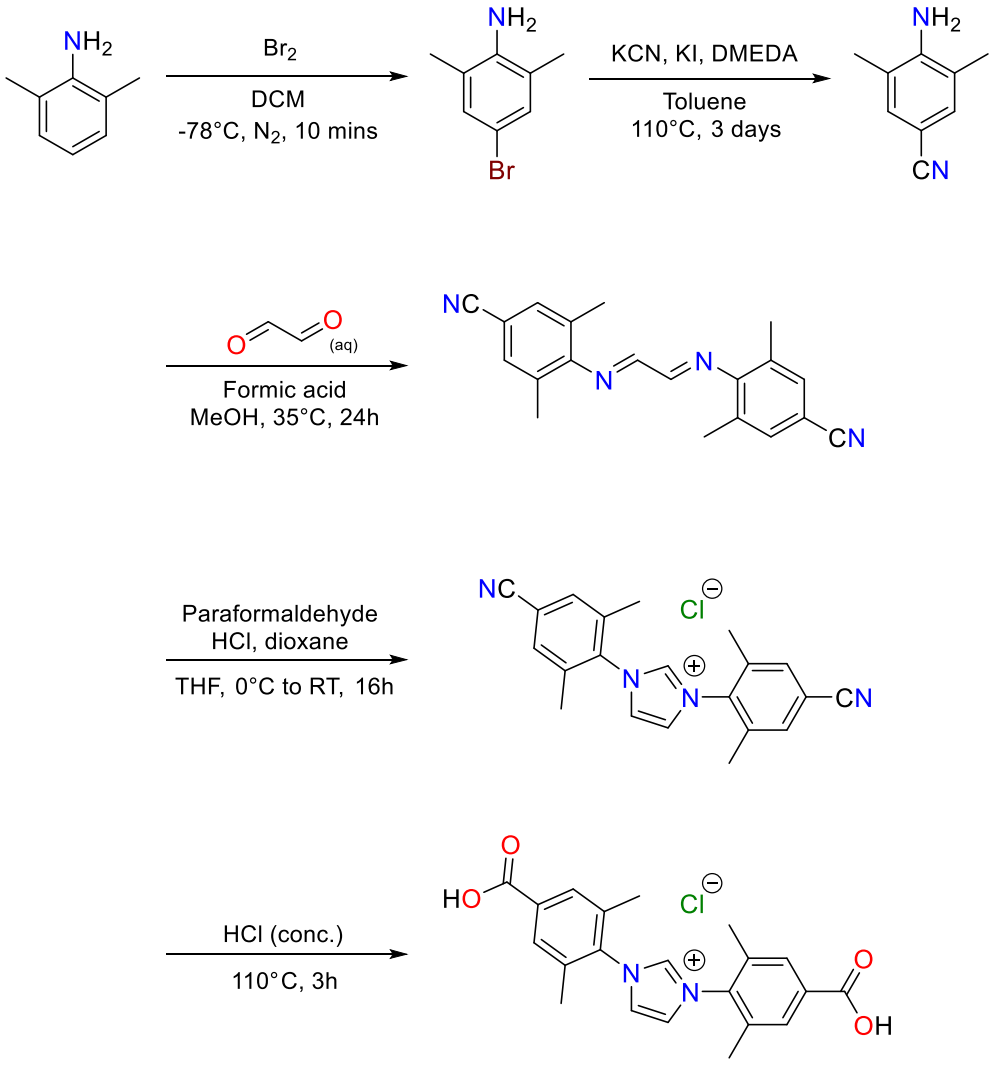


Figure 2.5: Organic linkers used in this work. R = H or Me.

Each linker was synthesised using the reported methods from the aforementioned publications. For **1.**2H and **2.**2H, the linker was synthesised in two steps via a diimine intermediate, starting from the relevant aminobenzoic acid derivative (Scheme 2.1). 4-Amino-3,5-dimethylbenzoic acid was not commercially available, but **3.**2H could be synthesised starting from 2,6-dimethylaniline (Scheme 2.2). Ion exchange from Cl^- to NO_3^- was conducted by dissolution of the linker in an aqueous solution of sodium hydroxide, followed by addition of an excess of nitric acid.



Scheme 2.1: Synthetic route to **1**.2H•Cl and **2**.2H•Cl. R = H or Me.



Scheme 2.2: Synthetic route to **3**.2H•Cl.

2.3.2 MOF Synthesis

The synthetic conditions used in this study were based on those utilised by Yao et al. for synthesis of MOFs with **2.**2H. Copper nitrate was used as the source of metal ions throughout, and the molar ratio of linker to metal salt (1:1.5) was also maintained. This allowed investigation of a range of other conditions, including different solvents, temperatures, concentrations, linker counterions and reaction times. Later in the study

modulation was also explored in terms of its effect on the phase obtained. Table 2.1 shows a summary of the variables investigated.

Table 2.1: Variables investigated in MOF syntheses with **2** and copper nitrate trihydrate.

Solvent	N,N′-Dimethylacetamide (DMA)
	N,N′-Dimethylformamide (DMF)
	N,N′-Diethylformamide (DEF)
	N-Methyl-2-pyrrolidone (NMP)
Temperature	100°C, 110°C, 120°C
Linker concentration	26 mM, 17.3 mM, 13 mM, 10.4 mM
Counterion	Chloride, Nitrate
Modulator	None, Acetic acid, Hydrochloric acid, Sulfuric acid

2.2H was the linker investigated most widely, with MOF syntheses using **3.**2H only conducted using the method by Yao et al. to serve as a direct comparison to other systems.

Five new MOF structures were discovered in this study - four with **2** as the linker and one with **3**. In each case the structure was determined by single crystal X-ray diffraction.

2.3.3 Crystal Structure Analysis

2-HexMOF

A synthesis using **2.**2H•NO_3 and $Cu(NO_3)_2 \cdot 3H_2O$ in DMA at 110°C overnight resulted in the formation of intergrown blue-green crystals with hexagonal rod morphology (Figure 2.6). The MOF crystallised in the space group P3/c1 and has the formula $[Cu(\mathbf{2})(H_2O)(NO_3)]_n(DMA)_{3n}$. The nitrate anion could not be located crystallographically; however the framework is cationic so its presence is implied. Additionally, FTIR analysis of the MOF shows a strong absorption at 1334 cm^{-1} (Appendix Figure 2.1), consistent with a nitrate N-O bond stretch. It was not possible to refine the positions of solvent molecules within the structure due to a significant degree of disorder resulting from the large pores. A solvent mask was therefore used to calculate the approximate number of solvent molecules present by assessing the remaining electron density. 181 electrons were found per asymmetric unit. The nitrate counterion is responsible for 31 of these, leaving 150 electrons which approximates to 3 molecules of DMA.

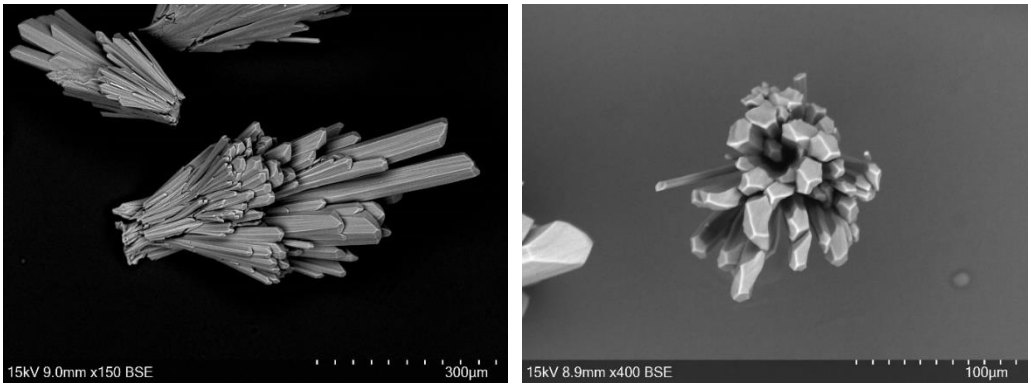


Figure 2.6: SEM images of **2-HexMOF** crystal 'bundles', showing hexagonal rod morphology.

The framework is composed of sql net constructions of the same connectivity as seen in the reported structures (Figure 2.7A). It is also isostructural with the MOF reported by Nickerl et al.[7], which uses **3** as the linker, with large hexagonal and smaller triangular channels running parallel to the c-axis in a Kagome lattice type arrangement (Figure 2.7B). These channels are formed by polycatenation of the MOF nets in three directions.

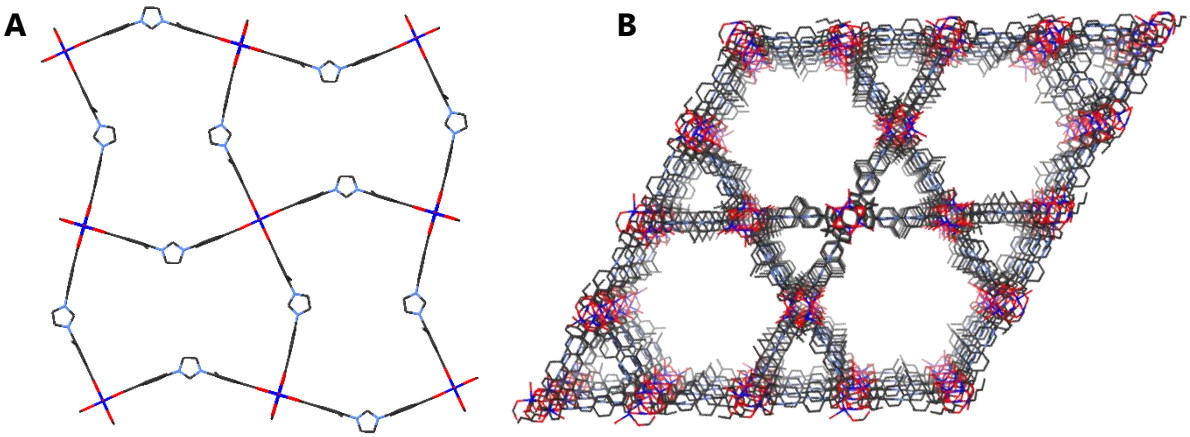


Figure 2.7: 2-HexMOF (A) 2-Dimensional net structure (B) Channels.

The MOF consists of 64.8% solvent-accessible void space, calculated using PLATON. The hexagonal channels have widths of 14.8 Å, measured between two C21 atoms and taking into account van der Waals radii of the atoms.

The phenyl rings in **2** have the ability to rotate, thus allowing the methyl substituents to be orientated in different directions within the MOF layers. In **2-HexMOF** there is some disorder in these orientations and the methyl groups were modelled in two parts. The planes of the phenyl rings lie at angles of 91° (C1-C6) and 88° (C13-C18) to the plane of the imidazolium ring, which itself lies in the plane of the 2D sheets as seen in

Figure 2.7A. The methyl groups, modelled in two parts (Figure 2.8B), are therefore directed into the void space of either the triangular or hexagonal channels.

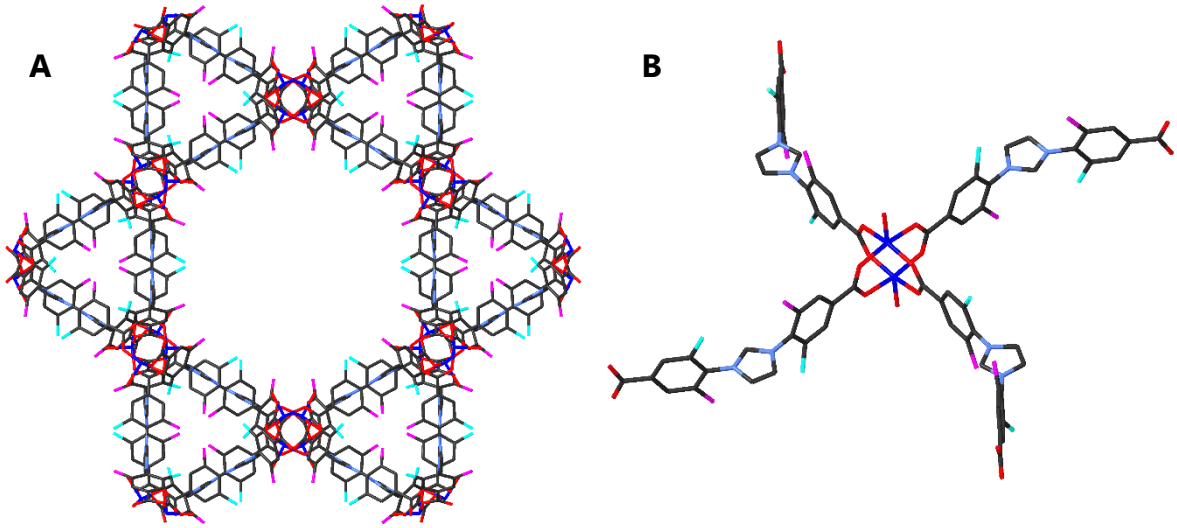


Figure 2.8: (A) View of a hexagonal channel and surrounding triangular channels in **2-HexMOF**. (B) Linkers around a metal cluster. Part 1 carbon atoms are shown in pink and part 2 carbon atoms in turquoise.

The approximate relative occupancies of the C19 (part 1) and C21 (part 2) carbons were initially determined by assigning free occupancy to these atoms. These settled at approximately 1/3 and 2/3 respectively, which is logical in the context of the wider structure. By virtue of the symmetry of the MOF, the C19 methyl groups are directed into the relatively small triangular channels. If all were present in that position, the C19-C19 distance from centre to centre would be 2.46 Å, less than the sum of their van der Waals radii. An occupancy of 1/3 for the C19 atom is therefore logical as steric crowding will be reduced, and the occupancy of C21 was thus set at 2/3. The occupancies of the methyl carbons C9 and C8 on the other phenyl ring were determined using a similar method. Allowing the occupancies of these carbon atoms to refine freely resulted in

similar relative occupancies as were seen for C19 and C21 respectively. This means the methyl groups in the same part are positioned on opposing sides of the two phenyl rings with respect to the imidazolium centre.

Powder X-ray diffraction studies of **2-HexMOF** as-synthesised and dried showed the MOF to be unstable with respect to solvent removal (Figure 2.9). This is likely due to the significant proportion of the structure taken up by solvent-accessible void space as well as the fact that the MOF sheets are catenated and thus have no bonds or strong interactions between them which might stabilise the structure.

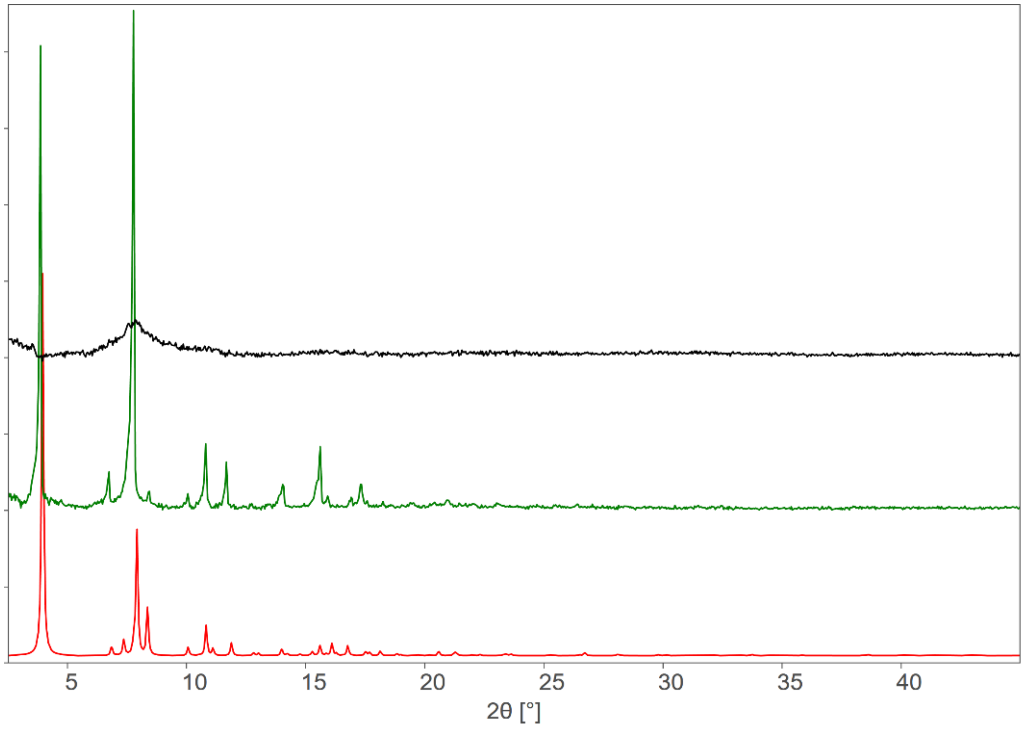


Figure 2.9: PXRD patterns of **2-HexMOF** as-synthesised (middle, green) and dried (top, black). The theoretical pattern (bottom, red) was calculated from single crystal data.

Interestingly, Yao et al. reported the synthesis of large single crystals by this method, however stated that they were unable to collect single crystal XRD data due to weak

diffraction. Powder XRD data is reported, and the paper concluded that the structure was isoreticular with the metalated MOF discussed in the introduction and shown in Figure 2.4. The powder XRD patterns of their metalated MOF and **2-HexMOF** are very similar, with the major distinguishing feature being an intense peak just below 4° 2θ (Figure 2.10). The powder pattern reported by Yao et al. appears to have been collected beginning at 5° 2θ, meaning it is not possible to determine from the provided data which MOF was obtained in their study. The diffraction from **2-HexMOF** during single crystal analysis was indeed weak, particularly at wider angles, likely due to the large amount of disordered solvent in the void space.

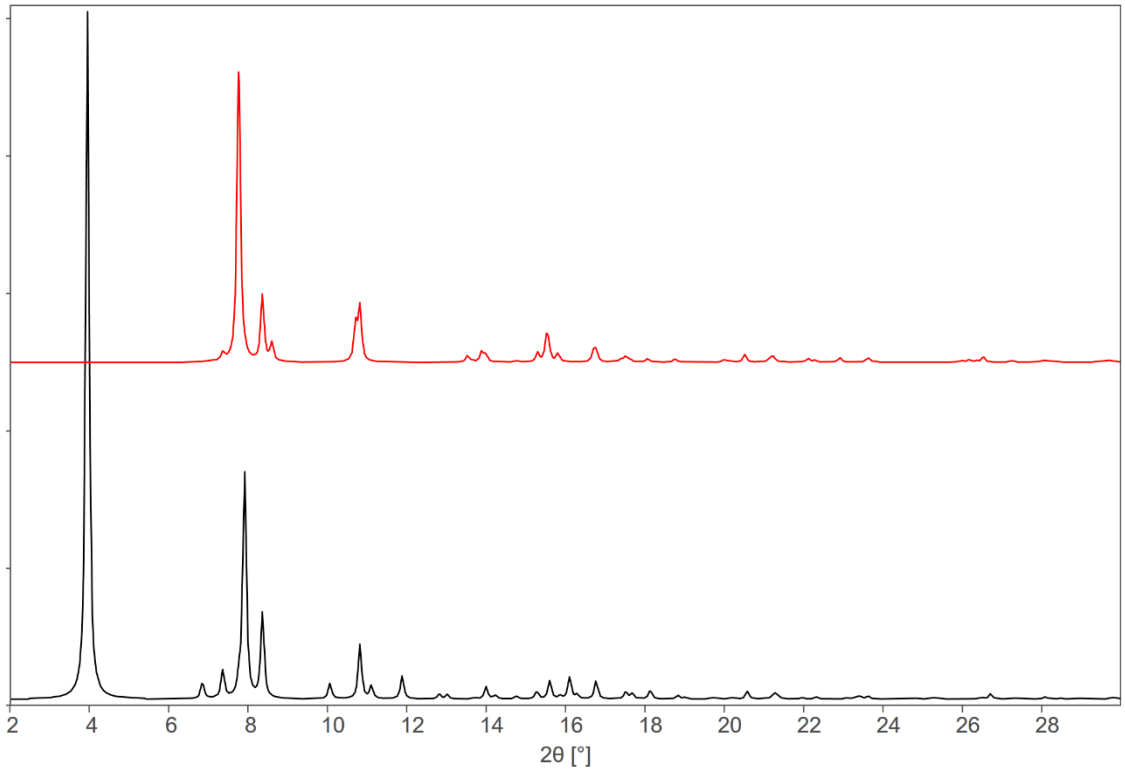


Figure 2.10: Calculated powder XRD patterns of Yao et al. metalated MOF (CSD Refcode CIWWAJ) (upper, red) and **2-HexMOF** (lower, black).

2-1DMOF

A synthesis was performed with the same conditions as were used for **2-HexMOF** but with a shorter reaction time of 4 hours. Under these conditions, blue needle-shaped crystals formed. These were found to be a non-porous 1-dimensional MOF which crystallises in the space group $Cmc2_1$, with the formula $[Cu(\mathbf{2})(H_2O)(NO_3)]_n$. The MOF chains grow parallel to the a-axis and are composed of distorted square planar copper atoms, with the copper lying 0.15 Å out of the plane. These are linked by molecules of **2** in trans-coordination sites, and the remaining two coordination sites are occupied by one water molecule and one nitrate ion (Figure 2.11). The copper ion, nitrate ligand and water oxygen atom lie on a mirror plane and thus each of these atoms has half occupancy in the asymmetric unit. The same applies to the imidazole N-**C**H-N carbon and proton on the other side of the asymmetric unit. The MOF is charge balanced, and there does not appear to be any residual solvent present in the structure.

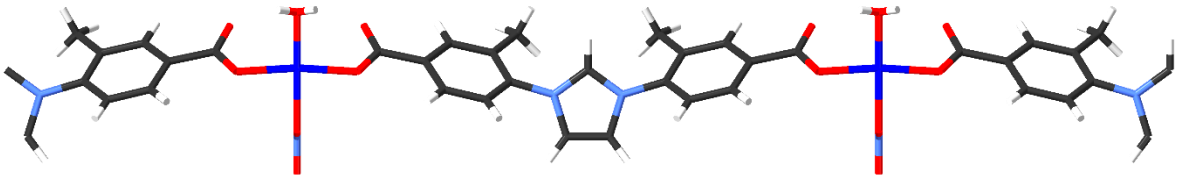


Figure 2.11: MOF chain in **2-1DMOF**.

Each chain appears to interact with four others via hydrogen bonding interactions. Two types of hydrogen bond form: between H_2O and carbonyl oxygen atoms (O-H--O); and between the slightly acidic N-C**H**-N proton and O3N of the nitrate ligand. (C-H--O). It was possible to crystallographically determine the position of H1W, the water

hydrogen atom, using electron density, which provides good evidence for its participation in hydrogen bonding.

The C-H···O hydrogen bonding interactions, which have a C···O length of 3.3 Å, link chains in the b-axis direction, with the chains arranged in an offset fashion along the a-axis (Figure 2.12A). Different "stacks" of chains are subsequently positioned in an offset fashion in the c-axis direction, such that they are interlinked by O-H···O hydrogen bonds with an O···O length of 2.7 Å (Figure 2.12B and C).

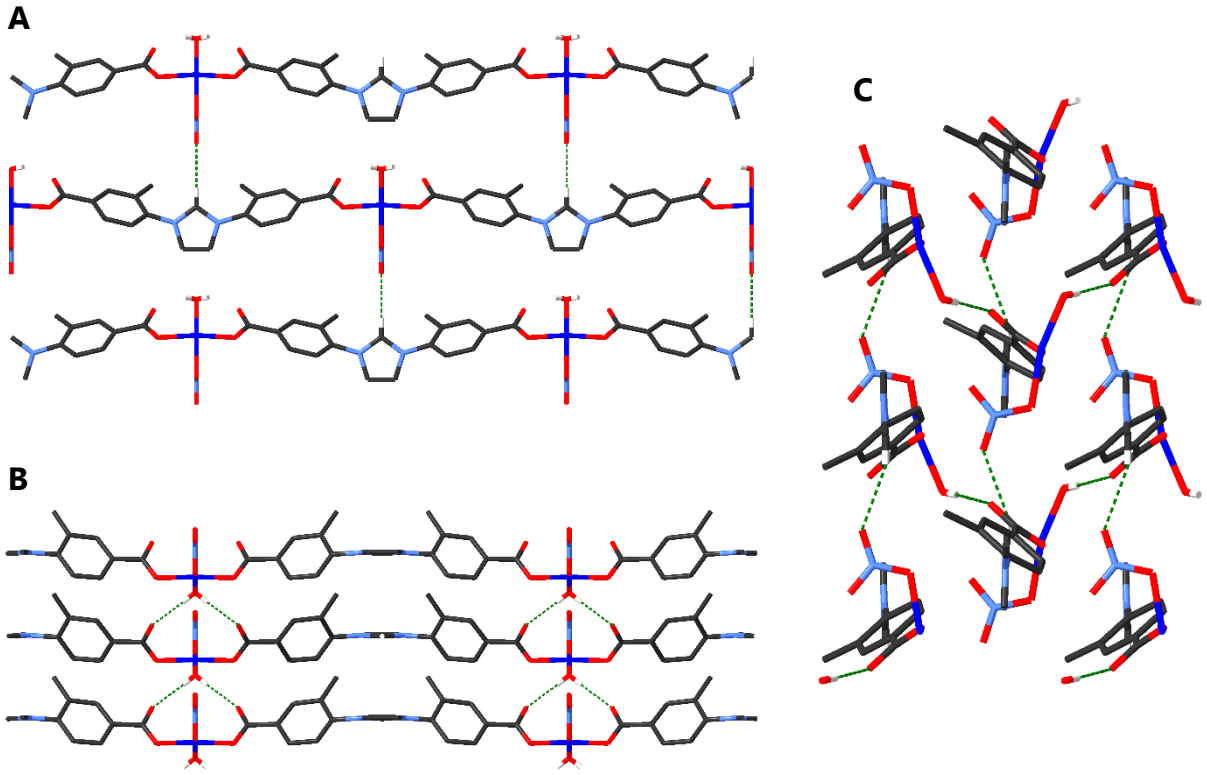


Figure 2.12: Hydrogen bonding interactions between adjacent chains in **2-1DMOF**. View along the (A) b-axis (B) c-axis (C) a-axis. For clarity, only hydrogen atoms involved in hydrogen bonding are shown.

The methyl groups of **2** in **2-1DMOF** are well ordered and, contrastingly to **2-HexMOF**, both have the same relative orientation with respect to the imidazolium ring. It is

possible that the methyl groups participate in weak hydrogen bonding interactions with the NO_3^- ligand on a neighbouring chain, which may explain their apparent directionality.

2-2DMOF-1

Where **2.**2H•Cl (as opposed to **2.**2H•NO_3) was used as the linker in framework synthesis, with $Cu(NO_3)_2$•$3H_2O$ in DMA at 110°C overnight, MOF crystals of square plate morphology formed. The MOF crystallised in the space group C2/c. The formula unit for the **2-2DMOF-1** is $([Cu(\mathbf{2}CH_2OH)(DMA)_{0.5}(H_2O)_{0.5}]Cl_x(NO_3)_{1-x}(DMA)_3)_n$. The structure is composed of the familiar sql MOF nets, with the same connectivity as in the reported structures and **2-HexMOF**, however rather than being catenated, the nets are layered (Figure 2.13). In this MOF, the nets are not entirely flat but are buckled slightly, with the vertical axes of the metal clusters angled at 18° with respect to one another. In the nets, the phenyl rings of **2** are angled at 110° (C1-C6) and 81° (C14-C19) from the plane of the imidazolium ring. Half of the axial coordination sites of the metal clusters appear to be occupied by dimethylacetamide and the other half by water. It was not possible to identify or locate anions within the framework, therefore the general formula above, as used by Nickerl et al.[7], acknowledges the likely presence of both chloride and nitrate ions within the framework, to a combined value of one molecule per asymmetric unit.

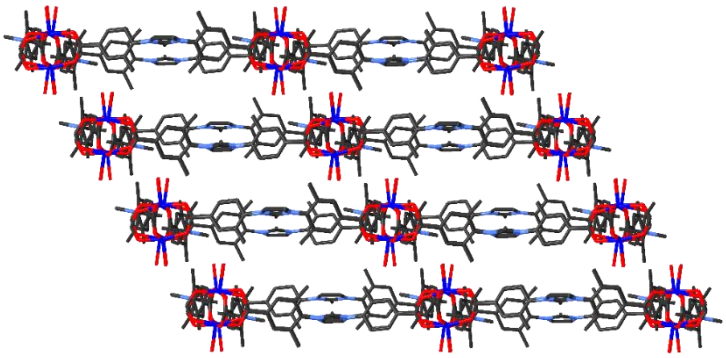


Figure 2.13: Layering of MOF nets in 2-2DMOF-1.

Layering of the MOF nets occurs in an ABAB fashion, best visualised along the normal to the plane of the imidazolium rings (Figure 2.14A). The structure contains channels that run parallel to the c-axis (Figure 2.14B). Void space was calculated by PLATON to constitute 53.7 % of the total unit cell volume.

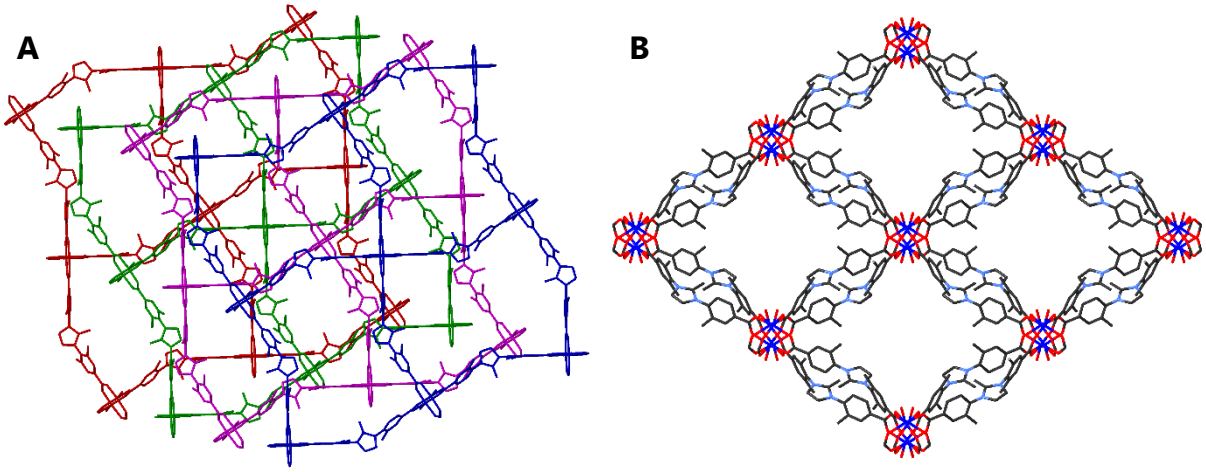


Figure 2.14: (A) Face-on perspective of layered MOF nets. The red and pink nets are equivalent, as are the green and blue nets. (B) Channels in **2-2DMOF-1**.

The linker, **2**, has undergone an in-situ reaction at the imidazolium during MOF synthesis. We believe the linker in the MOF to contain a -CH_2OH moiety bound to the N-**C**-N carbon. The carbon atom of this new substituent has been modelled; however

we were unable to locate the -OH group and hydrogen atoms, likely due to rotational disorder about that carbon atom. This substitution is a known reaction, with formaldehyde as the reagent.[10] The presence of formaldehyde in the MOF reaction is explained by the fact it is used in the synthesis of **2**. The additional substituent is unlikely to have had an impact on the packing of the extended MOF structure as the group appears to be directed into void space rather than partaking in any strong intermolecular interactions between MOF nets.

2-2DMOF-2

Turquoise single crystals of plate morphology formed in a synthesis using **2.**2H•NO_3 and $Cu(NO_3)_2$•$3H_2O$ in DMF (as opposed to DMA), with the same concentrations as were used for the synthesis of **2-HexMOF**. Analysis by SCXRD revealed these crystals to be a different layered 2-dimensional MOF, this time in the space group I2/m. It has the formula $([Cu_2(\mathbf{2})(\mathbf{2}CH_2OH)(DMF)_x(H_2O)_{1-x}](NO_3)(DMF)_3)_n$. In this structure residual electron density at the axial sites of the copper cluster is observed (Figure 2.15), however all attempts to model this, potentially as coordinated DMF, were unsuccessful. This means it was also not possible to determine the relative occupancies of DMF and water at this site, hence the general formula given above. A solvent mask was used to calculate the residual electron density in the void space of the structure. 158 electrons were found which approximates to 1 molecule of NO_3^- and 3 molecules of DMF.

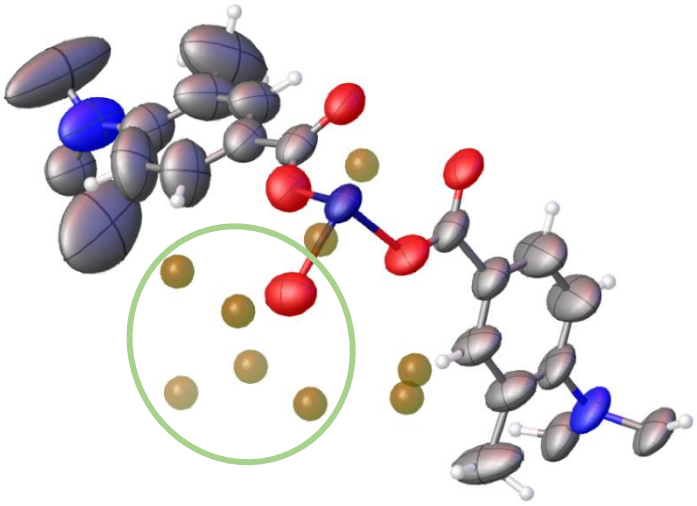


Figure 2.15: Dimethyl formamide was identifiable in the Q peaks of **2-2DMOF-2** (indicated by a green circle).

As with **2-2DMOF-1**, a layered structure composed of sql MOF nets is observed, however in this case there are two crystallographically independent molecules of **2** in the structure as opposed to the usual one. One of these, **2**-A, connects the metal clusters in the direction perpendicular to the crystallographic b-axis. The imidazolium ring of the **2**-A linkers lies in the plane of the net, with its connected phenyl rings at a relative rotation of approximately 74° either side (Figure 2.16A and B), calculated by measuring the angle between the planes of the respective rings. The methyl groups on **2**-A linkers are directed to opposite sides relative to the plane of the imidazolium ring.

The other linker molecule, **2**-B, connects the metal clusters in the direction parallel to the b-axis. The rotation of the linker with respect to **2**-A is such that the net takes on a slightly puckered conformation, similarly to **2-2DMOF-1** (Figure 2.16C). The axial positions of metal clusters linked by a molecule of **2**-A are at an angle of 30° to one

another. In a molecule of **2**-B the methyl groups are directed to the same side as one another, relative to the imidazolium ring. As in **2-2DMOF-1**, there appears to have been a reaction in-situ at the imidazolium N-**C**-N carbon of the **2**-B linker in **2-2DMOF-2**. We again believe the new substituent to be -CH_2OH, however as in **2-2DMOF-1** the position of only the carbon atom was refinable, with the assumption being that the substituents (two hydrogens and a hydroxy group) are rotationally disordered.

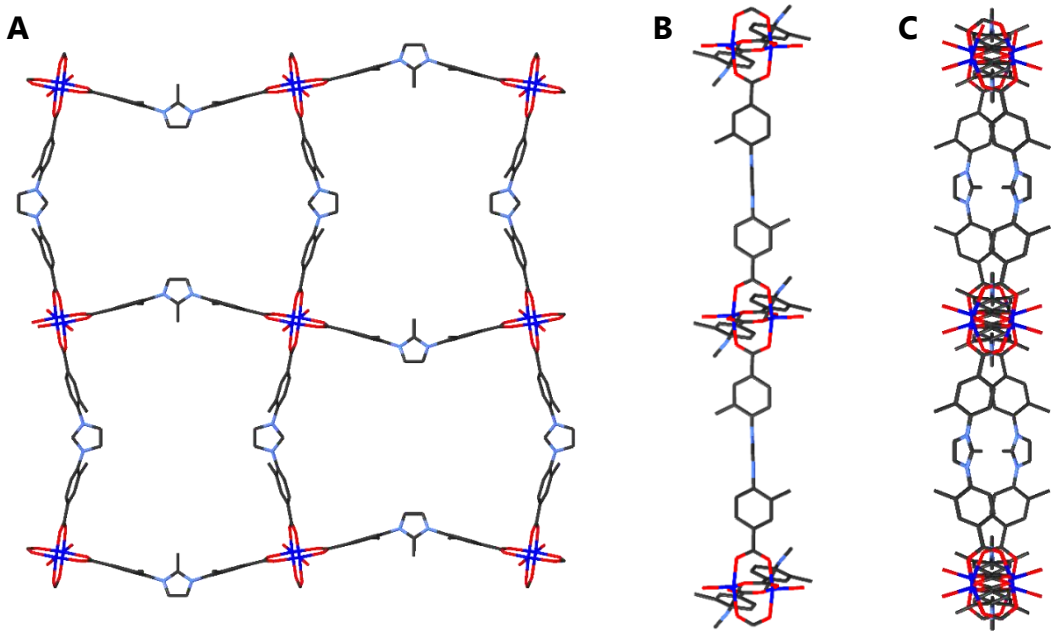


Figure 2.16: Net structure in **2-2DMOF-2**. (A) Face-on view, (B) View down length of **2**-B linkers, (C) View down length of **2**-A linkers.

Additionally, the anisotropic displacement parameters of some atoms in **2**-B were large, particularly the N-**C**-**C**-N carbon atoms of the imidazolium ring and the carbon atom of the new substituent. This indicates disorder which may either be dynamic, with some movement of the linker within the crystal, or static, there being two low energy conformations of the linker distributed across the crystal structure. In either case, the

N-**C**-N carbon appears to be the 'fixed' point, with a more symmetrical displacement parameter. Attempts were made to model the 'split' carbon atom C10 in two parts, however the model was not significantly improved by this undertaking.

The MOF nets are stacked upon one another in an ABCABC fashion which results in channels running through the structure parallel to the a- and c-axes (Figure 2.17A and B). The void space in the structure was estimated by PLATON to constitute 59.9% of the total volume of the MOF.

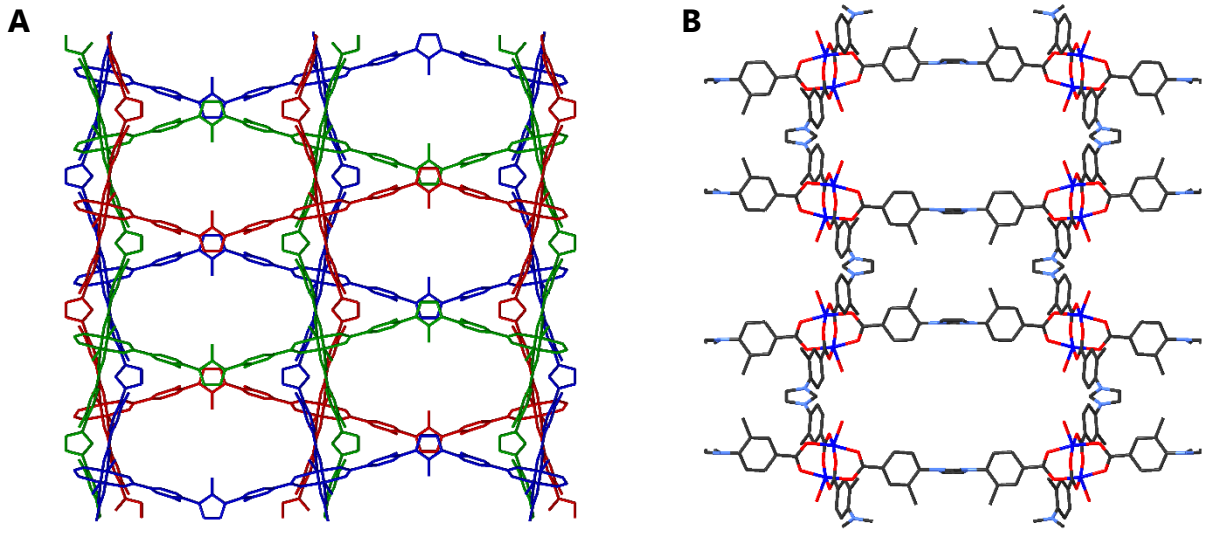


Figure 2.17: 2-2DMOF-2 visualised along the (A) c-axis, colour coded to show ABCABC stacking; (B) a-axis.

3-2DMOF

In a synthesis using **3.**2H•Cl and $Cu(NO_3)_2$•$3H_2O$ in DMA at 110°C overnight, green single crystals of plate morphology were obtained. The structure was determined to be a layered 2D MOF in the space group C2/c. The layers are composed of MOF nets with the same connectivity as in the previous structures discussed in this chapter (Figure

2.18A). The formula unit for **3-2DMOF** is $([Cu(\mathbf{3})(DMA)_{0.5}(H_2O)_{0.5}](Cl)_x(NO_3)_{1-x}(DMA)_4)_n$. Solvent in the structure is disordered, therefore a solvent mask was used to approximate the number of solvent molecules in the asymmetric unit. It was not possible to locate the position of the anions, however similarly to **2-2DMOF-1** - and the reported hexagonal polycatenated **3** MOF - it is likely there are both chloride and nitrate ions present.

In this MOF the phenyl rings are orientated at angles of 92° (C1-C6) and 81° (C14-C19) with respect to the imidazolium. The planes of the phenyl rings run parallel to the vertical axis of the metal clusters, which altogether results in nets in which the linkers are slightly bent up and down out of the plane (Figure 2.18B). The axes of the metal clusters are at approximately 10° angles with respect to one another.

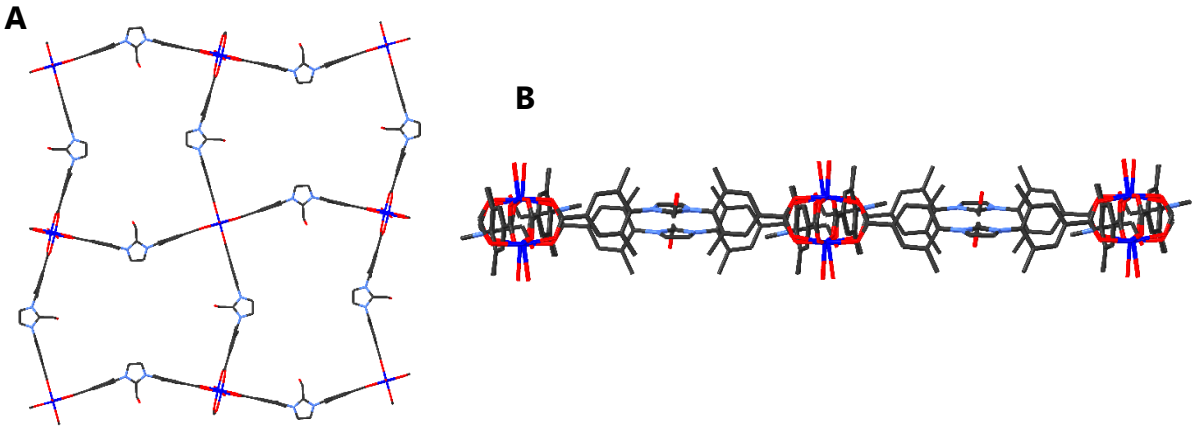


Figure 2.18: (A) Face-on and (B) Side-on view of a single MOF net in **3-2DMOF**.

The layers in **3-2DMOF** are stacked in an ABAB fashion (Figure 2.19A), offset from one another such that the metal cluster of one net resides above or below the 'window' of another and vice versa (Figure 2.19B). Perpendicular to the [1 1 0] plane, the structure

contains both rhombohedral and parallelogram shaped channels, with approximate window sizes of 6.7 x 6.7 Å and 12.8 x 3.5 Å respectively (Figure 2.19C), taking into account the van der Waals radii of the atoms. The structure contains 58.4% solvent-accessible void space as calculated by PLATON.

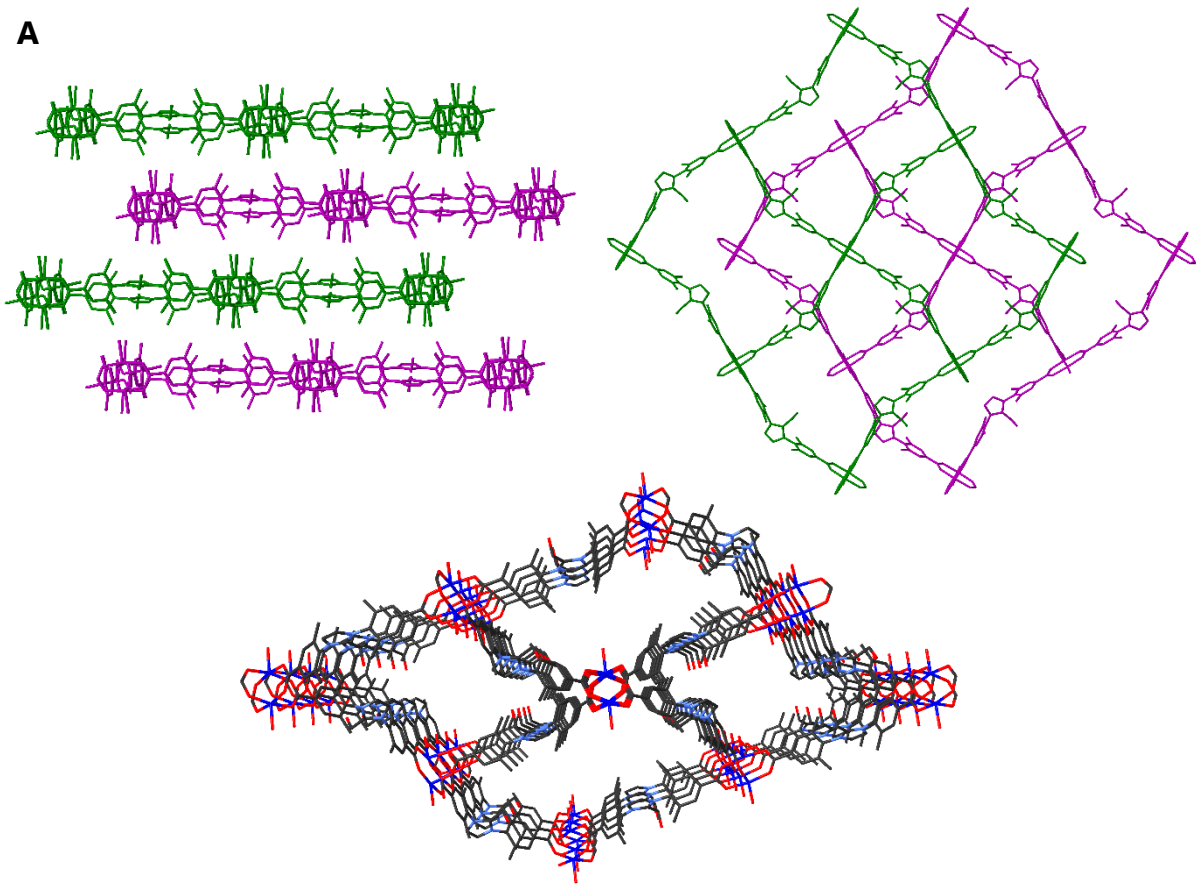


Figure 2.19: (A) Layering of MOF nets in **3-2DMOF** from side (B) Layering face-on view. Nets are colour coded green and pink to show equivalent layers. (C) Channels perpendicular to [1 1 0] plane.

In **3-2DMOF**, the linker has again undergone a reaction at the imidazole to substitute a -CH_2OH group at the N-**C**-N carbon. In this MOF both of the non-hydrogen atoms of the group were locatable by electron density. This supports the hypothesis presented in the discussions of the structures of **2-2DMOF-1** and **2-2DMOF-2**.

In this framework the -OH group in one MOF net appears to be positioned such that it is directed at the metal cluster of another net. There are no apparent strong intermolecular interactions of this group with other layers, but it is likely it forms hydrogen bonds with crystallographically unresolved solvent molecules in the void space.

2.3.4 A Note on Data Collections

It was significantly challenging to collect good quality data sets on all the structures discussed above, with the exception of **2-1DMOF**. As the MOFs contain large amounts of disordered solvent, the wider-angle reflections were generally weak and long collections were therefore required. In addition to this, crystals of **2-2DMOF-1** and **3-2DMOF** were prone to beam damage meaning the data quality suffered in these longer collections. Several attempts were made to collect all structures, both in-house and at external facilities including the synchrotron at Diamond Light Source, and the data presented herein are the best results we obtained for each MOF.

2.3.5 MOF Syntheses using **2**.2H: Changing Conditions

The 'control' conditions from which adjustments were then made are those used by Yao et al. in the synthesis of their non-metalated MOF, which we found to result in the formation of **2-HexMOF**. The materials and conditions used for each experiment are detailed in Table 2.2 in the experimental section for this chapter.

In some syntheses, a mixture of MOF phases were obtained. Powder X-ray analysis was conducted on bulk samples in order to assess the phases formed under different conditions and draw comparisons. The MOFs appeared to lose crystallinity upon grinding, thus powder diffraction measurements were conducted on samples as-synthesised, with entire crystals. This means that preferential orientation - intensity variation due to bias in orientations of certain crystallographic planes - should be taken into account when examining the resulting patterns, and that the relative proportions of the phases could not be accurately assessed.

Additionally, as discussed previously, the peaks in the powder XRD pattern for the metalated MOF synthesised by Yao et al. (CSD RefCode CIWWAJ) are in very similar positions to those in **2-HexMOF**. This, combined with the skew in relative intensities of peaks due to preferred orientation, means that in syntheses where **2-HexMOF** was observed, the possibility of the non-metalated analogue of the reported structure being present in some proportion cannot be ruled out. Only crystals of hexagonal rod morphology were observed in SEM however (Figure 2.6 and Appendix Figure 2.2), and during screening experiments for single-crystal analysis of multiple samples, on no occasion was the unit cell for CIWWAJ observed. As such, in subsequent discussions of powder analysis, the MOF reported by Yao et al. will not be discussed unless otherwise clearly relevant.

Temperature

Changing the temperature of MOF synthesis did not appear to have a significant impact on the structures formed. In syntheses conducted at temperatures 10°C either side of the control conditions for **2-HexMOF**, no additional peaks appeared in the powder diffraction patterns of the material formed (Figure 2.20).

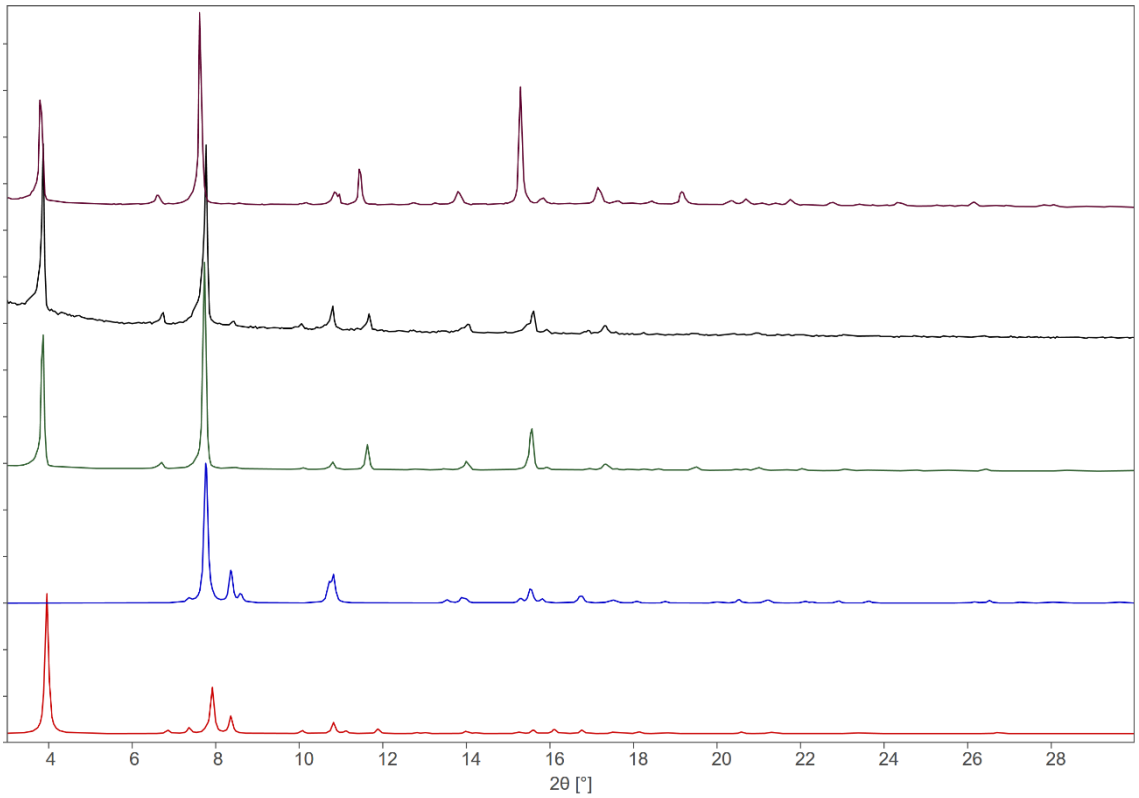


Figure 2.20: Powder XRD patterns of MOF syntheses using **2.**2H at different temperatures. From bottom to top: calculated patterns of CIWWAJ (red) and **2-HexMOF** (blue); experimental patterns from syntheses at 100°C (green), 110°C (black), 120°C (burgundy).

Counterion

In the control experiment, the linker, **2.**2H, had a nitrate anion associated with it, achieved through ion exchange after synthesis. The linker is synthesised with a chloride

ion to balance the charge, and in an experiment where **2.**2H•Cl was used in place of **2.**2H•NO_3 in MOF synthesis, **2-2DMOF-1** resulted. There are additionally some small peaks in the powder XRD pattern which indicate the presence of some **2-HexMOF**. Crystals of hexagonal rod morphology, consistent with previous syntheses of **2-HexMOF**, were observed in the vial.

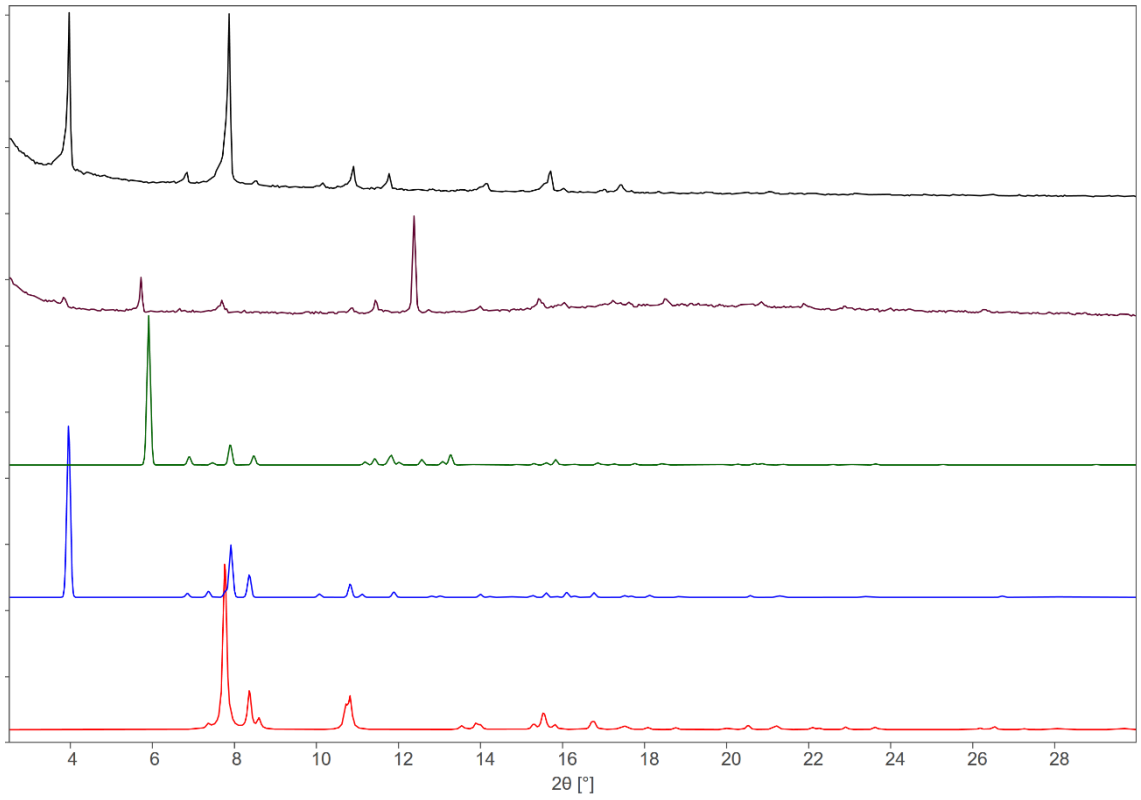


Figure 2.21: Powder XRD patterns from MOF syntheses with 2.2H, with different counterions associated with the linker. From bottom to top, calculated patterns for CIWWAJ (red), **2-HexMOF** (blue), **2-2DMOF-1** (green) and experimental patterns for syntheses using **2.**2H•Cl (purple) and **2.**2H•NO_3 (black).

Solvent

The solvent used for MOF synthesis appears to have a significant effect on the structure formed, even for solvents which are chemically similar to DMA. Where DMF was used

in place of DMA for synthesis, with all other conditions remaining the same, a mixture of **2-HexMOF** and **2-2DMOF-2** crystallised. When DEF was used, both single crystals and powder were produced, which were separated and analysed individually. The single crystal phase appears to consist of some **2-HexMOF** as well as potentially another unknown phase. The powder was poorly crystalline with low intensity peaks, however the positions of these peaks matches with those of CIWWAJ. From a synthesis using NMP, the resulting solid again provided low intensity of peaks in the powder XRD pattern, however the peak positions indicate the presence of **2-2DMOF-2**.

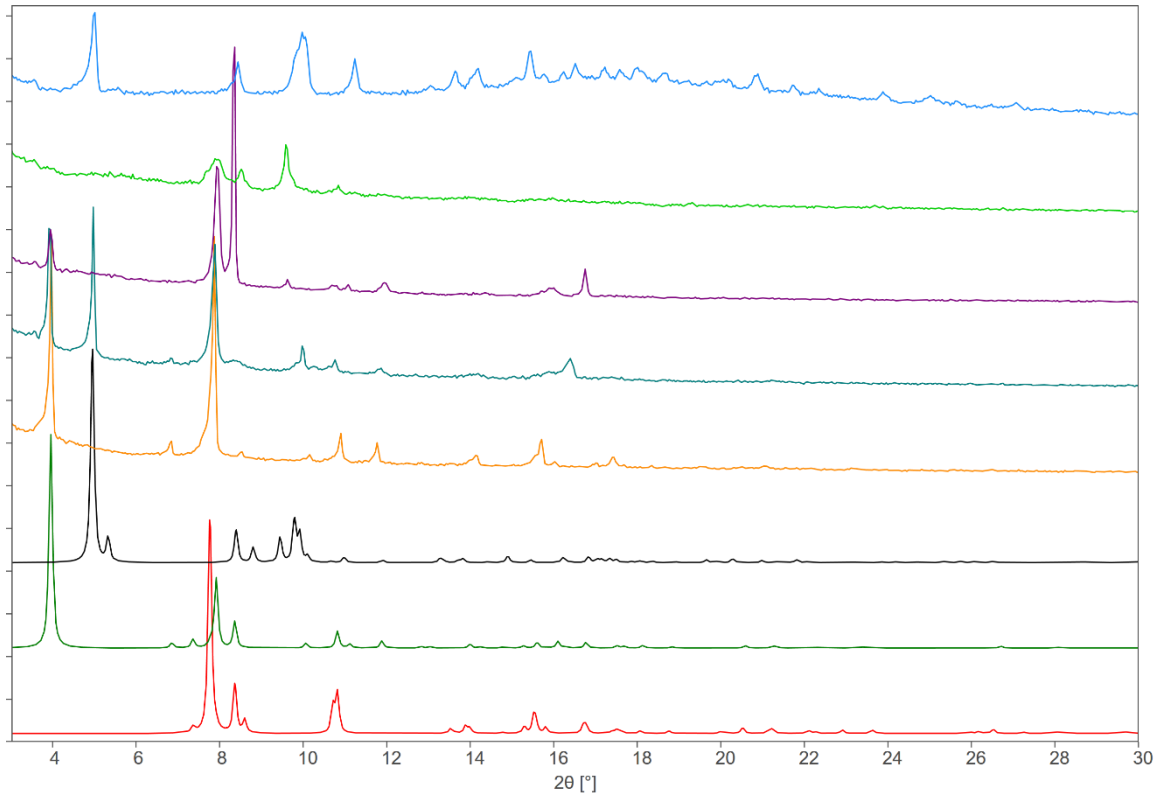


Figure 2.22: Powder XRD patterns of resulting solid from syntheses using different solvents. From bottom to top, calculated patterns for CIWWAJ (red), **2-HexMOF** (dark green), **2-2DMOF-2** (black) and experimental patterns for syntheses in: DMA (orange), DMF (teal), DEF - crystals (purple), DEF - powder (green), NMP (blue).

Reaction duration

In equivalent syntheses heated for different lengths of time, either **2-HexMOF** or **2-1DMOF** resulted. Experiments were conducted with heating times of 4h, 8h, 14h and 16h. The 4-hour and 8-hour long syntheses produced phase-pure **2-1DMOF**, and syntheses longer than 14 hours resulted in phase-pure **2-HexMOF**.

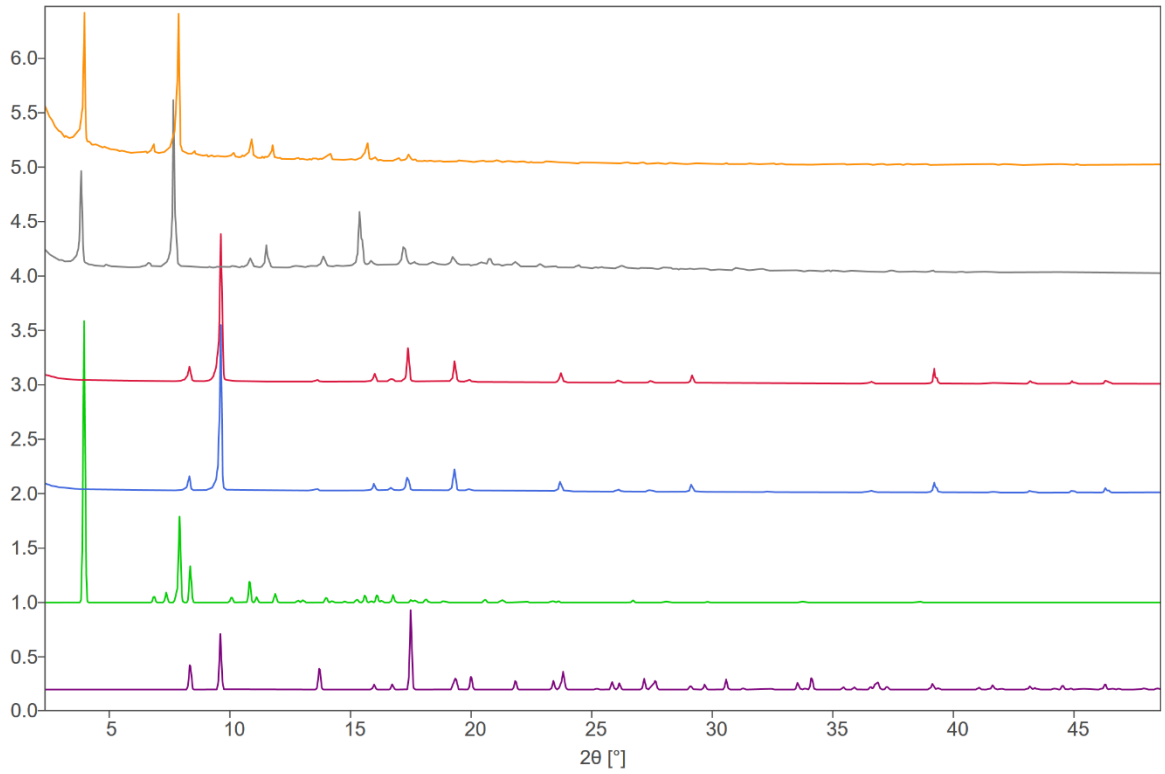


Figure 2.23: Powder XRD patterns of material obtained from syntheses conducted for different lengths of time. From bottom to top: calculated patterns of **2-1DMOF** (purple) and **2-HexMOF** (green), and experimental patterns from syntheses with durations of 4 hours (blue), 8 hours (red), 14 hours (grey), and 16 hours (orange).

Where DMF was used as the solvent, different phases were not obtained in syntheses heated for lengths of time between 4 and 16 hours (Appendix Figure 2.3).

Modulation

Three common acids used as modulators were added independently to the control synthesis conditions in order to assess whether they may affect MOF formation. When sulfuric or hydrochloric acid were added, no crystalline material formed, even after leaving the synthesis mixture heating for over 2 days. When acetic acid was added, the results were not materially different from the original synthesis in either phase or crystallinity (Appendix Figure 2.2).

2.4 Conclusions

Five new copper MOF structures were synthesised in this study, using methyl-substituted 1,3-bis(4-carboxyphenyl)imidazolium linkers. These are summarised in Figure 2.24 and Figure 2.25. All structures with the exception of **2-1DMOF** are composed of 2-dimensional MOF nets of sql topology, which are either layered or polycatenated in the extended structure. **2-HexMOF** is isostructural with a reported MOF synthesised using linker **3** and is a rare example of 3-fold inclined polycatenation.[7]

This work provides insight into how some control over product identity may be achieved, through small adjustments to the solvothermal synthetic conditions. In this, and in bringing together existing studies, the importance of consistency in synthetic methodology for MOF synthesis has also been highlighted, contributing to an increasingly frequent and relevant topic of discussion in the framework chemistry community.[11]

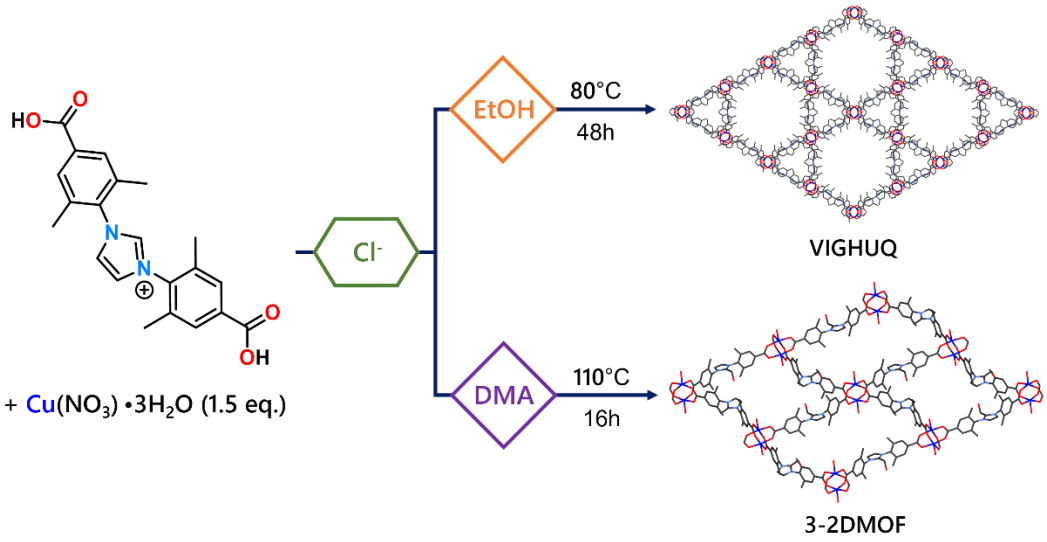


Figure 2.24: Flowchart summarising reported[7] and new MOFs synthesised using linker **3**.2H.

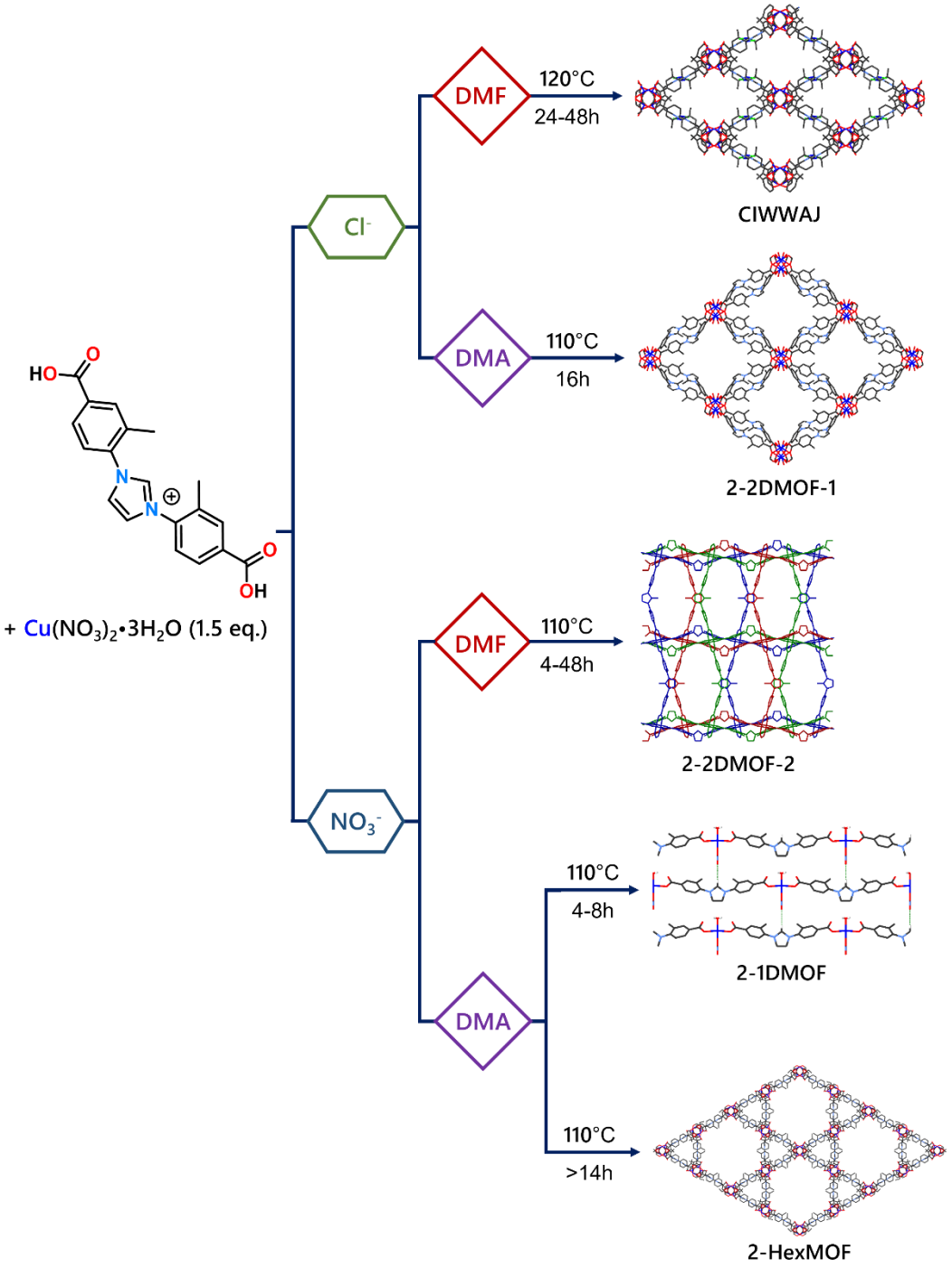


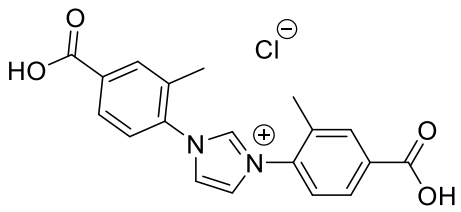
Figure 2.25: Flowchart summarising reported[9] and new MOFs synthesised with linker **2**.2H.

2.5 Experimental

2.5.1 Organic synthesis

Starting materials were purchased from Sigma Aldrich, Fluorochem and Fisher Scientific, and were used as received. NMR data was collected using either a Bruker AVANCE NEO 400 MHz or Bruker AVIII 400 MHz spectrometer and spectra were referenced to the corresponding residual solvent peaks. Mass spectral data was collected using a Waters Xevo-G2-XS or Waters Synapt G2-S instrument. Infrared spectra of solids were obtained via an Agilent Fourier Transform Spectrometer, FTIR-8400S, fitted with a Diamond ATR unit.

1,3-Bis(4-carboxy-2-methylphenyl)imidazolium chloride (**2**.2H•Cl)



A reported procedure was followed.[9] 3-Methyl-4-aminobenzoic acid (3.2 g, 21.6 mmol) was suspended in ethanol (10 mL). Formic acid (2 drops) and glyoxal solution (40% w/w in H_2O) (1.24 mL, 10.8 mmol) were added dropwise. The reaction mixture was stirred at 35°C for 24 hours. The resulting suspension was filtered, washed with water and dried under vacuum to obtain a pale orange solid which was used without further purification or characterisation.

The crude product from the previous step (0.74 g, 2.3 mmol) was suspended in THF (10 mL) under an atmosphere of nitrogen. Meanwhile, paraformaldehyde (92 mg, 3.0 mmol) was mixed with concentrated HCl (0.3 mL) and dioxane (0.6 mL) at 0°C. This was then added to the THF solution and stirred at room temperature overnight. The resulting suspension was filtered and washed with diethyl ether. The product was a beige solid. Yield: 0.45 g, 52 %.

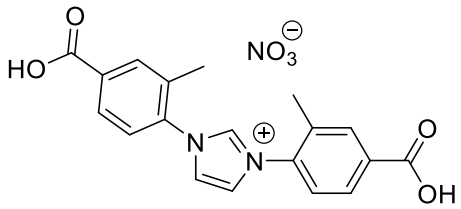
^{1}H NMR (400 MHz, DMSO-d_6) δ 13.36 (s, 2H), 10.02 (s, 1H), 8.41 (d, J = 1.6 Hz, 2H), 8.11 (s, 2H), 8.04 (d, J = 8.1 Hz, 2H), 7.82 (d, J = 8.2 Hz, 2H), 2.42 (s, 6H).

^{13}C NMR (101 MHz, DMSO-d_6) δ 166.29, 138.10, 137.31, 134.13, 132.83, 132.48, 128.16, 127.21, 124.00, 17.22.

MS (ESI$^+$) 337.1194 ($C_{19}H_{17}N_2O_4$ $[M]^+$ requires 337.1188).

IR (ATR) 3144 (ν C-H aromatic), 2880 (ν O-H) 2749 (ν C-H sp^3), 1713 (ν C=O), 1609 (ν C=C), 1543 (ν N=C-N), 1389 (ν C-H methyl), 1186 (ν C-O).

1,3-Bis(4-carboxy-2-methylphenyl)imidazolium nitrate (**2**.2H•NO_3)



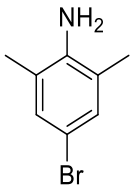
A reported procedure was followed.[9] 1,3-Bis(4-carboxy-2-methylphenyl)imidazolium chloride (0.45 g, 1.2 mmol) was dissolved in a solution of NaOH (0.14 g, 4.7 mmol) in H_2O (25 mL). Nitric acid (1M, 25 mL) was added and the solution was stirred for 1 hour. The solid product was collected by filtration, washed with water and dried under vacuum. Ion exchange was confirmed by dissolving a small amount of the product in a

1:1 mixture of methanol and water and adding a small amount of $AgNO_3$. No precipitate formed, implying an absence of chloride ions.

MS (ESI^+) 337.12 ($C_{19}H_{17}N_2O_4$ $[M]^+$ requires 337.1188).

IR (ATR) 3129 (ν C-H aromatic), 2924 (ν O-H), 1713 (ν C=O), 1542 (ν N=C-N), 1423, 1325 (ν N=O), 1180 (ν C-O).

4-Bromo-2,6-dimethylaniline



A reported procedure was followed.[7] 2,6-Dimethylaniline (8 mL, 65 mmol) was added to dichloromethane (200 mL) and cooled to -78°C under a nitrogen atmosphere. Bromine (3.5 mL, 68.3 mmol) was added slowly over 10 minutes, following which the solution was allowed to warm to room temperature. Sodium bisulfite (10% aqueous solution) (8 mL) was added to quench the reaction. The organic layer was collected and the aqueous layer washed with DCM (150 mL x 2). The organic layers were combined, dried with sodium sulfate and the solvent removed by rotary evaporation. The product was obtained as a brown crystalline solid. Yield: 12.01 g, 92%.

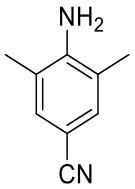
^{1}H NMR (400 MHz, $CDCl_3$) δ 7.09 (s, 2H), 3.58 (s, 2H), 2.17 (s, 6H).

^{13}C NMR (101 MHz, $CDCl_3$) δ 142.23, 130.99, 124.06, 109.88, 17.88.

MS (EI^+) 198.9990, 199.9892 ($C_8H_{10}NBr$ $[M]^+$ requires 198.9991 for ^{79}Br, 200.0025 for ^{80}Br).

IR (ATR) 3427, 3334 (ν N-H), 2973 (ν C-H aromatic), 2900 (ν C-H sp^3), 1628 (ν C=C aromatic), 1467 (ν C-H methyl), 1223 (ν C-N), 853 (ν N-H), 652 (ν C-Br).

4-Amino-2,6-dimethylbenzonitrile



A reported procedure was followed.[7] 4-Bromo-2,6-dimethylaniline (4.00 g, 20.0 mmol), potassium cyanide (1.56 g, 24.0 mmol) and dry potassium iodide (0.64 g, 4.0 mmol, 20 mol%) were added to a flame-dried Schlenk flask under an atmosphere of nitrogen. The solids were degassed further before adding dry toluene (14 mL) and 1,2-dimethylethylenediamine (2.2 mL, 20.0 mmol). The reaction mixture was stirred at 110°C for 3 days. After cooling to room temperature, ethyl acetate (100 mL) was added. The solution was washed with concentrated ammonia solution, followed by a further extraction with ethyl acetate. The organic layer was dried with sodium sulfate and the solvent removed by rotary evaporation. The crude product was purified by column chromatography (DCM/hexane 2:1). Yield: 1.23 g, 42%.

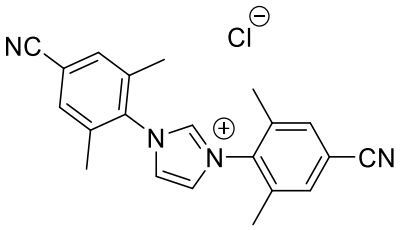
^{1}H NMR (400 MHz, $CDCl_3$) δ 7.22 (s, 2H), 4.05 (s, 2H), 2.16 (s, 6H).

^{13}C NMR (101 MHz, $CDCl_3$) δ 147.21, 132.27, 121.55, 120.60, 99.70, 17.41.

MS (ESI^+) 147.0927 ($C_9H_{10}N_2$ [M+H] requires 147.0922).

IR (ATR) 3477, 3384 (ν N-H), 2967 (ν C-H aromatic), 2907 (ν C-H sp^3), 2207 (ν C≡N), 1633 (ν C=C aromatic), 1602 (ν N-H), 1489 (ν C-H methyl), 1144 (ν C-N), 874 (ν N-H).

1,3-Bis(4-cyano-2,6-dimethylphenyl)imidazolium chloride



A reported procedure was followed.[7] To a suspension of 4-amino-2,6-dimethylbenzonitrile (0.50 g, 3.4 mmol) in ethanol (5 mL), formic acid (1 drop) and glyoxal (40% w/w in H_2O) (0.2 mL, 1.7 mmol) were added dropwise. The mixture was stirred at 35°C or 24 hours. The solvent was removed by rotary evaporation and the yellow solid crude product used in the next step without further purification or characterisation.

The diimide product (0.55 g, 1.7 mmol) was added to THF (5 mL) and cooled to 0°C under a nitrogen atmosphere. Paraformaldehyde (68 mg, 2.3 mmol) in concentrated HCl (0.3 mL) in dioxane (0.6 mL) was added and the reaction was stirred at 35°C overnight. Water and diethyl ether were added and a separation was performed. The solvent was removed from the aqueous layer to yield the product as a pale orange solid. Yield: 0.25 g, 40%.

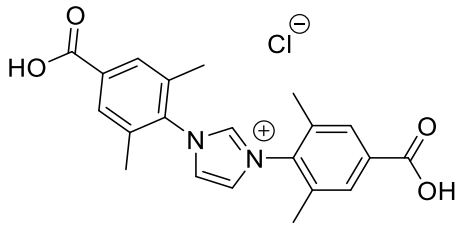
^{1}H NMR (400 MHz, DMSO-d_6) δ 9.82 (s, 1H), 8.40 (s, 2H), 7.98 (s, 4H), 2.22 (s, 12H).

^{13}C NMR (101 MHz, DMSO-d_6) δ 138.64, 137.10, 136.91, 132.55, 124.45, 117.69, 113.26, 16.89.

MS (ESI$^+$) 327.1614 ($C_{21}H_{19}N_4$ $[M]^+$ requires 327.1610).

IR (ATR) 3584, 3300, 3135 (ν C-H aromatic), 2926 (ν C-H sp^3), 2234 (ν C≡N), 1624 (ν C=C aromatic), 1541 (ν N=C-N), 1233 (ν C-H methyl).

1,3-Bis(4-carboxy-2,6-dimethylphenyl)imidazolium chloride (**3**.2H•Cl)



A reported procedure was followed.[7] 1,3-Bis(4-cyano-2,6-dimethylphenyl)imidazolium chloride (0.25 g, 0.7 mmol) was stirred in concentrated hydrochloric acid (20 mL) at 110°C for 4 hours. After cooling to room temperature, the resulting suspension was filtered and washed with water. Yield: 0.13 g, 46%.

^{1}H NMR (400 MHz, DMSO-d_6) δ 13.40 (s, 1H), 9.83 (s, 1H), 8.40 (s, 2H), 7.95 (s, 4H), 2.24 (s, 12H).

^{13}C NMR (101 MHz, DMSO-d_6) δ 166.35, 138.47, 136.70, 135.53, 132.87, 129.61, 124.56, 17.08.

MS (ESI^+) 365.1512 ($C_{21}H_{21}N_2O_4$ $[M]^+$ requires 365.1501).

IR (ATR) 3373 (ν O-H), 3139 (ν C-H aromatic), 3056 (ν C-H sp^3), 1698 (ν C=O), 1605 (ν C=C aromatic), 1545 (ν N=C-N), 1385 (ν C-H methyl).

2.5.2 MOF Synthesis

For scanning electron microscopy, samples were deposited onto conductive carbon tabs. The prepared samples were transferred to and imaged with a Hitachi TM4000Plus table top microscope equipped with an Oxford Instruments x-stream-2.

2-HexMOF

A reported procedure was followed.[9] **2**.2H•NO_3 (11 mg, 0.026 mmol) and $Cu(NO_3)_2$•$3H_2O$ (10 mg, 0.042 mmol, 1.5 equiv.) were dissolved in DMA (1mL) in a 20 mL scintillation vial and heated in an oven at 110°C for 16 hours. Turquoise hexagonal rod-shaped crystals resulted, which were washed twice with fresh DMA prior to structural analysis by SCXRD and PXRD. The resulting framework was different from the reported structure.

2-1DMOF

2.2H•NO_3 (11 mg, 0.026 mmol) and $Cu(NO_3)_2$•$3H_2O$ (10 mg, 0.042 mmol, 1.5 equiv.) were dissolved in DMA (1mL) in a 20 mL scintillation vial and heated in an oven at 110°C for 4 hours. Blue needle crystals resulted, which were washed twice with fresh DMA prior to structural analysis by SCXRD and PXRD.

2-2DMOF-1

2.2H•Cl (10 mg, 0.026 mmol) and $Cu(NO_3)_2$•$3H_2O$ (10 mg, 0.042 mmol, 1.5 equiv.) were dissolved in DMA (1mL) in a 20 mL scintillation vial and heated in an oven at 100°C for

16 hours. Turquoise crystals of both plate and hexagonal rod morphology resulted, which were washed twice with fresh DMA prior to structural analysis by SCXRD and PXRD.

2-2DMOF-2

2.2H•NO_3 (11 mg, 0.026 mmol) and $Cu(NO_3)_2$•$3H_2O$ (10 mg, 0.042 mmol, 1.5 equiv.) were dissolved in DMF (1 mL) in a 20 mL scintillation vial and heated in an oven at 100°C for 16 hours. Turquoise crystals of both plate and hexagonal rod morphology resulted, which were washed twice with fresh DMF prior to structural analysis by SCXRD and PXRD.

3-2DMOF

3.2H•Cl (10 mg, 0.026 mmol) and $Cu(NO_3)_2$•$3H_2O$ (10 mg, 0.042 mmol, 1.5 equiv.) were dissolved in DMA (1mL) in a 20 mL scintillation vial and heated in an oven at 100°C for 16 hours. Turquoise crystals of plate morphology resulted, which were washed twice with fresh DMA prior to structural analysis by SCXRD and PXRD.

Changing Conditions

In experiments investigating the impact of adjusting conditions from the control procedure, the procedures, equipment molar amounts of linker and metal salt, and volume of solvent were used as in the synthesis of **2-HexMOF** as described above. Table 2.2 details the materials and conditions used for these experiments, highlighting those in each case which differ from the control.

The resulting solid from each synthesis was washed twice in the reaction solvent prior to analysis by powder X-ray diffraction. PXRD analysis was conducted on the crystals as-synthesised, without grinding.

Table 2.2: Materials and conditions used in MOF syntheses for 'Changing Conditions' experiments. Variables differing from the control synthesis are highlighted in yellow. Details of the control synthesis are included in each case for completeness, however the same set of results from one control synthesis was used in the ensuing analysis.

Experiment	Counterion	Temp / °C	Solvent	Time / h	Modulator
Temperature	NO_3^-	100	DMA	16	None
	NO_3^-	110	DMA	16	None
	NO_3^-	120	DMA	16	None
Time - DMA	NO_3^-	110	DMA	4	None
	NO_3^-	110	DMA	8	None
	NO_3^-	110	DMA	14	None
	NO_3^-	110	DMA	16	None
Time - DMF	NO_3^-	110	DMF	4	None
	NO_3^-	110	DMF	8	None
	NO_3^-	110	DMF	14	None
	NO_3^-	110	DMF	16	None
Solvent	NO_3^-	110	DMA	16	None
	NO_3^-	110	DMF	16	None
	NO_3^-	110	DEF	16	None
	NO_3^-	110	NMP	16	None
Counterion	NO_3^-	110	DMA	16	None
	Cl^-	110	DMA	16	None
Modulator	NO_3^-	110	DMA	16	None
	NO_3^-	110	DMA	18	Acetic acid (conc.) 1 drop
	NO_3^-	110	DMA	72	HCl (conc.) 1 drop
	NO_3^-	110	DMA	42	H2SO4 (conc.) 1 drop

2.5.3 Crystallographic Analysis

Data for **2-HexMOF**, **2-1DMOF**, **2-2DMOF-2** and **3-2DMOF** were collected using a Rigaku Synergy-S dual source with a PhotonJet-S X-ray source and a HyPix-6000 detector. Data was collected at 100 K through the use of an Oxford Cryosystems cryostream device. Data was collected and processed using CrysAlisPro 171.42.49.57.

Data for **2-2DMOF-1** was collected by the UK National Crystallography Service under the name 2023NCS0022ps. Data was using a Rigaku 007HF diffractometer equipped with Arc)Sec VHF Varimax confocal mirrors and a UG2 goniometer and HyPix 6000HE detector. Data was collected at 100 K and processed using CrysAlisPro 1.171.42.79a.

Using Olex2[12], the structures were solved with the SHELXT[13] structure solution program using Intrinsic Phasing and refined with the SHELXL[14] refinement package using Least Squares minimisation. PLATON was used for calculations of solvent accessible void space.[15]

Powder XRD measurements were carried out at 298K using either a Bruker D8 Advance diffractometer (λ (CuKα1) = 1.5406 Å), or a PANalytical Empyrean diffractometer (λ (CuKα1) = 1.5406 Å) mounted on a zero background sample stage. Theoretical PXRD patterns were calculated from single crystal structures using Mercury 3.10.1.[16,17]

2-HexMOF

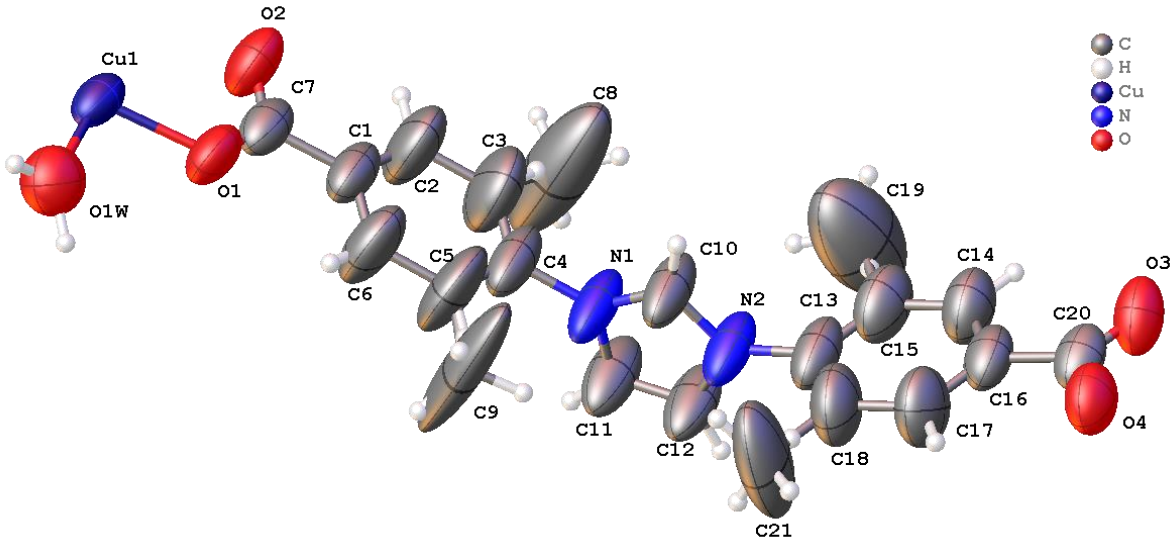


Figure 2.26: Asymmetric unit of **2-HexMOF** showing ellipsoids and atom labels for non-H atoms.

Crystal Data for $C_{19}H_{17}CuN_2O_5$ (*M* =416.89 g/mol): trigonal, space group P-3c1 (no. 165), *a* = 25.7697(12) Å, *c* = 23.9855(10) Å, *V* = 13794.2(14) Å^3, *Z* = 12, *T* = 100.15 K, μ(CuKα) = 0.788 mm^{-1}, *Dcalc* = 0.602 g/cm^3, 76033 reflections measured (6.86° ≤ 2Θ ≤ 157.838°), 9250 unique (R_{int} = 0.0719, R_{sigma} = 0.0341) which were used in all calculations. The final R_1 was 0.0799 (I > 2σ(I)) and wR_2 was 0.2840 (all data).

All hydrogen atoms in the structure were fixed as riding models and the isotropic thermal parameters (Uiso) were based on the Ueq of the parent atom.

The occupancies of methyl group carbon atoms C8 and C9, C19 and C21 were allowed to refine freely before being fixed at values of 1/3 for C9 and C19 and 2/3 for C8 and C21 based on the freely refined occupancies. These atoms were located in the electron density and their positions allowed to refine freely, with the exception of C19 which

was refined subject to bond distance restraints. The isotropic thermal parameters of the pairs of atoms C8 and C9, C19 and C21, were refined subject to restraints.

Disordered solvent and counterion molecules are present in the structure. As such, solvent mask was used to calculate the residual electron density in the void space of the structure. A solvent mask was calculated and 2172 electrons were found in a volume of 9089 $Å^3$ in 1 void per unit cell. This is consistent with the presence of 12 NO_3^- and 36 DMA molecules per unit cell which account for 2100 electrons per unit cell.

Powder XRD analysis was conducted on **2-HexMOF** both as single crystals and dried. The dried sample was obtained by leaving the sample open to the air after solvent exchange with acetone.

2-1DMOF

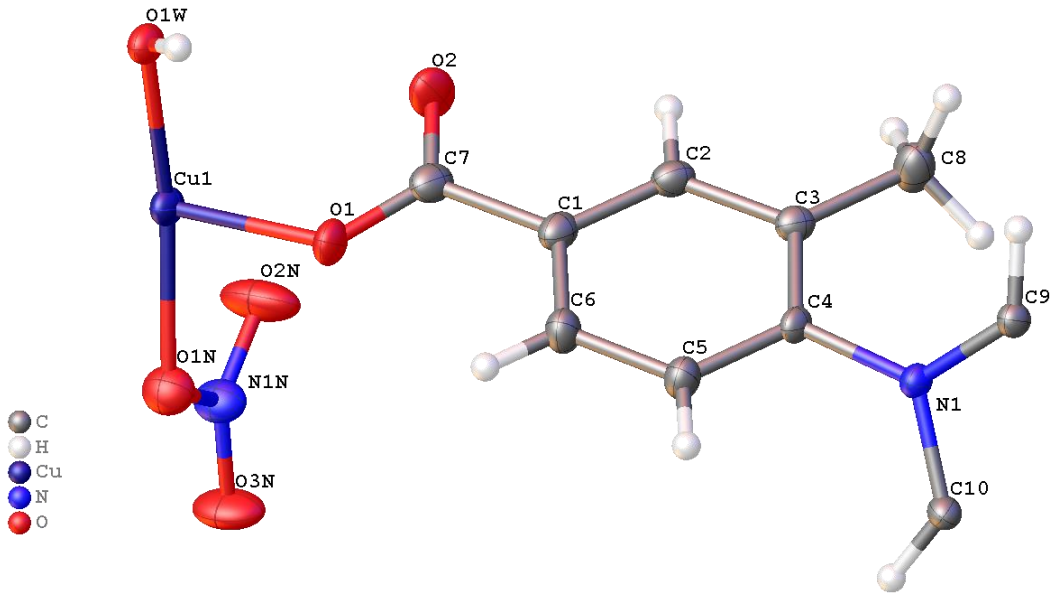


Figure 2.27: Asymmetric unit of **2-1DMOF** showing ellipsoids and atom labels for non-H atoms.

Crystal Data for $C_{19}H_{17}CuN_3O_8$ (*M* =478.89 g/mol): orthorhombic, space group $Cmc2_1$ (no. 36), *a* = 18.3961(3) Å, *b* = 12.9402(2) Å, *c* = 8.13150(10) Å, *V* = 1935.70(5) Å^3, *Z* = 4, *T* = 100.15 K, μ(CuKα) = 2.095 mm^{-1}, *Dcalc* = 1.643 g/cm^3, 9719 reflections measured (8.354° ≤ 2Θ ≤ 157.586°), 2005 unique (R_{int} = 0.0366, R_{sigma} = 0.0292) which were used in all calculations. The final R_1 was 0.0311 (I > 2σ(I)) and wR_2 was 0.0850 (all data).

All hydrogen atoms in the structure were fixed as riding models and the isotropic thermal parameters (Uiso) were based on the Ueq of the parent atom.

2-2DMOF-1

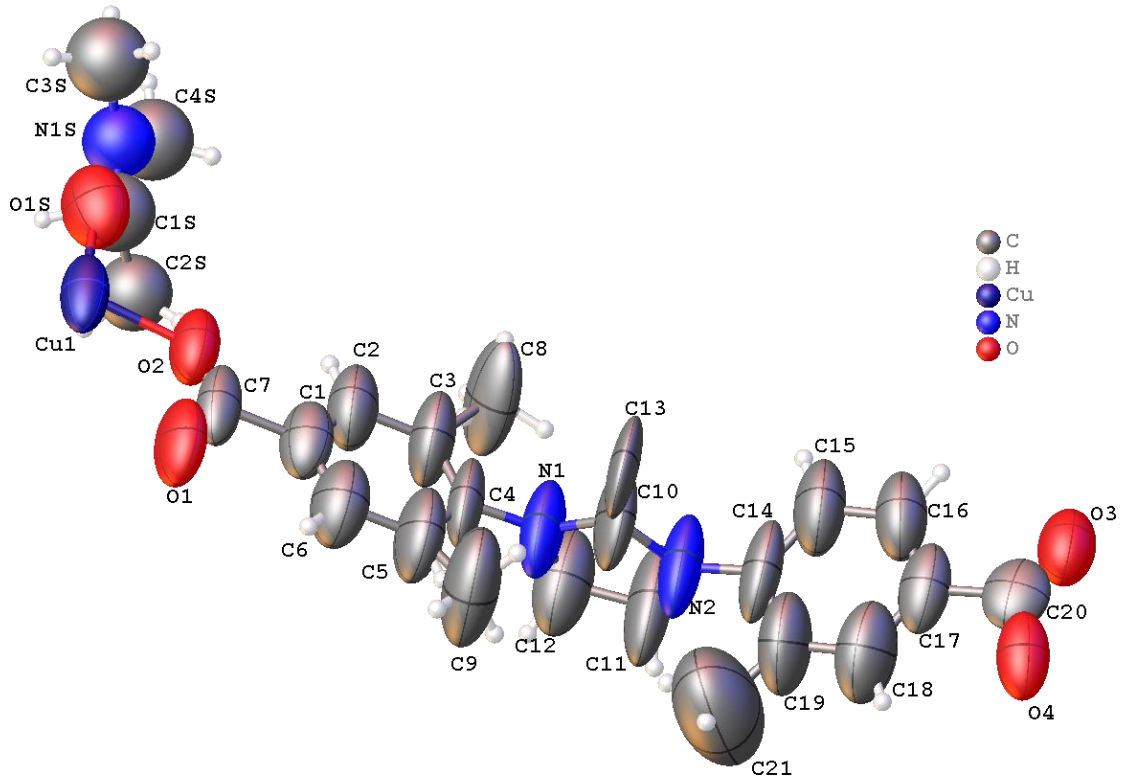


Figure 2.28: Asymmetric unit of **2-2DMOF-1** showing ellipsoids and atom labels for non-H atoms.

Crystal Data for $C_{22}H_{21.5}CuN_{2.5}O_5$ (*M* =464.46 g/mol): monoclinic, space group C2/c (no. 15), *a* = 18.4435(14) Å, *b* = 25.6029(16) Å, *c* = 18.0237(10) Å, *β* = 93.990(7)°, *V* = 8490.3(10) Å^3, *Z* = 8, *T* = 100.00(10) K, μ(Cu Kα) = 0.887 mm^{-1}, *Dcalc* = 0.727 g/cm^3, 29190 reflections measured (5.916° ≤ 2Θ ≤ 136.472°), 7515 unique (R_{int} = 0.1081, R_{sigma} = 0.1539) which were used in all calculations. The final R_1 was 0.1252 (I > 2σ(I)) and wR_2 was 0.3796 (all data).

C9 is thought to be part of a disordered methoxy (-CH_2OH) group for which the substituent hydrogen and oxygen atoms are rotationally disordered and not locatable in the electron density. These atoms were therefore included in the solvent mask calculations, and C9 left without substituents modelled in the final structure. Phenyl rings C1-C6 and C14-C19 and methyl groups C8, C9 and C21 were refined subject to restraints on geometry and thermal parameters.

A solvent mask was calculated and 1336 electrons were found in a volume of 4671 Å in one void per unit cell. This is consistent with the presence of 16 H, 8 OH, 8 NO_3^- and 20 DMA molecules per unit cell which account for 1296 electrons per unit cell.

The positions of the carbons C8 and C9 were located in the electron density. The occupancies of these disordered atoms were allowed to refine freely before being fixed at 1/2. All hydrogen atoms in the structure were fixed as riding models and the isotropic thermal parameters (Uiso) were based on the Ueq of the parent atom.

2-2DMOF-2

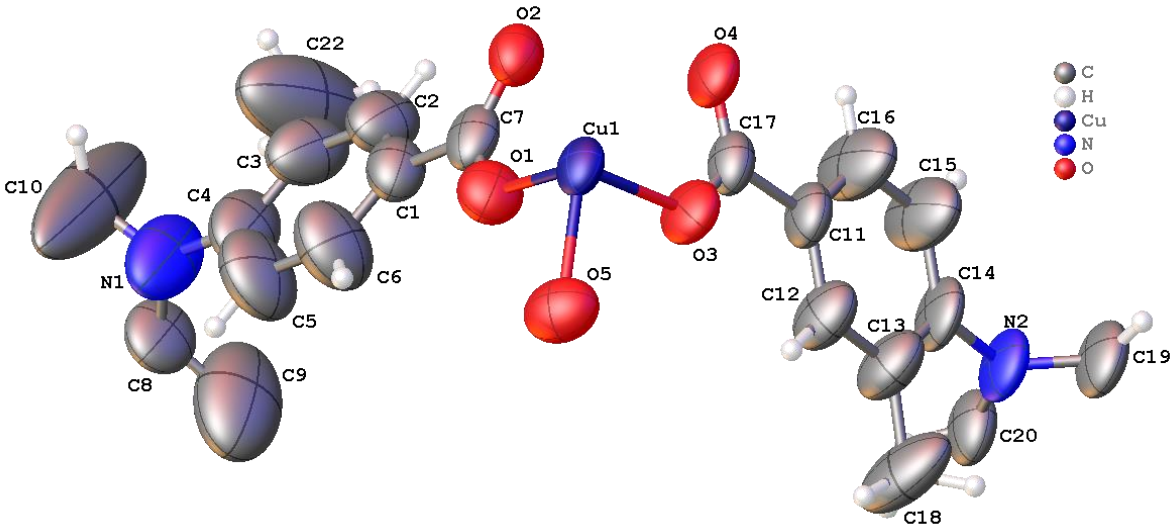


Figure 2.29: Asymmetric unit of **2-2DMOF-2** showing ellipsoids and atom labels for non-H atoms.

Crystal Data for $C_{78}H_{58}Cu_4N_8O_{20}$ (M =1681.48 g/mol): monoclinic, space group I2/m (no. 12), a = 11.09690(10) Å, b = 35.6442(5) Å, c = 18.8410(3) Å, β = 96.9480(10)°, V = 7397.64(17) Å^3, Z = 2, T = 100.15 K, μ(CuKα) = 0.984 mm^{-1}, $Dcalc$ = 0.755 g/cm^3, 57413 reflections measured (5.336° ≤ 2Θ ≤ 156.928°), 7520 unique (R_{int} = 0.0574, R_{sigma} = 0.0288) which were used in all calculations. The final R_1 was 0.0954 (I > 2σ(I)) and wR_2 was 0.3168 (all data).

C9 is thought to be part of a disordered methoxy (-CH_2OH) group for which the substituent hydrogen and oxygen atoms are rotationally disordered and not locatable in the electron density. These atoms were therefore included in the solvent mask calculations, and C9 left without substituents modelled in the final structure. O5 has also been modelled without its substituent atoms due to uncertainty in the identity of

the substituents. Phenyl rings C1-C6 and C11-C16 and methyl group C22 were refined subject to restraints on geometry and thermal parameters.

Disordered solvent and counterion molecules are present in the structure. As such, a solvent mask was used to calculate the residual electron density in the void space of the structure. A solvent mask was calculated and 1286 electrons were found in a volume of 4522 $Å^3$ in 1 void per unit cell. This is consistent with the presence of 4 H_2OH (part of disordered methoxy groups for which only the carbon atom could be modelled), 8 NO_3^- and 24 DMF molecules per unit cell which account for 1252 electrons per unit cell.

All hydrogen atoms in the structure were fixed as riding models and the isotropic thermal parameters (Uiso) were based on the Ueq of the parent atom.

3-2DMOF

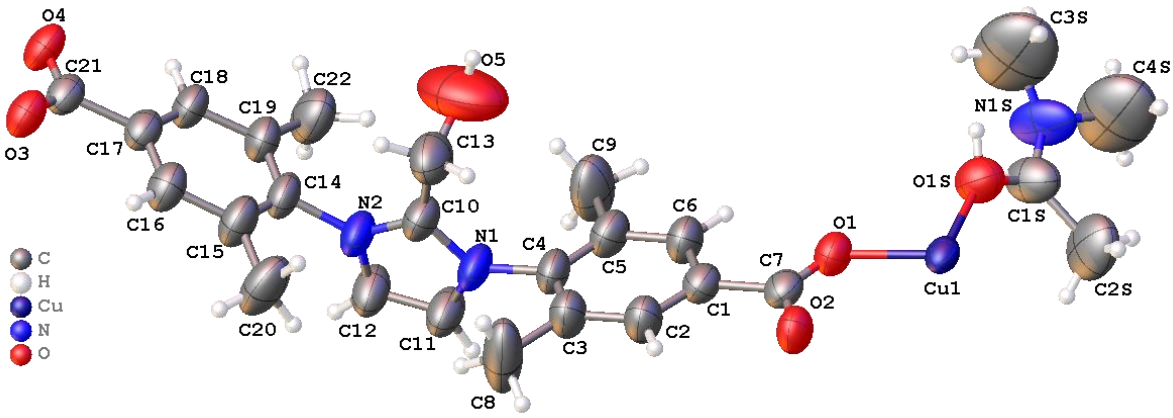


Figure 2.30: Asymmetric unit of **3-2DMOF** showing ellipsoids and atom labels for non-H atoms.

Crystal Data for $C_{24}H_{26.5}CuN_{2.5}O_6$ (M =509.52 g/mol): monoclinic, space group C2/c (no. 15), a = 16.3552(4) Å, b = 24.5756(5) Å, c = 26.0825(4) Å, β = 105.303(2)°, V =

10111.9(4) $Å^3$, Z = 8, T = 100.15 K, μ(CuKα) = 0.783 mm^{-1}, $Dcalc$ = 0.669 g/cm^3, 67808 reflections measured (6.658° ≤ 2Θ ≤ 157.626°), 10327 unique (R_{int} = 0.0694, R_{sigma} = 0.0426) which were used in all calculations. The final R_1 was 0.0763 (I > 2σ(I)) and wR_2 was 0.2635 (all data).

All hydrogen atoms in the structure were fixed as riding models and the isotropic thermal parameters (Uiso) were based on the Ueq of the parent atom.

Bond length and isotropic thermal parameter restraints were used to refine the positions the atoms in the coordinated dimethylacetamide molecule (C1S, C2S, C3S, C4S and N1S). The occupancy of these atoms was allowed to refine freely before being fixed at 1/2.

The structure contains disordered solvent and counterion molecules which could not be located in the electron density. A solvent mask was therefore used to estimate the number of molecules present by calculating the residual electron density. The solvent mask found 1770 electrons in a volume of 5891 $Å^3$ in 1 void per unit cell. This is consistent with the presence of approximately 4 NO_3^-, 4 Cl^- and 32 DMA molecules per unit cell which account for 1728 electrons per unit cell.

2.6 References

1 C. I. Ezugwu, N. A. Kabir, M. Yusubov and F. Verpoort, *Coord Chem Rev*, 2016, 307, 188–210.

2 R. S. Crees, M. L. Cole, L. R. Hanton and C. J. Sumby, *Inorg Chem*, 2010, **49**, 1712–1719.

3 X. Zhang, J. Sun, G. Wei, Z. Liu, H. Yang, K. Wang and H. Fei, *Angew Chem Int Ed*, 2019, **58**, 2844–2849.

4 J. Chun, I. G. Jung, H. J. Kim, M. Park, M. S. Lah and S. U. Son, *Inorg Chem*, 2009, **48**, 6353–6355.

5 S. Sen, T. Yamada, H. Kitagawa and P. K. Bharadwaj, *Cryst Growth Des*, 2014, **14**, 1240–1244.

6 C. Xu, Y. Liu, L. Wang, J. Ma, L. Yang, F.-X. Pan, A. M. Kirillov and W. Liu, *Dalton Trans*, 2017, **46**, 16426–16431.

7 G. Nickerl, A. Notzon, M. Heitbaum, I. Senkovska, F. Glorius and S. Kaskel, *Cryst Growth Des*, 2013, **13**, 198–203.

8 H.-J. Lee, H. Kwon, J. Sim, D. Song, Y. Kim, J. Kim, K. Kim and E. Lee, *CrystEngComm*, 2017, **19**, 1528–1534.

9 Q. Yao, X. Lu, K. Liu, C. Ma, J. Su, C. Lin, D. Li, J. Dou, J. Sun and W. Duan, *Dalton Trans*, 2019, **48**, 5144–5148.

10 M. A. DeBord, P. O. Wagers, S. R. Crabtree, C. A. Tessier, M. J. Panzner and W. J. Youngs, *Bioorg Med Chem Lett*, 2017, **27**, 196–202.

11 H. Boström, S. Emmerling, F. Heck, C. Koschnick, A. Jones, M. Cliffe, R. Al Natour, M. Bonneau, V. Guillerm, O. Shekhah, M. Eddaoudi, J. Lopez-Cabrelles, S. Furukawa, M. Romero-Angel, C. Marti-Gastaldo, M. Yan, A. Morris, I. Romero-Muñiz, Y. Xiong, A. Platero-Prats, J. Roth, W. Queen, K. Mertin, D. Schier, N. Champness, H. Yeung and B. Lotsch, *Adv Mater,* 2023, 2304832.

11 O. V Dolomanov, L. J. Bourhis, R. J. Gildea, J. A. K. Howard and H. Puschmann, *J Appl Crystallogr*, 2009, **42**, 339–341.

12 G. M. Sheldrick, *Acta Crystallogr A*, 2015, **71**, 3–8.

13 G. M. Sheldrick, *Acta Crystallogr C*, 2015, **71**, 3–8.

14 A. L. Spek, *Acta Crystallogr C*, 2015, **71**, 9–18.

15 C. F. Macrae, I. J. Bruno, J. A. Chisholm, P. R. Edgington, P. McCabe, E. Pidcock, L. Rodriguez-Monge, R. Taylor, J. van de Streek and P. A. Wood, *J Appl Crystallogr*, 2008, **41**, 466–470.

16 C. F. MacRae, I. Sovago, S. J. Cottrell, P. T. A. Galek, P. McCabe, E. Pidcock, M. Platings, G. P. Shields, J. S. Stevens, M. Towler and P. A. Wood, *J Appl Crystallogr*, 2020, **53**, 226–235.

3 CHAPTER THREE

Imidazolium-functionalised amidinium-carboxylate HOFs

3.1 Introduction

As discussed in Chapter 1, hydrogen-bonded organic frameworks (HOFs) are porous crystalline materials composed of organic molecules arranged into a crystalline structure held together by intermolecular hydrogen-bonding interactions.[1] A wide variety of functional groups may be and have been used to synthesise HOFs. Those of particular relevance to the work described in this chapter are amidinium and carboxylate functional groups (Figure 3.1).



Figure 3.1: Carboxylate functional group (left), amidinium functional group (right).

Both of these functional groups have the capacity to form a maximum of four hydrogen bonds with other species. There are several ways in which the two functional groups may interact, depending on the relative geometries of the groups within a structure. Some examples are shown in Figure 3.2. The end-to-end dual hydrogen bonding motif (Figure 3.2, left) is the 'ideal' mode of interaction. This interaction results in the groups forming what is known as an $R_2^2(8)$ dimer. This notation is derived from graph set

theory which was first applied to organic crystal structures by Kuleshova and Zorky, based on work by Wells.[2–4] Etter, and later Bernstein, developed this approach for more specific applications in the context of hydrogen bonding.[5–7] A general descriptor $G_d^a(n)$ is given. G denotes the fundamental pattern type – in this case, R, which indicates a ring. The subscript number, d, refers to the number of hydrogen bond donors partaking in the interaction; the superscript number, a, refers to the number of hydrogen bond acceptors, and n refers to the 'degree' of the pattern – the number of atoms contained in the pattern.

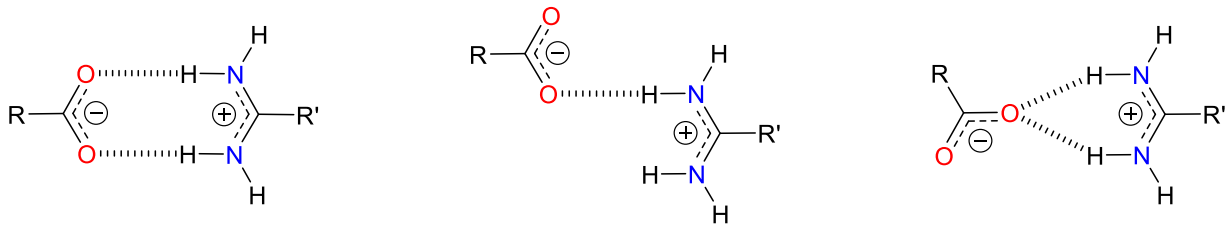


Figure 3.2: Examples of some amidinium-carboxylate hydrogen-bonding motifs.

Another advantage of using amidinium and carboxylate functional groups in HOFs is the fact that they possess opposite charges. This means that hydrogen bonds formed between the groups are strengthened by electrostatic attraction (known as charge-assisted H-bonds).[8] Strong hydrogen bonds are desirable in HOF synthesis as they should increase the stability of the framework, thus potentially increasing the likelihood of a structure to display permanent porosity. Ward et al. were first to leverage this concept for the design of porous frameworks, using guanidinium and carboxylate building blocks.[9]

In HOF synthesis, the presence of carboxylate groups may be achieved via in-situ deprotonation of the carboxylic acid derivative, which can aid the solubility of the component as well as allowing control over the extent of deprotonation.[10] It is therefore worth discussing the capability of carboxylic acid groups to form hydrogen bonds with one another and with carboxylate groups. An $R_2^2(8)$ dimer may be formed by intermolecular interactions between two carboxylic acid groups, each acting as a one H-bond donor and one H-bond acceptor (Figure 3.3A). It is also possible for a carboxylate group to act as an H-bond acceptor from the O-H group on a carboxylic acid (Figure 3.3B).



Figure 3.3: Hydrogen bonding interactions between (A) two carboxylic acid groups, and (B) one carboxylic acid and one carboxylate group.

In the 1990s Fischer et al. reported early examples of amidinium-carboxylate hydrogen-bonded frameworks, utilising a cyclic bisamidinium with an ethane linkage, and a range of dicarboxylate units.[11,12] More recently, a significant amount of development in the field has been conducted by White et al..[13] This group reported the first 3-dimensional amidinium-carboxylate HOF which was synthesised from aqueous solution.[14] They use a molecular tectonics approach similar to that used in the design of many metal-organic frameworks; employing rigid, directional building blocks to elicit some degree of control over the structure of the resulting framework (Figure 3.4).[15] In a subsequent

study it was found that the use of extended and more flexible building blocks result in reduced predictability of framework structures.[16]

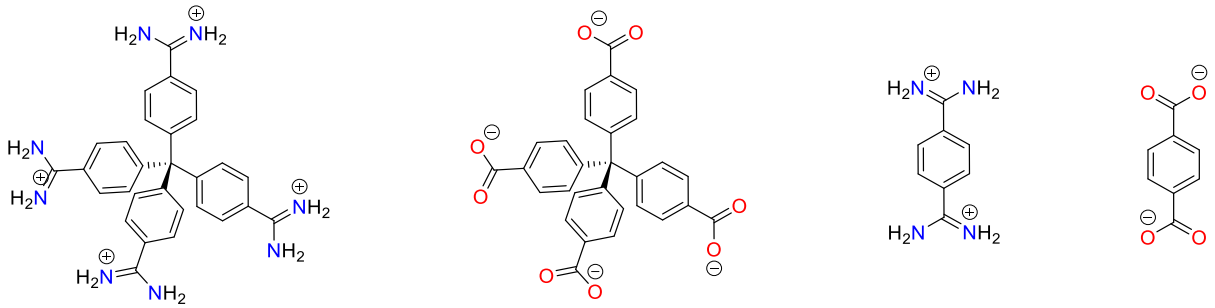


Figure 3.4: Examples of building blocks employed by White et al. in HOF synthesis.[16,17]

Reaching beyond structural studies, recent developments in the field have begun to look into potential applications of amidinium-carboxylate HOFs. Materials with properties such as fluorescence, enzyme encapsulation and controlled molecular reorganisation have been reported.[18–20]

3.2 Aims

This chapter concerns the synthesis of amidinium-carboxylate HOFs containing imidazolium-based linkers from solutions of their components. The rationale for tecton choice, structures of a range of HOFs, and attempts to further differentiate these frameworks through pre- and post-synthetic metalation are described in detail.

The framework is intended to be used as a scaffold to support an NHC-metal-amide complex in the pores, with the imidazolium compound serving the dual purpose of linker in the framework and ligand in the complex. This would open up the possibility

of performing detailed studies of complexes by single crystal X-ray diffraction in order to gain insight into their behaviour in the enclosed environment.

3.3 Results and Discussion

3.3.1 Initial Building Block Synthesis

A range of carboxylic acid-functionalised compounds with imidazolium centres were synthesised. The compounds are similar to those used for metal-organic framework (MOF) synthesis in Chapter 2, although in this case they contain four carboxylic acid groups and some variation in flexibility (Figure 3.5). As a straight diamidinium compound was used as one tecton, tetracarboxylate compounds were designed in order to increase the likelihood of forming a two-or three-dimensional framework.

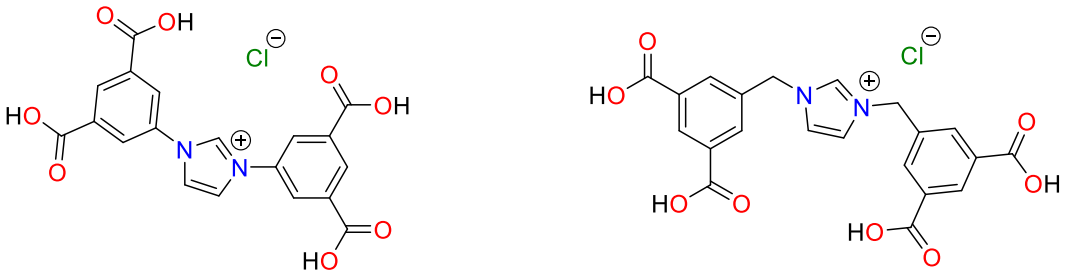
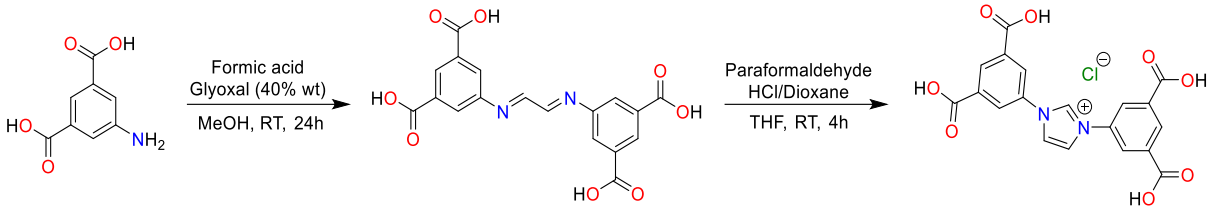


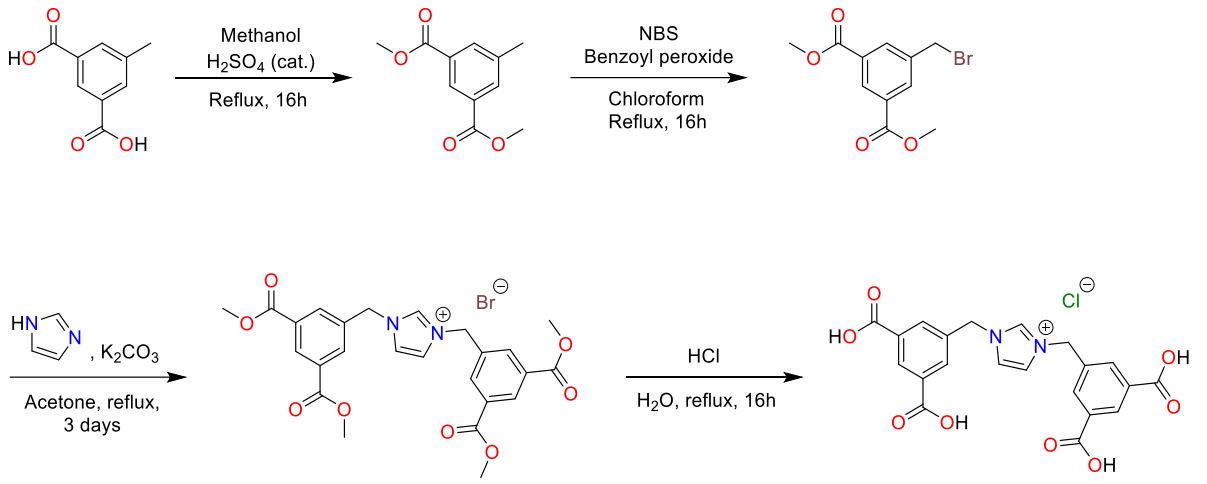
Figure 3.5: Imidazolium-containing components used in this work: **4**.4H•Cl (left) and **5**.4H•Cl (right).

The synthesis of the more rigid of the two carboxylate tectons, 1,3-bis(dicarboxyphenyl)imidazolium chloride (**4**.4H•Cl) was performed from an amine starting material, via a diimide intermediate and following a reported procedure (Scheme 3.1).[21]



Scheme 3.1: Synthetic route to **4**.4H•Cl.

The second carboxylate compound, 1,3-bis(dicarboxybenzyl)imidazolium chloride (**5**.4H•Cl), bears less resemblance to the type of molecule typically employed in HOF synthesis. Due to the flexible methylene bridge between the imidazolium moiety and each phenyl ring, there is more variability in terms of the relative direction of the carboxylic acid groups and therefore the geometry of the hydrogen bonding interactions. A four-step synthesis (Scheme 3.2) was used to form this compound, beginning with 5-methylisophthalic acid. This compound was esterified and brominated and subsequently reacted with imidazole to form the methyl ester of the linker. This process was adapted from a synthesis for 1,3-bis(4-methoxybenzyl)imidazolium bromide.[22] Hydrolysis was then performed under acidic conditions. Saponification was found to be an unsuitable method for removal of the ester group as it caused cleavage of the imidazole-methylisophthalate bonds.



Scheme 3.2: Synthetic route to 5.4H•Cl

The amidinium moiety used in this work was terephthalamidinium (**6**•2Cl)(Figure 3.6). This was decided to be a suitable compound for use due to its binary functionality which would allow formation of extended structures, as well as its rigidity. Given the flexibility imparted by the methyl group of the imidazolium linkers, a rigid secondary tecton was selected to increase the likelihood of some and consistency in structure of the resulting frameworks. A reported procedure was followed for the synthesis of this material.[23]

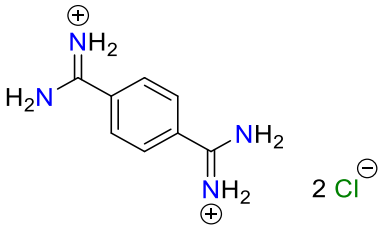


Figure 3.6: Amidinium tecton, **6**•2Cl.

3.3.2 Initial HOF Synthesis and Analysis

Crystallisation of hydrogen-bonded organic frameworks was carried out in aqueous solution. The method was adapted from a reported procedure by White et al. for the co-crystallisation of terephthalate and a tetraamidinium tetraphenylmethane compound.[14] Aqueous solutions of each component were prepared separately, with sodium hydroxide used to deprotonate the carboxylic acid groups of the imidazolium-containing compound and increase the solubility of this linker. The solution of the amidinium component was then added gently, dropwise, to the solution of the imidazolium compound, in order to allow slow mixing. The same procedure was used for all attempts at framework synthesis, with varying linker concentrations, ratios and counterions.

All linker syntheses as described above produce the chloride salts of the respective compounds. These were either used as-synthesised or ion-exchanged to produce the equivalent hexafluorophosphate salt.

All attempted HOF syntheses using **4**.4H as the imidazolium-containing component were unsuccessful, with all starting materials remaining in solution even when left over a period of more than 6 months.

Crystallisations using the more flexible linker **5**.4H were successful however, with single crystals forming in syntheses using both the chloride and hexafluorophosphate salts. For successful syntheses, co-crystallisation occurred at room temperature over varying

periods of time, between 3 and 10 days. The crystals were characterised using single crystal X-ray diffraction, and the structures analysed in detail.

HOF **A**

In a synthesis using **5**.4H•PF_6 and **6**•2PF_6, structure **A**, [**5**$_6$**6**$_9$(H_2O)$_{58}$]$_n$, crystallised in the triclinic space group $P\bar{1}$. The asymmetric unit comprises three molecules of **5**, four and a half molecules of **6** and 27 molecules of H_2O, the latter calculated by evaluating the electron density using a solvent mask. All molecules of **5** are fully deprotonated with an overall charge of -3, and all molecules of **6** are fully protonated with a charge of +2. The framework is therefore charge balanced, and there are no counterions present.

All three molecules of **5** in the framework have the same connectivity in terms of linker-linker hydrogen bonding. Two of the carboxylate groups partake in the anticipated dual hydrogen bonding interaction with molecules of **6**, one forms both a dual hydrogen bond and an additional single H-bond, and the final carboxylate group does not participate in any linker-linker hydrogen bonds. The four and a half molecules of **6** can be split into two groups by their connectivity. Three of the amidinium molecules (**A6a**, coloured green in figures) form the dual hydrogen bonding interaction at both ends. The other one and a half (**A6b**, coloured pink in figures) form both a dual hydrogen bond and an additional single hydrogen bonding interaction at both amidinium groups. All amidinium-carboxylate hydrogen bonds in framework **A** (Figure 3.7) have N···O distances between 2.74 Å and 2.88 Å.

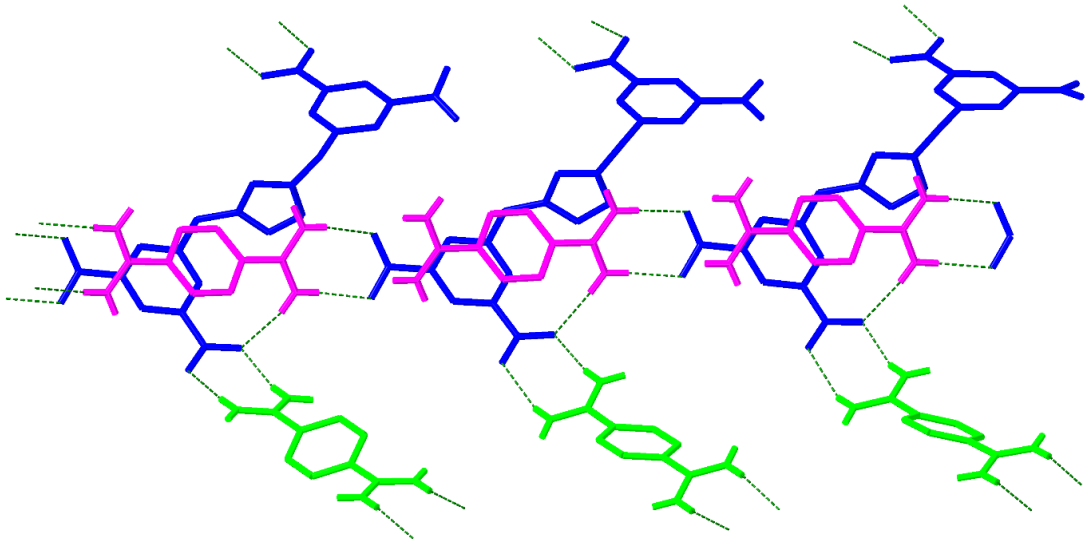


Figure 3.7: Amidinium-carboxylate hydrogen bonding interactions in structure **A**.

The result of these interactions is a bilayer structure in which the two types of amidinium linker can be assigned different roles. **A6a** linkers connect molecules of **5** within the layers, whilst **A6b** linkers span the layers, forming the bilayer (Figure 3.8A). There are no linker-linker hydrogen bonds between separate bilayers, however there is π-π stacking between **A5** and **A6b** linkers. These stacking interactions extend between bilayers as well as within them and have centroid-centroid distances of 3.61 Å to 3.77 Å between the aryl rings. Although a solvent mask was used to calculate the total number of water molecules in the structure, some molecules of H_2O could be crystallographically resolved. The water molecules that could be modelled are distributed throughout the structure, avoiding the π-π stacking regions (Figure 3.8B).

It should be noted that attempts to reproduce framework **A** were unsuccessful.

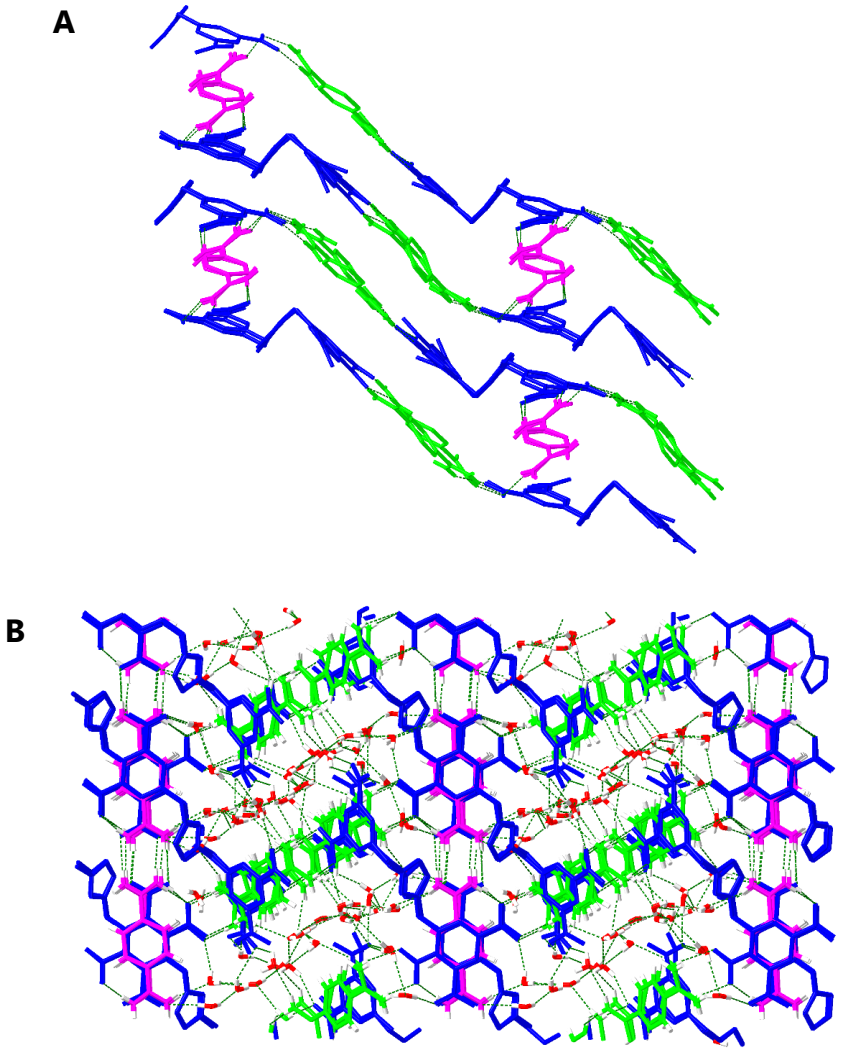


Figure 3.8: (A) Bilayer structure of **A**. (B) Face-to-face π-π stacking interactions and arrangement of water molecules in framework **A**.

HOF **B**

Where **5**.4H•Cl and **6**•2Cl were used as the starting materials, framework **B**, [**5**$_2$**6**$_3$(H$_2$O)$_{10}$]$_n$ formed, also in the space group $P\bar{1}$. The asymmetric unit has the same ratio of **5** to **6** as structure **A**, with one molecule of **5** and one and a half of **6**. Ten molecules of water are also present. **5** is again fully deprotonated and **6** fully protonated, and the framework is charge balanced without any counterions. There are

one and a half crystallographically independent molecules of **6** in the asymmetric unit, here denoted as **B6a** and **B6b**. **B6a** partakes in the dual $R_2^2(8)$ hydrogen-bonding interaction at both amidinium termini, with one of the -NH_2 groups on either end forming an additional H- bond with a different carboxylate group. This means that each molecule of **B6a** interacts with four carboxylate groups. One amidinium group of **B6b** partakes in the dual H-bond interaction, with the amidinium group at the other side of the linker forming a single hydrogen bond with a carboxylate group. Each molecule of **B6b** thus interacts with two carboxylate groups. The N···O distances of all amidinium-carboxylate H-bonds (Figure 3.9) are between 2.77 Å and 2.88 Å. All H-bond donors or acceptors on both linkers that are not involved in hydrogen bonding with another linker appear to form at least one hydrogen bond with water molecule(s) based on the calculated positions of the hydrogen atoms. All crystallographically identifiable water molecules in the structure appear to be hydrogen-bonded to at least one organic component.

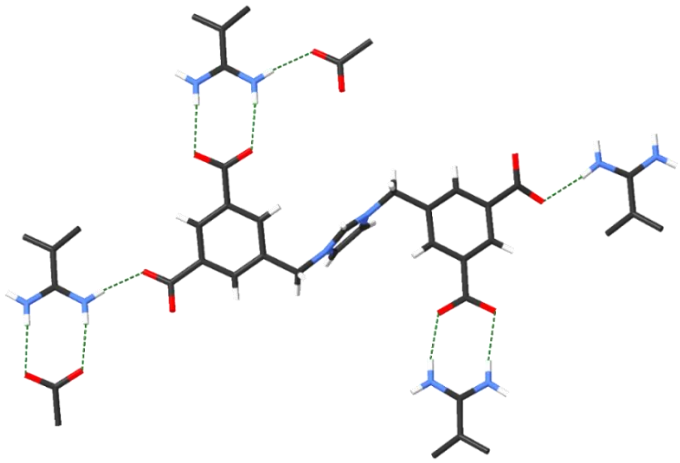


Figure 3.9: Carboxylate-amidinium hydrogen bonding interactions in HOF **B**, displayed around a molecule of **B5**.

Looking at the structure more broadly, the linkers are arranged into 2D sheets which are stacked on top of each other in an offset fashion (Figure 3.10A). Molecules of **B6b** are arranged such that the aryl rings are engaged in face-to-face π-π stacking interactions with a centroid-centroid distance of 3.78 Å. Water molecules, which are likely structurally significant, are arranged between the layers (Figure 3.10B). The imidazolium ring is out of the plane of the sheets, which gives rise to an additional interaction between linkers. The orientation of the ring is such that the calculated position of the N-C**H**-N proton of **5** places it directed into the space between the 2D sheets. Although all hydrogens in this structure are placed in calculated positions, electron density for this proton was observed. This orientation allows the slightly acidic N-C**H**-N proton to partake in hydrogen bonding with a carboxylate oxygen atom on a different molecule of **5**, in an adjacent sheet. The C···O distance for this hydrogen bond is 3.04 Å. This indicates it is a weaker interaction than the amidinium-carboxylate hydrogen bonds, which would be expected due to the smaller difference in electron density in the N-C**H**-N hydrogen bond donor than that of N-H.

The small distance between layers and the fact that the N-C**H**-N proton is involved in structural hydrogen bonding means that framework **B** is unlikely to be suitable for the incorporation of carbene-metal complexes.

From the fact that frameworks **A** and **B** differ in structure, it appears that the counterions associated with the tectons have some influence on the framework formed. The fact that hexafluorophosphate ions are larger and more weakly hydrogen

bonding than chloride ions may be an influencing factor as they may be less strongly bound to the organic ions in the starting solution.

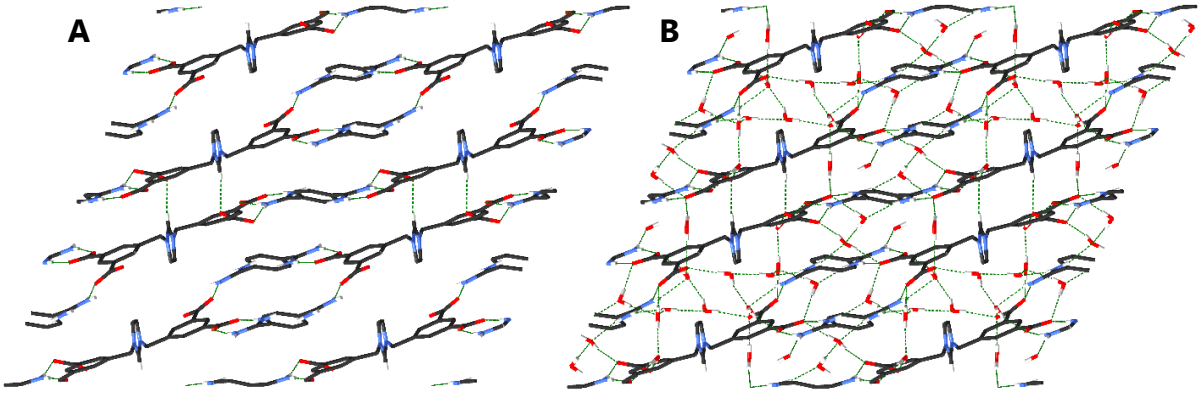


Figure 3.10: Framework **B** viewed along the a-axis, showing stacking of the sheets. (A) Water molecules not shown. (B) Water molecules and associated hydrogen bonding network displayed.

3.3.3 Modified Imidazolium Building Block

Having observed that the imidazolium N-C**H**-N proton is capable of participating in structurally significant hydrogen bonding interactions, we were interested to investigate how a different group attached to that carbon would impact the structure. An analogous molecule was therefore devised, using methylimidazole rather than imidazole in the centre (Figure 3.11). This was synthesised using the same method as for linker **5** tecton, and was used as the chloride salt.

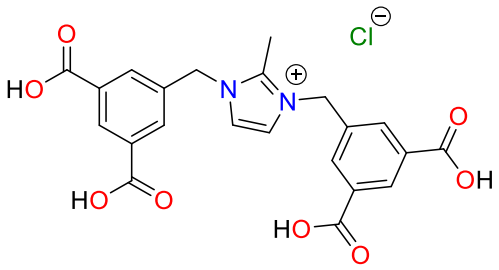


Figure 3.11: Modified linker, N,N'-bis(3,5-dicarboxybenzyl)-2-methylimidazolium chloride.

3.3.4 Second-phase HOF Synthesis and Analysis

Framework synthesis using this modified linker (**7**.4H•Cl) was performed using the as-synthesised chloride salts of both components. The crystallisation method was the same as was used for framework **B**. Within 24 hours, yellow crystals of two different morphologies had formed in the vial - a mixture of plates and some needles. Both were analysed by SCXRD, and the structures again examined in detail. In both cases, the methylimidazolium moiety in the carboxylate molecule is disordered over two positions, with the flexibility to rotate around the methyl bridges and face one of two directions. It may be the reduced propensity of the N-C(**CH₃**)-N methyl group to hydrogen bond in comparison with the N-C**H**-N proton which reduces the likelihood of a preferred orientation of the imidazolium ring in these structures compared with those synthesised using linker **5**.

HOF **C**

The crystals of plate morphology (Framework **C**) have the formula $[\mathbf{7}_2\mathbf{6}_3(H_2O)_{26}]_n$ and crystallise in the space group $P\bar{1}$. There is one molecule of **7** in the asymmetric unit,

one and a half molecules of **6** and thirteen water molecules. As with the previous frameworks, the structure is charge balanced by virtue of the organic moieties.

This structure is rather different from the frameworks discussed previously, with the water molecules playing a more distinctive structural role. Whereas in structures **A** and **B** the organic components are hydrogen bonded in networks of 2-dimensional sheets, here they appear to form distinct chains of five organic molecules (Figure 3.12) which are then interlinked by water molecules. It may be debatable therefore whether this structure should be considered a HOF in that the organic compounds in themselves do not form an extended framework structure. A molecule of **7** interacts with amidinium molecules at two of the four carboxylate groups, with the remaining groups only hydrogen-bonded to water molecules. All hydrogen bonds between the organic building blocks are of the $R_2^2(8)$ motif, with little variation in the N···O distances, these having lengths of 2.77 to 2.79 Å.

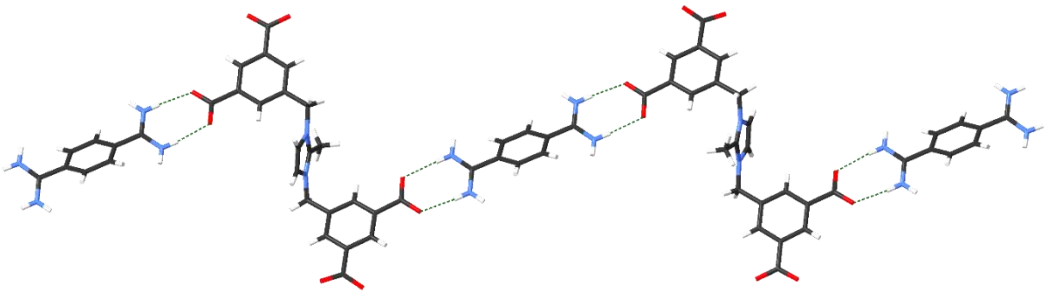


Figure 3.12: Pentamolecular hydrogen-bonded chain in framework **C**.

Looking at the broader structure, the chains of organic molecules are linked in all directions by hydrogen-bonded water molecules. Four water molecules (two crystallographically distinct pairs - O3W and O4W) are of particular note in the

structure. The oxygen atom of each water molecule forms two H-bonds, one with the terminal amidinium group of the chain, and one with another water molecule. This effectively extends the chains shown in Figure 3.12. One hydrogen on each water molecule is then available to hydrogen bond with a carboxylate oxygen in a different chain above or below the plane. Figure 3.13 shows these interactions in detail.

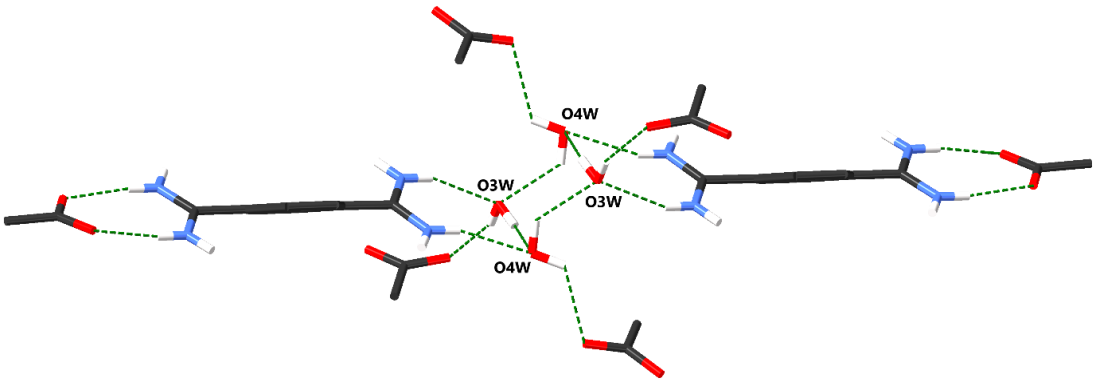


Figure 3.13: Hydrogen-bonding interactions of O3W and O4W in framework **C**.

The interactions of the water molecules effectively make the framework a three-dimensional structure, however the other water molecules present are also hydrogen bonded to the organic components and form a network which aids in packing of the chains (Figure 3.14). By virtue of the hydrogen bonding of the water molecules shown in Figure 3.13 above, the chains are layered in an offset fashion rather than directly one on top of another. There do not appear to be any appreciable π-π stacking interactions in the structure.

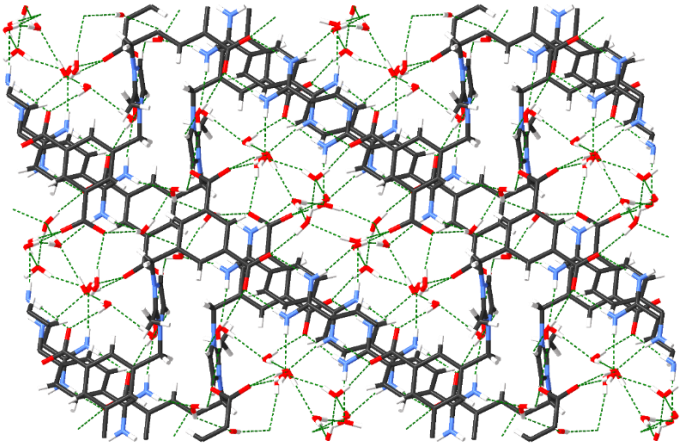


Figure 3.14: Structure **C** viewed down the b-axis, showing the complete hydrogen bonded network.

HOF **D**

The other, needle shaped, crystals retrieved from the same synthesis were found to be a HOF structure in which the carboxylate component remained protonated at one of the four carboxylate functional groups. This resulted in a structure with the formula $[(\mathbf{7}.H)_2\mathbf{6}_2(H_2O)_{16}]_n$ and is in the space group $P\bar{1}$. There is one molecule of **7**.H, one molecule of **6** and eight molecules of water in the asymmetric unit. As with all structures already discussed, this framework is charge balanced - here the carboxylate component has an overall charge of -2, and amidinium component +2. As mentioned previously, the methylimidazolium moiety is disordered across two geometries by virtue of rotation around the methyl bridges. One molecule of water is also disordered, appearing in a different location depending on the relative rotation of the methylimidazolium group.

The retention of a proton on one functional group of the imidazolium linker gives rise to the potential for carboxylic acid-carboxylate hydrogen bonding, and this does appear in structure **D**. The protonated carboxylic acid group on one molecule of **7**.H interacts with a carboxylate group on another molecule of **7**.H, effectively forming chains of this linker. Due to the packing of the crystal, two crystallographically equivalent groups on different molecules interact with one another (O3I···H3···O3I and O6I···H6···O6I). This means the carboxylic acid proton is present in half occupancy at both of these two oxygens on each molecule of **7**.H. The chains of **7**.H are then crosslinked by the remaining two carboxylate groups partaking in $R_2^2(8)$ interactions with molecules of **6** (Figure 3.15). This results in a layered construction, with the sheets stacked in an offset fashion (Figure 3.16). The hydrogen bonds in this framework have N···O lengths of 2.77 to 2.79 Å and O···O lengths of 2.48 Å. There do not appear to be any π-π stacking interactions influencing the structure, but again a network of hydrogen-bonded water molecules is present in any void space.

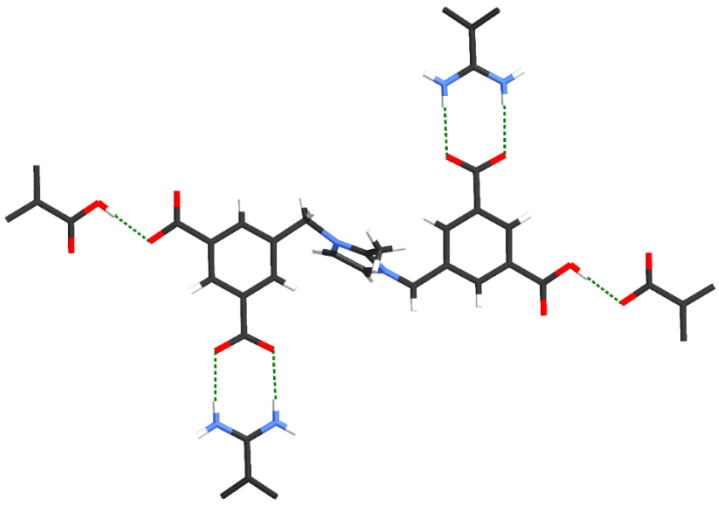


Figure 3.15: Hydrogen bonding interactions of organic components in framework **D**, displayed around a molecule of **7**.H. Disorder and water molecules are omitted for clarity.

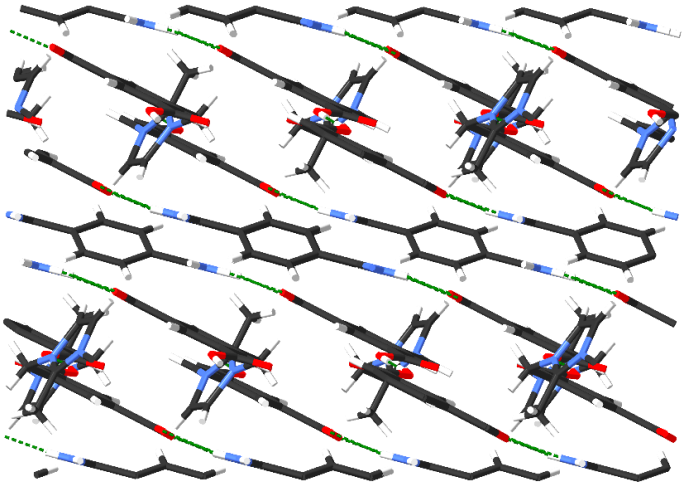


Figure 3.16: Layered structure of framework **D** - the layers run from top left to bottom right in this figure. Disorder and water molecules are omitted for clarity.

Observing the framework from different angles, this structure notably appears to contain channels perpendicular to the [0 1 1] plane, in which the methylimidazolium methyl group is directed towards the void space (Figure 3.17).

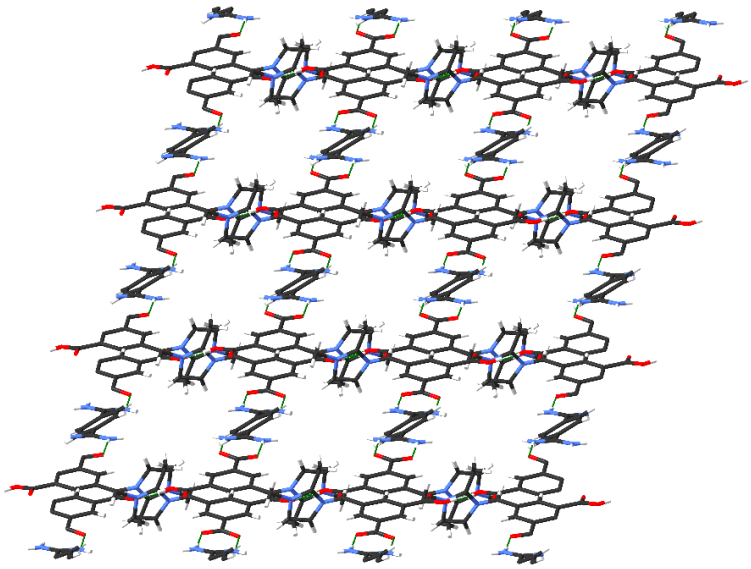


Figure 3.17: HOF **D** viewed perpendicular to the [0 1 1] plane, showing channels running through the structure. Disorder and water molecules omitted for clarity.

These were promising results in terms of the potential for metal complex incorporation at the 2-position on the imidazolium, and prompted investigation into whether this framework may be synthesised using the non-methylated imidazolium linker.

HOF **E**

The synthesis of a HOF containing a partially protonated carboxylate linker using **5**.4H•Cl and **6**•2Cl was successful. In order to achieve this, the same method was used as for all previous frameworks, however sodium hydroxide was added to **5**.4H in a 3:1 ratio in order to allow one carboxylic acid group to remain.

Again, framework **E** has no counterions present in its structure as the linker charges are balanced. Framework **E** has the formula [(**5**.H)**6**$(H_2O)_8]_n$ and is in the $P\overline{1}$ space group. There is one molecule of **5**, one molecule of **6** and eight molecules of water in the asymmetric unit.

The hydrogen bonding between the organic components is the same as was observed in framework **D**, with molecules of **5**.H linked in chains via carboxylic acid-carboxylate hydrogen bonds and molecules of **6** forming dual H-bond interactions at the remaining carboxylate groups (Figure 3.18). There is slightly more variation in this structure in terms of N-H···O hydrogen bond lengths, with N···O distances of 2.72 Å to 2.83 Å. The carboxylic acid proton appears to be fully ordered in this structure - the packing occurs slightly differently despite the broad framework structure being consistent with previous results. The O-H···O hydrogen bond has an O···O distance of 2.58 Å.

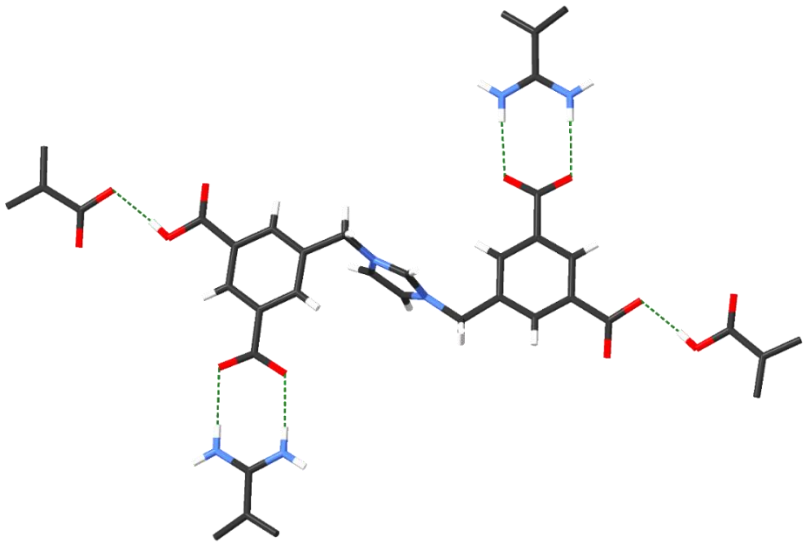


Figure 3.18: Linker-linker hydrogen bonds in framework **E**, centred around a molecule of **5**.H.

Again, framework **E** forms a layered structure (Figure 3.19A) which appears to contain potential void space, with the channels this time running parallel to the b-axis (Figure 3.19B). The layers do not appear to be interconnected by linker-linker interactions, and water is again present in the structure, arranged in the void space of the channels as a hydrogen-bonded network (Appendix Figure 3.1). As was hoped based on framework **D**, the orientation of the imidazolium moiety is such that the N-C**H**-N proton appears to be directed into the void space of the framework, giving rise to the potential for post-synthetic modification with a metal complex. In contrast to the HOFs synthesised with building block **7** - and consistently with frameworks **A** and **B** - the imidazolium moiety appears to be fully ordered in this structure.

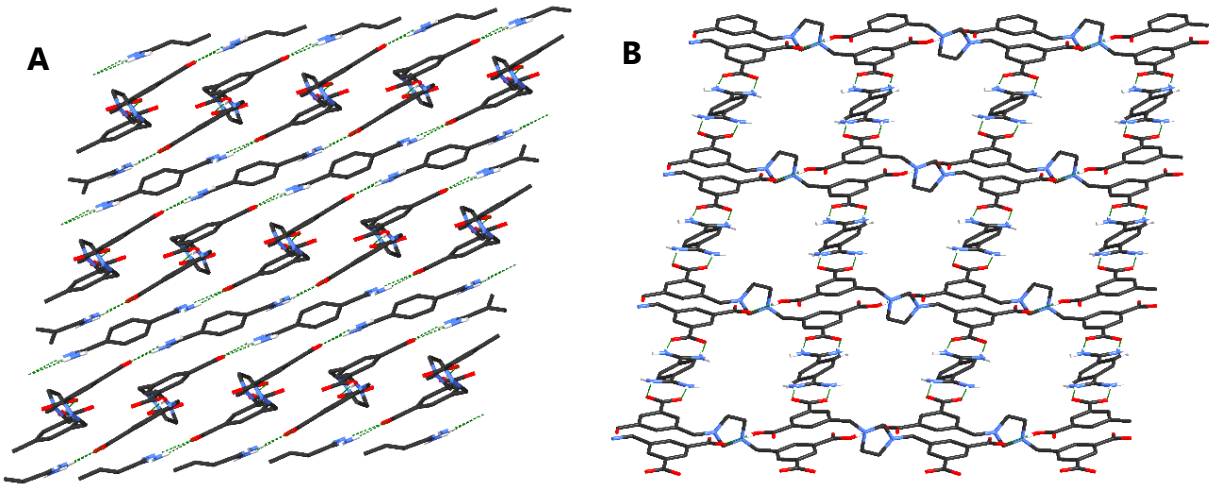


Figure 3.19: Framework **E** viewed along (A) c-axis (B) b-axis. Hydrogen atoms which are not involved in hydrogen bonding interactions and water molecules are omitted for clarity.

Powder X-ray diffraction analysis was performed on the bulk sample of framework **E**, both solvated and following drying under vacuum, in order to assess whether the framework would stay intact upon solvent removal from the channels. Due to preferential orientation, the experimental powder pattern of the solvated structure displays some discrepancies in peak intensities compared with the calculated pattern obtained from SCXRD data. Interestingly, and surprisingly, this preferred orientation effect did not appear to be reduced by grinding of the crystals (Figure 3.20). After drying under vacuum, the crystallinity of the HOF is clearly compromised, with low intensity peaks which do not align well with the calculated or experimental patterns. This result is unsurprising given that the crystal structure shows the water molecules to have a structural role.

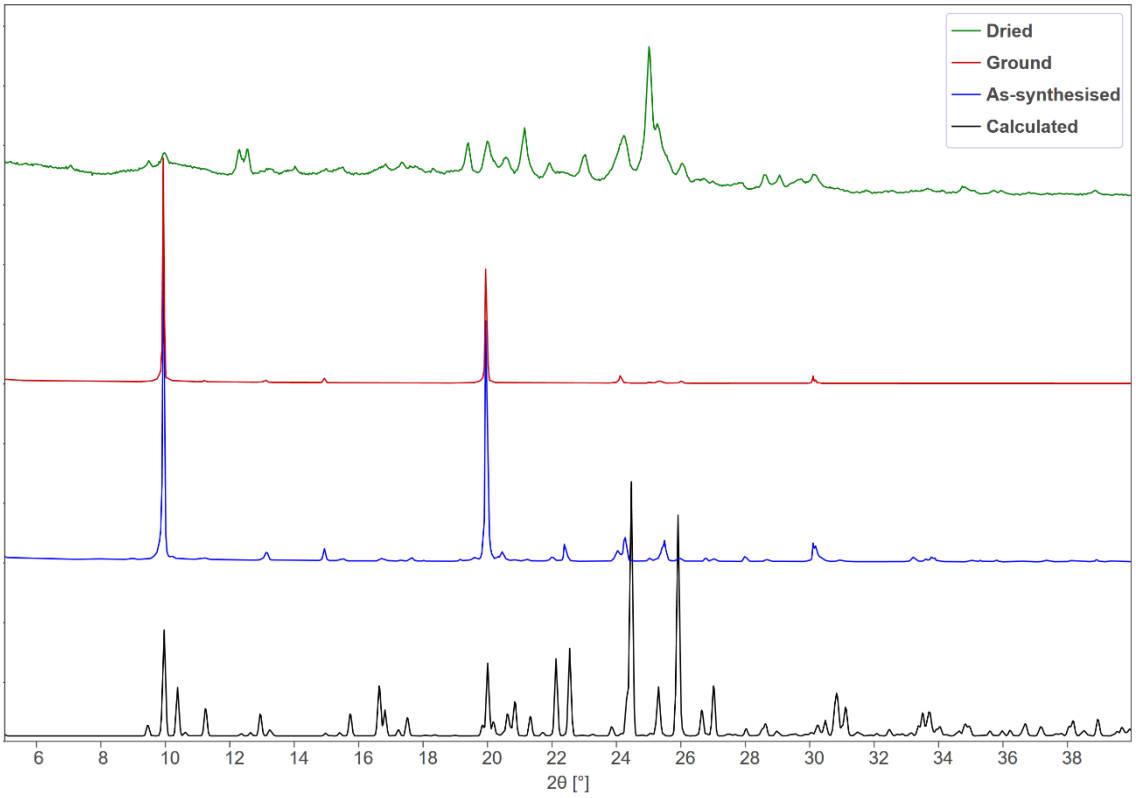


Figure 3.20: Powder patterns of HOF E. From bottom to top: calculated pattern from SC data (black); experimental patterns of HOF as-synthesised (blue), ground (red), dried (green).

3.3.5 Metalation

As highlighted in the introduction chapter, there are two main routes to a metalated framework: pre- or post-synthesis of the framework structure. The targeted complex was **5**-Ag-Cl. This was chosen as a starting point for metalation studies as 2-coordinate Ag(I) complexes of imidazolyl carbenes are well known, and the chloride ligand provides a good base for further modification if incorporation of this target is successful.

Metalation of ligand **5** was attempted prior to framework synthesis. Attempted syntheses in this case were performed in water with added sodium hydroxide. The sodium hydroxide deprotonated the carboxylic acid groups which increases solubility, and should also facilitate formation of the carbene by aiding the removal of the N-C**H**-N proton. Water soluble Ag(I) salts silver trifluoroacetate and silver nitrate were selected for use as the metal source. At the end of the reactions, dilute hydrochloric acid was added to the solution, to pH 6-7, in order to re-protonate the carboxylate groups and obtain a solid product. In both cases, a pale pink solid was retrieved. IR analysis of each product did not show any evidence of change in absorption bands in comparison with the starting material.

It was thought that the addition of hydrochloric acid may interfere with any complex formed, so metalation reactions were attempted at the concentration required for HOF synthesis, such that at the end of the reaction the amidinium solution counterpart could be directly added, with no workup of the metal complex. These attempts were also unsuccessful, with no crystals having formed after more than 6 months.

The alternative route of post-synthetic metalation was then explored using HOF **C**. Attempts to exchange the solvent in the framework using methanol, acetone, acetonitrile and DCM were all unsuccessful, which was expected due to the networks of hydrogen bonded water molecules within the structure. Post-synthetic metalation was therefore conducted on HOF **E** in its mother liquor. The same water-soluble silver salts were employed as were used in the pre-synthetic metalation attempts. One week

after experiments using silver trifluoroacetate and silver nitrate, some colour change from colourless to yellow was observed in the crystals. Upon closer examination whilst preparing the crystals for analysis by SCXRD, it was found that the original HOF crystals were no longer intact, and disintegrated on contact. Amongst the remains of the HOF material, however, yellow single crystals were recovered. These were found to be hydrogen-bonded co-crystals of the amidinium HOF component and the anion from the silver salt (Figure 3.21). The nitrate co-crystal is a hydrate, containing some hydrogen-bonded water molecules.

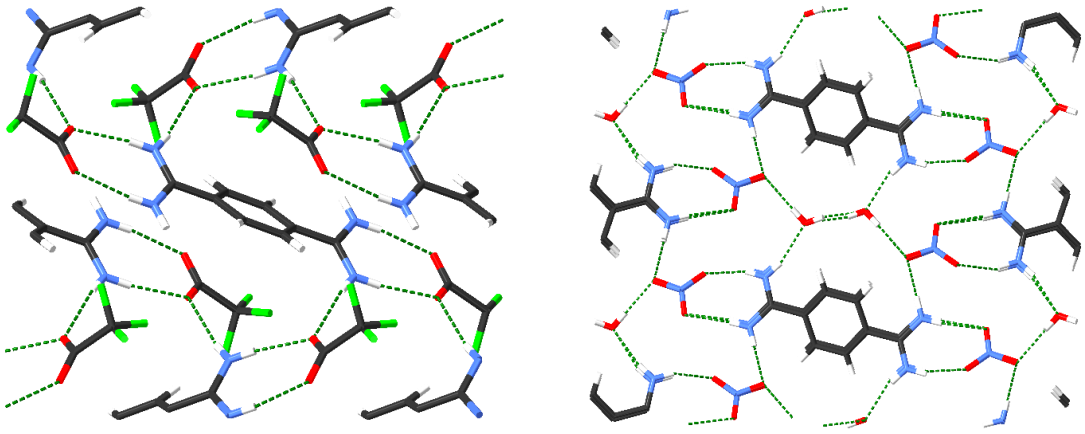


Figure 3.21: Cocrystals of **6** with trifluoroacetate (left) and nitrate (right).

3.4 Conclusions

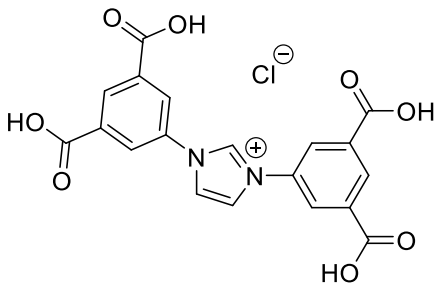
Five new imidazolium-containing amidinium-carboxylate HOFs were synthesised in the course of this work. The range of structures formed is consistent with observations in the literature that the use of flexible building blocks reduces the predictability of resulting structures.[13] Interestingly, no crystalline material was obtained from equivalent syntheses using the less flexible carboxylate building block **4**. Following the results of syntheses using compounds **7** (a methylimidazole analogue of **5**) and **6**, incomplete deprotonation of the carboxylic acid component was leveraged in order to obtain a HOF (structure **E**) with solvent-accessible channels and accessible N-C**H**-N protons with potential to form NHC-metal complexes within the framework. A tangential study attempting to produce a metalated version of framework **E**, via both pre- and post-synthetic routes did not yield any success at this stage.

3.5 Experimental

3.5.1 Organic synthesis

Starting materials were purchased from Sigma Aldrich, Fluorochem and Fisher Scientific, and were used as received. NMR data was collected using either a Bruker AVANCE NEO 400 MHz or Bruker AVIII 400 MHz spectrometer and spectra were referenced to the corresponding residual solvent peaks. Mass spectral data was collected using a Waters Xevo-G2-XS or Waters Synapt G2-S instrument. Infrared spectra of solids were obtained via an Agilent Fourier Transform Spectrometer, FTIR-8400S, fitted with a Diamond ATR unit.

Bis(3,5-dicarboxyphenyl)imidazolium chloride (**4**.4H•Cl)



A reported procedure was followed.[21] 5-Aminoisophthalic acid (2.00 g, 11.0 mmol) was suspended in methanol (10 mL). Formic acid (1 drop) and glyoxal solution (40% w/w in H_2O) (1.02 mL, 8.9 mmol) were added dropwise. The reaction mixture was stirred at room temperature for 24 hours, then filtered, washed with cold methanol and dried under vacuum to obtain a pale orange solid which was used without further purification or characterisation.

The crude product from the previous step (1.00 g, 2.6 mmol) was suspended in THF (10 mL) and degassed with N_2. Meanwhile, paraformaldehyde (0.10 g, 3.3 mmol) was mixed with concentrated HCl (0.32 mL, 3,9 mmol) and dioxane (1 mL) at 0°C. This was then added to the THF solution and stirred at room temperature for 4 hours. The resulting suspension was filtered and washed with diethyl ether. The product was a pale pink solid. Yield: 0.73 g, 65 %.

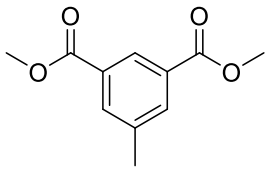
^{1}H NMR (400 MHz, DMSO-d_6) δ 10.72 (t, J = 1.4 Hz, 1H), 8.77 (d, J = 1.5 Hz, 2H), 8.68 (d, J = 1.4 Hz, 4H), 8.62 (t, J = 1.4 Hz, 2H).

^{13}C NMR (101 MHz, DMSO-d_6) δ 165.41, 136.61, 135.43, 133.40, 130.76, 127.10, 122.30.

MS (ESI$^+$) 397.0669 ($C_{19}H_{13}N_2O_8$ $[M]^+$ requires 397.0672).

IR (ATR) 3406 (ν O-H), 3146 (ν C-H aromatic), 2932 (ν C-H sp^3), 1722 (ν C=O), 1604 (ν C=C), 1550 (ν N=C-N), 1206 (ν C-O).

Dimethyl 5-methylisophthalate



5-Methylisophthalic acid (4.00 g, 22.2 mmol) was added to methanol (60 mL). Concentrated sulfuric acid (1.6 mL) was added to the solution dropwise at 30°C. The reaction was heated at reflux overnight before cooling to room temperature. Saturated sodium hydrogen carbonate solution was added to neutralise the solution. The mixture was then filtered to collect the pale yellow solid which was washed with a minimal amount of cold methanol and dried under vacuum. Yield: 3.99 g, 86%.

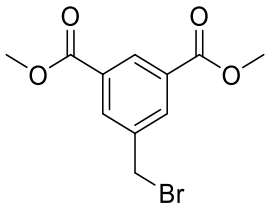
^{1}H NMR (400 MHz, $CDCl_3$) δ 8.48 (s, 1H), 8.04 (s, 2H), 3.94 (s, 6H), 2.45 (s, 3H).

^{13}C NMR (101 MHz, $CDCl_3$) δ 166.60, 138.85, 134.58, 130.65, 128.12, 52.45, 21.28.

MS (ASAP^{+}) m/z 209.0817 ($C_{11}H_{12}O_4$ [M+H] requires 208.0814).

IR (ATR) 3085 (ν C-H aromatic), 2954 and 2853 (ν C-H sp^3), 1723 (ν C=O), 1607 (ν C=C), 1441 (ν C-H), 1243 (ν C-O).

Dimethyl 5-bromomethylisophthalate



Method adapted from a reported procedure.[24] Dimethyl 5-methylisopthalate (3.93 g, 18.9 mmol) was dissolved in chloroform (100 mL). N-bromosuccinamide (3.60 g, 20.2 mmol) and benzoyl peroxide (0.08 g, 0.33 mmol) were added. The mixture was heated at reflux overnight, and was then filtered whilst hot. The solvent was removed from the filtrate by rotary evaporation, and the resulting white solid product was washed with minimal cold ethanol. Yield: 3.47 g, 64%.

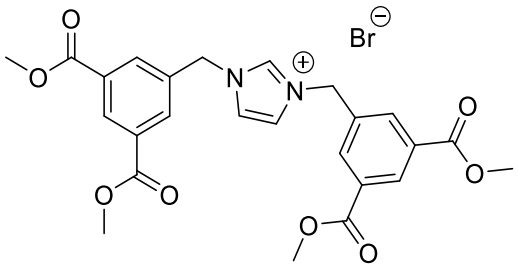
^{1}H NMR (400 MHz, $CDCl_3$) δ 8.60 (s, 1H), 8.25 (s, 2H), 4.54 (s, 2H), 3.95 (s, 6H).

^{13}C NMR (101 MHz, $CDCl_3$) δ 165.84, 138.98, 134.34, 131.47, 130.69, 52.67, 31.63.

MS (ASAP^{+}) m/z 286.9923 ($C_{11}H_{11}BrO_4$ $[M+H]^{+}$ requires 286.9919)

IR (ATR) 3074 and 3049 (ν C-H aromatic), 2953 and 2844 (ν C-H sp^3), 1717 (ν C=O), 1603 (ν C=C), 1433 (ν C-H), 1210 (ν C-O), 692 (ν C-Br).

N,N′-bis((3,5-dimethoxycarbonyl)benzyl)imidazolium bromide



Method adapted from a reported procedure for the synthesis of N,N′-bis(4-methoxycarbonylbenzyl)imidazolium bromide.[22] Imidazole (0.30 g, 4.35 mmol) and potassium carbonate (0.60 g, 4.35 mmol) were stirred in acetone (50 mL). Dimethyl 5-(bromomethyl)isophthalate (2.50 g, 8.7 mmol) was added and the mixture was heated at reflux for 3 days. The mixture was cooled to room temperature then was filtered. The white solid product was washed with a small amount of water, followed by acetone. Yield: 0.82 g, 39%.

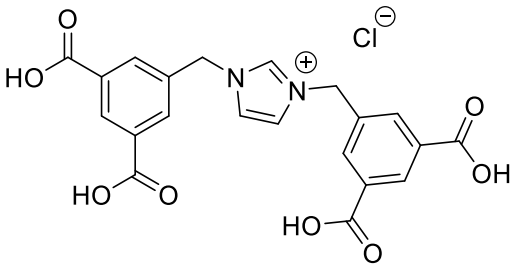
^{1}H NMR (400 MHz, DMSO-d_6) δ 9.49 (s, 1H), 8.45 (s, 2H), 8.32 (s, 4H), 7.93 (s, 2H), 5.63 (s, 4H), 4.36 (q, J = 7.1 Hz, 8H), 1.32 (t, J = 7.1 Hz, 12H).

^{13}C NMR (101 MHz, DMSO-d_6) δ 164.51, 136.74, 136.31, 133.88, 131.18, 129.69, 123.02, 61.45, 51.07.

MS (ESI$^+$) m/z 481.1617 ($C_{25}H_{25}N_2O_8$ $[M]^+$ requires 481.1611).

IR (ATR) 3077 (ν C-H aromatic), 2954 and 2858 (ν C-H sp^3), 1737 and 1718 (ν C=O), 1608 (ν C=C), 1542 (ν N=C-N), 1438 (ν C-H), 1249 (ν C-O).

N,N′-bis(3,5-dicarboxybenzyl)imidazolium chloride (**5**.4H•Cl)



N,N′-bis((3,5-ethoxycarbonyl)benzyl)imidazolium bromide (0.548 g, 0.9 mmol) was stirred in a 3:1 mixture of water and concentrated HCl at 100°C overnight. The mixture was cooled to room temperature and was then filtered. The white solid product was washed twice with water and twice with acetone. Yield: 0.41 g, 81%.

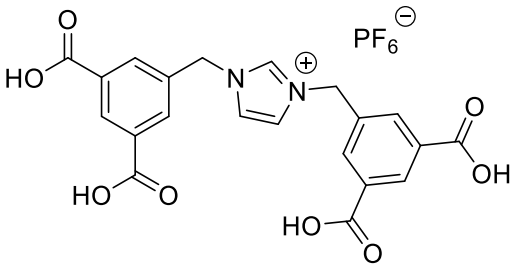
^{1}H NMR (400 MHz, DMSO-d_6) δ 13.39 (s, 4H), 9.46 (s, 1H), 8.46 (s, 2H), 8.28 (s, 4H), 7.91 (s, 2H), 5.58 (s, 4H).

^{13}C NMR (101 MHz, D_2O + NaOH) δ 175.22, 138.53, 134.52, 132.20, 130.57, 123.69, 53.53.

MS (ESI$^+$) m/z 425.0986 ($C_{21}H_{17}N_2O_8$ $[M]^+$ requires 425.0985).

IR (ATR) 3147 (broad, ν O-H), 3077 (ν C-H aromatic), 2954 and 2856 (ν C-H sp^3), 1718 (ν C=O), 1609 (ν C=C), 1566 (ν N=C-N), 1184 (ν C-O).

N,N-bis(3,5-dicarboxybenzyl)imidazolium hexafluorophosphate (**5**.4H•PF_6)

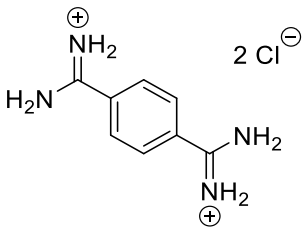


5.4H•Cl (0.77 g, 1.7 mmol) was stirred in ethanol (50 mL) and heated to 60°C. Ammonium hexafluorophosphate (2.77 g, 17.0 mmol) was added and heating was continued for 1h. The resultant mixture was cooled to room temperature, filtered, and the white solid product was washed with copious ethanol. Yield: 0.81 g, 85%.

Presence of PF_6^- anion confirmed by **MS** (ESI^-) m/z 144.9640 (PF_6 $[M]^-$ requires 144.9642)

^{31}P NMR (400 MHz, DMSO-d_6) δ -144 (pseudo-pentet).

Terephthalamidine dichloride (**6**•2Cl)



A reported procedure was followed.[23] To a solution of benzene-1,4-dicarbonitrile (0.80 g, 6.2 mmol) in THF (20 mL), $LiN(SiMe_3)_2$ solution (1M in THF, 25 mL, 25 mmol) was added dropwise over 30 min at 0 °C. The mixture was stirred at room temperature for 3 h and then cooled to 0 °C in an ice bath. The reaction was quenched by careful addition

of 6 M HCl– EtOH (25 mL) and the mixture was set aside overnight. The precipitate was then filtered, washed with Et_2O, and the powder was recrystallized from H_2O–EtOH mixture. Yield: 0.45 g, 31%.

SCXRD analysis was performed in addition to the characterisation below - details are in the Crystallographic Analysis section.

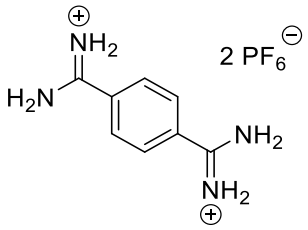
^{1}H NMR (400 MHz, D_2O) δ 7.99 (s, 4H).

^{13}C NMR (101 MHz, D_2O) δ 165.86, 132.91, 128.65.

MS (ESI$^+$) m/z 163.0988 ($C_8H_{11}N_4$ [M-H]$^+$ requires 163.0984).

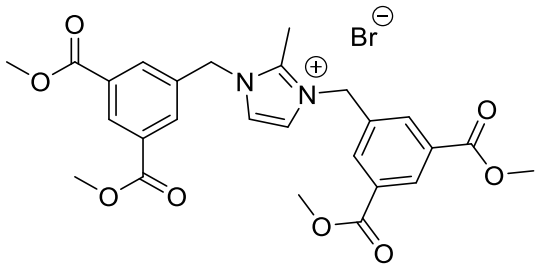
IR (ATR) 3000 (broad, ν N-H), 1693 and 1657 (ν C=N), 1542 (ν N-H).

Terephthalamidinium dihexafluorophosphate (**6**•$2PF_6$)



6•2Cl (0.22 g, 0.93 mmol) was stirred in ethanol (30 mL) and heated to 60°C. Ammonium hexafluorophosphate (1.51 g, 9.3 mmol) was added and heating was continued for 1h. The resultant mixture was cooled to room temperature, filtered, and the white solid product was washed with copious ethanol.

N,N-bis((3,5-dimethoxycarbonyl)benzyl)-2-methylimidazolium bromide



Dimethyl 5-bromomethylisophthalate (0.91 g, 3.2 mmol), 2-methylimidazole (0.13 g, 1.6 mmol) and potassium carbonate (0.22 g, 1.6 mmol) were added to acetone (50 mL) and heated at reflux for 2 days. The reaction mixture was then cooled to room temperature, filtered and washed with acetone to obtain the product as a white solid. Yield: 0.81 g, 87%.

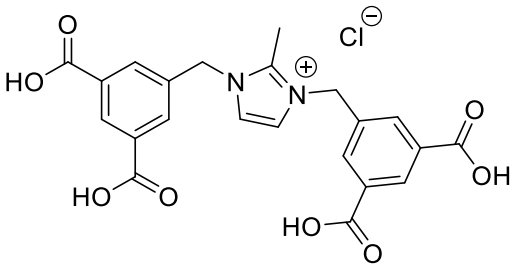
^{1}H NMR (400 MHz, DMSO-d_6) δ 8.47 (s, 2H), 8.22 (s, 4H), 7.82 (s, 2H), 5.58 (s, 4H), 3.90 (s, 12H), 3.37 (s, 3H), 2.66 (s, 3H).

^{13}C NMR (101 MHz, DMSO) δ 165.48, 145.74, 136.45, 133.84, 131.42, 130.09, 122.53, 53.15, 50.34, 10.47.

MS (ESI$^+$) m/z 495.1772 ($C_{27}H_{26}N_2O_8$ [M$^+$] requires 495.1767).

IR (ATR) 1718 (ν C=O), 1606 (ν C=C), 1436 (ν C-H sp^3), 1322 and 1210 (ν C-O ester).

N,N-bis((3,5-dicarboxybenzyl)-2-methylimidazolium chloride (**7**.4H•Cl)



N,N-bis((3,5-diethoxycarbonyl)benzyl)-2-methylimidazolium bromide (0.81 g, 1.4 mmol) was stirred in water and concentrated HCl (3:1 v/v) (40 mL) at 100°C overnight. The reaction mixture was then cooled to room temperature, filtered, washed with copious water and dried under vacuum. Yield: 0.39 g, 59%.

^{1}H NMR (400 MHz, DMSO-d_6) δ 8.45 (s, 2H), 8.18 (s, 4H), 7.82 (s, 2H), 5.56 (s, 4H), 2.68 (s, 3H).

^{13}C NMR (101 MHz, D_2O + NaOH) δ 174.24, 137.49, 133.63, 130.39, 129.25, 121.78, 121.08, 51.17.

MS (ESI$^+$) m/z 439.1150 ($C_{22}H_{19}N_2O_8$ $[M]^+$ requires 439.1141).

IR (ATR) 2967 (broad, ν O-H), 1702 (ν C=O), 1641 (ν C=C), 1280 and 1238 (ν C-O).

3.5.2 HOF Synthesis

HOF **A**

A solution of **6**•2PF_6 (55 mg, 0.12 mmol) in water (3.75 mL) was added gently, dropwise, to a solution of **5**.4H•PF_6 (17 mg, 0.03 mmol) in NaOH (1 M, 0.1 mL) and water (3.65 mL). The vial was sealed and the resulting clear, colourless solution was left to stand at

room temperature. Colourless crystals formed after 4 days. The original solution was removed, and the crystals were washed several times with water and stored in water.

HOF **B**

A solution of **6**•2Cl (28 mg, 0.12 mmol) in water (3.75 mL) was added gently, dropwise, to a solution of **5**.4H•Cl (14 mg, 0.03 mmol) in NaOH (1 M, 0.1 mL) and water (3.65 mL). The vial was sealed and the resulting clear, colourless solution was left to stand at room temperature. Colourless crystals formed within 1 day. The original solution was removed, the crystals were washed several times with water and stored in water.

HOFs **C** and **D**

A solution of **6**•2Cl (34 mg, 0.144 mmol) in water (3.75 mL) was added gently, dropwise, to a solution of **7**.4H•Cl (17 mg, 0.36 mmol) in NaOH (1 M, 0.1 mL) and water (3.65 mL). The vial was sealed and the resulting clear, colourless solution was left to stand at room temperature. Yellow crystals of both plate (framework **C**) and needle (framework **D**) morphology formed within 1 day. The original solution was removed, the crystals were washed several times with water and stored in water.

HOF **E**

A solution of **6**•2Cl (21 mg, 0.09 mmol) in water (3.75 mL) was added gently, dropwise, to a solution of **5**.4H•Cl (17 mg, 0.36 mmol) in NaOH (1 M, 0.1 mL) and water (3.65 mL). The vial was sealed and the resulting slightly cloudy solution was left to stand at room temperature. The solution became clear after approximately 1 hour and colourless

crystals formed after 3 days. The original solution was removed, and the crystals were washed several times with water.

3.5.3 Crystallographic Analysis

Powder XRD measurements were carried out at 298K using either a Bruker D8 Advance diffractometer (λ (CuKα1) = 1.5406 Å), or a *PANalytical* Empyrean diffractometer (λ (CuKα1) = 1.5406 Å) mounted on a zero background sample stage. Theoretical PXRD patterns were calculated from single crystal structures using Mercury 3.10.1.[25,26]

Single crystal data was collected using either a Rigaku Synergy-S dual source with a PhotonJet-S X-ray source and a HyPix-6000 detector or an Agilant SuperNova Dual diffractometer with Atlas CCD detector using monochromated Cu Kα radiation (γ = 1.54184 Å). Data was collected at 100 K through the use of an Oxford Cryosystems cryostream device. Data was collected and processed using CrysAlisPro 171.42.49.57.

Using Olex2[27], the structures were solved with the SHELXT[28] structure solution program using Intrinsic Phasing and refined with the SHELXL[29] refinement package using Least Squares minimisation.

6•2Cl

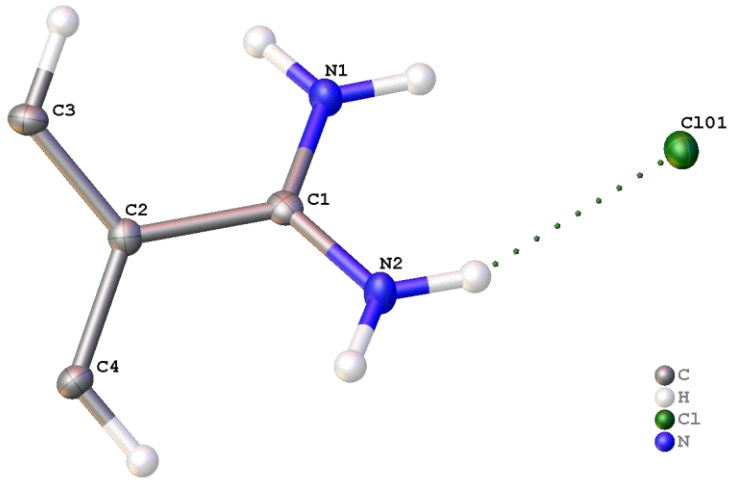


Figure 3.22: Asymmetric unit of **6**•2Cl, showing ellipsoids and atom names for non-hydrogen atoms.

Crystal Data for $C_8H_{12}Cl_2N_4$ (M =235.12 g/mol): monoclinic, space group C2/c (no. 15), a = 17.0547(8) Å, b = 9.60180(10) Å, c = 9.9341(5) Å, β = 139.733(9)°, V = 1051.46(15) Å^3, Z = 4, T = 100.15 K, μ(CuKα) = 5.288 mm^{-1}, $Dcalc$ = 1.485 g/cm^3, 15455 reflections measured (12.224° ≤ 2Θ ≤ 157.394°), 1104 unique (R_{int} = 0.0250, R_{sigma} = 0.0085) which were used in all calculations. The final R_1 was 0.0287 (I > 2σ(I)) and wR_2 was 0.0812 (all data).

All hydrogen atoms were fixed as riding models and the isotropic thermal parameters (Uiso) were based on the Ueq of the parent atom.

HOF **A**

Crystal Data for $C_{99}H_{93}N_{24}O_{53}$ (*M* =2466.97 g/mol): triclinic, space group P-1 (no. 2), *a* = 11.9854(3) Å, *b* = 18.4055(5) Å, *c* = 27.5891(5) Å, *α* = 90.642(2)°, *β* = 100.377(2)°, *γ* = 90.987(2)°, *V* = 5985.0(2) Å^3, *Z* = 2, *T* = 100.01(10) K, μ(Cu Kα) = 0.977 mm^{-1}, *Dcalc* = 1.369 g/cm^3, 108973 reflections measured (7.5° ≤ 2Θ ≤ 145.82°), 22111 unique (R_{int} = 0.0584, R_{sigma} = 0.0346) which were used in all calculations. The final R_1 was 0.1201 (I > 2σ(I)) and wR_2 was 0.4085 (all data).

The structure contains solvent water molecules which are somewhat disordered. The oxygen atoms of these water molecules were located using electron density. The occupancies of these oxygen atoms were allowed to refine freely and were then fixed at the nearest ¼. The majority settled at occupancies of 1, with the exception of O3W, O5W, O17W and O24W which were assigned occupancies of 0.75 each. Hydrogen atoms of the water molecules were not added due to uncertainty in their positions large high shifts in the refinement. Hydrogen atoms on the organic components were fixed as riding models and the isotropic thermal parameters (Uiso) were based on the Ueq of the parent atom.

Refinement using PLATON SQUEEZE [30]

Crystal Data for $C_{99}H_{93}N_{24}O_{24}$ (*M* =2002.97 g/mol): triclinic, space group P-1 (no. 2), *a* = 11.9854(3) Å, *b* = 18.4055(5) Å, *c* = 27.5891(5) Å, *α* = 90.642(2)°, *β* = 100.377(2)°, *γ* = 90.987(2)°, *V* = 5985.0(2) Å^3, *Z* = 2, *T* = 100.01(10) K, μ(CuKα) = 0.682 mm^{-1}, *Dcalc* = 1.111 g/cm^3, 108973 reflections measured (7.5° ≤ 2Θ ≤ 145.82°), 22111 unique (R_{int} =

0.0584, R_{sigma} = 0.0346) which were used in all calculations. The final R_1 was 0.1030 (I > 2σ(I)) and wR_2 was 0.2973 (all data).

A solvent mask was applied to the same data set as described above, using PLATON SQUEEZE.[30] A solvent mask was calculated and 547 electrons were found in a volume of 1439Å^3 in 1 void per unit cell. This is consistent with the presence of 55 H_2O per Unit Cell which account for 550 electrons per unit cell. This approximately agrees with the number of water molecules that were located in the electron density in the original structure solution - 56 water molecules were modelled.

Hydrogen atoms on the organic components were fixed as riding models and the isotropic thermal parameters (Uiso) were based on the Ueq of the parent atom.

HOF **B**

Crystal Data for $C_{33}H_{51}N_8O_{18}$ (M =847.81 g/mol): triclinic, space group P-1 (no. 2), a = 10.90463(6) Å, b = 13.13252(7) Å, c = 16.11161(7) Å, α = 108.8183(4)°, β = 106.4158(5)°, γ = 99.2833(5)°, V = 2012.288(19) Å^3, Z = 2, T = 99.99(10) K, μ(Cu Kα) = 0.980 mm^{-1}, $Dcalc$ = 1.399 g/cm^3, 141801 reflections measured (6.208° ≤ 2Θ ≤ 157.122°), 8094 unique (R_{int} = 0.0429, R_{sigma} = 0.0143) which were used in all calculations. The final R_1 was 0.0473 (I > 2σ(I)) and wR_2 was 0.1409 (all data).

All hydrogen atoms were fixed as riding models and the isotropic thermal parameters (Uiso) were based on the Ueq of the parent atom.

HOF **C**

Crystal Data for $C_{34}H_{59}N_8O_{21}$ (M =915.89 g/mol): triclinic, space group P-1 (no. 2), a = 10.9916(2) Å, b = 12.6417(2) Å, c = 17.0730(3) Å, α = 75.536(2)°, β = 83.406(2)°, γ = 84.446(2)°, V = 2276.22(7) Å^3, Z = 2, T = 100.15 K, μ(CuKα) = 0.954 mm^{-1}, $Dcalc$ = 1.336 g/cm^3, 43924 reflections measured (5.37° ≤ 2Θ ≤ 157.114°), 9338 unique (R_{int} = 0.0302, R_{sigma} = 0.0223) which were used in all calculations. The final R_1 was 0.0500 (I > 2σ(I)) and wR_2 was 0.1443 (all data).

All hydrogen atoms were fixed as riding models and the isotropic thermal parameters (Uiso) were based on the Ueq of the parent atom.

The solvent water molecules in this structure were located by electron density. The majority of the water molecules are well ordered and have an occupancy of one. The occupancies of O2W and O3W were allowed to refine freely and were then fixed at 0.7 and 0.3 respectively and the atoms placed in Part 1 and Part 2 respectively.

The methylimidazole moiety in the molecule of **7** exhibits rotational disorder about the methylene bridges C9I and C14I. The atoms in both parts were located in the electron density and their occupancies allowed refine freely before being fixed. The major component, N1I-C10I(C13I)-N2I-C11I-C12I, was placed in Part 1 and atoms assigned fixed occupancies of 0.8. The minor component, N3I-C23I(C26I)-N4I-C24I-C25I, was placed in Part 2 and atoms assigned fixed occupancies of 0.2.

HOF **D**

Crystal Data for $C_{30}H_{43}N_6O_{16}$ (*M* =743.70 g/mol): triclinic, space group P-1 (no. 2), *a* = 8.9978(8) Å, *b* = 10.9592(9) Å, *c* = 19.1015(12) Å, *α* = 84.858(6)°, *β* = 85.177(6)°, *γ* = 67.627(8)°, *V* = 1732.2(3) Å^3, *Z* = 2, *T* = 100.15 K, μ(CuKα) = 0.996 mm^{-1}, *Dcalc* = 1.426 g/cm^3, 20408 reflections measured (8.742° ≤ 2Θ ≤ 158.544°), 6859 unique (R_{int} = 0.0426, R_{sigma} = 0.0451) which were used in all calculations. The final R_1 was 0.0606 (I > 2σ(I)) and wR_2 was 0.2344 (all data).

All hydrogen atoms were fixed as riding models and the isotropic thermal parameters (Uiso) were based on the Ueq of the parent atom, with the exception of H4WA and H4WB which were refined subject to bond length restraints.

The methylimidazole moiety in the molecule of **7**.H exhibits rotational disorder about the methylene bridges C9I and C14I. The atoms in both parts were located in the electron density and their occupancies allowed refine freely before being fixed. Both components settled at occupancies of 0.5 and were therefore fixed at that value. N1I-C10I(C13I)-N2I-C11I-C12I was placed in Part 1 and N3I-C23I(C26I)-N4I-C24I-C25I was placed in Part 2.

HOF **E**

Crystal Data for $C_{29}H_{42}N_6O_{16}$ (*M* =730.68 g/mol): triclinic, space group P-1 (no. 2), *a* = 9.1258(2) Å, *b* = 11.2188(3) Å, *c* = 18.1912(3) Å, *α* = 83.368(2)°, *β* = 77.454(2)°, *γ* = 71.878(2)°, *V* = 1725.47(7) Å^3, *Z* = 2, *T* = 100.15 K, μ(CuKα) = 0.989 mm^{-1}, *Dcalc* =

1.406 g/cm^3, 52554 reflections measured (8.304° ≤ 2Θ ≤ 146.856°), 6851 unique (R_{int} = 0.0312, R_{sigma} = 0.0159) which were used in all calculations. The final R_1 was 0.0344 (I > 2σ(I)) and wR_2 was 0.0969 (all data).

All hydrogen atoms were fixed as riding models and the isotropic thermal parameters (Uiso) were based on the Ueq of the parent atom.

Powder XRD analysis was performed on HOF E:

- As single crystals;
- After grinding in a pestle and mortar in the presence of a small amount of mother liquor;
- After drying under vacuum for 1 day.

6-Trifluoroacetate Co-crystal

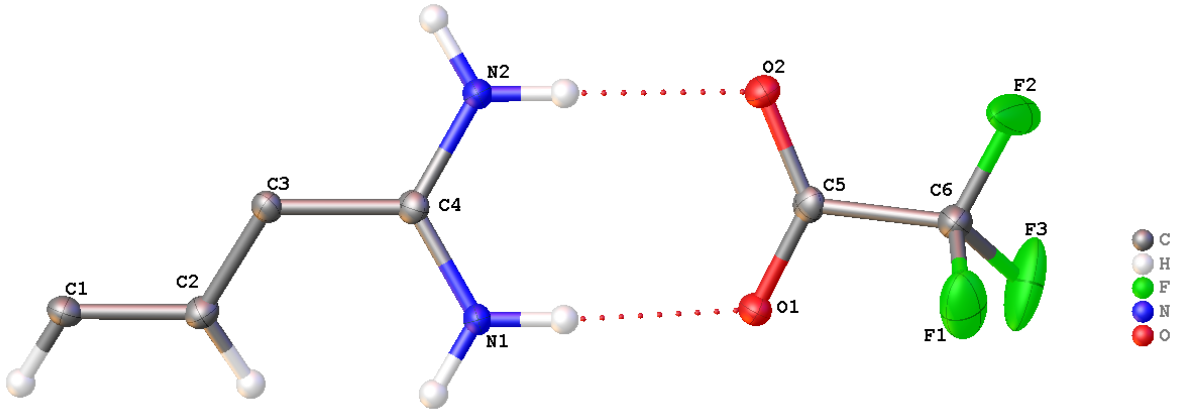


Figure 3.23: Asymmetric unit of **6**-Trifluoroacetate co-crystal, showing ellipsoids and atom names for non-hydrogen atoms.

Crystal Data for $C_{12}H_{12}F_6N_4O_4$ (M =390.26 g/mol): monoclinic, space group $P2_1/c$ (no. 14), a = 7.49620(10) Å, b = 7.75570(10) Å, c = 13.04280(10) Å, β = 91.5020(10)°, V = 758.025(15) Å^3, Z = 2, T = 100.00(10) K, μ(Cu Kα) = 1.578 mm^{-1}, $Dcalc$ = 1.710 g/cm^3, 13275 reflections measured (11.81° ≤ 2Θ ≤ 154.264°), 1531 unique (R_{int} = 0.0275, R_{sigma} = 0.0148) which were used in all calculations. The final R_1 was 0.0733 (I > 2σ(I)) and wR_2 was 0.1866 (all data).

All hydrogen atoms were fixed as riding models and the isotropic thermal parameters (Uiso) were based on the Ueq of the parent atom.

6-Nitrate Co-crystal

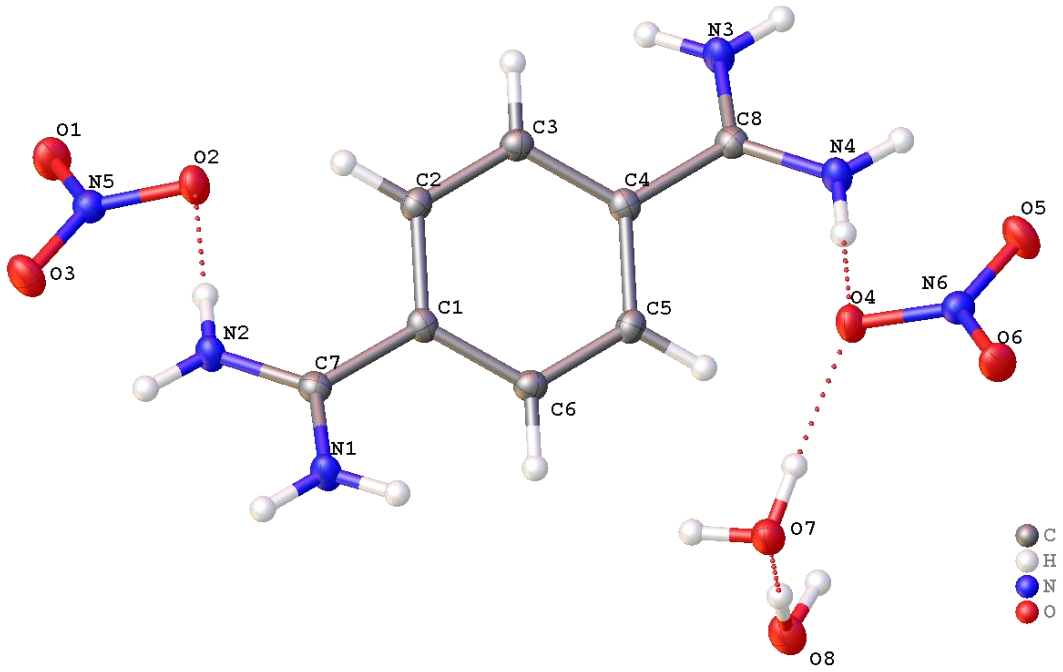


Figure 3.24: Asymmetric unit of **6**-Nitrate co-crystal, showing ellipsoids and atom names for non-hydrogen atoms.

Crystal Data for $C_8H_{16}N_6O_8$ (M =324.27 g/mol): monoclinic, space group $P2_1/n$ (no. 14), a = 7.16210(10) Å, b = 21.5892(3) Å, c = 8.93490(10) Å, β = 95.2650(10)°, V = 1375.72(3) Å^3, Z = 4, T = 100.15 K, μ(CuKα) = 1.221 mm^{-1}, $Dcalc$ = 1.566 g/cm^3, 25561 reflections measured (8.19° ≤ 2Θ ≤ 156.94°), 2866 unique (R_{int} = 0.0421, R_{sigma} = 0.0180) which were used in all calculations. The final R_1 was 0.0398 (I > 2σ(I)) and wR_2 was 0.1201 (all data).

All hydrogen atoms were fixed as riding models and the isotropic thermal parameters (Uiso) were based on the Ueq of the parent atom.

3.6 References

1 P. Li, M. R. Ryder and J. F. Stoddart, *Acc Mater Res*, 2020, **1**, 77–87.

2 M. B. Hursthouse, D. S. Hughes, T. Gelbrich and T. L. Threlfall, *Chem Cent J*, 2015, **9**, 1.

3 L. N. Kuleshova and P. M. Zorky, *Acta Crystallogr B*, 1980, 36, 2113–2115.

4 A. F. Wells, Three-dimensional nets and polyhedra, New York, New York, 1977.

5 M. C. Etter, *Acc Chem Res*, 1990, **23**, 120–126.

6 M. C. Etter, *J Phys Chem*, 1991, **95**, 4601–4610.

7 J. Bernstein, R. E. Davis, L. Shimoni and N.-L. Chang, *Angew Chem Int Ed*, 1995, **34**, 1555–1573.

8 S. Lie, T. Maris, C. Malveau, D. Beaudoin, F. Helzy and J. D. Wuest, *Cryst Growth Des*, 2013, **13**, 1872–1877.

9 V. A. Russell, M. C. Etter and M. D. Ward, *J Am Chem Soc*, 1994, **116**, 1941–1952.

10 W. Liang, F. Carraro, M. B. Solomon, S. G. Bell, H. Amenitsch, C. J. Sumby, N. G. White, P. Falcaro and C. J. Doonan, *J Am Chem Soc*, 2019, **141**, 14298–14305.

11 O. Félix, M. W. Hosseini, A. De Cian and J. Fischer, *Angew Chem Int Ed*, 1997, **36**, 102–104.

12 M. W. Hosseini, R. Ruppert, P. Schaeffer, A. De Cian, N. Kyritsakas and J. Fischer, *J Chem Soc Chem Commun*, 1994, 2135–2136.

13 N. G. White, *Chem Comm*, 2021, **57**, 10998–11008.

14 M. Morshedi, M. Thomas, A. Tarzia, C. J. Doonan and N. G. White, *Chem Sci*, 2017, **8**, 3019–3025.

15 M. Morshedi, J. S. Ward, P. E. Kruger and N. G. White, *Dalton Trans*, 2018, **47**, 783–790.

16 S. A. Boer, M. Morshedi, A. Tarzia, C. J. Doonan and N. G. White, *Chem Eur J*, 2019, **25**, 10006–10012.

17 S. A. Boer, L.-J. Yu, T. L. Genet, K. Low, D. A. Cullen, M. G. Gardiner, M. L. Coote and N. G. White, *Chem Eur J*, 2021, **27**, 1768–1776.

18 H. Jiang, L. Xie, Z. Duan, K. Lin, Q. He, V. M. Lynch, J. L. Sessler and H. Wang, *Chem Eur J*, 2021, **27**, 15006–15012.

19 S. A. Boer, L. Conte, A. Tarzia, M. T. Huxley, M. G. Gardiner, D. R. T. Appadoo, C. Ennis, C. J. Doonan, C. Richardson and N. G. White, *Chem Eur J*, 2022, **28**, e202201929.

20 J. Tang, J. Liu, Q. Zheng, W. Li, J. Sheng, L. Mao and M. Wang, *Angew Chem Int Ed*, 2021, **60**, 22315–22321.

21 S. Sen, S. Neogi, A. Aijaz, Q. Xu and P. K. Bharadwaj, *Inorg Chem*, 2014, **53**, 7591–7598.

22 X. Zhang, J. Sun, G. Wei, Z. Liu, H. Yang, K. Wang and H. Fei, *Angew Chem Int Ed*, 2019, **58**, 2844–2849.

23 K. Wang, L.-M. Yang, X. Wang, L. Guo, G. Cheng, C. Zhang, S. Jin, B. Tan and A. Cooper, *Angew Chem Int Ed*, 2017, **56**, 14149–14153.

24 D. Wang, J. Song, J. Wang, Z. Zhang, Q. Shen, J. Wang, H. Guo, R. Wang, C. Xie, W. Lu and M. Liu, *Adv Funct Mater*, 2020, **30**, 2004783.

25 C. F. Macrae, I. J. Bruno, J. A. Chisholm, P. R. Edgington, P. McCabe, E. Pidcock, L. Rodriguez-Monge, R. Taylor, J. van de Streek and P. A. Wood, *J Appl Crystallogr*, 2008, **41**, 466–470.

26 C. F. MacRae, I. Sovago, S. J. Cottrell, P. T. A. Galek, P. McCabe, E. Pidcock, M. Platings, G. P. Shields, J. S. Stevens, M. Towler and P. A. Wood, *J Appl Crystallogr*, 2020, **53**, 226–235.

27 O. V Dolomanov, L. J. Bourhis, R. J. Gildea, J. A. K. Howard and H. Puschmann, *J Appl Crystallogr*, 2009, **42**, 339–341.

28 G. M. Sheldrick, *Acta Crystallogr A*, 2015, **71**, 3–8.

29 G. M. Sheldrick, *Acta Crystallogr C*, 2015, **71**, 3–8.

30 A. L. Spek, *Acta Crystallogr C*, 2015, **71**, 9–18.

4 CHAPTER FOUR

Mechanochemical synthesis of co-crystals of cyanuric acid and trithiocyanuric acid

4.1 Introduction

Co-crystal formation by mechanochemical methods is a growing field, particularly with a view to applications in the pharmaceutical industry, due to the reduced solvent and energy usage requirements.[1–4] Direct mixing of solid components has been shown to give rise to polymorphic forms of co-crystals which are not accessible via solution methods, as well as those which are.[5,6] This study aims to extend the existing portfolio of systems studied.

Hydrogen-bonded structures of cyanuric acid (CA) and thiocyanuric acid (TCA) (Figure 4.1) are well known in the literature. These molecules contain three hydrogen bond donating and three hydrogen bond accepting groups. Both are self-complementary and studies of the extended crystal structures of each individually have been carried out.[7–12] More relevantly to this study however, each has been paired with a wide range of additional molecules for co-crystal synthesis.

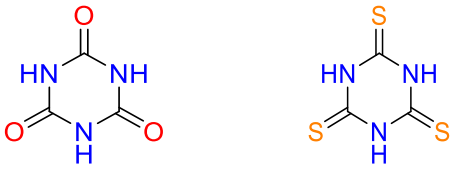


Figure 4.1: Cyanuric acid (left) and trithiocyanuric acid (right).

Two-component co-crystals of cyanuric acid have been studied since the early 1990s, beginning with investigations by Whitesides et al. into adducts of cyanuric acid and melamine.[13–16] Soon after, investigations were extended to the co-crystallisation of trithiocyanuric acid and melamine by Rao et al..[17] The field quickly expanded in the early 2000s to include co-crystallisations of CA or TCA with a range of molecules, commonly containing pyridyl hydrogen bond acceptors.[18–20] These readily interact with the hydrogen bond donors on CA and TCA, with additional weak hydrogen-bonding interactions sometimes able to form using the hydrogen bond accepting groups of CA and TCA (Figure 4.2).[21] The supramolecular motifs and hydrogen bonding interactions which occur in these structures have been studied in detail, as well as the impact of changing synthetic conditions, such as the selection of solvent, on the resulting structure(s).[21–23]

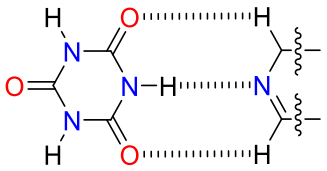


Figure 4.2: Hydrogen bonding interactions between CA and a pyridine functional group.

There are a small number of recent publications which report the use of mechanochemical techniques to synthesise co-crystals of cyanuric acid with either melamine or alkyl halides.[18,24,25] To our knowledge, the synthesis of trithiocyanuric acid co-crystals by this method has not been studied previously.

4.2 Aims

With this study we aimed to develop a reliable methodology for the synthesis of CA and TCA co-crystals by mechanochemistry. This methodology is implemented for a range of systems, and the results compared to structures obtained by solution methods in order to probe firstly the feasibility of mechanochemical techniques for the formation CA or TCA-containing co-crystals, and secondly the accordance in results, if any, between the two synthetic techniques. This work additionally provided a foundation for the mechanochemical synthesis of a HOF using related compounds, which is discussed in Chapter 5.

4.3 Results And Discussion

4.3.1 Method Development

Method development was primarily performed using cyanuric acid and melamine (CA/M) as the starting materials. The main variables investigated were the solvent used for liquid-assisted grinding (LAG) and the volume of solvent added. Milling was conducted in 5 mL stainless steel jars with two balls of 7 mm diameter, for a period of 90 minutes. A 1:1 molar ratio of starting materials was used, with a combined mass of approximately 120-160 mg solid.

N,N-Dimethylformamide (DMF) was selected for use in tests regarding the optimum milling time and volume of solvent. This is due to the fact it is a commonly used solvent

in framework synthesis, and initial tests indicated it would be effective in this reaction. Experiments were conducted on CA/M with solvent volumes from 10 to 150 μL as well as dry, and the products were analysed using powder X-ray diffraction (PXRD). The volume of solvent did not appear to have a significant effect on the product formed, with all powder patterns showing a loss of starting material peaks and formation of peaks at 11° and 28° 2θ which align with the intense peaks in the powder pattern of a reported structure of a CA/M co-crystal with CSD code QACSUI (Appendix Figure 4.1). Where volumes of solvent between 25 μL and 100 μL were used, the material post-milling was of a clay-like consistency which clung to the milling balls or was compacted at one or both ends of the jar. Due to concern that the efficiency of mixing in these cases was likely to be inconsistent, it was decided these volumes would not be used in future experiments. 125 μL solvent was therefore used in subsequent experiments as the material post-milling was well distributed around the cavity of the milling jar.

We were next interested to investigate how and whether the solvent used to facilitate co-crystal formation affected the product formed. The solvents investigated were N,N-dimethylformamide (DMF), N-methylpyrrolidone (NMP), methanol (MeOH), acetonitrile (MeCN) and tetrahydrofuran (THF). Experiments were conducted on the CA/M system using 125 μL of each of these solvents and the products were again analysed using PXRD (Figure 4.3). Success in co-crystallising CA/M by milling with water as the LAG additive has been reported in the literature, however in prior use of our

equipment we have found water to cause rusting and damage to the milling jars and balls, therefore the decision was taken to exclude it from use in this study.[18]

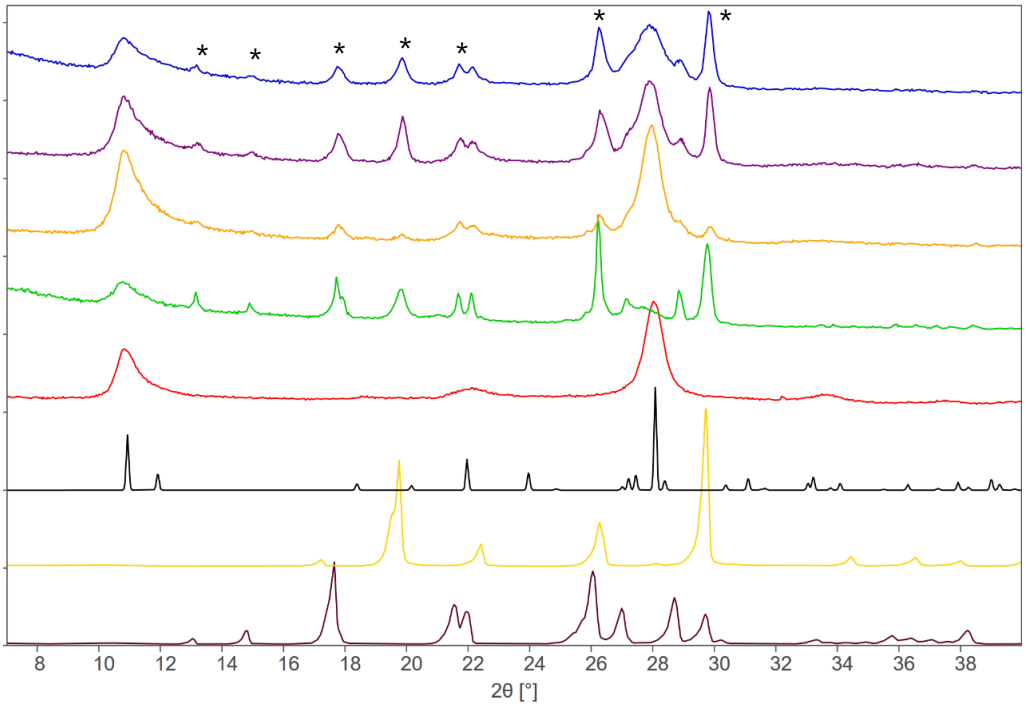


Figure 4.3: Powder XRD patterns of CA/M milling products from syntheses using different solvents for LAG. From bottom to top: experimental patterns of starting materials melamine (maroon) and cyanuric acid (gold); calculated pattern of QACSUI (black); experimental patterns of syntheses using DMF (red), NMP (green), MeOH (orange), MeCN (purple) and THF (blue).

The powder patterns of all syntheses show evidence of the product phase, QACSUI, being formed, with peaks at 2θ values of 11° and 28°, however peaks matching the starting materials are also present in the majority of patterns. These peaks are those marked with asterisks in Figure 4.3, above the PXRD pattern from the synthesis using THF.

The conversion to the co-crystal product appears most complete in the syntheses where DMF or methanol were used for LAG. Methanol is commonly used in

recrystallisation co-crystal syntheses of systems involving cyanuric and trithiocyanuric acid, so the fact it produced promising results in these milling experiments was relatively unsurprising. These factors combined lead to the decision that methanol and DMF would be taken forward for use in the wider study.

Similar experiments were also performed on the trithiocyanuric acid and melamine (TCA/M) co-crystal system in order to investigate whether similar results were obtained and ensure the proposed method was likely to be suitable for a wider range of systems. TCA/M was milled with different volumes of DMF, from 25 to 125 μL, and with 125 μL of MeOH. All powder patterns of the resulting materials are very similar and appear to match the calculated pattern for the TCA/M co-crystal with CSD Refcode QACTAP01, with an absence of starting material peaks (Figure 4.4). More detailed analysis of the powder patterns will be discussed below.

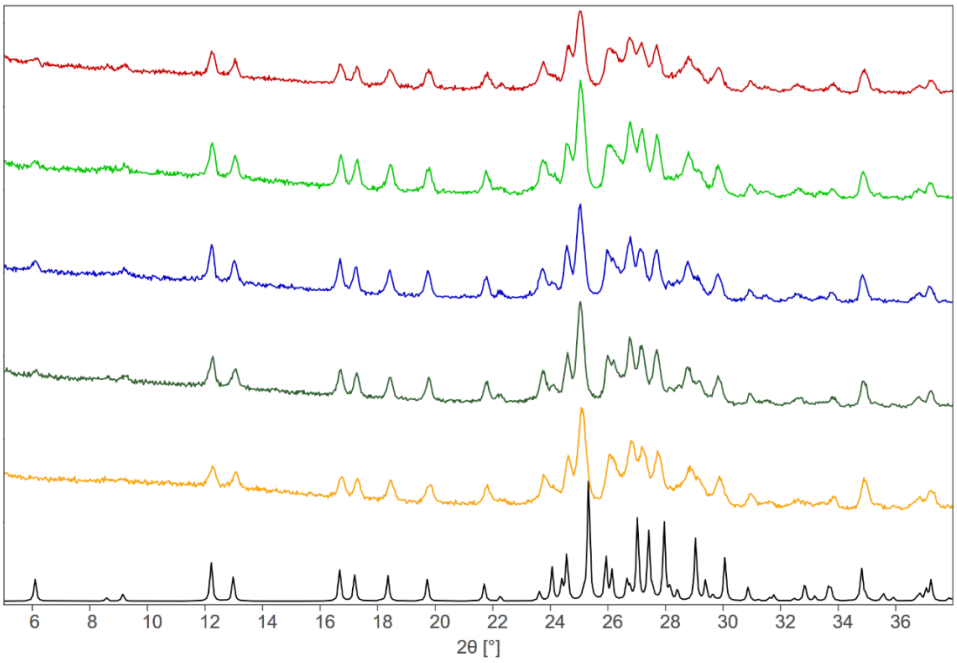


Figure 4.4: Powder patterns of TCA/M milling products from syntheses using different LAG conditions. From bottom to top: calculated pattern of TCA/M co-crystal with CSD Refcode QACTAP01 (black); experimental patterns of syntheses using 25 µL DMF (orange), 50 µL DMF (dark green), 100 µL DMF (blue), 125 µL DMF (light green), 125 µL MeOH (red).

Due to the success in milling of the CA/M and TCA/M co-crystal systems, the study was expanded to investigate the suitability of this methodology for a wider range of cyanuric acid and trithiocyanuric acid co-crystal systems. The method for subsequent experiments employed the use of 5 mL stainless steel jars and 2 x 7 mm stainless steel balls, 120-150 mg combined mass of solid starting material and 125 µL DMF or methanol, with a milling duration of 90 minutes and frequency of 30 Hz.

Cyanuric acid (CA) and trithiocyanuric acid (TCA) were each milled with melamine (M), 4,4'-bipyridine (BPY), trans-1,2-bis(4-pyridyl)ethene (DPE), 1,3,5-triazine (TAZ) and

pyrazine (PAZ) (Figure 4.5). Powder X-ray diffraction was used as the major method for analysis of the products formed.

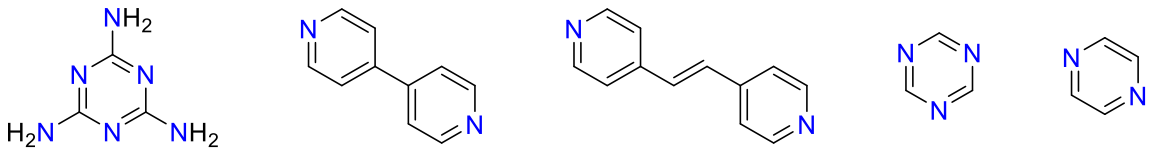


Figure 4.5: Substances paired with CA and TCA for co-crystal formation in this study. From left to right: melamine (M); 4,4′-bipyridine (BPY); trans-1,2-bis(4-pyridyl)ethene (DPE); 1,3,5-triazine (TAZ); pyrazine (PAZ).

4.3.2 Reported Structures

Prior to continuation of the milling experiments, searches of the Cambridge Structural Database (CSD) were conducted for each of the systems using the programme ConQuest. The calculated powder patterns of any existing co-crystal structures with atomic coordinates reported were compared with the experimental patterns from the corresponding milled syntheses. Refinements were performed to confirm the identity of the products wherever possible. The results from these searches of the CSD are recorded in Table 4.1. Figure 4.6 shows representations of the structures that have atomic coordinates reported.

Table 4.1: Results from ConQuest searches of the CSD for reported co-crystals in September 2022. Asterisks indicate solvent-containing structures. Red text indicated structures for which the CIF does not contain atomic coordinates.

System	CSD Refcode(s) of Co-crystals
CA/M	QACSUI[17], QACSUI01[26]
TCA/M	QACTAP[17], QACTAP01[27]
CA/DPE	HADKUT[23], HADKUT01[23]
TCA/DPE	FOSFEB[21]
CA/BPY	VEXQOE[22], VEXQUK[22]
TCA/BPY	*NOVZON[28], *NOVZON01, *NOWBAC[29], *EHIRUI[28], *EHIRES[28], *EHIRIW[28], *EHIROC[28], *EHIRAO[28], *YOTSIL[30], YOTSOR[30]
CA/TAZ	No results returned
TCA/TAZ	FOSDUP[21]
CA/PAZ	No results returned
TCA/PAZ	FOSFAX[21]

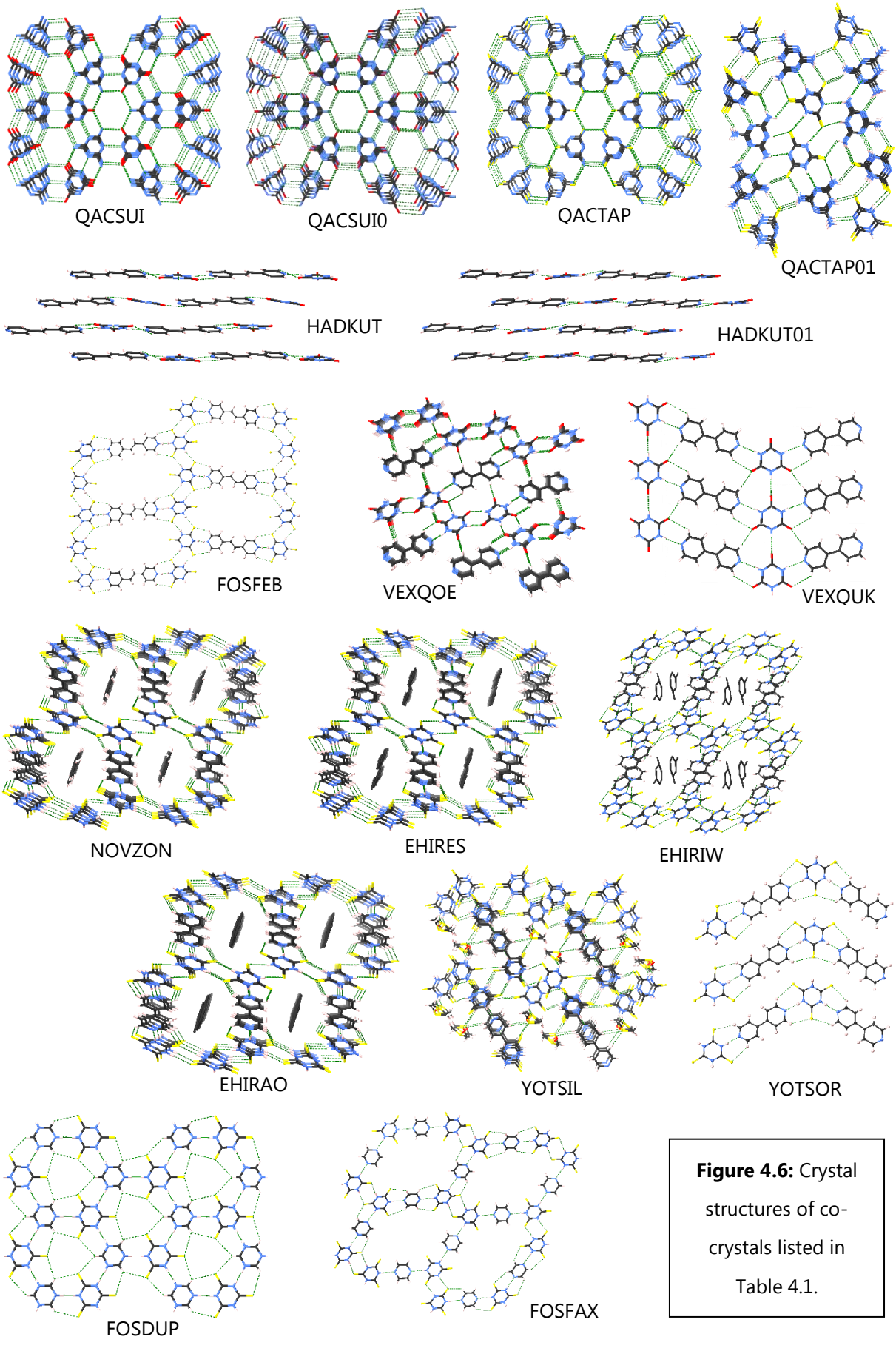


Figure 4.6: Crystal structures of co-crystals listed in Table 4.1.

4.3.3 Method Implementation

CA/M

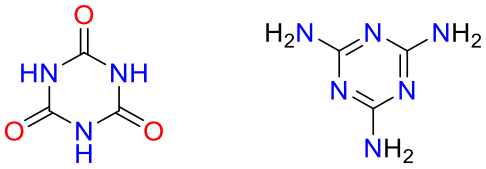


Figure 4.7: Chemical structures of cyanuric acid (left) and melamine (right).

As already discussed, the powder patterns of the products of ball milling cyanuric acid and melamine with DMF (CA/M-DMF) or methanol (CA/M-MeOH) appeared to match the structure reported in the CSD as QACSUI. The experimental powder patterns of the products were refined against the CSD structure to confirm this (Figure 4.8).

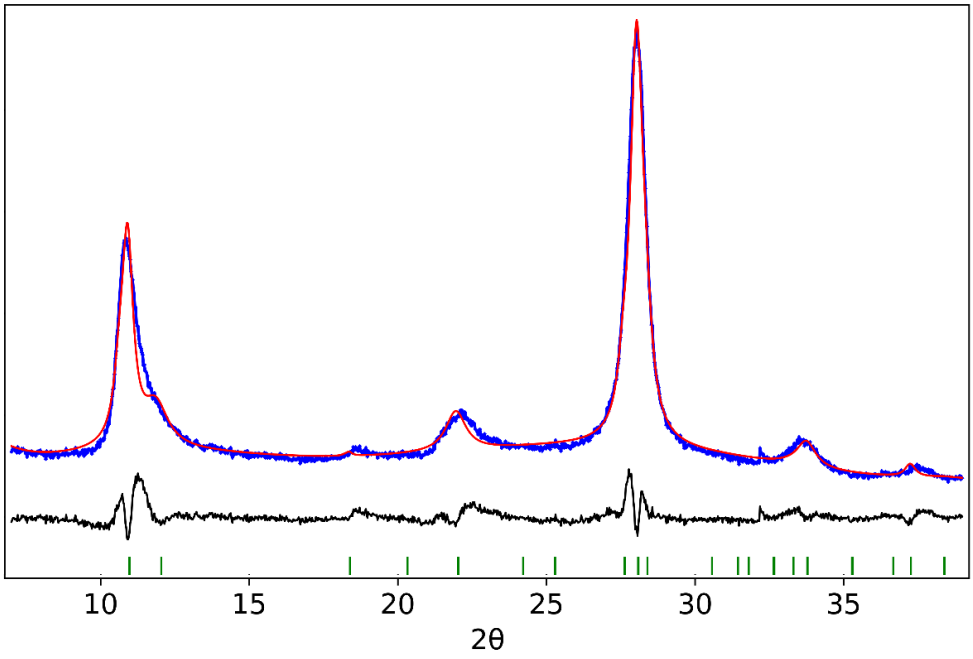


Figure 4.8: Experimental (blue ticks), calculated (red line), difference plot (I_{obs}-I_{calc}) (black line, botttom panel) and Bragg positions (green ticks, bottom panel) for the LeBail refinement of experimental diffraction data of CA/M-DMF collected at room temperature by using single crystal data from QACSUI as starting parameters.

The results of the LeBail refinement confirm a match of both CA/M-DMF (Figure 4.8) and CA/M-MeOH (Appendix Figure 4.2) with the reported structure QACSUI. There are no peaks in the experimental pattern of CA/M-DMF which do not correspond with the calculated structure, indicating that no crystalline starting materials remain. In CA/M-MeOH however, there does appear to be some residual starting material.

The peaks in the experimental patterns are however quite significantly broadened. The co-crystal structure is composed of layers of hydrogen-bonded cyanuric acid and melamine which are stacked upon one another, facilitated by π-π stacking interactions. Hydrogen-bonded nanosheets of this system have been studied by Zhang et al., and the powder pattern profile for their nanosheet structure appears markedly similar to our ball milled product.[31] Peak broadening can however also be caused by small particle sizes of crystallites, and it is plausible that the ball milling method may produce a product with small particle sizes.[32] Analysis by electron microscopy may provide more information as to the morphology and particle size of the milled product, however that was beyond the scope of this particular study.

TCA/M

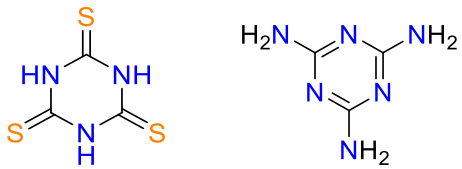


Figure 4.9: Chemical structures of trithiocyanuric acid (left) and melamine (right).

Two TCA/M co-crystal structures are reported in the CSD, both of which have a 1:1 ratio of TCA to melamine. One structure (CSD RefCode QACTAP, crystallised from water) is analogous to the CA/M co-crystal discussed above. The molecules are arranged in a 'rosette' configuration, with each TCA molecule forming three sets of triple hydrogen bonding interactions with adjacent melamine molecules, and vice versa. This forms planar 2-dimensional sheets which stack upon one another assisted by π-π interactions in an ABAB fashion. The other structure (CSD RefCode QACTAP01, crystallised from DMSO) has a slightly more complex arrangement of TCA and melamine molecules, with pairs of TCA molecules and pairs of melamine molecules interlinked by hydrogen bonds. In this case adjacent molecules are not in the same plane but twisted with respect to one another. Face-to-face π-π interactions remain an important feature of the structure nonetheless.

Milling of trithiocyanuric acid and melamine with either DMF or methanol produced the phase QACTAP01 in both cases, confirmed by LeBail refinement (Figure 4.10 and Appendix Figure 4.3). As with the CA/M products, there are no residual starting material peaks or peaks which do not align with the calculated structure, indicating good conversion to the product. It is interesting to note that despite analogous co-crystals of CA/M and TCA/M being known, the mechanochemical syntheses of the two systems appear to favour different structures.

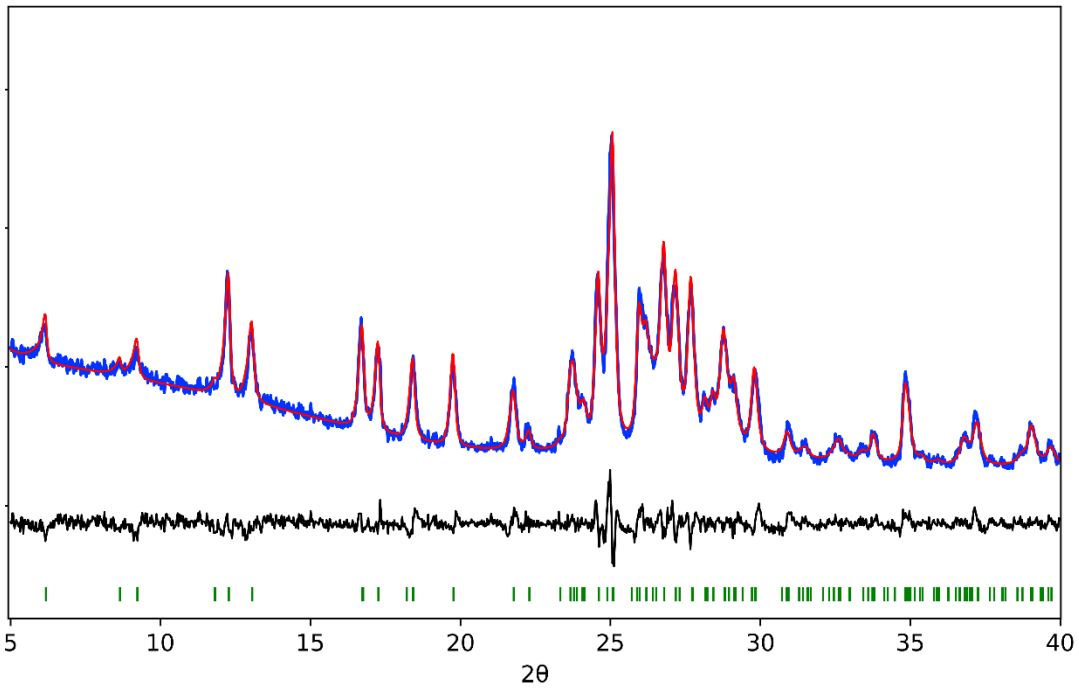


Figure 4.10: Experimental (blue ticks), calculated (red line), difference plot (I_{obs}-I_{calc}) (black line, botttom panel) and Bragg positions (green ticks, bottom panel) for the LeBail refinement of experimental diffraction data of TCA/M-DMF collected at room temperature by using single crystal data from QACTAP01 as starting parameters.

CA/BPY

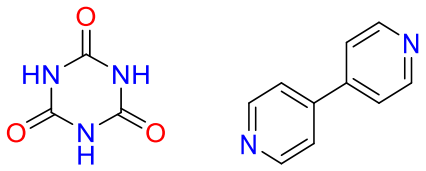


Figure 4.11: Chemical structure of cyanuric acid (left) and 4,4′-bipyridine (right).

Two CA/BPY co-crystal structures are reported in the CSD (RefCodes VEXQUK and VEXQOE). The structure VEXQUK is a 1:1 adduct of CA and BPY crystallised from water, an ABAB layered structure formed of chains of CA and BPY linked by hydrogen bonds between the cyanuric acid molecules. VEXQOE is a 2:1 adduct crystallised from methanol, a structure fully interlinked by virtue of hydrogen bonding interactions.

Milling of cyanuric acid and 4,4′-bipyridine with DMF formed a product whose diffraction pattern closely resembles that of the reported phase VEXQUK. LeBail refinement confirmed a good fit between the experimental and reported structures (Figure 4.12).

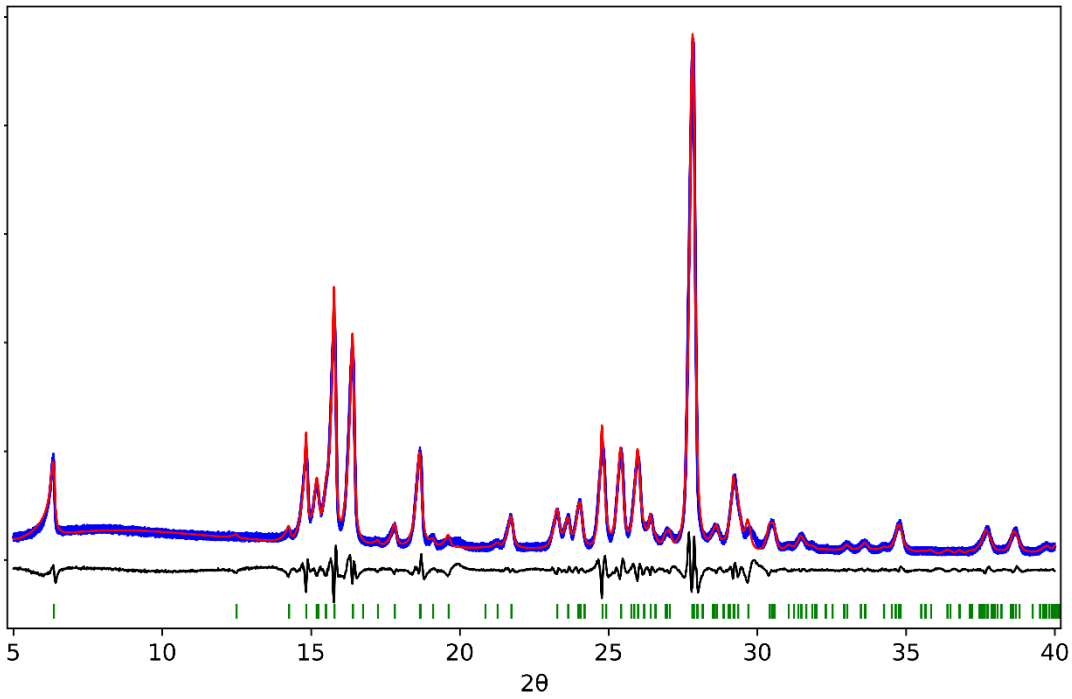


Figure 4.12: Experimental (blue ticks), calculated (red line), difference plot (I_{obs}-I_{calc}) (black line, botttom panel) and Bragg positions (green ticks, bottom panel) for the LeBail refinement of experimental diffraction data of CA/BPY-DMF collected at room temperature by using single crystal data from VEXQUK as starting parameters.

Where methanol was used as the solvent for LAG, a mixture of both reported phases, VEXQUK and VEXQOE, was produced (Figure 4.13). The appearance of peaks in the experimental pattern with 2θ values between 7° and 12° were key indicators of the formation of the VEXQOE phase in this synthesis.

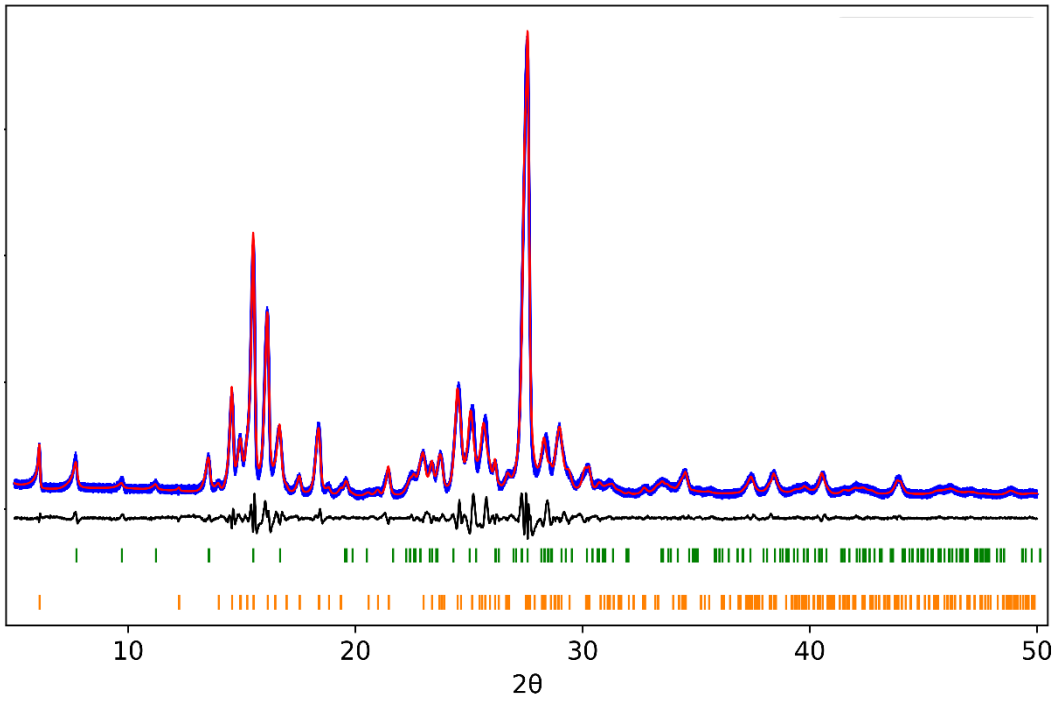


Figure 4.13: Experimental (blue ticks), calculated (red line), difference plot (I_{obs}-I_{calc}) (black line, botttom panel) and Bragg positions (green (VEXQOE) and orange (VEXQUK) ticks, bottom panel) for the LeBail refinement of experimental diffraction data of CA/BPY-MeOH collected at room temperature by using single crystal data from VEXQUK and VEXQOE as starting parameters.

This difference between the results of syntheses using DMF and methanol shows that the solvent chosen for LAG can impact not only whether, or how efficiently, a co-crystal phase is produced, but also the structure of the product. This is consistent with observations made by Peddireddi et al. in the single crystal syntheses of VEXQUK and VEXQOE.[22] Our results are also consistent with the reported syntheses in that it was the synthesis in which methanol was used for LAG which resulted in some production of the VEXQOE co-crystal.

TCA/BPY

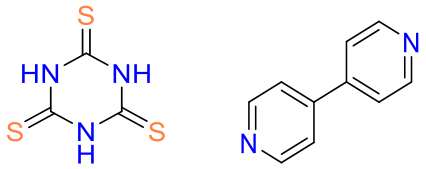


Figure 4.14: Chemical structures of trithiocyanuric acid (left) and 4,4′-bipyridine (right).

Of the ten systems studied in this project, trithiocyanuric acid and 4,4′-bipyridine returned the largest number of hits in the CSD for co-crystals. These reported structures stem from work by Pedireddi et al., in which it is shown that the solvent used in co-crystal synthesis can influence the resulting structure.[28–30] There was some expectation from the outset therefore that the solvents used in our LAG syntheses would impact the co-crystal structure(s) formed.

When TCA/BPY was milled with methanol (TCA/BPY-MeOH), the co-crystal phase produced is consistent with the reported structure with CSD Refcode YOTSOR (Figure 4.15). The single crystal phase is crystallised from a DMSO-methanol solvent mix. This co-crystal is composed solely of TCA and BPY molecules, with no residual solvent in the network. The structure is similar to that of the CA/BPY co-crystal VEXQUK, although with a larger distance between the chains of TCA and BPY molecules than CA and BPY molecules (O--N distance between molecules of CA = 2.93 Å in VEXQUK; S--N distance between molecules of TCA = 4.20 Å in YOTSOR).

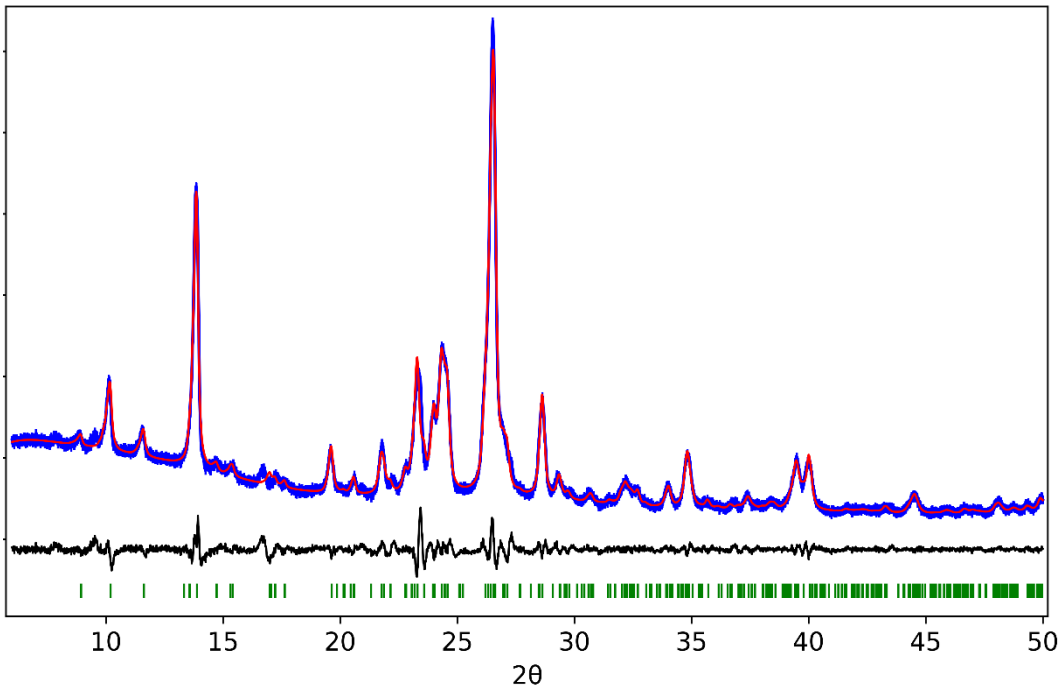


Figure 4.15: Experimental (blue ticks), calculated (red line), difference plot (I_{obs}-I_{calc}) (black line, botttom panel) and Bragg positions (green ticks, bottom panel) for the LeBail refinement of experimental diffraction data of TCA/BPY-MeOH collected at room temperature by using single crystal data from YOTSOR as starting parameters.

Where DMF was used as the solvent for LAG, the experimental powder pattern closely resembles a mixture of reported co-crystals YOTSIL and EHIRIW, with a good fit obtained from LeBail refinement using these two phases (Figure 4.16). Interestingly, both of these reported structures have solvent incorporated - dimethyl sulfoxide in YOTSIL and m-xylene in EHIRIW. Clearly neither of these solvent molecules are likely to be present in the milled synthesis, implying a similar new structure may have been produced, which we believe likely to have DMF molecules incorporated in the hydrogen bonding network. Attempts to grow single co-crystals of TCA/BPY from DMF were unsuccessful.

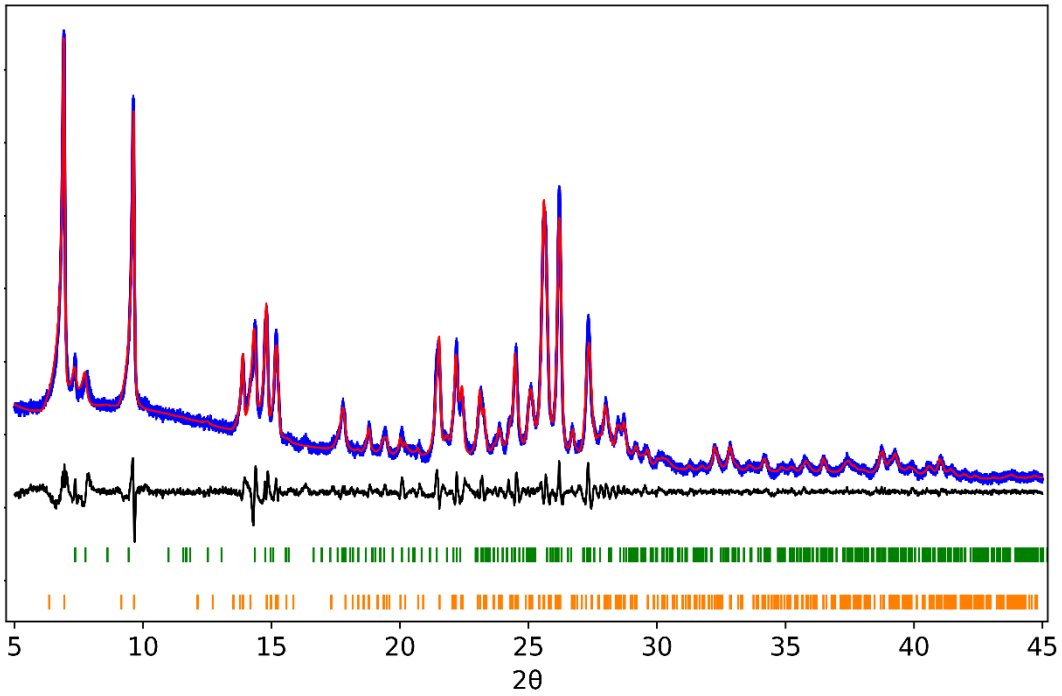


Figure 4.16: Experimental (blue ticks), calculated (red line), difference plot (I_{obs}-I_{calc}) (black line, botttom panel) and Bragg positions (green (EHIRIW) and orange (YOTSIL) ticks, bottom panel) for the LeBail refinement of experimental diffraction data of TCA/BPY-DMF collected at room temperature by using single crystal data from EHIRIW and YOTSIL as starting parameters.

Single crystal

Alongside the milling experiments, a reported method for single crystal synthesis of a TCA/BPY structure with CSD Refcode NOWBAC was repeated.[29] The crystallographic information file (CIF) for this structure in the CSD does not contain atomic coordinates, which prevented examination of the calculated powder pattern. A later publication by one of the same authors reports that *"solvent molecules are not located in the electron density map*".[30] The crystallisation was performed by layering solutions of trithiocyanuric acid and bipyridine in methanol and chloroform respectively, followed

by slow evaporation of the solvents. Yellow needle-shaped crystals were formed with unit cell parameters closely matching that of the reported phase NOWBAC (Table 4.2).

Table 4.2: Unit cell parameters of the reported TCA/BPY structure NOWBAC and the TCA/BPY crystals synthesised during this project.

Unit cell parameters	a (Å)	b (Å)	c (Å)	α (°)	β (°)	γ (°)
NOWBAC	11.29	13.02	16.62	72.48	72.04	64.73
TCA/BPY	11.23	12.79	16.55	73.06	71.80	64.49

The main TCA/BPY hydrogen-bonded structure of NOWBAC is described in both the original and more recent publications. The crystals we synthesised have the same structure providing further evidence that we were successful in reproducing the reported synthesis. The hydrogen bonding network is composed of a 2:1 ratio of TCA and BPY molecules, with chains of TCA molecules interlinked by BPY molecules to form 2-dimensional sheets (Figure 4.17A). These are layered upon one another in the extended structure which has channels running parallel to the c-crystallographic axis (Figure 4.17B). We were able to resolve the additional electron density and found that the structure contained hydrogen-bonded chains of 1:1:1 TCA, BPY and MeOH (Figure 4.17C) running through the channels parallel to the c-axis (Figure 4.17D).

The structure we synthesised crystallises in the space group P1, whereas the NOWBAC is reported as $P\bar{1}$, which can be explained by the fact that the 1-dimensional chains in

the channels, which were not resolved in the reported structure, break the symmetry of the crystal structure.

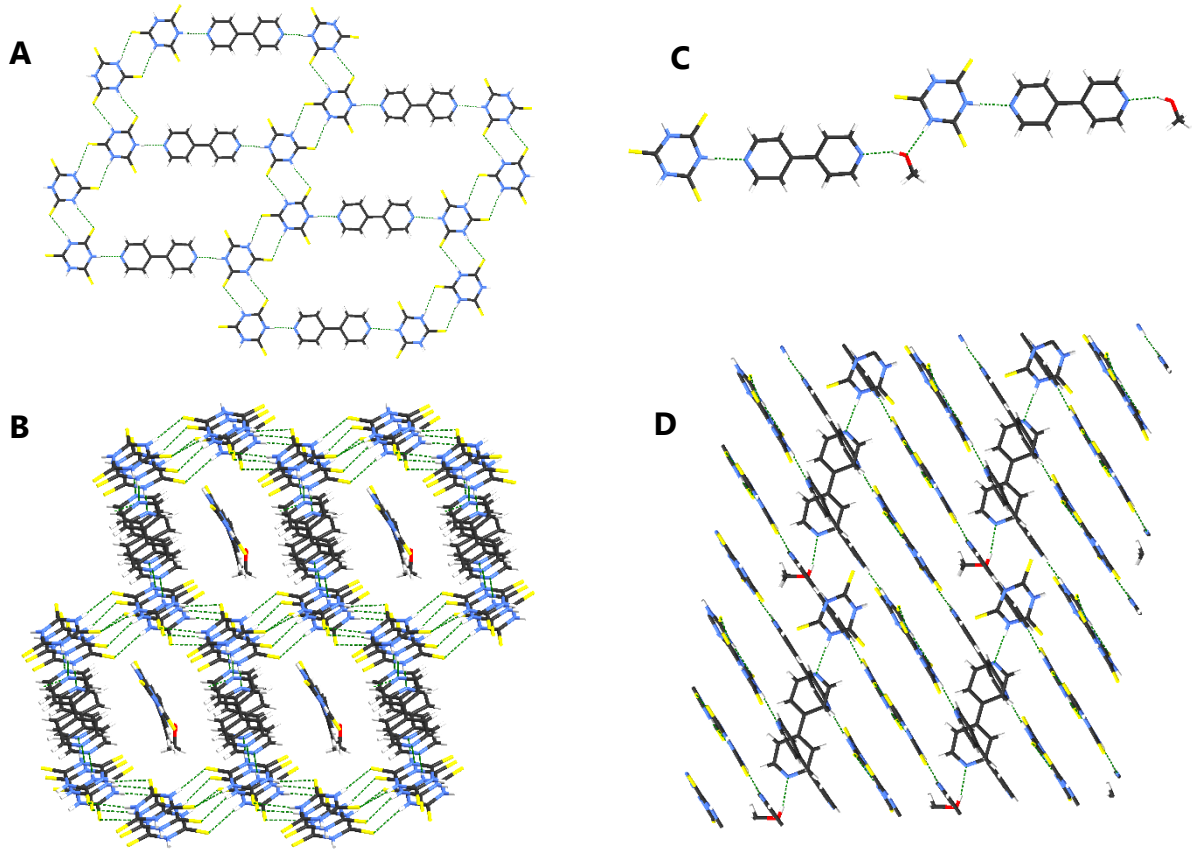


Figure 4.17: Crystal structure of TCA/BPY co-crystallised from MeOH/$CHCl_3$. (A) Hydrogen-bonded layer structure (B) View of channels along the c-axis (C) 1-dimensional hydrogen-bonded chains of TCA, BPY and MeOH (D) View along the a-axis showing stacked layers and chains. Carbon atoms are shown in black, hydrogen atoms light grey, nitrogen atoms blue, oxygen atoms red and sulfur atoms yellow.

After cross-examination of the calculated powder pattern of this structure with the experimental pattern of the milling product, this phase does not appear to be formed by the mechanochemical method. The data remains valuable however in providing further information on the reported structure.

CA/DPE

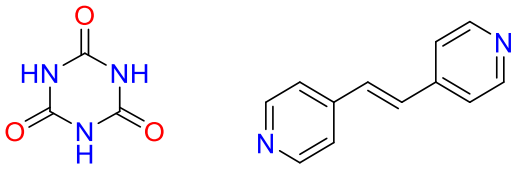


Figure 4.18: Chemical structures of cyanuric acid (left) and trans-1,2-bis(4-pyridyl)ethene (right)

Two existing structures of CA/DPE co-crystals are reported in the CSD. Both structures are layered, with a 1:1 ratio of CA to DPE molecules. There are two slightly different configurations of CA and DPE in 2D sheets, with both configurations appearing in the structure with RefCode HADKUT01, and only one appearing in the structure with RefCode HADKUT.[23]

When the two starting materials are milled with DMF, the powder pattern of the product appears to resemble the calculated pattern of HADKUT more closely than HADKUT01. LeBail refinement was carried out on CA/DPE-DMF with HADKUT as the starting phase, and indeed the refinement showed a good match between the experimental pattern and reported structure (Figure 4.19). The results of the CA/DPE-MeOH synthesis were very similar to those for CA/DPE-DMF (Appendix Figure 4.4).

Two peaks in the experimental powder pattern, at 7.5° and 16.8° 2θ (marked by asterisks in Figure 4.19), are not modelled by the refinement and therefore imply the presence of a small amount of impurity. The peak at 7.5° in particular does not align with any peaks in the calculated patterns of reported starting material or co-crystal structures.

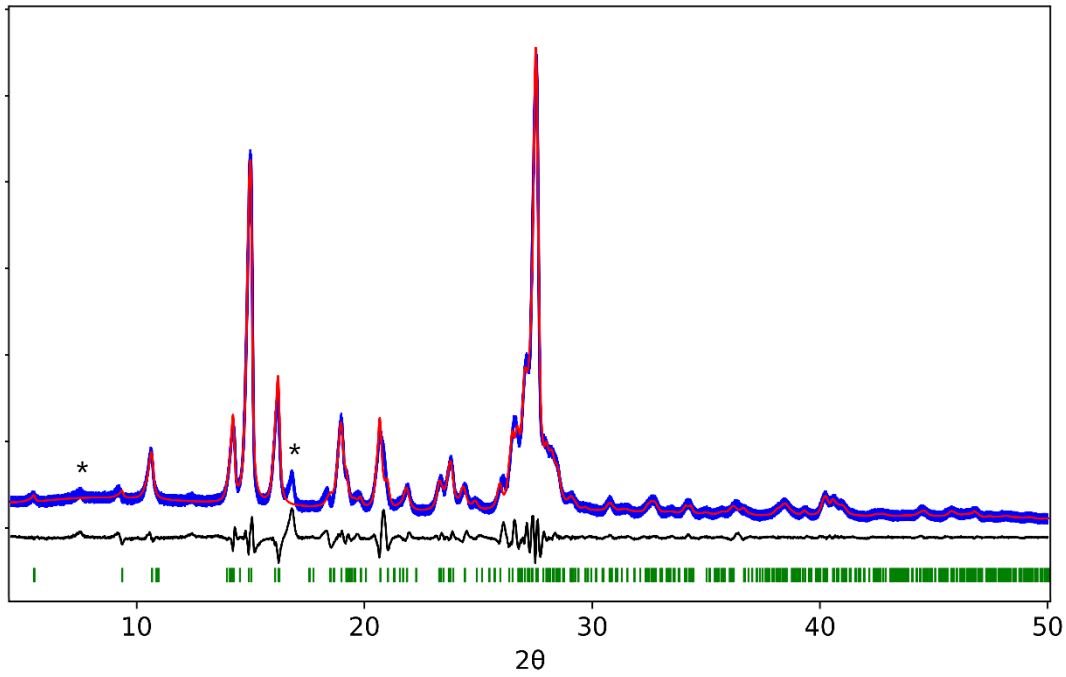


Figure 4.19: Experimental (blue ticks), calculated (red line), difference plot (I_{obs}-I_{calc}) (black line, botttom panel) and Bragg positions (green ticks, bottom panel) for the LeBail refinement of experimental diffraction data of CA/DPE-DMF collected at room temperature by using single crystal data from HADKUT as starting parameters.

TCA/DPE

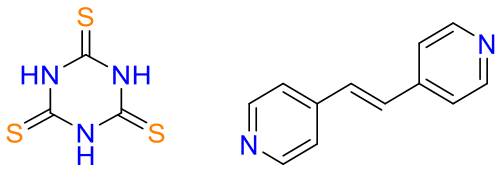


Figure 4.20: Chemical structures of trithiocyanuric acid (left) and trans-1,2-bis(4-pyridyl)ethene (right)

One crystal structure of a TCA/DPE co-crystal is reported in the CSD, with RefCode FOSFEB.

The experimental powder patterns of the products of milling TCA and DPE with either DMF or methanol are for the most part very similar to one another, with the exception

of some additional peaks, most notably one at 12.6° 2θ (marked with an asterisk in Figure 4.21) appearing in the pattern of TCA/DPE-DMF but not in that of TCA/DPE-MeOH. Visual comparison of both experimental patterns with the calculated powder pattern of FOSFEB indicates some similarities between the milled products and the known co-crystal structure, however there is notable deviation particularly at higher angles (Figure 4.21). This suggests that the major phase formed from ball milling is likely to be different from the reported structure, however it may have some structural similarities. The additional peak in TCA/DPE-DMF may indicate the formation of a secondary phase during this experiment.

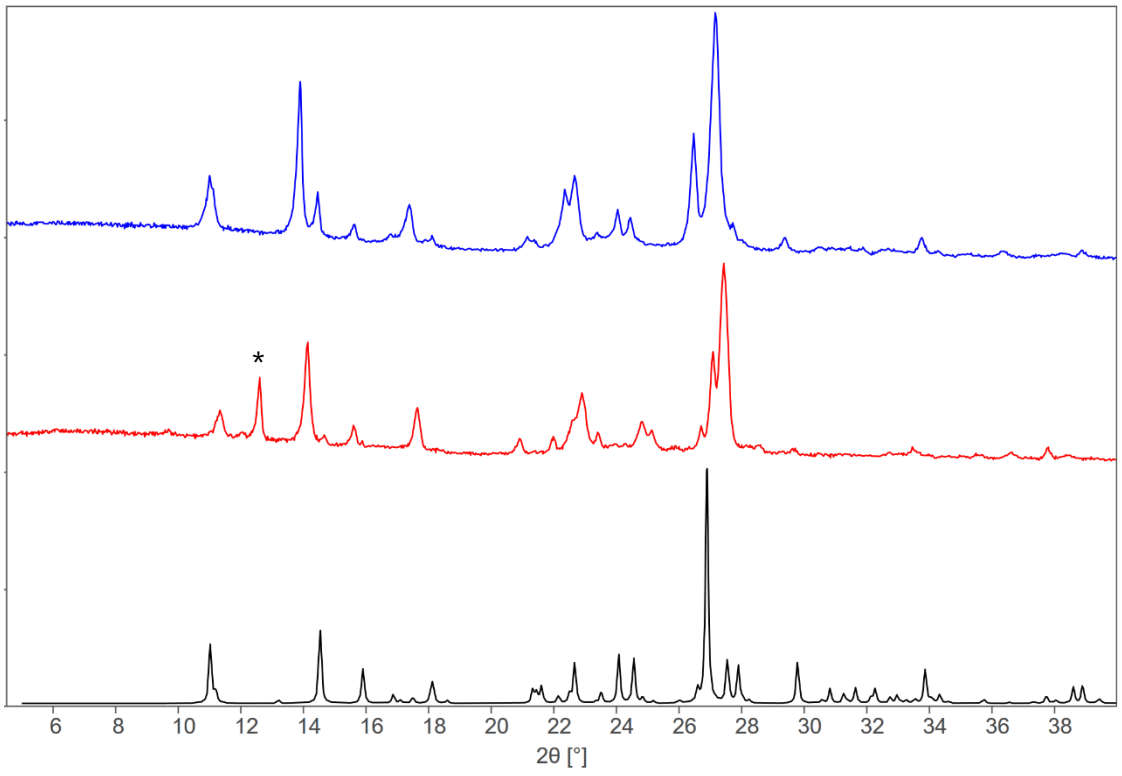


Figure 4.21: From bottom to top - Calculated powder XRD pattern of FOSFEB (black); experimental powder XRD patterns of TCA/DPE-DMF (red) and TCA/DPE-MeOH (blue).

Single crystal

During the course of this work we repeated the reported procedure by which the structure FOSFEB was obtained. A new single crystal structure was produced which was analysed by SCXRD. The calculated powder pattern of this new co-crystal was taken into account in analysis of the ball milled products of TCA/DPE, however there were not any marked similarities between the two.

The new co-crystals were synthesised by slow evaporation from methanol solution over a period of 7 days. The crystals that formed were very delicate needle multicrystals which were challenging to separate and mount in preparation for SCXRD analysis without compromising the integrity of the crystals. Several attempts were made to collect data and the best obtained is discussed herein, however the crystal was a twin in which the reflections of one could not be separated from the other without severely reducing the data quality.

The structure bears close resemblance to that of the TCA/BPY co-crystal discussed previously. The co-crystal has a 2:1 ratio of TCA molecules to DPE molecules and is in the space group P1. It is a layered structure, with the layers composed of TCA chains interlinked by molecules of DPE (Figure 4.22A). The layers stack in such a way that channels run through the structure (Figure 4.22B). Running through these channels are repeating hydrogen-bonded chains of methanol, DPE and TCA (Figure 4.22C).

The significant similarity between the TCA/DPE and TCA/BPY co-crystals synthesised during this project is interesting, and a natural link may be drawn to the concept of

reticular synthesis. The use of DPE in place of BPY results in a slightly elongated unit cell along the c-axis, and slightly different angles (Table 4.3), however the overall structures are directly comparable in terms of the arrangement of molecules and intermolecular interactions, down to the 1-dimensional chain in the pores. This is particularly notable given the relatively weak N-H···S hydrogen bonding interactions in these co-crystals and the wide range of modes of interaction that could take place which could result in the formation of different structures.

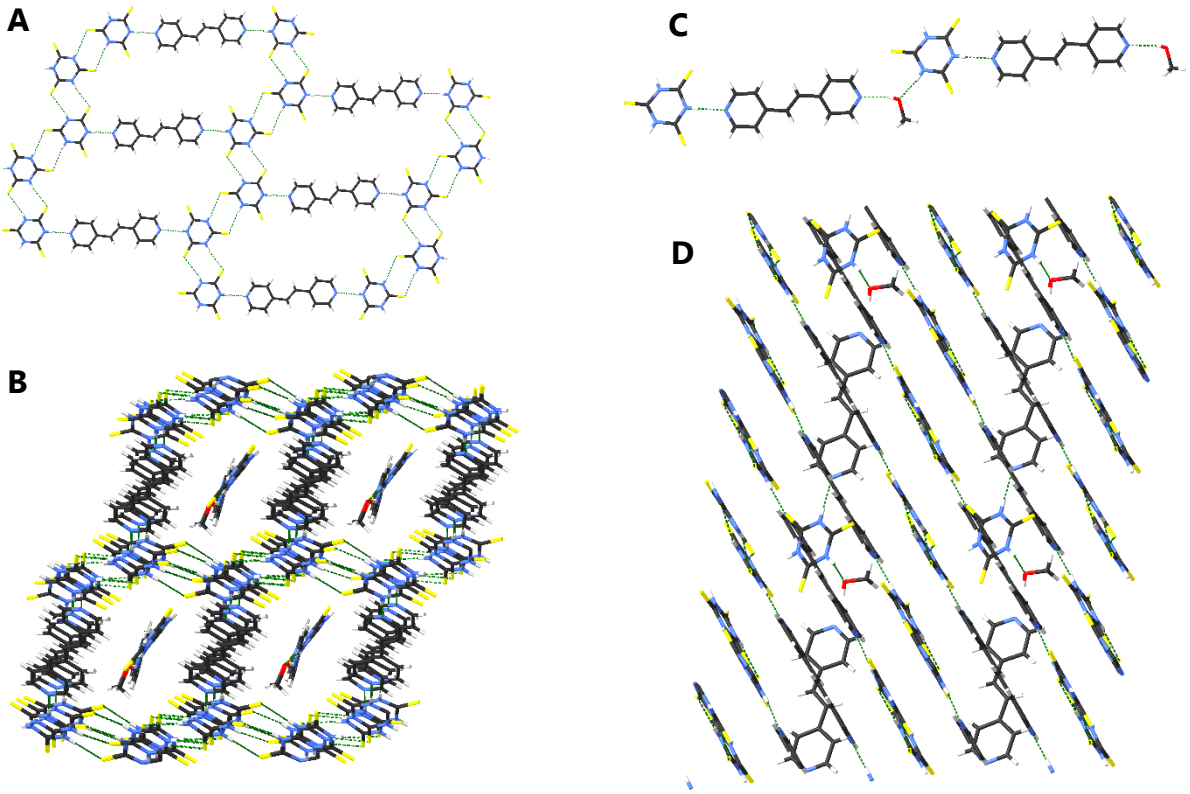


Figure 4.22: Crystal structure of TCA/BPY co-crystallised from MeOH. (A) Hydrogen-bonded layer structure (B) View of channels (C) 1-dimensional hydrogen-bonded chains of TCA, BPY and MeOH (D) View along the a-axis showing stacked layers and chains. Carbon atoms are shown in black, hydrogen atoms light grey, nitrogen atoms blue, oxygen atoms red and sulfur atoms yellow.

Table 4.3: Unit cell parameters of TCA/BPY and TCA/DPE co-crystals synthesised during this study, determined by SCXRD.

Unit cell parameters	a (Å)	b (Å)	c (Å)	α (°)	β (°)	γ (°)
TCA/BPY	11.23	12.79	16.55	73.06	71.80	64.49
TCA/DPE	11.24	12.16	18.23	77.17	76.25	63.16

CA/TAZ

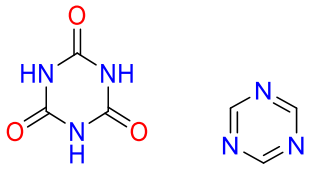


Figure 4.23: Chemical structures of cyanuric acid (left) and 1,3,5-triazine (right).

No co-crystal structures of cyanuric acid and 1,3,5-triazine are reported in the CSD. Ball milling experiments using these materials were conducted nonetheless, however the depth of analysis possible is clearly more limited than for most of the systems studied in this work. Visual comparisons were conducted, however, between the powder pattern of the product and starting materials to assess whether a new phase may have been made. Figure 4.24 shows the experimental powder patterns of each relevant material.

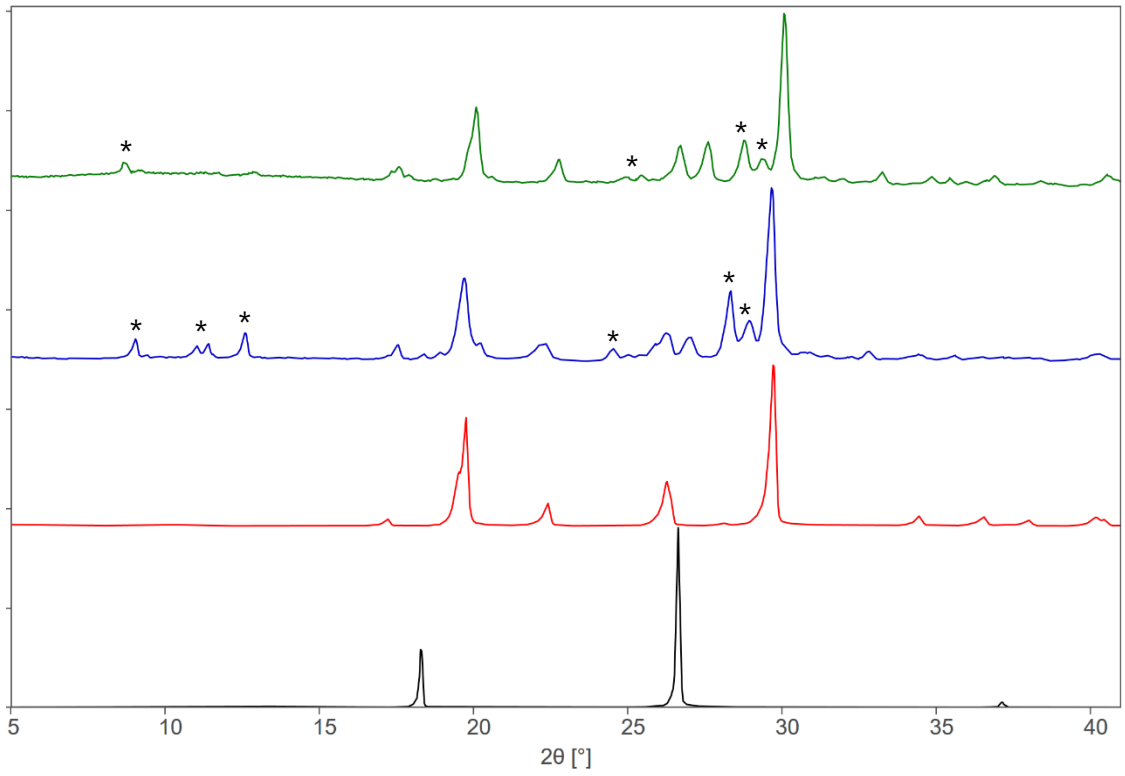


Figure 4.24: Experimental powder XRD patterns of (from bottom to top) 1,3,5-triazine (black), cyanuric acid (red), CA/TAZ-DMF (blue), CA/TAZ-MeOH (green).

There are notable similarities between the PXRD profiles of cyanuric acid and the products of both mechanochemical syntheses, indicating some starting material is likely to remain. There are however several peaks (indicated with asterisks in Figure 4.24) in the product PXRD patterns which do not appear in the experimental or calculated (from CSD structures) patterns of either starting material. This implies a new phase, or phases, has been formed in at least some measure. Attempts were made to co-crystallise CA/TCA from methanol and DMF solutions, however these were unsuccessful.

TCA/TAZ

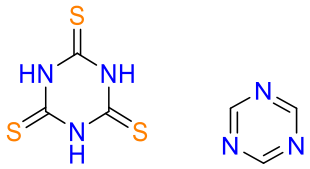


Figure 4.25: Chemical structures of trithiocyanuric acid (right) and 1,3,5-triazine (left).

Only one co-crystal structure of TCA/TAZ is reported in the CSD. Initial examination of the powder pattern of the milling product TCA/TAZ-DMF indicated some similarity to the reported structure FOSDUP. LeBail refinement was performed on the experimental pattern using FOSDUP as starting parameters, which confirmed some degree of structural similarity, however the fitting of the powder pattern was not entirely satisfactory (Figure 4.26). Some of the major peaks between 20° and 30° 2θ could be modelled as well as smaller peaks at higher angles, however there are several reflections not accounted for. Of particular note are two peaks at 9.0° and 9.7° 2θ, which are not present in the powder patterns of FOSDUP or either starting material. These imply the formation of a different extended structure with a relatively large d-spacing of 9.8 Å for the lowest angle peak. These peaks are not observed in the calculated patterns of any reported crystal structures of TCA or TAZ independently, implying a new co-crystal phase may have been produced. Attempts were made to crystallise TCA/TAZ co-crystals from DMF solution; however these endeavours were unsuccessful.

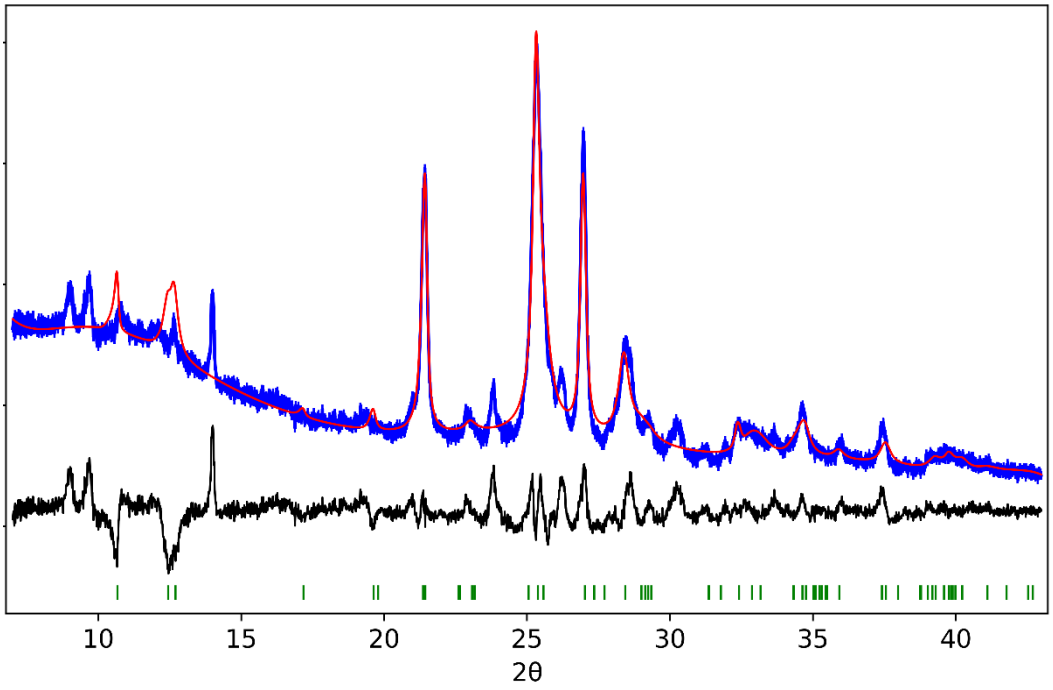


Figure 4.26: Experimental (blue ticks), calculated (red line), difference plot (I_{obs}-I_{calc}) (black line, bottom panel) and Bragg positions (green ticks, bottom panel) for the LeBail refinement of experimental diffraction data of TCA/TAZ-DMF collected at room temperature by using single crystal data from FOSDUP as starting parameters.

The single-crystal synthesis of FOSDUP is conducted from methanol solution, so there was some expectation that milling of TCA and BPY with MeOH may be more likely to produce the same phase. In fact the product of TCA/BPY-MeOH resulted in a product with a powder pattern similar to that of TCA/BPY-DMF, which had some resemblance to the co-crystal phase FOSDUP, but for which the LeBail refinement was unable to model several peaks in the pattern (Appendix Figure 4.5). As with TCA/TAZ-DMF, there is a peak in the experimental pattern at a relatively low 2θ angle of 8.9° which does not match up to the calculated patterns of any reported crystal structures of the starting materials. It is unclear whether the additional product is the same as was produced

from the DMF LAG experiment or is a different structure, due to the general low intensity of the peaks in the experimental powder patterns.

CA/PAZ

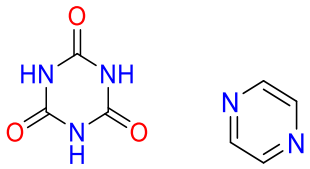


Figure 4.27: Chemical structures of cyanuric acid (left) and pyrazine (right).

As was the case with CA/TAZ, no co-crystals of cyanuric acid and pyrazine are reported in the CSD. This means analysis again is by visual comparison of the experimental powder patterns of the product and starting materials. The powder pattern of CA/PAZ milled with DMF matches that of the starting material cyanuric acid (Appendix Figure 4.6), implying no co-crystallisation took place during this process. Where methanol was used for LAG however (CA/PAZ-MeOH), the PXRD pattern of the product does not resemble those of either starting material which suggests the formation of a new phase (Figure 4.28). Our attempts to obtain cyanuric acid-pyrazine co-crystal by slow evaporation from methanol solution were unsuccessful.

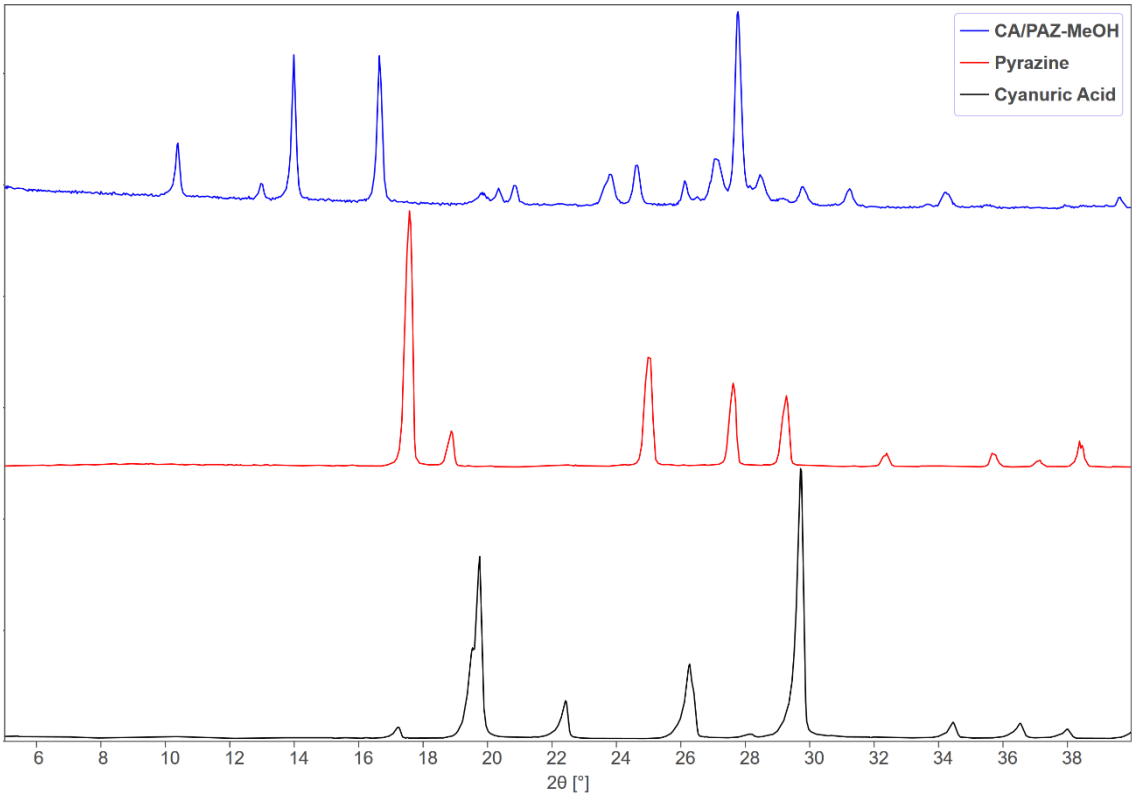


Figure 4.28: Experimental powder XRD patterns of (from bottom to top) cyanuric acid (black), pyrazine (red) and CA/PAZ-MeOH (blue).

TCA/PAZ

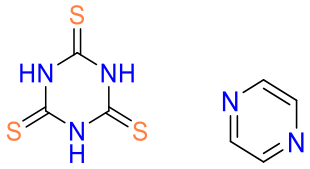


Figure 4.29: Chemical structures of trithiocyanuric acid (left) and pyrazine (right).

The final system investigated was trithiocyanuric acid and pyrazine. There is one reported co-crystal structure in the CSD, which has the Refcode FOSFAX. The powder patterns of milling products of TCA and PAZ with DMF or methanol were very similar, and LeBail refinement confirmed that the product in both cases closely matches the

reported co-crystal phase (Figure 4.30 and Appendix Figure 4.7). There do not appear to be any residual starting material peaks.

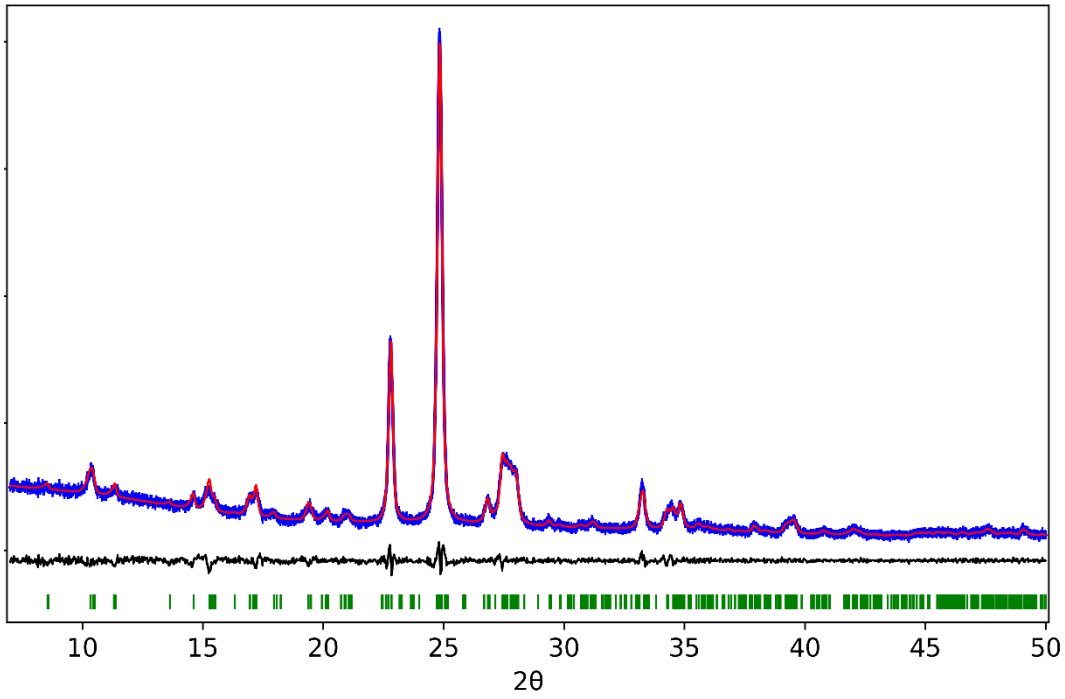


Figure 4.30: Experimental (blue ticks), calculated (red line), difference plot (I_{obs}-I_{calc}) (black line, bottom panel) and Bragg positions (green ticks, bottom panel) for the LeBail refinement of experimental diffraction data of TCA/PAZ-DMF collected at room temperature by using single crystal data from FOSFAX as starting parameters.

4.3.4 Limitations in Structure Elucidation

Due to the nature of the mechanochemical technique and the weak intermolecular interactions which lead to the co-crystal structures, powder XRD analysis is by far the most informative analytical technique which could be used to determine the product(s) formed. For systems for which reported crystal structures do not exist, or for which the milled material does not correlate with a reported structure, it was therefore challenging to gain significant insight into the structure of the product using the

techniques available to us. Where this was the case, attempts were made to crystallise the relevant systems from solution, however as discussed in the results and discussion section, these attempts were for the most part unsuccessful. Space group and unit cell parameter determination from experimental powder patterns was considered as a possibility, however this was decided against for several reasons. Firstly, it was not uncommon for the mechanochemical syntheses to result in the production of more than one co-crystal phase. This meant we could not be certain that a single phase had been formed in the cases where there were no relevant pre-existing structures, reducing the reliability of any potential unit cell determination. Additionally, due to the complex nature of the co-crystal structures that can form - with or without solvent molecules in the structure - it was not easy to predict what the symmetry of the product(s) may be.

4.4 Conclusions

We have developed a method for mechanochemical synthesis of 2-component co-crystals of cyanuric acid or trithiocyanuric acid. A liquid-assisted grinding technique was used, and this method reliably results in the conversion of the starting materials to co-crystal phase(s). LAG experiments using either DMF or methanol were conducted on CA and TCA each with five complementary molecules. In all but one case, powder XRD analysis showed the structure of the product to be different from the starting materials. The LAG solvent appears to have some influence on the structure formed in some cases.

Where structural data for relevant co-crystals is recorded in the CSD, in many cases the mechanochemical method reproduced a reported structure. There were several syntheses however for which the powder XRD pattern of the product did not correspond to that of a reported co-crystal or of the starting materials, indicating the possible formation of a new co-crystal phase. Elucidation of structural information of these potential new phases may be an avenue for future investigations.

Table 4.4 summarises the results presented in this chapter, which highlights in several ways the value of mechanochemistry – for synthesis of known materials with reduced solvent requirements; for increased control over polymorphism; as a route to new materials.

Table 4.4: Summary of co-crystal systems studied, reported structures and results of milling experiments.

System	CSD Refcodes of structures with atomic coordinates	New SC?	DMF LAG Product(s)	MeOH LAG Product(s)
CA/M	QACSUI, QACSUI01		QACSUI	QACSUI
TCA/M	QACTAP, QACTAP01		QACTAP01	QACTAP01
CA/DPE	HADKUT, HADKUT01		HADKUT	HADKUT
TCA/DPE	FOSFEB	Yes	New phase(s)	New phase(s)
CA/BPY	VEXQOE, VEXQUK		VEXQUK	VEXQOE + VEXQUK
TCA/BPY	NOVZON, NOWBAC, EHIRUI, EHIRES, EHIRIW, EHIROC, EHIRAO, YOTSIL, YOTSOR	Yes	DMF analogue of EHIRIW + YOTSIL?	YOTSOR
CA/TAZ			New phase(s)	New phase(s)
TCA/TAZ	FOSDUP		New phase(s)	New phase(s)
CA/PAZ			No reaction	New phase(s)
TCA/PAZ	FOSFAX		FOSFAX	FOSFAX

4.5 Experimental

4.5.1 Equipment

Starting materials were purchased from Sigma Aldrich or Fluorochem and used as received. A Retsch Mixer Mill MM400 was used to conduct ball milling experiments.

4.5.2 Ball milling

General method

A 5 mL stainless steel milling jar was loaded with two 7 mm stainless steel milling balls, the solid materials (total mass between 120 and 150 mg) and solvent (100 to 125 μL). The jar was firmly tightened and inverted several times, then ball milled for 90 minutes at 30 Hz. After milling, the product was extracted from the jar and stored in a capped vial before being analysed by powder X-ray diffraction.

Details of masses and volumes of materials used for each experiment are shown in Table 4.5 below.

Table 4.5: Materials used in ball milling experiments.

Experiment	Material 1	Mass	Material 2	Mass	Solvent	Volume
CA/M-DMF	CA	61 mg	M	60 mg	DMF	125 μL
CA/M-MeOH	CA	61 mg	M	60 mg	MeOH	125 μL
TCA/M-DMF	TCA	84 mg	M	60 mg	DMF	100 μL
TCA/M-MeOH	TCA	84 mg	M	60 mg	MeOH	100 μL
CA/DPE-DMF	CA	61 mg	DPE	86 mg	DMF	125 μL

Experiment	Material 1	Mass	Material 2	Mass	Solvent	Volume
CA/DPE-MeOH	CA	61 mg	DPE	86 mg	MeOH	125 µL
TCA/DPE-DMF	TCA	84 mg	DPE	86 mg	DMF	100 µL
TCA/DPE-MeOH	TCA	84 mg	DPE	86 mg	MeOH	125 µL
CA/BPY-DMF	CA	61 mg	BPY	74 mg	DMF	100 µL
CA/BPY-MeOH	CA	61 mg	BPY	74 mg	MeOH	100 µL
TCA/BPY-DMF	TCA	84 mg	BPY	74 mg	DMF	100 µL
TCA/BPY-MeOH	TCA	84 mg	BPY	74 mg	MeOH	100 µL
CA/PAZ-DMF	CA	90 mg	PAZ	56 mg	DMF	100 µL
CA/PAZ-MeOH	CA	90 mg	PAZ	56 mg	MeOH	100 µL
TCA/PAZ-DMF	TCA	97 mg	PAZ	44 mg	DMF	100 µL
TCA/PAZ-MeOH	TCA	97 mg	PAZ	44 mg	MeOH	100 µL
CA/TAZ-DMF	CA	92 mg	TAZ	57 mg	DMF	100 µL
CA/TAZ-MeOH	CA	92 mg	TAZ	57 mg	MeOH	100 µL
TCA/TAZ-DMF	TCA	101 mg	TAZ	46 mg	DMF	100 µL
TCA/TAZ-MeOH	TCA	101 mg	TAZ	46 mg	MeOH	100 µL

4.5.3 Powder XRD Analysis

Powder XRD measurements were carried out at 298 K using either a Bruker D8 Advance diffractometer (λ (CuKα1) = 1.5406 Å), or a PANalytical Empyrean diffractometer (λ (CuKα1) = 1.5406 Å) mounted on either a welled or zero background sample stage.

ConQuest was used to search for existing co-crystal structures recorded in the CSD.[33] CrystalDiffract was used to generate theoretical powder XRD patterns and for examination of experimental patterns. LeBail refinements were performed using GSAS-II.[34] Parameters refined: unit cell; particle size (using isotropic model); microstrain (using generalised model); sample displacement; background.

Table 4.6: Summary of the parameters obtained from LeBail refinements.

Experiment	Phase	a [Å]	b [Å]	c [Å]	α [°]	β [°]	γ [°]	V [Å^3]	Rwp	Rexp	GOF
CA/M-DMF	QACSUI	14.69	9.65	3.52	90	89.96	90	498.93	6.62	2.49	2.66
CA/M-MeOH	QACSUI01	15.11	9.65	3.55	90	90.35	90	517.49	10.49	2.73	3.86
TCA/M-DMF	QACTAP01	16.02	3.82	20.54	90	109.78	90	1184.20	5.84	3.73	1.57
TCA/M-MeOH	QACTAP01	15.94	3.82	20.50	90	109.75	90	1174.31	5.86	3.74	1.57
CA/BPY-DMF	VEXQUK	6.86	28.81	7.15	90	115.43	90	1276.63	9.35	1.85	5.05
CA/BPY-MeOH	VEXQOE	4.32	9.23	11.62	79.08	87.78	90.20	454.88	7.43	1.99	3.75
	VEXQUK	6.86	28.84	7.16	90	115.37	90	1280.84			
TCA/BPY-DMF	EHIRIW	10.28	11.67	12.33	102.81	93.52	89.76	1439.61	5.27	1.99	2.66
	YOTSIL	7.30	12.77	13.94	92.91	91.68	91.86	1296.69			
TCA/BPY-MeOH	YOTSOR	8.92	8.46	20.45	90	90.95	90	1541.70	6.23	2.52	2.48
CA/DPE-DMF	HADKUT	19.05	6.72	32.71	90	91.62	90	4184.78	9.49	1.53	6.19
CA/DPE-MeOH	HADKUT	19.26	6.79	32.84	90	92.01	90	4292.27	10.57	1.50	7.06
TCA/PAZ-DMF	FOSFAX	19.77	13.00	19.47	90	119.90	90	4338.18	5.48	4.13	1.33
TCA/PAZ-MeOH	FOSFAX	19.73	12.99	19.43	90	119.86	90	4318.82	5.73	4.46	1.29

4.5.4 Single-crystal XRD Analysis

Single-crystal XRD data was collected using a Rigaku Synergy-S dual source with a PhotonJet-S X-ray source and a HyPix-6000 detector. Data was collected at 100 K through the use of an Oxford Cryosystems cryostream device. Data was collected and processed using CrysAlisPro 171.42.49.57.

Using Olex2[35], the structures were solved with the SHELXT[36] structure solution program using Intrinsic Phasing and refined with the SHELXL[37] refinement package using Least Squares minimisation.

TCA/BPY Single Crystal

Crystal Data for $C_{62}H_{57}N_{29}OS_{21}$ (M = 1897.62 g/mol): triclinic, space group P1 (no. 1), a = 11.23080(10) Å, b = 12.7850(2) Å, c = 16.5528(2) Å, α = 73.0560(10)°, β = 71.8020(10)°, γ = 64.4940(10)°, V = 2003.38(5) Å^3, Z = 1, T = 100.15 K, μ(CuKα) = 5.755 mm^{-1}, *Dcalc* = 1.573 g/cm^3, 77743 reflections measured (5.716° ≤ 2Θ ≤ 158.24°), 15577 unique (R_{int} = 0.0371, R_{sigma} = 0.0268) which were used in all calculations. The final R_1 was 0.0381 (I > 2σ(I)) and wR_2 was 0.1079 (all data).

All hydrogen atoms in the structure were fixed as riding models and the isotropic thermal parameters (Uiso) were based on the Ueq of the parent atom.

TCA/DPE Single Crystal

Crystal Data for $C_{70}H_{65}N_{29}OS_{21}$ (M = 2001.77 g/mol): triclinic, space group P1 (no. 1), a = 11.24180(10) Å, b = 12.1621(2) Å, c = 18.2277(2) Å, α = 77.1690(10)°, β = 76.2480(10)°, γ = 63.1550(10)°, V = 2140.84(5) Å^3, Z = 1, T = 100.00(10) K, μ(Cu Kα) = 5.420 mm^{-1}, *Dcalc* = 1.553 g/cm^3, 41137 reflections measured (8.22° ≤ 2Θ ≤ 157.718°), 13754 unique (R_{int} = 0.0477, R_{sigma} = 0.0493) which were used in all calculations. The final R_1 was 0.0521 (I > 2σ(I)) and wR_2 was 0.1497 (all data).

All hydrogen atoms in the structure were fixed as riding models and the isotropic thermal parameters (Uiso) were based on the Ueq of the parent atom.

The crystals obtained were delicate needle multicrystals, which presented difficulties in selecting and mounting a single crystal for diffraction experiments. This data set was the best we obtained and was from a twinned crystal, hence the Flack parameter of 0.36. The reflections from each twin were significantly overlapped meaning it was not possible to extract the data from each individually and still obtain a structure solution.

4.6 References

1 A. Delori, T. Friščić and W. Jones, *CrystEngComm*, 2012, **14**, 2350–2362.

2 S. R. Bysouth, J. A. Bis and D. Igo, *Int J Pharm*, 2011, **411**, 169–171.

3 M. Gajda, K. P. Nartowski, J. Pluta and B. Karolewicz, *Eur J Pharm Biopharm*, 2018, **131**, 48–59.

4 M. Solares-Briones, G. Coyote-Dotor, J. C. Páez-Franco, M. R. Zermeño-Ortega, C. M. de la O Contreras, D. Canseco-González, A. Avila-Sorrosa, D. Morales-Morales and J. M. Germán-Acacio, *Pharmaceutics*, 2021, **13**, 790.

5 E. Y. Cheung, S. J. Kitchin, K. D. M. Harris, Y. Imai, N. Tajima and R. Kuroda, *J Am Chem Soc*, 2003, **125**, 14658–14659.

6 D. R. Weyna, T. Shattock, P. Vishweshwar and M. J. Zaworotko, *Cryst Growth Des*, 2009, **9**, 1106–1123.

7 I. Brito, J. Albanez and M. Bolte, *Acta Crystallogr E*, 2010, **66**, o2382–o2383.

8 F. Guo, E. Y. Cheung, K. D. M. Harris and V. R. Pedireddi, *Cryst Growth Des*, 2006, **6**, 846–848.

9 Q. Li, S. Li, K. Wang, Y. Zhou, Z. Quan, Y. Meng, Y. Ma and B. Zou, *J Phys Chem C*, 2017, **121**, 1870–1875.

10 E. H. Wiebenga and N. F. Moerman, *Z Kristallogr Cryst Mater*, 1938, **99**, 217–229.

11 E. H. Wiebenga, *J Am Chem Soc*, 1952, **74**, 6156–6157.

12 V. R. Pedireddi and D. Belhekar, *Tetrahedron*, 2002, **58**, 2937–2941.

13 C. T. Seto and G. M. Whitesides, *J Am Chem Soc*, 1990, **112**, 6409–6411.

14 J. A. Zerkowski, C. T. Seto and G. M. Whitesides, *J Am Chem Soc*, 1992, **114**, 5473–5475.

15 C. T. Seto and G. M. Whitesides, *J Am Chem Soc*, 1993, **115**, 905–916.

16 J. A. Zerkowski, J. C. MacDonald, C. T. Seto, D. A. Wierda and G. M. Whitesides, *J Am Chem Soc*, 1994, **116**, 2382–2391.

17 A. Ranganathan, V. R. Pedireddi and C. N. R. Rao, *J Am Chem Soc*, 1999, **121**, 1752–1753.

18 M. Kralj, S. Lukin, G. Miletić and I. Halasz, *J Org Chem*, 2021, **86**, 14160–14168.

19 K. Wzgarda-Raj, A. J. Rybarczyk-Pirek, S. Wojtulewski and M. Palusiak, *Acta Crystallogr C*, 2021, **77**, 49–55.

20 S. Marivel, E. Suresh and V. R. Pedireddi, *Tetrahedron Lett*, 2008, **49**, 3666–3671.

21 S. P. Argent, E. Golden, D. J. Ring, A. J. Blake and N. R. Champness, *Cryst Growth Des*, 2019, **19**, 5945–5954.

22 A. Ranganathan, V. R. Pedireddi, G. Sanjayan, K. N. Ganesh and C. N. R. Rao, *J Mol Struct*, 2000, **522**, 87–94.

23 S. A. Barnett, A. J. Blake and N. R. Champness, *CrystEngComm*, 2003, **5**, 134–136.

24 O. Shemchuk, F. Grepioni and D. Braga, *Cryst Growth Des*, 2020, **20**, 7230–7237.

25 H. Niu, W. Zhao, H. Lv, Y. Yang and Y. Cai, *J Chem Eng*, 2021, **411**, 128400.

26 T. J. Prior, J. A. Armstrong, D. M. Benoit and K. L. Marshall, *CrystEngComm*, 2013, **15**, 5838–5843.

27 Y.-S. Jun, J. Park, S. U. Lee, A. Thomas, W. H. Hong and G. D. Stucky, *Angew Chem Int Ed*, 2013, **52**, 11083–11087.

28 A. Ranganathan, V. R. Pedireddi, S. Chatterjee and C. N. R. Rao, *J Mater Chem*, 1999, **9**, 2407–2411.

29 V. R. Pedireddi, S. Chatterjee, A. Ranganathan and C. N. R. Rao, *J Am Chem Soc*, 1997, **119**, 10867–10868.

30 V. Nagarajan and V. R. Pedireddi, *Cryst Growth Des*, 2014, **14**, 4803–4810.

31 J.-X. Wu, P. P. Bag, Y.-T. Xu, L. Gong, C.-T. He, X.-M. Chen and J.-P. Zhang, *Adv Mater*, 2021, **33**, 2007368.

32 T. Ungár, *Scr Mater*, 2004, **51**, 777–781.

33 I. J. Bruno, J. C. Cole, P. R. Edgington, M. Kessler, C. F. Macrae, P. McCabe, J. Pearson and R. Taylor, *Acta Crystallogr B*, 2002, **58**, 389–397.

34 B. H. Toby and R. B. Von Dreele, *J Appl Crystallogr*, 2013, **46**, 544–549.

35 O. V Dolomanov, L. J. Bourhis, R. J. Gildea, J. A. K. Howard and H. Puschmann, *J Appl Crystallogr*, 2009, **42**, 339–341.

36 G. M. Sheldrick, *Acta Crystallogr A*, 2015, **71**, 3–8.

37 G. M. Sheldrick, *Acta Crystallogr C*, 2015, **71**, 3–8.

5 CHAPTER FIVE

Mechanochemical synthesis of a PTCDI/Melamine HOF

5.1 Introduction

Self-assembled aggregates of 3,4,9,10-perylenetetracarboxylic diimide (PTCDI) and melamine (M) hydrogen-bonded aggregates on surfaces were first reported by Champness et al. in 2003.[1] The two molecules are complementary in terms of the presence and geometry of hydrogen bonding groups, and are capable of forming triple hydrogen bonding interactions as shown in Figure 5.1A. As an extended structure on surfaces, the two components can form a honeycomb network, with the hydrogen bonding capabilities of both molecules fully utilised (Figure 5.1B).[1] Later work showed that the surface substrate can influence the assembly of the components, with alternative arrays able to form.[2] These networks have been shown to be an effective template for arrangement of other molecules onto surfaces, such as fullerenes, polyoxometalate hybrid species and thiols.[2–6]

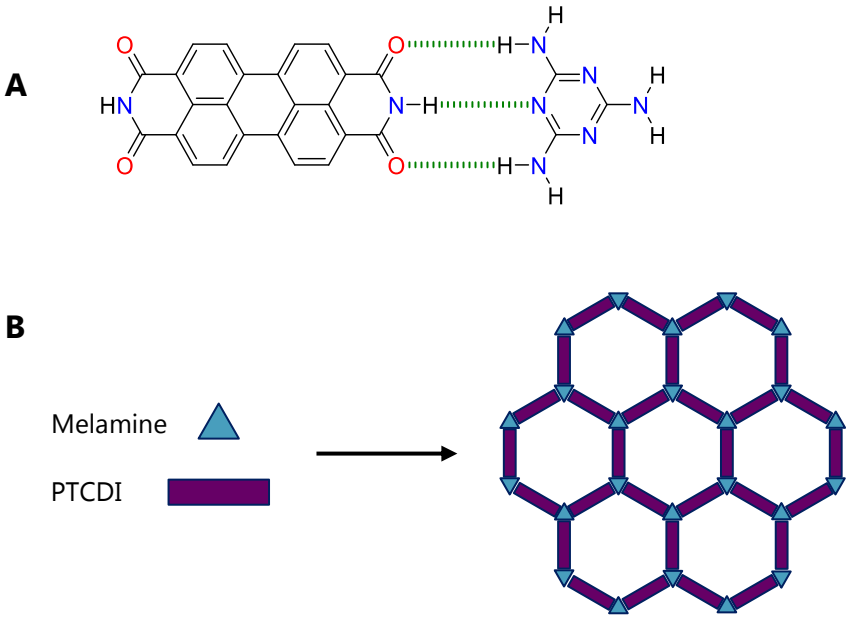


Figure 5.1: (A) End-to-end triple hydrogen-bonding interaction of PTCDI and melamine. Hydrogen bonds are represented as green dashed lines. (B) Schematic representation of the supramolecular honeycomb structure of PTCDI/M.

The surface chemistry of derivative systems has also been studied, such as those incorporating substituted PTCDI molecules or compounds with similar functionalities, such as 1,4,5,8-naphthalenetetracarboxylic diimide (NTCDI).[7–11] Interestingly, the honeycomb assembly was found to form less readily for the NTCDI/melamine analogue than for PTCDI/melamine.[10,12,13]

Despite the depth and breadth of research into the surface chemistry of PTCDI/melamine hydrogen-bonded arrays, there have been no reports thus far of this system as a bulk material. We attribute this predominantly to the significantly low solubility of PTCDI in the majority of solvents, which precludes the crystallisation of a PTCDI/M hydrogen-bonded organic framework (HOF) by conventional solution-based methods.

As described in chapter 1, mechanochemical methods have widely been used for the synthesis of co-crystals and metal-organic frameworks (MOFs).[14–16]The first examples of hydrogen-bonded organic frameworks (HOFs) by this technique have however only very recently been reported, and at the time of this project's inception there were no such examples.[17]

5.2 Aims

We proposed the use of mechanochemical techniques to synthesise a PTCDI/melamine HOF as a bulk phase. This chapter reports the method development process as well as discussion of the analysis of the resulting material. We also investigate the potential for expansion of the methodology for synthesis of a related system using NTCDI.

5.3 Results and Discussion

5.3.1 PTCDI/Melamine

Preliminary Method Development

Similarly to the method development for the mechanochemical synthesis of co-crystals discussed in Chapter 4, an "informed trial-and-error" approach was utilised to work towards the synthesis of a PTCDI-Melamine HOF. In this case there were no pre-existing single crystal synthetic methodologies to base any starting point from, largely due to the insolubility of the perylene diimide starting material which precludes synthesis via

a 'traditional' solution-phase route. Powder X-ray diffraction was used as the primary method of assessing the success of any attempted syntheses in producing crystalline framework material. The diffraction patterns of both starting materials were obtained for comparison with those of ball-milled product material (Figure 5.2).

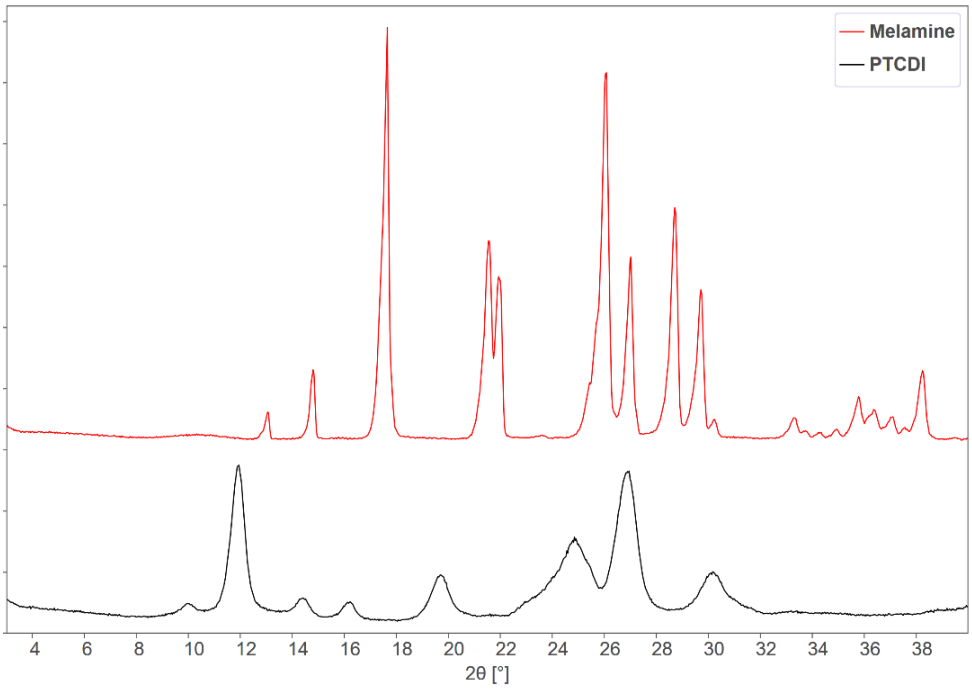


Figure 5.2: Experimental powder patterns of starting materials PTCDI (lower, black) and melamine (upper, red).

An arbitrary standard procedure was devised for initial investigations, which employed the use of a 25 mL capacity stainless steel milling jar loaded with two 10 mm diameter stainless steel balls. Approximately 100 mg of solid starting materials were used, and 100 µL of solvent to facilitate grinding. A mixer ball mill was used and milling was carried out at a frequency of 30 Hz for 45 minutes.

The first variable investigated was the solvent added as the liquid-assisted grinding (LAG) additive. Milling experiments were conducted using acetone, ethanol, methanol, THF, DMF or DEF. With the exception of the experiment using DMF, the PXRD patterns of all attempts matched up with the powder patterns of one or both starting materials. Where DMF was used as the solvent however, there was some indication of a new crystalline phase being present. Where in all other cases the diffraction pattern slopes steadily down at low values of 2θ as the background recedes, in the experiment using DMF there is a slight uplift at around 3.1° 2θ before this downturn, as well as some smaller additional peaks below 8° 2θ which do not occur in the powder patterns of the starting materials. These are marked with asterisks in Figure 5.3. The diffraction peak at 3.1° 2θ implies a d-spacing of 28.5 Å in the new phase. A lattice parameter of 34.6 Å was observed in the honeycomb structure on an Ag/Si(111) surface, so allowing for some variation in structure of the bulk phase, the data aligns approximately with our expectations for the desired honeycomb HOF structure.[1] Based on this initial promising result, we continued method development using DMF as the LAG additive.

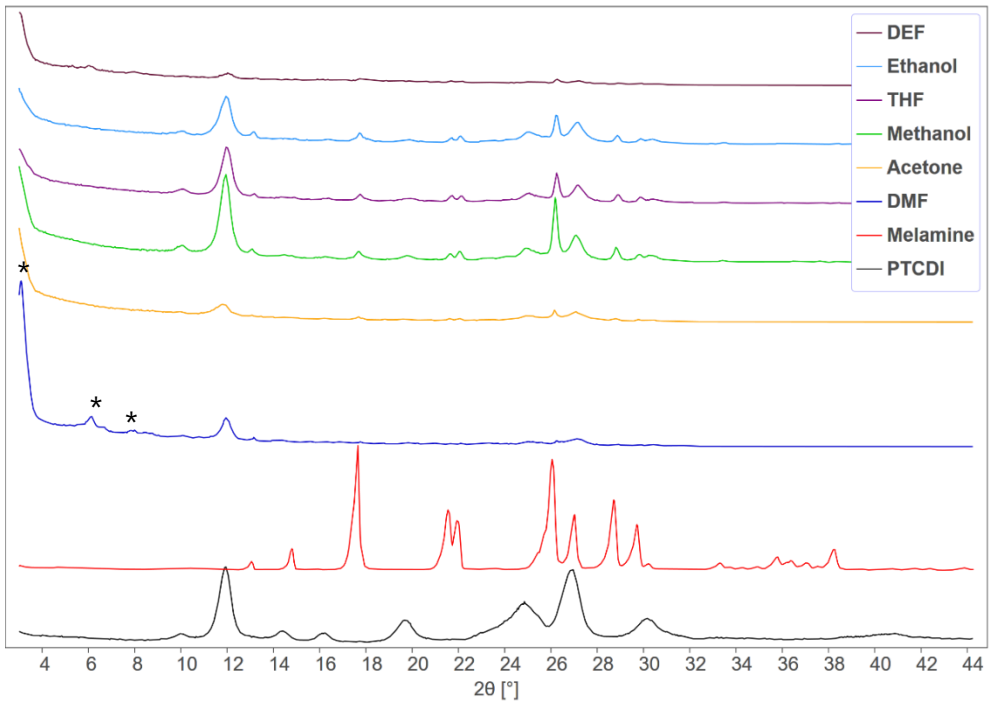


Figure 5.3: Experimental PXRD patterns of (from bottom to top) starting materials PTCDI (black) and melamine (red); milling experiments using DMF (blue), acetone (orange), methanol (green), THF (purple), ethanol (pale blue), and DEF (brown) as LAG additives.

A 1:1 molar ratio of PTCDI to melamine was used in the initial experiments. We were interested to investigate whether adjusting the amounts of each starting material with respect to one another would have any impact on the powder pattern of the resulting material. Where a 3:2 ratio of PTCDI to melamine was used, the results were similar to those obtained from a 1:1 ratio. Interestingly however, in experiments using a larger amount of melamine with respect to PTCDI (2:3 or 3:4 PTCDI:M), the appearance of the new peaks in the resulting powder pattern was significantly diminished (Figure 5.4). Subsequent experiments were conducted using the original 1:1 ratio of the two components.

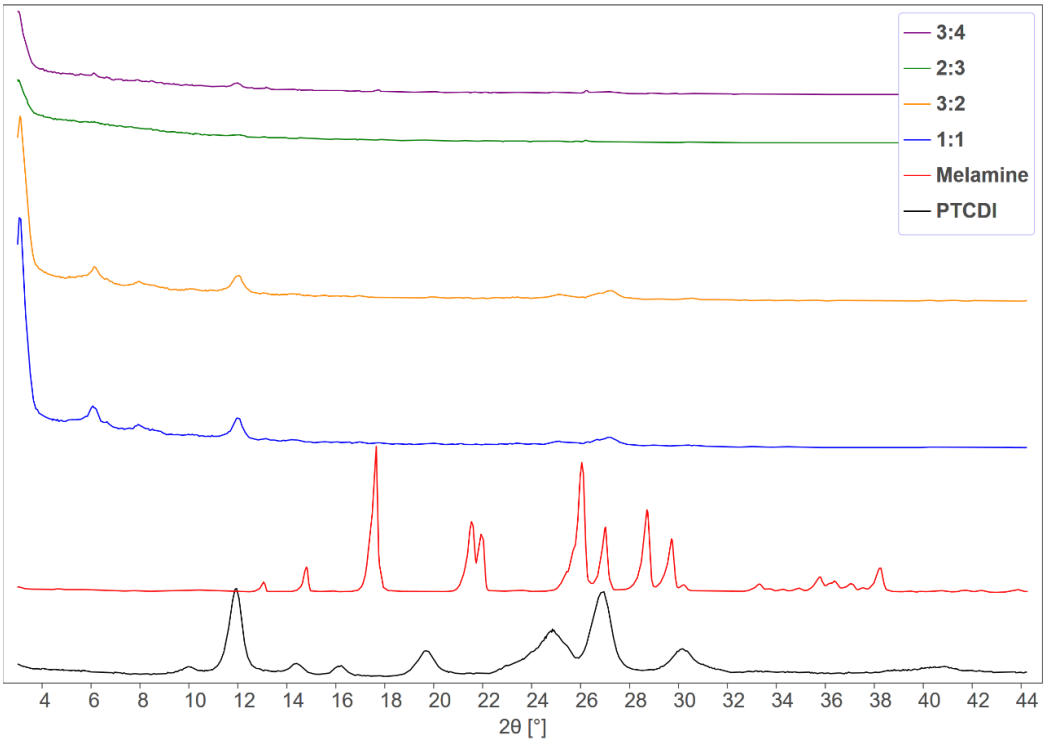


Figure 5.4: Experimental PXRD patterns of (from bottom to top): starting materials PTCDI (black), melamine (red); product of ball milling PTCDI and melamine in a 1:1 (blue), 3:2 (orange), 2:3 (green) and 3:4 (purple) molar ratio.

With initial results appearing promising, we next turned our attention to the residual peaks in the powder XRD patterns which indicate that starting material, namely PTCDI, remains present in the ball-milled product. We performed ball milling experiments with increased duration in order to investigate whether this would push the reaction further towards completion. Ball milling experiments were performed with durations from 45 minutes to 180 minutes. There were no significant differences in the profiles of the powder patterns, with peaks attributed to the presence of PTCDI still present in the pattern of the longest run (Appendix Figure 5.1). There was however a notable increase in the intensity of the new-phase peaks compared with starting material peaks in the

PXRD pattern of the 3-hour run, which may imply an improved yield of the proposed framework.

The instrument used for initial powder XRD measurements was recommended only for data collection beginning at 3° 2θ. As the most intense peak signifying the presence of the new phase is at 3.1° 2θ however, a different instrument which allowed measurements to be taken from 2.0° 2θ was later employed in order to obtain a more complete profile of the material.

Predicted structures

As the PTCDI/M system had not before been synthesised as a bulk solid, there was no existing single-crystal data which could be used for structural comparisons with our results. We collaborated for this project with a computational chemist, Dr Matthew Addicoat (Nottingham Trent University), in order to obtain predicted crystal structures. Two structures were calculated and optimised by our collaborator using Universal Force Field calculations with explicit treatment of hydrogen bonds.[18] Both predicted structures were based on the honeycomb arrangement of PTCDI and melamine molecules. One models direct 'eclipsed' stacking of honeycomb sheets in an AA fashion (Figure 5.5A and B), and the other models offset ABAB stacking of the sheets, in which the melamine 'vertices' of one layer reside above or below the hexagonal void spaces of the next (Figure 5.5C and D).

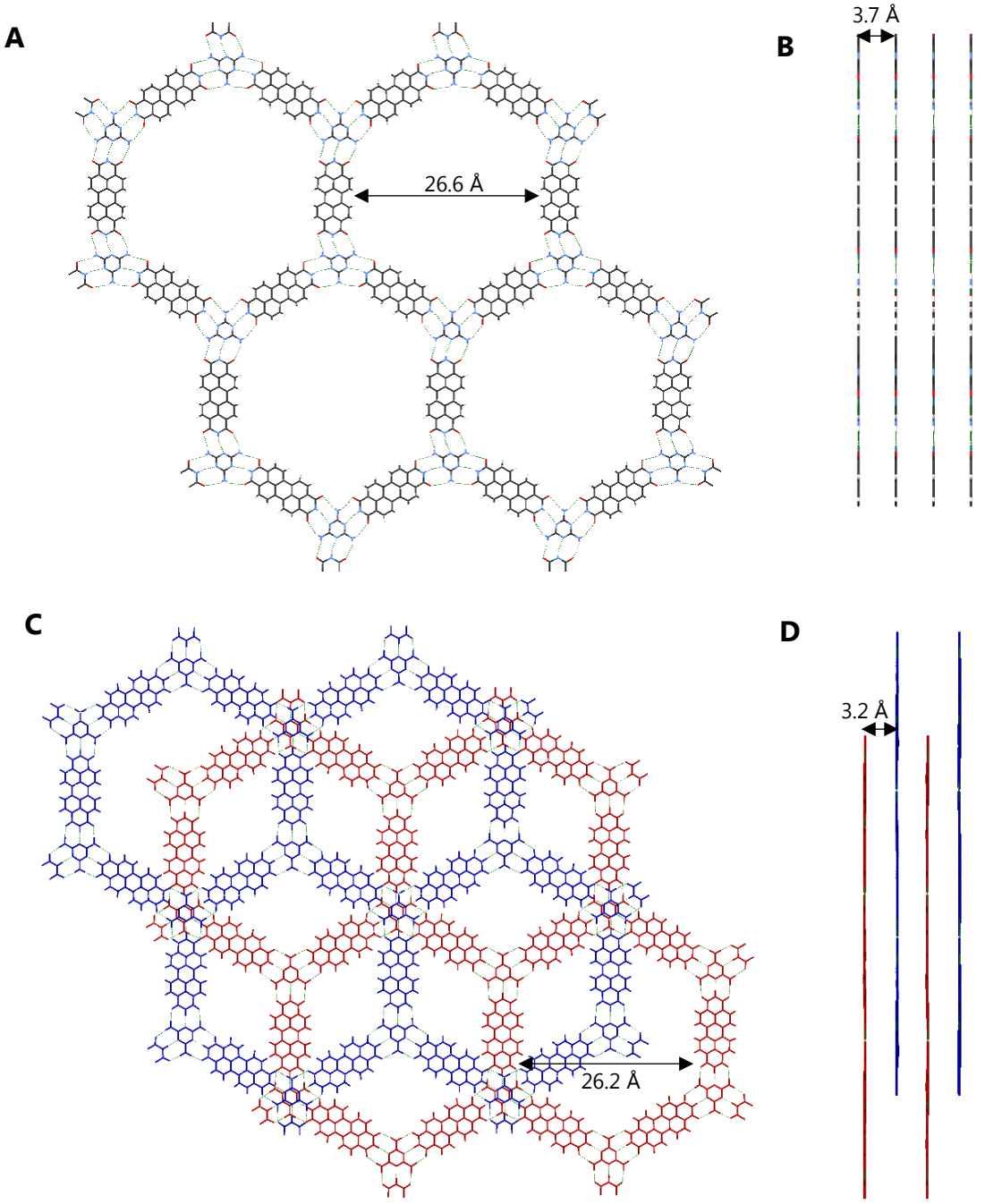


Figure 5.5: Predicted structures of PTCDI/M honeycomb HOF. (A) AA structure viewed along c-axis. (B) AA structure viewed along b-axis. (C) Layering of AB structure viewed along c-axis, colour coded to distinguish layers. (D) Stacking of AB structure viewed along b-axis.

The simulated powder diffraction pattern of each predicted structure was calculated and compared with the experimental pattern from our PTCDI/M ball milling

experiments. A strong resemblance is evident between both calculated patterns and our product (Figure 5.6), providing good evidence for the formation of a honeycomb HOF structure via ball milling. The experimental powder XRD patterns aligns more closely in terms of peak positions and overall profile with the AA-layered structure, with a lack of reflections between 14 and 18° 2θ which are the key distinguishing factor of the AB-layered structure. Peaks marked with asterisks in the experimental pattern are attributed to the presence of residual starting material.

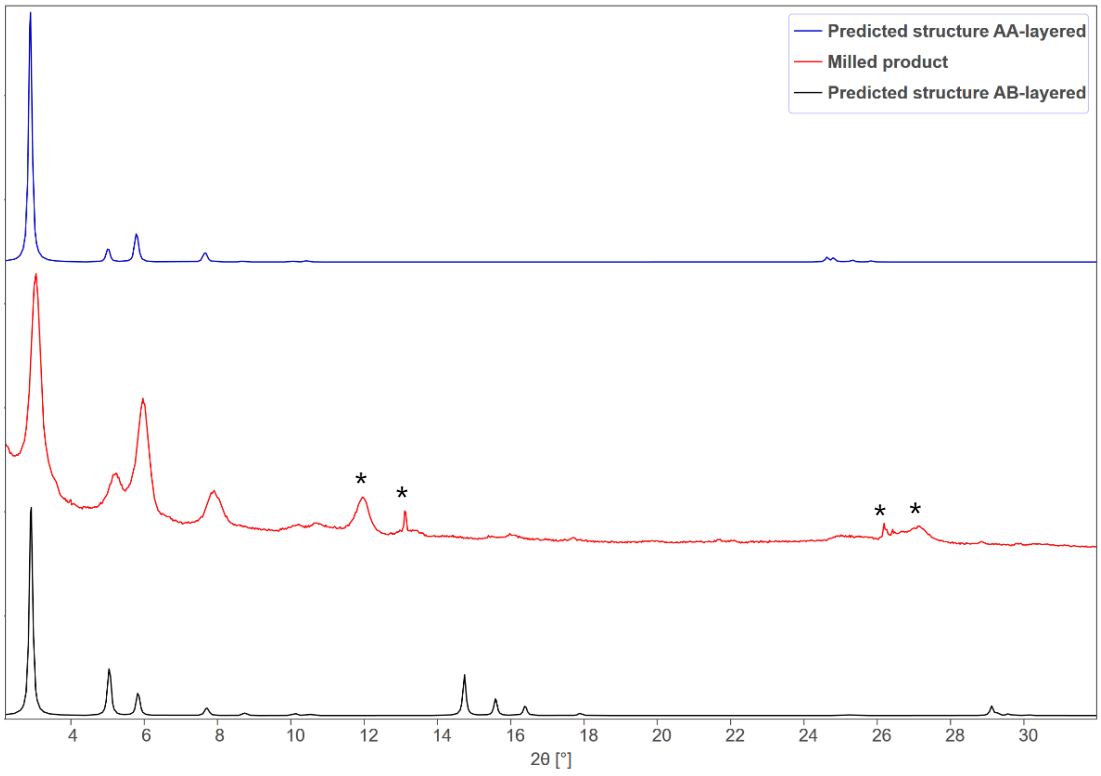


Figure 5.6: Powder XRD patterns of (from bottom to top): calculated pattern of AB predicted structure (black); experimental PTCDI/M milled product (red); calculated pattern of AA predicted structure (blue).

Further Method Development

Additional variables including the number and size of milling balls were examined for any impact on either formation of the HOF structure or presence of starting materials, but no improvements were made on the product presented above. During these proceedings however, damage was sustained to the equipment used due to the significantly low loading of milling jars and it was necessary to adapt the method. This additionally presented an opportunity for investigation into a wider range of variables which may influence the likelihood of HOF formation or lack thereof.

The manufacturer's recommendation is that the material to be milled makes up 1/3 of the volume of the milling jar. Scaled-up experiments with respect to the starting materials were therefore performed, however we found that the HOF was less likely to form under these conditions. Increasing the duration of milling time had little to no effect, and adjusting the amount of solvent with respect to the solid materials improved matters a little, however the results remained poorer than those obtained using our original optimised method (Appendix Figure 5.2).

We adapted our method to syntheses using 5 mL milling jars in place of 25 mL jars. Following optimisations of a range of parameters including the size and number of balls, mass of solid material, volume of DMF, milling frequency, and milling duration, we obtained a product of more comparable quality to that of the original optimised method, based on the experimental PXRD profiles (Figure 5.7). The factor which

appeared to have the largest effect on HOF formation was the loading of the jar, which is in line with our observations from syntheses in milling jars of larger volume.

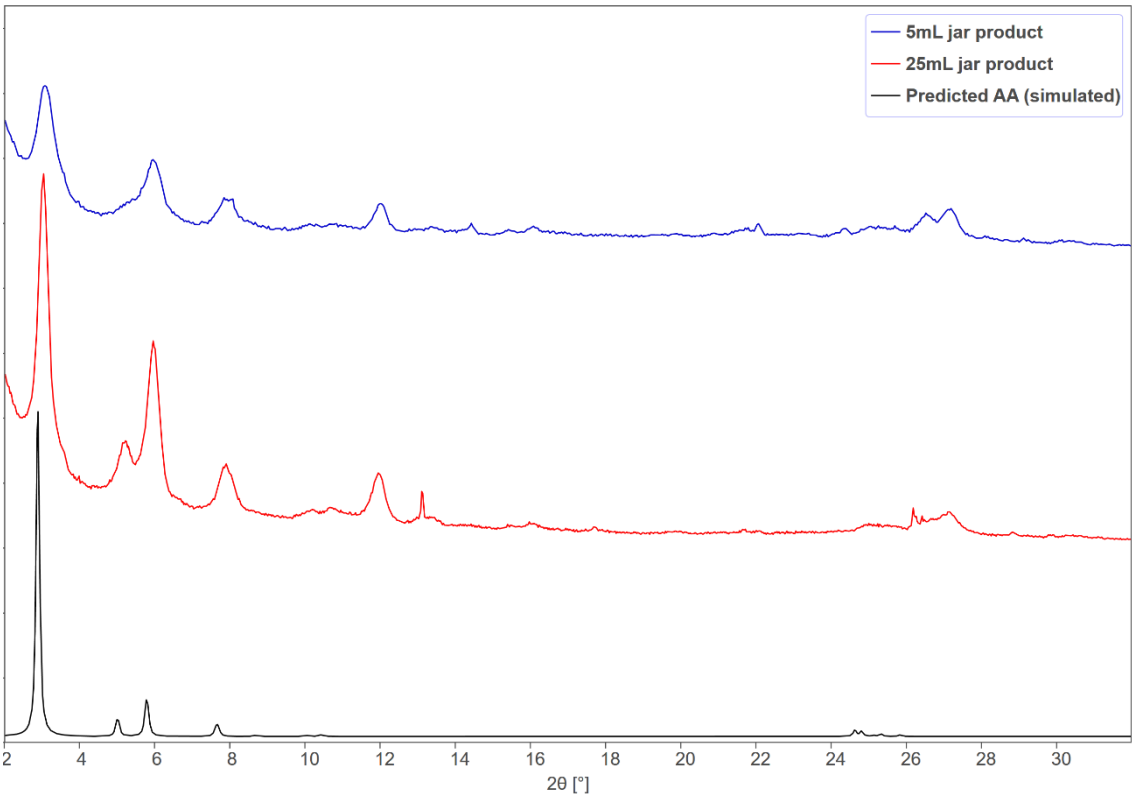


Figure 5.7: PTCDI/M HOF powder data (from bottom to top): calculated pattern of AA-layered predicted structure (black); experimental pattern of product from 25 mL jar optimised method (red); experimental pattern of product from 5 mL jar optimised method (blue).

Workup

All powder patterns discussed to this point were obtained from product material scraped from the milling jars, with no other workup involved. As the presence of starting material peaks in the PXRD patterns of milled products was ubiquitous, we investigated whether some washing of the material may help to isolate the HOF phase. Syntheses were performed using the 5mL jar optimised method, and the resulting

material extracted from the jars using ethanol, methanol, IPA or DMF. Following centrifugation, the solid material was pipetted onto a zero-background sample stage, any residual solvent was absorbed and PXRD analysis was carried out. In all cases apart from DMF extraction, starting material peaks remain in the powder patterns, and the HOF peaks are of reduced intensity in comparison with those attributed to PTCDI and/or melamine (Figure 5.8). This indicates that rather than having the desired effect of removing starting material, the use of solvent leads to the breakdown of the HOF. In the case of DMF extraction, the material is almost entirely amorphous.

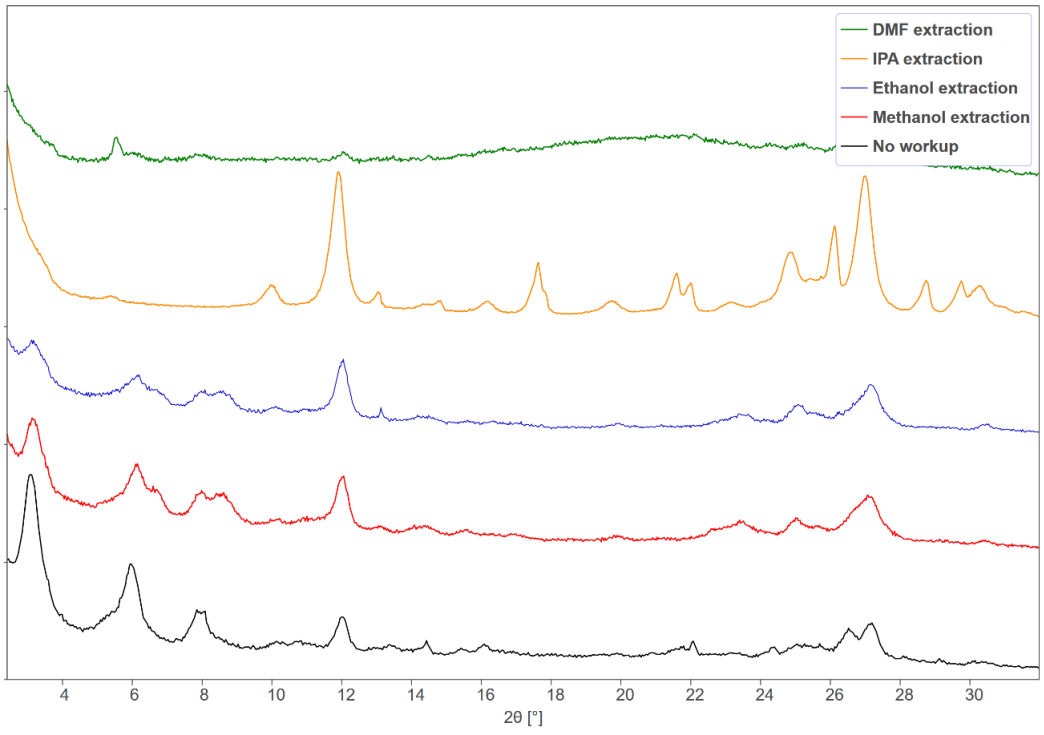


Figure 5.8: PXRD patterns of PTCDI/M milling product material obtained by (from bottom to top): direct removal of material (black); methanol extraction (red); ethanol extraction (blue); IPA extraction (orange) and DMF extraction (green).

Thermogravimetric analysis (TGA) was next carried out in order to investigate whether it may be possible to remove residual starting materials from the HOF via heating. TGA was carried out on both starting materials as well as the mechanochemical product material (Figure 5.9).

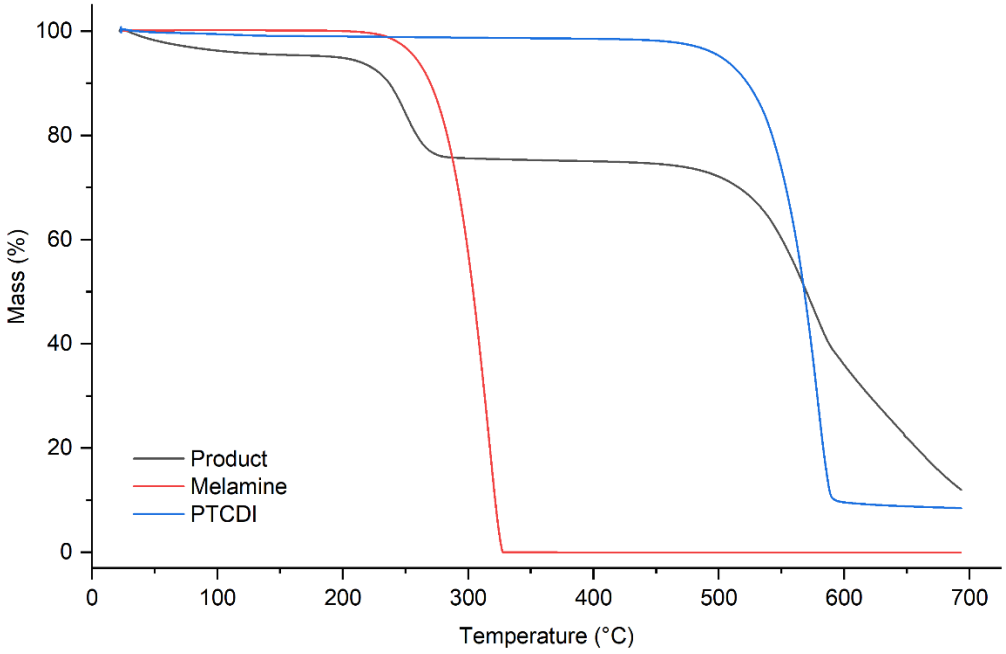


Figure 5.9: TGA profiles of mechanochemical product material (black), melamine (red) and PTCDI (blue).

There is a clear loss of mass in the product profile at 220-275°C which aligns with the decomposition temperature of melamine. Another 'step' in the profile begins at approximately 480°C and continues at a similar gradient to 585°C, which aligns with the decomposition temperature of PTCDI. A notable change in gradient occurs at 585°C however, and this continues to the maximum measurement temperature of 700°C.

Following these results, we were interested to investigate whether the material remaining after heating to 585°C may be the PTCDI/M HOF. A sample of milled product

was heated in a furnace to 600°C, and the residual material was analysed using powder XRD. The resulting powder pattern however showed that the material was amorphous, meaning no crystalline HOF remained (Appendix Figure 5.3).

5.3.2 NTCDI/Melamine

Following the successful synthesis of a PTCDI/melamine HOF by mechanochemistry, we were interested to investigate whether the method could be successfully adapted for production of similar systems. As mentioned in the introduction to this chapter, NTCDI/melamine is another system which has been studied on surfaces, however much like PTCDI/melamine it has not been obtained as a bulk solid. Similar barriers to its synthesis by solution-based methods exist, in that NTCDI is poorly soluble in many solvents. The method first tested for preparation of NTCDI/melamine HOF was based on the optimised methods for PTCDI/melamine. The initial results presented little promise, with PXRD revealing the material to be largely amorphous beside the presence of one or two starting material peaks (Figure 5.10). Some alterations to the method were made in order to assess whether changing variables such as the amounts of solid and liquid materials used, size and number of milling balls, milling duration, and milling frequency. These attempts however returned similar results.

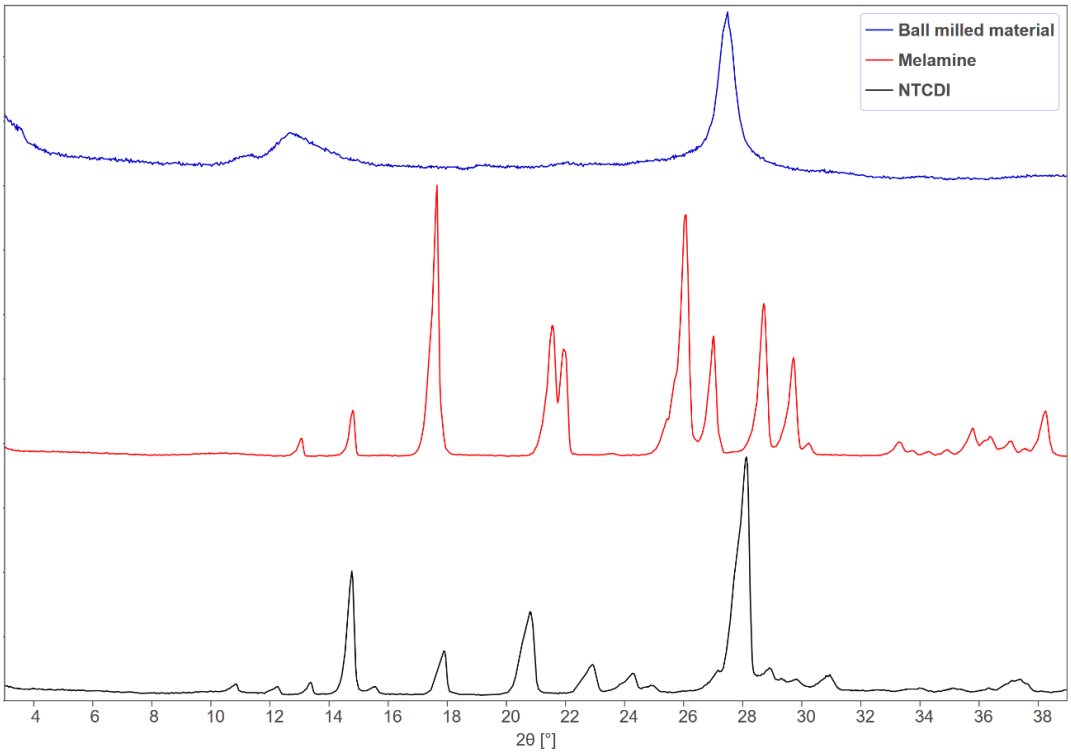


Figure 5.10: Experimental PXRD patterns of (from bottom to top): NTCDI (black), melamine (red) and NTCDI/M-DMF ball milled material (blue)

5.4 Conclusions

A PTCDI/melamine HOF was synthesised using ball milling. Powder X-ray diffraction analysis in conjunction with computationally generated predicted structures shows that the structure is likely to be a honeycomb 2D-sheet structure with direct stacking of the layers in the bulk phase. This is the first example of a two-component HOF to be synthesised using mechanochemical techniques. These results further establish the value of mechanochemical synthesis as an alternative pathway to synthesise materials which are not accessible, or not easily accessible, via more conventional solution processing methods.

We had little success in extending the method to the synthesis of an NTCDI/melamine HOF. The honeycomb arrangement of NTCDI/melamine molecules on surfaces was reportedly more challenging to obtain than the PTCDI/melamine analogue. An interesting parallel may be drawn therefore between the literature surface work results and our mechanochemical experiments.

5.5 Experimental

5.5.1 Equipment

Starting materials were purchased from Sigma Aldrich or Fluorochem and used as received. A Retsch Mixer Mill MM400 was used to conduct ball milling experiments. Infrared spectra of solids were obtained via an Agilent Fourier Transform Spectrometer, FTIR-8400S, fitted with a Diamond ATR unit. Thermogravimetric analysis was carried out using a PerkinElmer TGA8000.

Powder X-ray diffraction measurements were carried out at 298K using either a Bruker D8 Advance diffractometer (λ (CuKα1) = 1.5406 Å), or a PANalytical Empyrean diffractometer (λ (CuKα1) = 1.5406 Å) mounted on either a welled or zero background sample stage.

5.5.2 Reaction Procedures

PTCDI/M HOF: 25 mL Jar Optimised Method

A 25 mL stainless steel milling jar was loaded with two 10 mm stainless steel milling balls. PTCDI (78 mg, 0.2 mmol), melamine (25 mg, 0.2 mmol) and DMF (100 μL) were added and the jar was firmly tightened. Milling was conducted for 3 hours at 30 Hz, following which the jar was left open to the air for 1 hour, the deep purple solid was scraped from the jar and analysed as-is by powder X-ray diffraction.

PTCDI/M HOF: 5 mL Jar Optimised Method

A 5 mL stainless steel milling jar was loaded with two 7 mm stainless steel milling balls. PTCDI (20 mg, 0.05 mmol), melamine (5 mg, 0.05 mmol) and DMF (25 µL) were added and the jar was firmly tightened. Milling was conducted for 3 hours at 30 Hz, following which the jar was left open to the air for 1 hour, the deep purple solid was scraped from the jar and analysed as-is by powder X-ray diffraction.

Synthesis of NTCDI

Naphthalene-1,4,5,8-tetracarboxylic dianhydride (1.0 g, 3.7 mmol) was stirred in glacial acetic acid (30 mL) at room temperature. Ammonium acetate (4.0 g, 51.8 mmol, 14 eq.) was added and the reaction mixture was heated at reflux for 24 hours. The resulting mixture was filtered, washed with copious water and the yellow solid was dried under vacuum. Yield: 0.88 g, 89%.

IR (ATR): 3174 (ν N-H), 3071, 2862 (ν C-H), 1679 (ν C=O), 1581 (ν C=C).

PXRD:

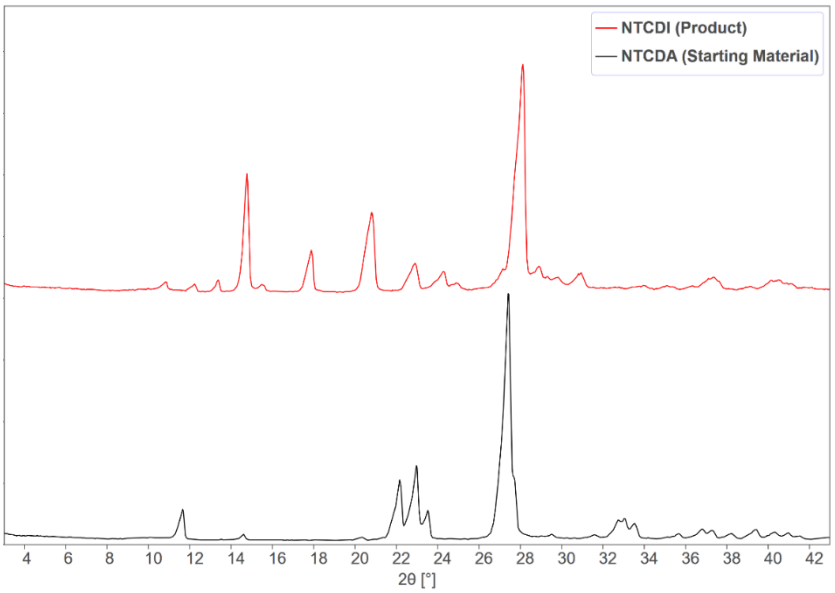


Figure 5.11: Powder XRD patterns of NTCDA (black, lower) and NTCDI (red, upper).

5.6 References

1 J. A. Theobald, N. S. Oxtoby, M. A. Phillips, N. R. Champness and P. H. Beton, *Nature*, 2003, **424**, 1029–1031.

2 F. Silly, A. Q. Shaw, K. Porfyrakis, G. A. D. Briggs and M. R. Castell, *Appl Phys Lett*, 2007, **91**, 253109.

3 A. Lombana, C. Rinfray, F. Volatron, G. Izzet, N. Battaglini, S. Alves, P. Decorse, P. Lang and A. Proust, *J Phys Chem C*, 2016, **120**, 2837–2845.

4 A. Saywell, G. Magnano, C. J. Satterley, L. M. A. Perdigão, N. R. Champness, P. H. Beton and J. N. O'Shea, *J Phys Chem C*, 2008, **112**, 7706–7709.

5 L. M. A. Perdigão, P. A. Staniec, N. R. Champness and P. H. Beton, *Langmuir*, 2009, **25**, 2278–2281.

6 R. Madueno, M. T. Räisänen, C. Silien and M. Buck, *Nature*, 2008, **454**, 618–621.

7 M. T. Räisänen, A. G. Slater (née Phillips), N. R. Champness and M. Buck, *Chem Sci*, 2012, **3**, 84–92.

8 A. J. Pollard, E. W. Perkins, N. A. Smith, A. Saywell, G. Goretzki, A. G. Phillips, S. P. Argent, H. Sachdev, F. Müller, S. Hüfner, S. Gsell, M. Fischer, M. Schreck, J. Osterwalder, T. Greber, S. Berner, N. R. Champness and P. H. Beton, *Angew Chem Int Ed*, 2010, **49**, 1794–1799.

9 L. M. A. Perdigão, A. Saywell, G. N. Fontes, P. A. Staniec, G. Goretzki, A. G. Phillips, N. R. Champness and P. H. Beton, *Chem Eur J*, 2008, **14**, 7600–7607.

10 L. M. A. Perdigão, G. N. Fontes, B. L. Rogers, N. S. Oxtoby, G. Goretzki, N. R. Champness and P. H. Beton, *Phys Rev B*, 2007, **76**, 245402.

11 A. G. Phillips, L. M. A. Perdigão, P. H. Beton and N. R. Champness, *Chem Comm*, 2010, **46**, 2775–2777.

12 C.-A. Palma, J. Bjork, M. Bonini, M. S. Dyer, A. Llanes-Pallas, D. Bonifazi, M. Persson and P. Samorì, *J Am Chem Soc*, 2009, **131**, 13062–13071.

13 J. Teyssandier, N. Battaglini, M. Seydou, G. Anquetin, B. Diawara, X. Sun, F. Maurel and P. Lang, *J Phys Chem C*, 2013, **117**, 8737–8745.

14 M. Klimakow, P. Klobes, A. F. Thünemann, K. Rademann and F. Emmerling, *Chem Mater*, 2010, **22**, 5216–5221.

15 S. Głowniak, B. Szczęśniak, J. Choma and M. Jaroniec, *Mater Today*, 2021, **46**, 109–124.

16 T. Friščić, in *Encyclopedia of Inorganic and Bioinorganic Chemistry*, 2014, pp. 1–19.

17 W.-K. Qin, D.-H. Si, Q. Yin, X.-Y. Gao, Q.-Q. Huang, Y.-N. Feng, L. Xie, S. Zhang, X.-S. Huang, T.-F. Liu and R. Cao, *Angew Chem Int Ed*, 2022, **61**, e202202089.

18 D. E. Coupry, M. A. Addicoat and T. Heine, *J Chem Phys*, 2017, **147**, 161705.

6 CONCLUSIONS

The research presented in this thesis surrounds the synthesis and analysis of a range of metal-organic and hydrogen-bonded organic framework materials. The primary focus of this work was to explore how subtle changes in synthetic conditions, or the use of different techniques, can influence the resulting structures. The second and third chapters provide insights into the importance of maintaining methodological consistency during framework material synthesis, as well as the capability to leverage this sensitivity for control over the product(s).

In Chapter 2, methyl-substituted 1,3-bis(4-carboxyphenyl)imidazolium linkers were employed in the synthesis of five new copper MOFs. The outcomes of the syntheses were influenced by the number of methyl substituents, the counterion associated with the linker, reaction duration and choice of solvent. Among the newly synthesised structures, four were constructed of MOF nets with sql topology, consistent with structures reported in the literature. The nets were either polycatenated or layered to form the extended structure. This study contributes to a more comprehensive understanding of the range of supramolecular architectures obtainable, by exercising control over synthetic conditions.

Next, Chapter 3 presents five new hydrogen-bonded organic frameworks constructed from tetracarboxylic acid and di-amidinium components. The non-linearity and flexibility of the carboxylate linkers, imparted by a central imidazolium moiety and

methylene bridging groups respectively, are notable in comparison with the rigid, more geometrically regular compounds conventionally leveraged in HOF constructions. All structures were assembled in layers formed of hydrogen-bonded sheets of differing geometries. Methyl substitution at the N-**C**-N carbon and the extent of carboxylate linker deprotonation were controlled in order to explore the modes of hydrogen bonding interactions and the subsequent influence on the overall structure. These experiments culminated in the formation of a potentially porous HOF containing channels with the imidazolium group available for coordination. Little success was had in preliminary experiments exploring the potential for metal complex incorporation into this structure, however future studies may yield more concrete conclusions in this area.

In the third and fourth chapters, mechanochemical techniques were used for the preparation of hydrogen-bonded co-crystals and HOFs. The findings were compared with literature preparations for similar systems, where reported, in order to investigate the extent of concurrence between different synthetic methodologies.

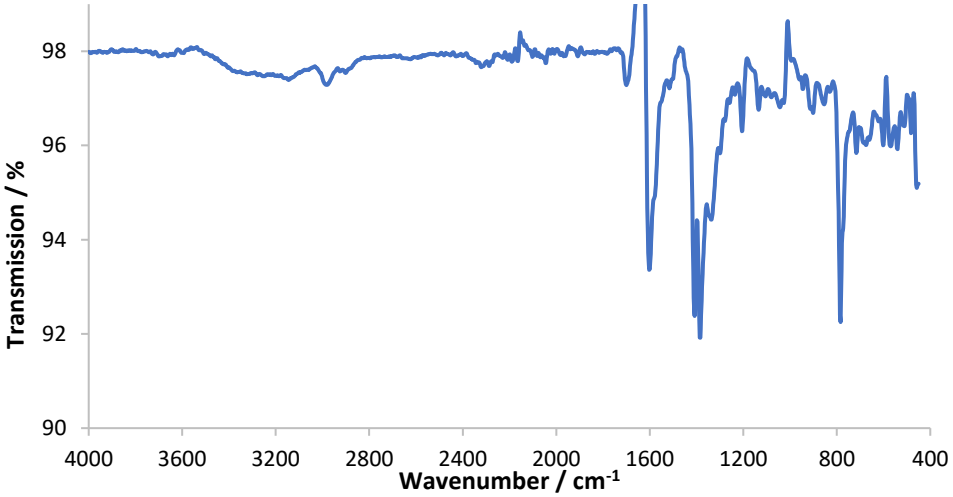
Accordingly, ten 2-component co-crystal systems involving cyanuric acid or trithiocyanuric acid were investigated in Chapter 4. The complementary molecules paired with each of these starting materials were melamine, 4,4’-bipyridyl, trans-1,2-dipyridylethene, triazine and pyrazine. A reliable mechanochemical methodology was developed for the formation of co-crystal phases using the materials of interest. Powder XRD analysis of the products was compared with relevant structures recorded

in the CSD to identify the phase formed. Known phases were produced in some cases, however some of the mechanochemical products did not align with known structures recorded in the CSD, suggesting novel structures have been synthesised. Identification of these new phase is a promising avenue for future studies.

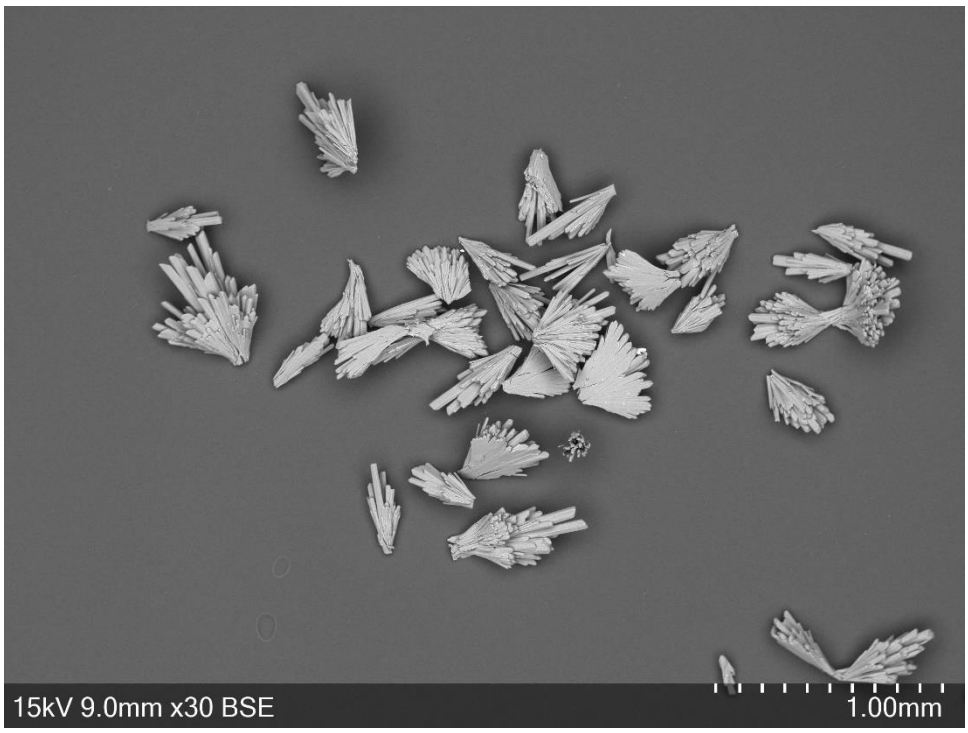
The method development performed in Chapter 4 provided a foundation for the work in Chapter 5. Here, the first example of a mechanochemically synthesised hydrogen-bonded organic framework is reported. The HOF is composed of PTCDI and melamine which is of additional significance as formation of this system has only previously been achieved on surfaces. Computational modelling assisted the identification of the HOF phase as a honeycomb 2-dimensional sheet structure with direct stacking of the layers. In addition to the achievement of obtaining this elusive bulk-phase HOF, this work highlights the relevance of non-conventional techniques such as mechanochemistry for the discovery of new materials. Reproduction of these results for an analogous NTCDI and melamine HOF was at this stage unsuccessful, which mirrors observations in the surface chemistry of these systems.

7 APPENDIX

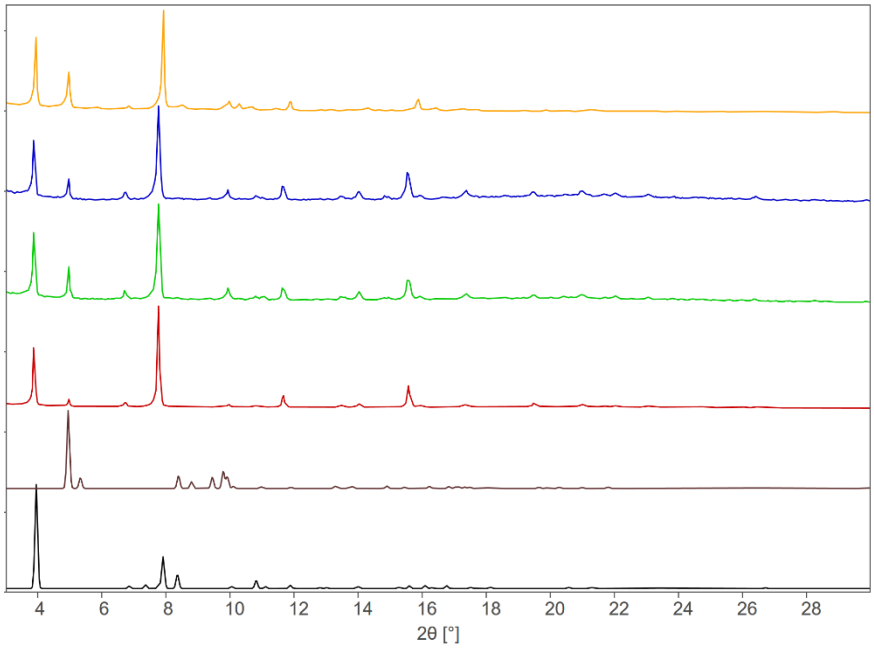
Chapter 2



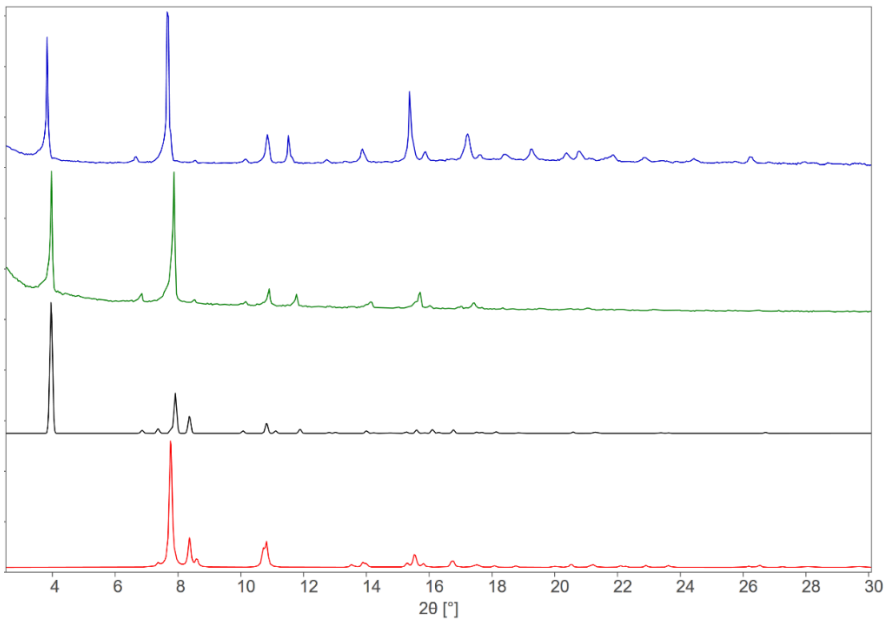
Appendix Figure 2.1: IR spectrum of 2-HexMOF, with DMA used as background.



Appendix Figure 2.2: SEM image of crystals resulting from **2-HexMOF** synthesis.

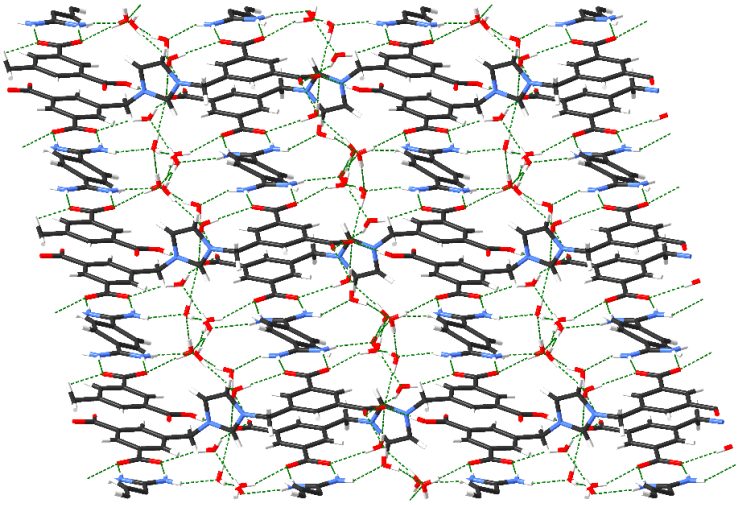


Appendix Figure 2.3: Powder XRD patterns of material obtained from MOF syntheses of different durations using DMF as the solvent. From bottom to top: calculated patterns of **2-HexMOF** (black) and **2-2DMOF-2** (brown); and experimental patterns from syntheses of duration 4 hours (red), 8 hours (green), 14 hours (blue) and 16 hours (orange).



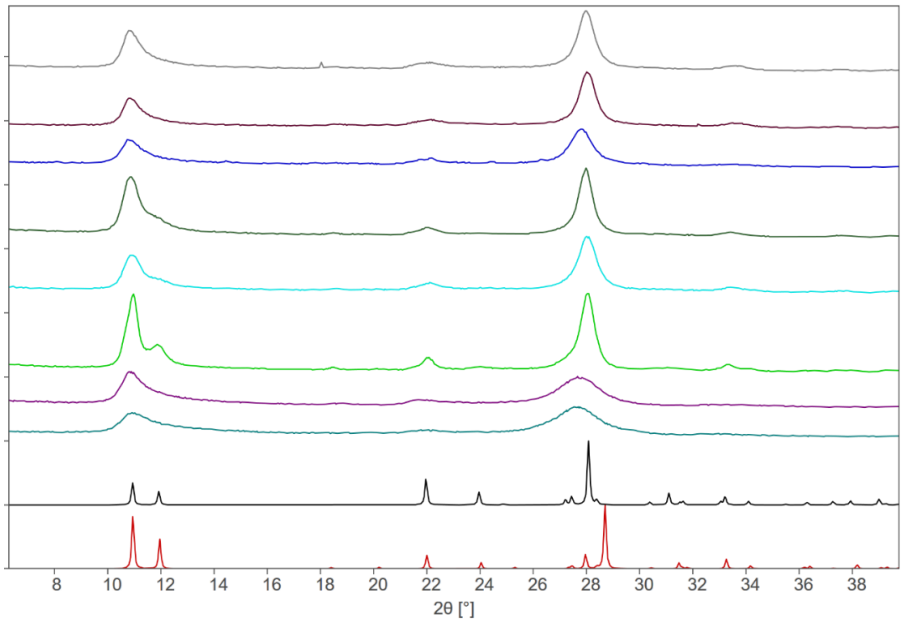
Appendix Figure 2.4: Powder XRD patterns of material obtained from MOF syntheses with acetic acid modulator. From bottom to top: calculated patterns of CIWWAJ (red) and **2-HexMOF** (black), and experimental patterns from syntheses with no modulator added (green) and acetic acid modulator added (blue).

Chapter 3

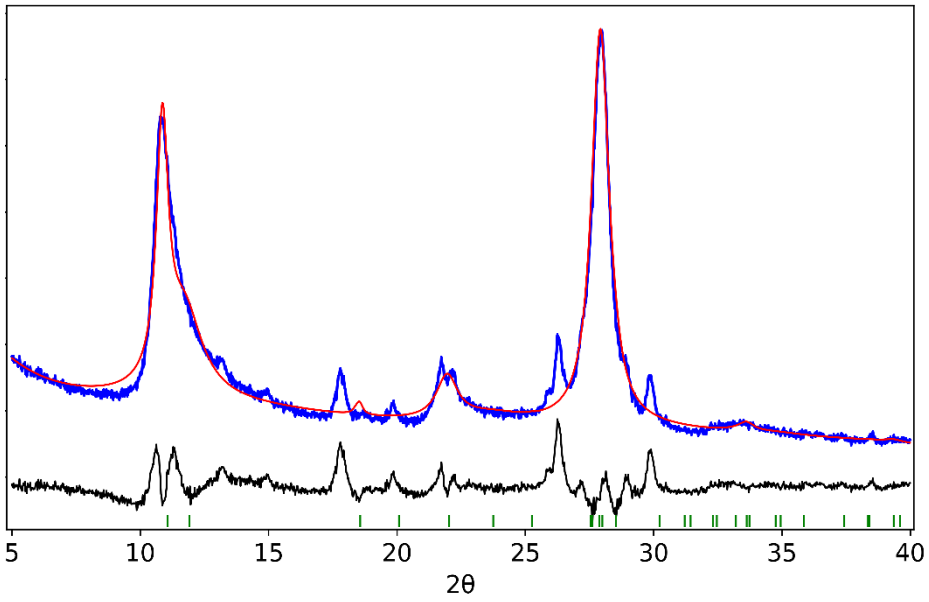


Appendix Figure 3.1: View down b-axis of HOF E, showing hydrogen-bonded network of water molecules throughout the structure.

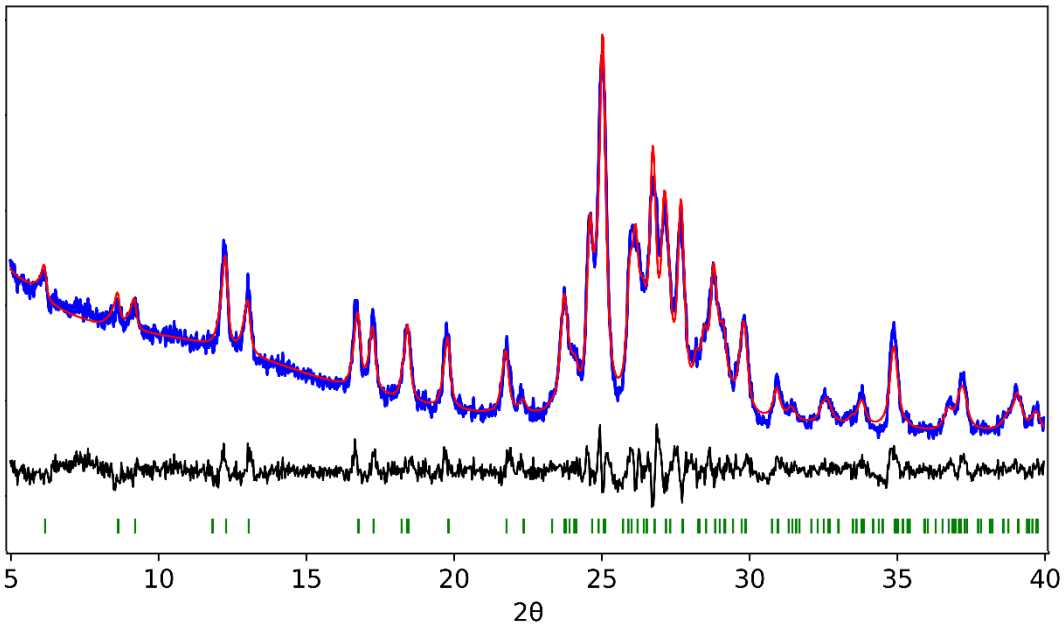
Chapter 4



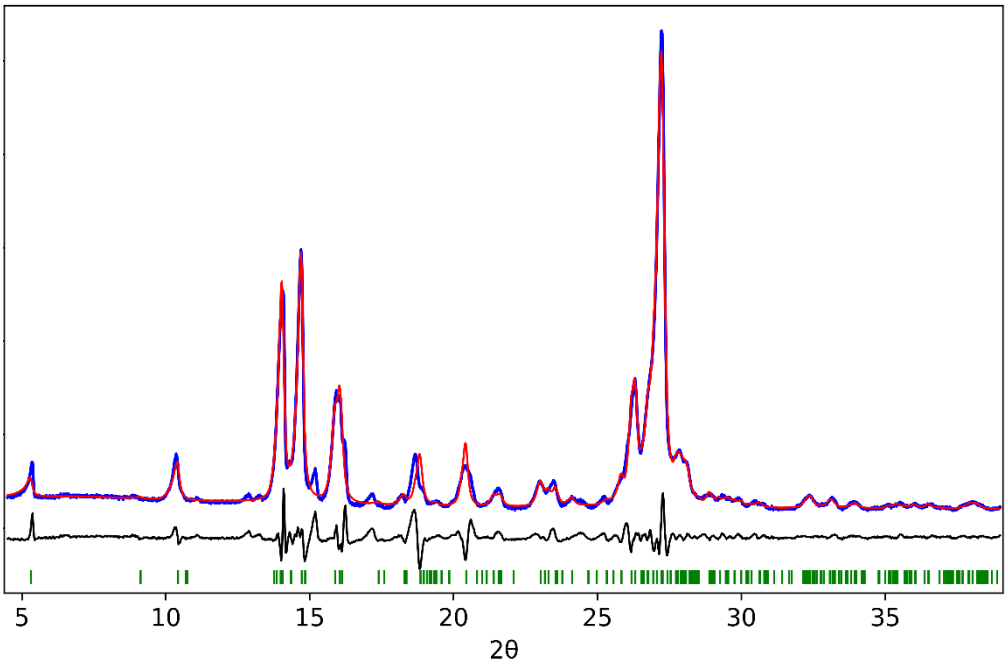
Appendix Figure 4.1: Powder XRD patterns of CA/M milling products from syntheses using various volumes of DMF. From bottom to top: calculated patterns of QACSUI01 (red) and QACSUI (black) and experimental patterns of syntheses using no solvent (teal), 10 µL DMF (purple), 25 µL DMF (pale green), 50 µL DMF (turquoise), 75 µL DMF (dark green), 100 µL DMF (blue), 125 µL DMF (maroon) and 150 µL DMF (grey).



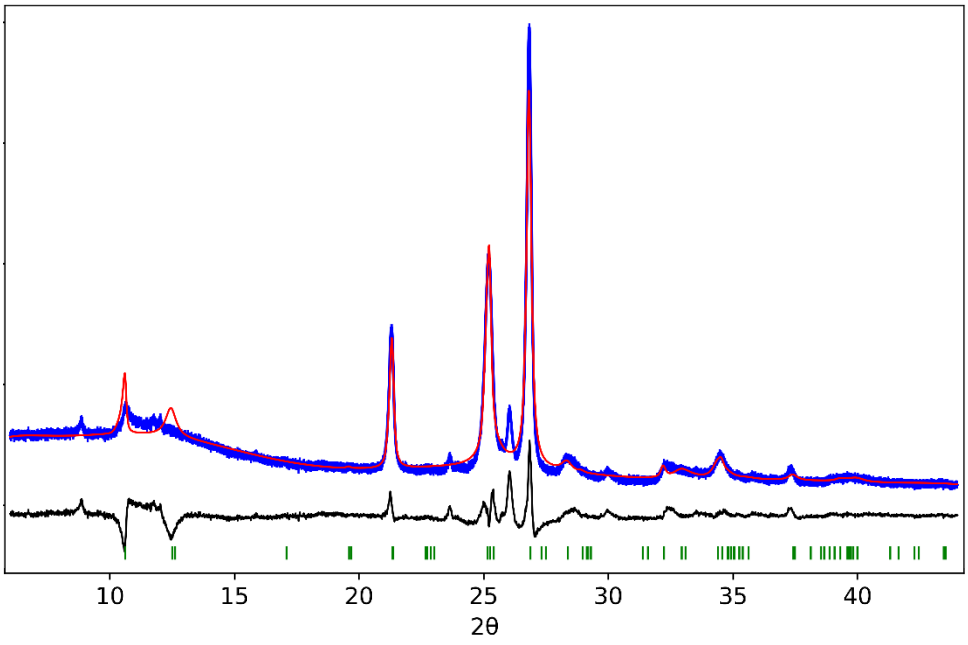
Appendix Figure 4.2: Experimental (blue ticks), calculated (red line), difference plot (I_{obs}-I_{calc}) (black line, botttom panel) and Bragg positions (green ticks, bottom panel) for the LeBail refinement of experimental diffraction data of CA/M-MeOH collected at room temperature by using single crystal data from QACSUI as starting parameters.



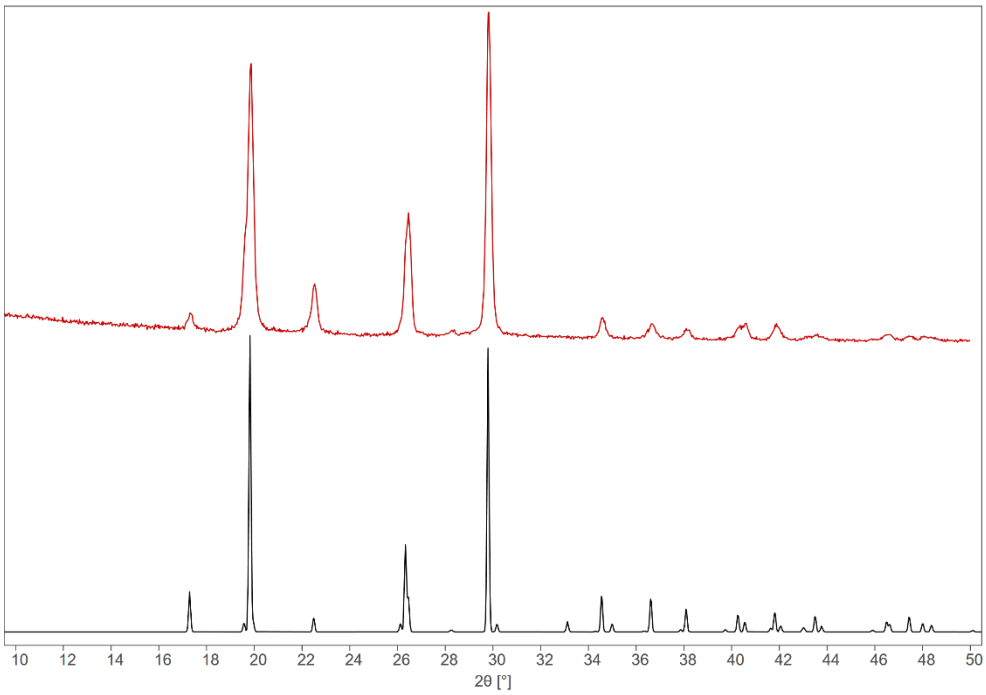
Appendix Figure 4.3: Experimental (blue ticks), calculated (red line), difference plot (I_{obs}-I_{calc}) (black line, botttom panel) and Bragg positions (green ticks, bottom panel) for the LeBail refinement of experimental diffraction data of TCA/M-MeOH collected at room temperature by using single crystal data from QACTAP01 as starting parameters.



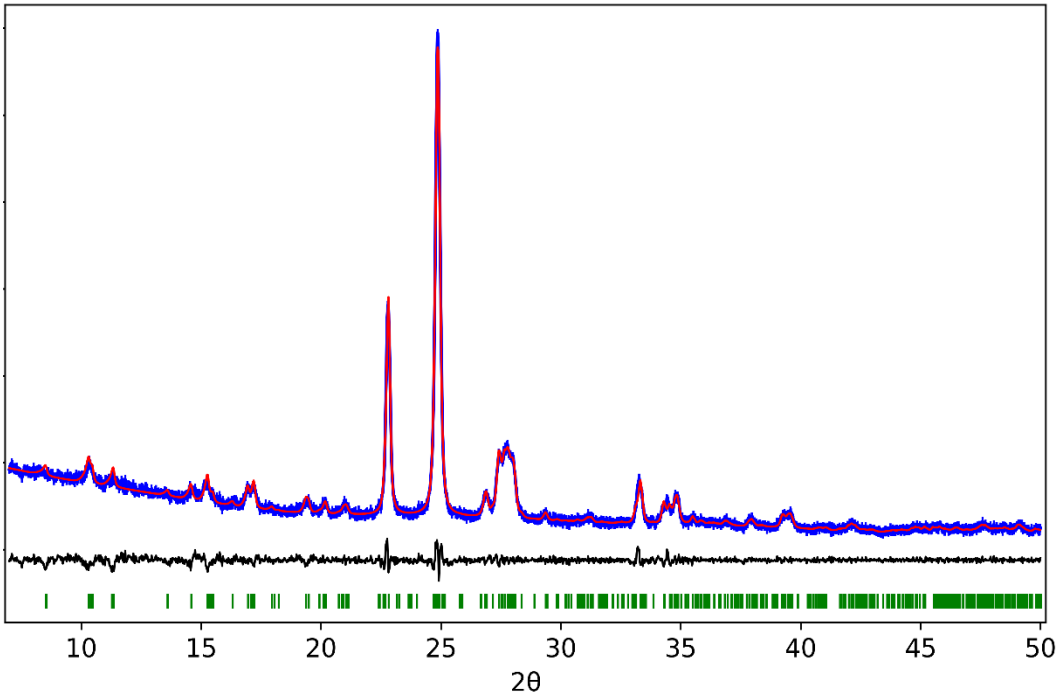
Appendix Figure 4.4: Experimental (blue ticks), calculated (red line), difference plot (I_{obs}-I_{calc}) (black line, botttom panel) and Bragg positions (green ticks, bottom panel) for the LeBail refinement of experimental diffraction data of CA/DPE-MeOH collected at room temperature by using single crystal data from HADKUT as starting parameters.



Appendix Figure 4.5: Experimental (blue ticks), calculated (red line), difference plot (I_{obs}-I_{calc}) (black line, botttom panel) and Bragg positions (green ticks, bottom panel) for the LeBail refinement of experimental diffraction data of TCA/TAZ-MeOH collected at room temperature by using single crystal data from FOSDUP as starting parameters.

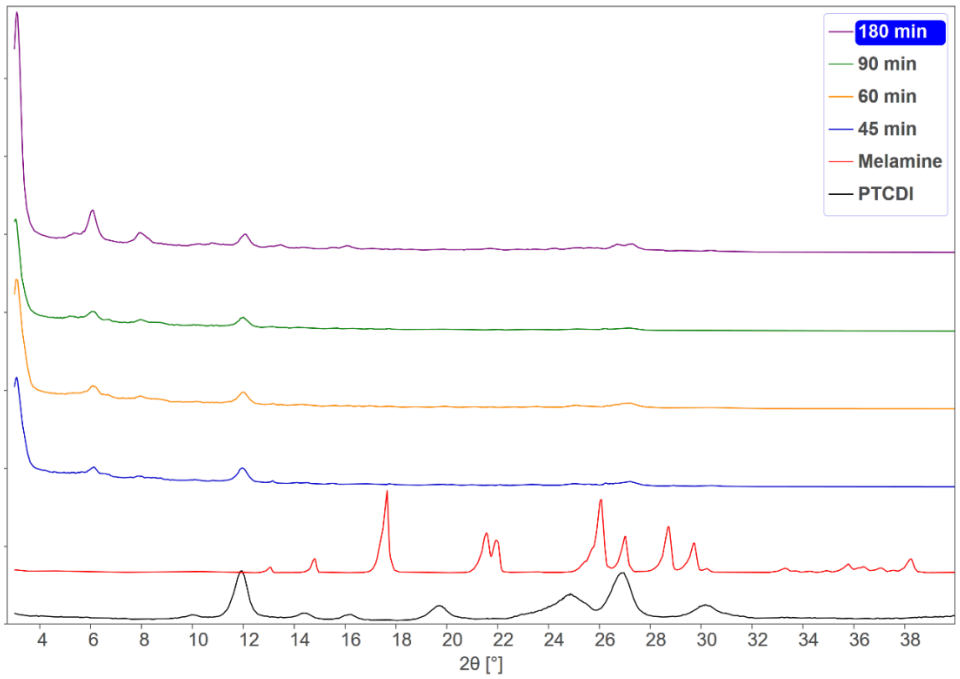


Appendix Figure 4.6: Powder XRD patterns of cyanuric acid (calculated from CSD CYURAC10) (lower, black) and the product of milling cyanuric acid and pyrazine in DMF (upper, red).

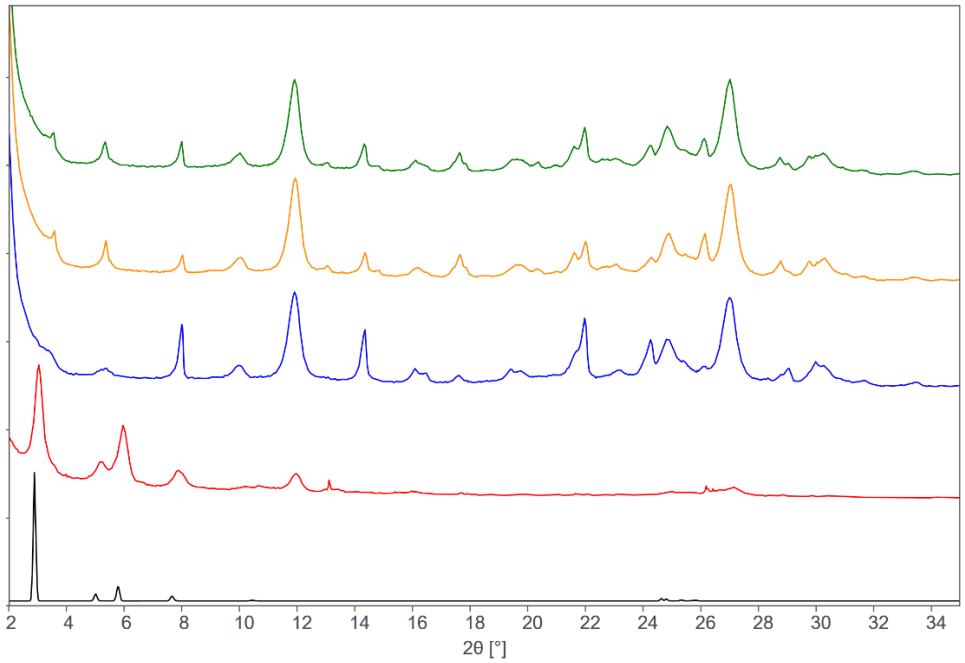


Appendix Figure 4.7: Experimental (blue ticks), calculated (red line), difference plot (I_{obs}-I_{calc}) (black line, bottom panel) and Bragg positions (green ticks, bottom panel) for the LeBail refinement of experimental diffraction data of TCA/PAZ-MeOH collected at room temperature by using single crystal data from FOSFAX as starting parameters.

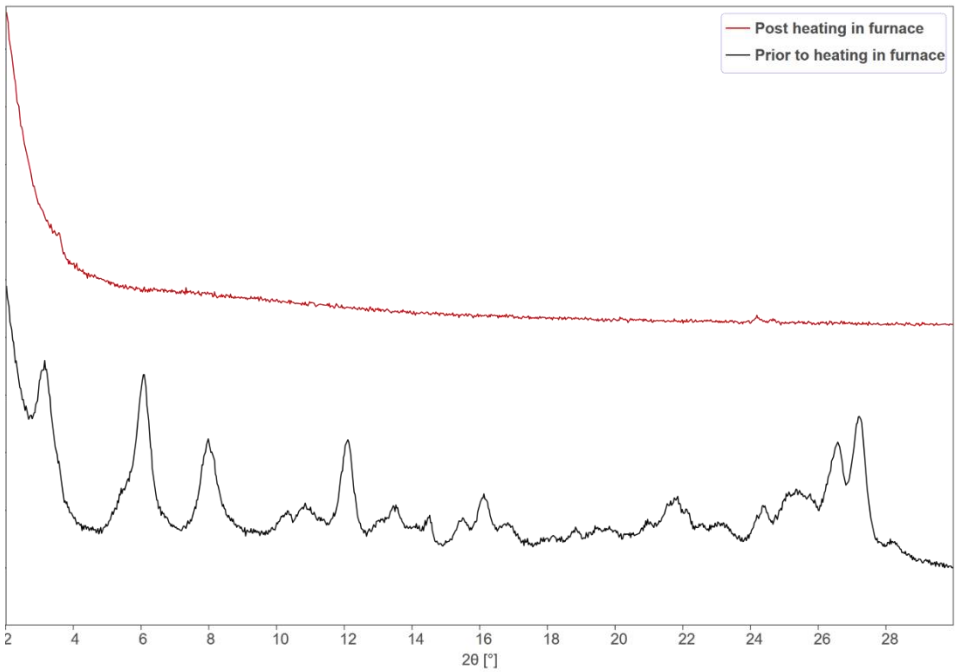
Chapter 5



Appendix Figure 5.1: Powder XRD patterns of PTCDI/M milling products from different experiment durations. From bottom to top: experimental patterns of starting materials PTCDI (black) and melamine (red); and ball-milled syntheses with durations 45 minutes (blue), 60 minutes (orange), 90 minutes (green) and 180 minutes (purple).



Appendix Figure 5.2: Powder XRD patterns of PTCDI/melamine (from bottom to top): calculated pattern of AA-layered predicted structure (black); experimental pattern of product obtained from optimised method (red); product from 5x scaled-up synthesis, milling time 3h (blue); product from scaled-up synthesis with a reduced volume of solvent added, milling time 3h (orange); product from scaled-up synthesis with reduced solvent volume, milling time 7.5h.



Appendix Figure 5.3: Powder XRD patterns of PDI/melamine HOF as-synthesised (lower, black) and after heating to 700°C (upper, red).